Mobile Rayleigh Fading Channels: Modeling, Estimation and Achievable Information Rates

Rauf Iqbal

BSc (Electrical Engineering)

August 2009

A THESIS SUBMITTED FOR THE DEGREE OF DOCTOR OF PHILOSOPHY
OF THE AUSTRALIAN NATIONAL UNIVERSITY

Applied Signal Processing Group
Department of Information Engineering
Research School of Information Sciences and Engineering
The Australian National University

Declaration

The contents of this thesis are the results of original research and have not been submitted for a higher degree to any other university or institution.

Much of the work in this thesis has been published, has been submitted or is to be submitted for publication as journal papers or conference proceedings. These papers are:

1. Rauf Iqbal, Thushara D. Abhayapala, Tharaka A. Lamahewa and Javed Ahmed, "Achievable Information Rates Over Generalized Rayleigh Fading Channels", To be submitted to *IEEE Transactions on Wireless Communications*, Jan/Feb 2010. [Impact Factor: 1.184]

2. Rauf Iqbal, Thushara D. Abhayapala, Parastoo Sadeghi and Javed Ahmed,"Mobile Rayleigh Fading Channels: A Technique to Improve Performance of PACE Using Modified Peaky Signaling", To be submitted to *IEEE Transactions on Wireless Communications*, Jan/Feb 2010.

3. Rauf Iqbal, Thushara D. Abhayapala, Javed Ahmed and Tharaka A. Lamahewa, "Statistical Characterization of a Type of non-WSS Mobile Rayleigh Fading Channels", To be submitted to *IET Communications*, Jan/Feb 2010. [Impact Factor: 0.533]

4. T. A. Lamahewa, T. D. Abhayapala, Rauf Iqbal and Chandra Athaudage,"A Framework to Calculate Space-Frequency Correlation in Multi-carrier Systems", A Revision Submitted to *IEEE Transactions on Wireless Communications*, Jun. 2009.

5. Rauf Iqbal, Thushara D. Abhayapala, Javed Ahmed and Tharaka A. Lamahewa, "Wigner-Ville Distribution of a Type of Non-Stationary Mobile Rayleigh Fading Channels", in *Proc. IEEE International Multitopic Conference (INMIC)*, December 2009, Islamabad, Pakistan.

6. Rauf Iqbal, Thushara D. Abhayapala and Javed Ahmed and Tharaka Lamahewa," Improved Performance of Gaussian Signaling Over Mobile Rayleigh Fading Channels in the Low SNR Regime", Accepted in *The 7th International Bhurban Conference on Applied Sciences & Technology (IBCAST)*, Islamabad, Pakistan , Jan. 2010.

7. Rauf Iqbal, Thushara D. Abhayapala, Parastoo Sadeghi, " A technique to improve MMSE performance of PACE in time-selective Rayleigh Fading Channels", in *Proc. 11th Canadian Workshop on Information Theory* (CWIT), pp. 175-160, Ottawa, Canada, May 2009.

8. Rauf Iqbal, Parastoo Sadeghi, and Thushara D. Abhayapala, "Constant Power Signaling in Rayleigh Fading Channels: Joint Output Probability Distribution and Information Rate Bounds", in *Proc. 2009 World Congress on Computer Science and Information Engineering* (CSIE 2009) ,Los Angeles/Anaheim, USA, Mar-Apr 2009.

9. Rauf Iqbal, Thushara D. Abhayapala, and Tharaka A. Lamahewa, " Generalised Clarke Model for Mobile Radio Reception", *IET Communications*, pp. 644-654, Apr. 2009. [Impact Factor: 0.533]

10. Rauf Iqbal and Thushara D. Abhayapala,"On Statistics of the Mobile Rayleigh Fading Channel in Non-Isotropic Scattering Environments", in *Proc. IEEE 7th International Symposium on Communications and Information Technologies (ISCIT)*, pp. 814-818, Oct. 2007.

11. Rauf Iqbal, and Thushara D. Abhayapala, "Impact of Mobile Acceleration on the Statistics of Rayleigh Fading Channel", in *Proc. IEEE 8th Australian Communication Theory Workshop, AusCTW07*, Adelaide, Australia, pp. 129-133, Feb. 2007.

12. Rauf Iqbal, Thushara D. Abhayapala, and Tharaka A. Lamahewa, "Information Rates of Time-Varying Rayleigh Fading Channels in Non-Isotropic Scattering Environments", in *Proc. 5th Workshop of the Internet Telecommunications and Signal Processing, WITSP'2006*, Hobart, Australia Dec. 2006 (ISBN: 0 9756934 2 5).

The research work presented in this thesis has been performed jointly with the following people: Associate Prof. Dr. Thushara D. Abhayapala (my PhD supervisor, ANU), Dr. Tharaka A. Lamahewa (Research Fellow, ANU), Dr. Parastoo Sadeghi (Fellow (Senior

Lecturer), ANU), Dr. Chandra Athaudage (University of Melbourne) and Dr. Javed Ahmed (National University of Sciences and Technology (NUST), Pakistan). The substantial majority of this work was my own.

Rauf Iqbal
Research School of Information Sciences and Engineering (RSISE),
ANU College of Engineering and Computer Sciences (CECS),
The Australian National University, Canberra, ACT 0200,
Australia.

Acknowledgements

The work presented in this thesis would not have been possible without the support of the following individuals who are gratefully acknowledged below:

- I owe a great deal of gratitude to my supervisor, Associate Prof. Dr. Thushara D. Abhayapala, for his very kind guidance, support, encouragement, friendship, technical insights and discussions throughout my PhD study. I would also like to thank Dr. Tony S. Pollock, who initially acted as my co-supervisor but left Australian National University (ANU), for his guidance at very early stages of my PhD studies.

- I am very thankful to Dr. Tharaka A. Lamahewa (ANU), Dr. Parastoo Sadeghi, Dr. Chandra Athaudage (University of Melbourne) and Dr. Javed Ahmed (NUST) for their collaboration on some work presented in this thesis and numerous helpful discussions.

- I gratefully acknowledge the help and support provided by Prof. Dr. Rodney A. Kennedy (head of the department) and Dr. Jochen Trumpf. I am very thankful to Thushara, Rod and Jochen in arranging my scholarship. Thanks to Dr. Rasika R. Perera (IP Australia), Dr. Leif Hanlen (National ICT Australia (NICTA)) and Dr. David Smith (NICTA) for many useful discussion I had with them. Ms Lesley Goldburg, the department administrator, and Ms. Debbie Pioch are gratefully acknowledged for all their assistance.

- Special thanks are due to Mr. Khalid Akbar (National Engineering an Scientific Commission, Pakistan) for his kind support which made it possible for me to complete this thesis in time.

- I am deeply indebted to my parents, siblings (Farooq, Fakhra and Nasira), my wife Sana and cute daughter Maryam, for their prayers and unwavering moral support. Without their encouragement and help, it may not have been possible for me to complete this thesis.

Abstract

As the title suggests, this thesis is broadly devoted to three aspects of wireless communications — channel modeling, channel estimation and achievable rates over mobile wireless Rayleigh fading channels. The channel modeling part which models the Rayleigh fading in general scattering environments can further be subdivided into two parts — single-input single-output (SISO) (stationary and non-stationary) time-selective modeling, and orthogonal frequency-division multiplexing (OFDM) based space-frequency selective single-input multiple-output (SIMO) channel modeling. The channel estimation part concerns the development of a SISO pilot-aided channel estimation (PACE) scheme in conjunction with peaky signaling to improve the performance. The utility of both the SISO stationary channel model and the SISO channel estimation parts is highlighted by deriving the achievable information rates over Rayleigh fading channels.

The SISO channel modeling is, in fact, a generalization of the Clarke's well known stationary Rayleigh fading channel model from two aspects. Firstly, the proposed 2D SISO channel model describes the Rayleigh fading statistics in general two-dimensional (2D) scattering environments unlike classical Clarke's model which assumes 2D isotropic scattering environment. The usefulness of this generalized model is highlighted by comparing them firstly on the basis of their statistics — the autocorrelation and the power spectral density (PSD) — and secondly on the basis of overall performance of the communications system. The results suggest that the truncated-uniform, truncated-Gaussian, truncated-Laplacian and von Mises distributions can be considered equivalent if the angular spread of the scattering around the mobile receiver is either sufficiently small or large. Specifically, the truncated-Gaussian and von Mises distributions are almost identical for all angular spreads and mobile dynamics. Secondly, we propose a SISO non-stationary Rayleigh fading model which allows the mobile to have constant acceleration as opposed to constant mobile velocity assumption of Clarke's stationary model. The Wigner-Ville and instantaneous power spectra are derived for the non-stationary channel process. Specifically, the Wigner-Ville distribution is shown to be a natural generalization of the Clarke's model from stationary to non-stationary scenario. We also explore the impact of mobile acceleration on the performance of non-coherent systems in terms

of frame overhead and payload, particularly, as a function of initial mobile velocity and carrier frequency, and discuss the feasibility of the use of higher carrier frequencies in the future wireless communications systems. The OFDM-based SIMO channel model establishes a framework for the calculation of space-frequency cross correlation (SFCC) for OFDM-based SIMO system in general 2D and 3D scattering environments. SFCC for 2D elliptical and inverted-parabolic scattering models is evaluated to exhibit usefulness of the SIMO model.

In channel estimation part of this thesis, we propose a slight modification of the so-called peaky signaling which, in conjunction with added signal processing at the receiver end, promises a significant improvement in the performance of pilot-aided channel estimation (PACE) over Rayleigh fading channels. Under the assumption of equal total available power, we analyze the performance of the proposed PACE scheme(s) against the non-peaky signaling. We consider two different cases: Firstly, the pilot and data symbol powers are constrained to be equal and, then, are allowed to be unequal. The proposed scheme is shown to significantly improve the overall performance of the PACE based communications system in the limit of zero signal-to-noise ratio (SNR). In fact, the gain in overall achievable rates with the proposed scheme in the low SNR regime can be as much as the number of idle degrees of freedom (*dof*) in the peaky signaling. Finally, we discuss the possible directions for the future research highlighting the potential usefulness of the channel modeling and estimation approaches employed in this thesis for efficient design and analysis of communications systems.

List of Acronyms

CSI	channel state information
PACE	pilot-aided channel estimation
SISO	single-input single-output
MIMO	multiple-input multiple-output
SIMO	single-input multiple-output
OFDM	orthogonal frequency-division-multiplexing
APD	azimuth power distribution
AOA	angle-of-arrival
AGC	automatic gain control
WSSUS	wide-sense-stationary uncorrelated scattering
ACF	autocorrelation function
PSD	power spectral density
WVD	Wigner-Ville distribution
DWVD	discrete-time Wigner-Ville distribution
IPS	instantaneous power spectrum
MIPS	mean instantaneous power spectrum
DMIPS	discrete-time mean instantaneous power spectrum
rms	root-mean-square
MPSK	M-ary phase-shift-keying
AWGN	additive white Gaussian noise
SNR	signal-to-noise ratio
FIR	finite impulse response
IIR	infinite impulse response
OLD	Oversample-Low pass filter-Downsample
MMSE	minimum mean square error
NE	No-enhancement
PE	Pilot-enhancement
DE	Data-enhancement
PDE	pilot and data enhancement

SFCC	space-frequency cross correlation
CTFT	continuous-time Fourier transform
DTFT	discrete-time Fourier transform
GSM	Global System for Mobile communications
WRLS	windowed recursive least squares
RLS	recursive least squares
WiMax	Worldwide Interoperability for Microwave Access
TF	time-frequency
STFT	short-time Fourier transform
CATFR	Correlation Approach to time-frequency Representations
TFED	time-frequency energy distribution
RCK	Rihaczek distribution
SOTV	spectrum of time variation
BMFC_{dtft}	Bessel-Modulated Fourier Chirp Transform
$\overline{\mathrm{DMIPS}}$	Windowed discrete-time mean instantaneous power spectrum
dof	degrees of freedom

Notations and Symbols

$\boldsymbol{A}^T$	transpose of matrix $\boldsymbol{A}$
$\boldsymbol{A}^H$	conjugate transpose of matrix $\boldsymbol{A}$
i	$\sqrt{-1}$
$\boldsymbol{a}^*$	complex conjugate of $\boldsymbol{a}$
$*$	linear convolution operator
$\odot$	periodic convolution operator
$\mathbb{E}\{\cdot\}$	mathematical expectation
$\Re\{\cdot\}$	real part operator
$\Im\{\cdot\}$	imaginary part operator
ρ	signal-to-noise ratio
$\mathrm{diag}(\boldsymbol{a})$	a diagonal matrix with $\boldsymbol{a}$ as its diagonal
$\log$	natural logarithm
$\mathcal{R}^+$	positive reals
$\mathbb{C}$	complex numbers
$\mathbb{Z}$	integers
$\mathcal{N}(\boldsymbol{m}, \boldsymbol{A})$	normal distribution with mean $\boldsymbol{m}$ and covariance matrix $\boldsymbol{A}$
NIgain	non-isotropicity gain
$\boldsymbol{a} \cdot \boldsymbol{b}$	dot product between vectors $\boldsymbol{a}$ and $\boldsymbol{b}$
$\mathcal{F}$	continuous-time Fourier transform
$\mathcal{D}$	degree of non-isotropicity
σ_ϵ^2	minimum mean square error
$\mathcal{G}$	MMSE gain offered by proposed peaky signaling over non-peaky signaling
$\mathcal{G}^U$	MMSE gain when the Doppler spectrum is Uniform
$\mathcal{G}^C$	MMSE gain when the Doppler spectrum is Clarke's U-shaped
$\mathcal{S}$	sensitivity of MMSE gain to mobile direction of travel
$\mathcal{R}_g$	percentage information rate gain
γ	the fraction of total available bandwidth allocated to pilot symbols
μ	the fraction of power allocated to pilot symbols

γ_{opt} optimal fraction of total available bandwidth allocated to pilot symbols

μ_{opt} optimal fraction of power allocated to pilot symbols

$y_{\otimes x}$ y modulo x

Contents

Declaration i

Acknowledgements v

Abstract vii

List of Acronyms ix

Notations and Symbols xi

1 Introduction 1

1.1 Background and Motivation 1

1.2 Radio Wave Propagation and Modeling: Preliminaries 6

1.2.1 Types of Fading 6

1.2.2 Mathematical Modeling of Fading 8

1.2.3 Statistical Modeling of Multipath Fading 9

1.3 Multipath Rayleigh Fading: Dependence on Scattering Environment . . 10

1.3.1 Isotropic Scattering: Uniform and Non-Uniform AOA 11

1.3.2 Non-Isotropic Scattering: Uniform and Non-Uniform AOA . . . 13

1.4 Non-Stationary Mobile Rayleigh Fading Channels 14

1.5 Mobile Rayleigh Fading Channels: Input-Output Model 15

1.6 Capacity of Mobile Rayleigh Fading Channels 16

1.6.1 No-CSI Cost Function 17

1.6.2 Achievable Rates with Gaussian Signaling 18

1.6.3 Achievable Rates with MPSK Signaling 19

1.7 Pilot-Aided Channel Estimation for Mobile Rayleigh Fading Channels . 19

1.8 Outline of Thesis 21

1.8.1 Overview 21

1.8.2 Questions to be Answered in this Thesis 22

1.8.3 Content and Contribution of Thesis 23

2 Generalized Clarke Model for Mobile Radio Reception **27**
2.1 Background 27
2.2 Channel model 29
2.2.1 Autocorrelation of the Channel Fading Process 33
2.2.2 Spectral Density of the Channel Fading Process: 35
2.2.3 Common Non-isotropic Scattering Distributions 35
2.2.4 Truncation of Series Expansions 36
2.3 Effect of Non-Isotropicity and Mobile Velocity on Channel Statistics . . 39
2.3.1 Clarke's Model as a Special Case 41
2.3.2 Effect of Mobile Velocity 42
2.3.3 Effect of Non-isotropicity 44
2.4 A Comparative Study of Non-isotropic Scattering Environments 46
2.4.1 Numerical Results and Discussion 48
2.5 Applications of the Generalized Clarke model 51
2.6 Summary and Contributions 52

3 Achievable Information Rates Over Generalized Rayleigh Fading Channels 53
3.1 Background 53
3.2 Channel Model 55
3.3 No-CSI Cost in Truncated-Uniform Scattering 56
3.4 Achievable Information Rates: Gaussian and Constant Power Signaling 58
3.5 Analysis of No-CSI Cost Function 59
3.5.1 No-CSI Cost for Infinite Block Length 59
3.5.2 Factors Affecting Information Rate Loss 60
3.6 Analysis of Two Non-Isotropic Communications Scenarios 67
3.6.1 Non-Isotropic Scattering with Isotropic Receive Antenna 68
3.6.2 Isotropic Scattering with Non-Isotropic Receive Antenna 69
3.7 Non-Isotropic Scattering Distributions: A Comparative Study 72
3.8 Marginal Gaussianity does not Imply Joint Gaussianity: A Practical Example 76
3.8.1 Joint Distribution of the Output: Mathematical Analysis 78
3.8.2 Joint Distribution of the Output: Numerical Analysis 79
3.8.3 Implications of Non-Gaussianity of Channel Output on Information Rates 81
3.9 Summary and Contributions 83

4 Rayleigh Fading Statistics with Constant Mobile Acceleration **87**
4.1 Introduction and background 87

4.1.1 Time-Varying Spectrum Due to Mobile Acceleration 88
4.1.2 Time-Varying Channel Coherence Time 88
4.1.3 A Brief Background on Non-Stationary Modeling 89
4.2 Problem Statement And Continuous-Time Channel Model 91
4.2.1 Types of Non-Stationary Gaussian Channel Processes 92
4.2.2 Is Non-Stationarity Due to Mobile Acceleration Separable from Stationary Statistics? 94
4.3 Joint Time-Frequency Analysis 95
4.3.1 Short-Time Fourier Transform (STFT) 96
4.3.2 Cohen's Class Distribution Functions 96
4.4 Discrete-Time Non-Stationary Channel Process and TF Distributions . . 103
4.4.1 Discretization of Continuous-Time Channel Process 103
4.4.2 Discretization of Continuous-Time TF Distributions 104
4.5 Spectral Analysis of Non-Stationary Gaussian Channel Process 106
4.5.1 Formulation of Instantaneous Channel ACF 106
4.5.2 Formulation of Non-Stationary Spectra: DWVD and DMIPS . 111
4.5.3 Analysis of DWVD and DMIPS Channel Spectra in Isotropic Scattering 117
4.6 Bounded Mobile Velocity and Finite Sampling Rate 120
4.6.1 Analog Prefilter Bandwidth 120
4.6.2 Windowing 121
4.6.3 Windowed DMIPS spectrum 123
4.7 Mobile Acceleration Impact on Non-Coherent Mobile Communications 126
4.7.1 Numerical Analysis and Discussion 128
4.8 Summary and Contributions 137

5 Improved MMSE Performance of PACE over Rayleigh Fading Channels 139
5.1 Introduction 139
5.2 Channel Model and Signaling Scheme 142
5.2.1 Channel Model 142
5.2.2 Modified Peaky Signaling Scheme 142
5.2.3 Specification of Transmission Parameters 145
5.2.4 Process of Downsampling and Problem Statement 145
5.3 Derivation of Optimal Wiener Smoother and MMSE 148
5.3.1 MMSE for uniform and Clarke's Doppler Spectra 150
5.3.2 MMSE Performance: Proposed Signaling versus Non-Peaky Signaling Scheme 150
5.3.3 Numerical Analysis of MMSE gain 151

5.4 Optimal Resource Allocation: Mathematical Problem Formulation . . . 154
5.4.1 Expressions for Pilot and Data Symbol Powers 154
5.4.2 Optimality Criterion 158
5.5 Optimal Resource Allocation: Unequal Pilot and Data Symbol Powers 159
5.5.1 Case 1: Optimal Pilot Insertion Rate Equals Nyquist Rate . . . 160
5.5.2 Case 2: Optimal Pilot Insertion Frequency is Greater than Nyquist Rate 169
5.6 Optimal Resource Allocation: Equal Pilot and Data symbol Power . . . 171
5.7 Summary and Contributions 176

6 A Framework to Calculate Space-Frequency Correlation in MultiCarrier Systems 179
6.1 Introduction 179
6.2 Space-Frequency Selective Channel Model for MultiCarrier OFDM . . 183
6.3 Space-Frequency Cross Correlation for MultiCarrier OFDM 185
6.3.1 2D Scattering Environment 186
6.3.2 3D Scattering Environment 187
6.3.3 Some Comments on Extension to MIMO-OFDM 188
6.4 Special Cases of Space-Frequency Correlation for MultiCarrier OFDM 189
6.5 Numerical Analysis of Space Frequency Correlation for MultiCarrier OFDM 192
6.6 Generalization of Space-Frequency Cross Correlation for a 2-Carrier SIMO system 193
6.7 Summary and Contributions 203

7 Conclusions and Future Research Directions 205
7.1 Conclusions 205
7.2 Future Research Directions 207

Appendices

Appendix A 209
A.1 Proof of Equation (2.18) 209

Appendix B 211
B.1 Extrema of Information Rate Cost function 211
B.2 Information Rate Penalty for a Single Point Scatterer Case 214

Appendix C **215**

C.1 Discrete-Time Fourier Transform of Bessel Function With Quadratic Argument 215

Appendix D **219**

D.1 Optimal Wiener Filter and MMSE 219

D.2 MMSE for Uniform and Clarke's Doppler Spectra 223

D.3 Maximum of MMSE Gain Function 224

D.4 Some Auxiliary Constants Used in Chapter 5 227

D.5 Proof: Optimally $\mathcal{E}_p^{\mathrm{PE}} > \mathcal{E}_s$ (Unequal Pilot and Data Powers) 228

Appendix E **231**

E.1 Derivation of Frequency-Selective Channel Model 231

E.2 Derivation of the Space-Frequency Correlation Function 233

Bibliography **235**

List of Figures

1.1 A comparison of computational complexity of the proposed 2D model and the one derived from 3D model [1]. The convergence of the latter model to the true Clarke's U-shaped spectrum [2] is not achieved even after 10.6 seconds. 5

1.2 A Rayleigh distributed envelope of the time-varying complex Gaussian channel process when the highest Doppler frequency is 100 Hz. 11

1.3 No CSI cost function as a function of block length of transmission. . . . 18

2.1 Illustration of the key parameters: direction of mobile travel ϕ_v, mobile velocity $\boldsymbol{v}$, direction of wave arrival β, time instances j' and j, and the origin 'O' of the co-ordinate system. 32

2.2 The truncation behavior of $\Phi(k)$: $\phi_v = 45$, $f_{\mathrm{D}} = 0.05$ and $\beta_0 = 90°$. The approximation based on the argument of the Bessel function proposed in [3] is quite good as the figure suggests only an insignificant increase in accuracy (at larger lags) as $|m_{max}|$ increases from 32 to 200. 36

2.3 The truncation behavior of $\Phi(\omega)$: $\phi_v = 45$, $f_{\mathrm{D}} = 0.05$ and $\beta_0 = 90°$. . . 39

2.4 Illustration of an truncated-isotropic scattering scenario where the scattered power is uniformly distributed with magnitude $1/2\Delta_r$ over a part of the azimuth with a mean angle β_0 and a maximum deviation of Δ_r on each side of the mean. The direction of the mobile travel ϕ_v is also shown. 40

2.5 The plot of squared absolute autocorrelation of the channel process as a function of time lag k for different directions of mobile travel 41

2.6 Effect of the mobile direction of travel $\phi_v = 0°, 45°$, and $90°$ on the Power Spectral Density (PSD) when $\beta_0 = 90°$, $\Delta_r = 60°$ and $f_{\mathrm{D}} = 0.05$. The symmetric U-shaped PSD in case of isotropic scattering is also shown which is independent of the direction of travel. 42

2.7 Effect of non-isotropicity on squared absolute autocorrelation as a function of time lag k when $\phi_v = 0°$, $\beta_0 = 90°$ and $f_{\mathrm{D}} = 0.05$. The autocorrelation for the isotropic case is also shown. 43

2.8 Effect of the degree of non-isotropicity on PSD when $\phi_v = 0°$, $\beta_0 = 90°$ and $f_D = 0.05$. The PSD for the isotropic case is also shown. 44
2.9 Autocorrelation of received signal envelope for different scattering environments when angular spread of the scattering is $5°$, $f_D = 0.05$, $\phi_v = 45°$ and $\beta_0 = 90°$. 45
2.10 Autocorrelation of received signal envelope for different scattering environments when angular spread of the scattering is $25°$. 46
2.11 Autocorrelation of received signal envelope for different scattering environments when angular spread of the scattering is $45°$. 47
2.12 PSD of the received signal envelope for different scattering environments for different mobile directions of travel. The angular spread is $5°$, $f_D = 0.05$ and $\beta_0 = 90°$. 48
2.13 PSD of the received signal envelope for different scattering environments when angular spread is $25°$. 49
2.14 PSD of the received signal envelope for different scattering environments when angular spread is $45°$. 50

3.1 Effect of changing mobile direction of travel on information rate loss due to unknown CSI in truncated-isotropic environment 61
3.2 Impact of mobile direction of travel on non-isotropicity gain 61
3.3 Non-isotropicity gain versus block length for different Δ_r 62
3.4 The penalty due to channel unpredictability because of no-CSI as a function of non-isotropicity for different transmission block lengths 63
3.5 Effect of SNR and non-isotropicity on information rate cost for unknown CSI 63
3.6 Non-isotropicity gain versus non-isotropicity for different normalized fading rates 66
3.7 Sensitivity of non-isotropicity gain to mobile direction of travel as a function of angular spread for different normalized fading rates 66
3.8 Impact of non-isotropicity on Gaussian signaling lower bound as a function of SNR for different fading rates 67
3.9 Non-isotropicity gain for Gaussian signaling versus angular spread for different normalized fading rates when a non-isotropic antenna is used at the mobile receiver in isotropic environment. 68
3.10 Impact of non-isotropicity on Gaussian signaling lower bound in the low SNR regime for different normalized fading rates 69
3.11 Impact of non-isotropicity on Gaussian signaling lower bound as a function of SNR for different fading rates 70

3.12 Impact of non-isotropicity on MPSK signaling upper bound as a function of SNR for different fading rates 71

3.13 Comparison of non-isotropicity gain for different scattering environments as a function of angular spread 72

3.14 Comparison of non-isotropicity gain for different scattering distributions as a function of block length 73

3.15 Comparison of non-isotropicity gain as a function of mobile direction of travel, ϕ_v 73

3.16 Achievable information rates as a function of SNR when the scattering distribution is truncated-isotropic 75

3.17 The gain sensitivity, $\mathcal{S}$, for different scattering environments as a function of angular spread 76

3.18 A contour plot of joint distribution of real parts of 2-dimensional Gaussian channel vector 80

3.19 A contour plot of joint distribution of the real parts of 2-dimensional Gaussian channel multiplied by i.i.d. BPSK input 82

3.20 A contour plot of joint distribution of the real parts of 2-dimensional Gaussian channel multiplied by i.i.d. 16-PSK input 83

3.21 Comparison of information rate upper bounds 84

4.1 The mobile is moving at an angle ϕ_v with respect to x-axis with initial speed $|\boldsymbol{v}_0|$ and constant acceleration α in the direction of movement. A plane wave is shown incident on the receive antenna at an angle β and Π^{dwvd} defined in (4.69) is also depicted. 92

4.2 The ACF of DWVD as a function of the lag k and absolute time index n: $|\boldsymbol{v}_0| = 20$m/sec, $\alpha = 10$m/sec^2, f_c =2GHz and $T_s = 5$msec. Increasing τ and n have the effect of reducing the autocorrelation faster. 110

4.3 The ACF of DMIPS as a function of the lag k and absolute time index n: $|\boldsymbol{v}_0| = 20$m/sec, $\alpha = 10$m/sec^2, f_c =2GHz and $T_s = 5$msec. Increasing τ and n have the effect of reducing the autocorrelation faster. 111

4.4 The 2D view of the $\text{Arg}_{\text{DVWD}} - \text{Arg}_{\text{DMIPS}}$: $|\boldsymbol{v}_0| = 20$m/sec, $\alpha = 10$m/sec^2, f_c =2GHz and $T_s = 5$msec. 112

4.5 The 2D view of ACF for zeroth order Bessel function of the first kind as a function (Clarke's model) as a function of the lag k and absolute time index n: $|\boldsymbol{v}_0| = 20$m/sec, $\alpha = 10$m/sec^2, f_c =2GHz and $T_s = 5$msec. Observe that the absolute time does not change the ACF. 113

4.6 The 2D view of ACF for DWVD (isotropic scattering) as a function of the lag k and absolute time index n: $|\boldsymbol{v}_0| = 20$m/sec, $\alpha = 10$m/sec^2, f_c =2GHz and $T_s = 5$msec. Increasing τ and n have the effect of reducing the autocorrelation faster. 114

4.7 The 2D view of ACF for DMIPS (scattering environment) as a function of the lag k and absolute time index n: $|\boldsymbol{v}_0| = 20$m/sec, $\alpha = 10$m/sec^2, f_c =2GHz and $T_s = 5$msec. Increasing τ and n have the effect of reducing the autocorrelation faster. 115

4.8 The plot of $J_0(a\,k)$ and $J_0(a\,k^2)$. We can observe the quadratic argument makes the Bessel function non-stationary so that its spectrum is lag-dependent. $J_0(a\,k^2)$ oscillates faster with lag k implying that it is no more a bandlimited like $J_0(a\,k)$ which is limited to $|\omega| \leq a$. 123

4.9 Non-stationary DMIPS spectrum by Blackman-Tukey method. The finite window length is assumed to be 51 samples in the lag domain. We assume that the carrier frequency is 2GHz, $T_s = 2.65$msec, $|\boldsymbol{v}_0| = 20$m/sec and the acceleration $\alpha = 10$m/sec^2. As can be observed, the instantaneous Doppler spread increases linearly with n exhibiting the same U-shaped behavior characteristic of the Clarke's model. Notice that the poor resolution in the frequency domain is due to the finiteness of the window function. 124

4.10 The general structure of a transmission frame. 128

4.11 The instantaneous percentage decrease in the duration of radio frame (with respect to $\alpha = 0$m/sec) for different mobile accelerations assuming mobile speed of 1 m/s, $T_s = 3.69$ micro second and $f_c = 2$ GHz. Notice that the carrier frequency and the symbol duration correspond to GSM communications. 129

4.12 The percentage change in the duration of radio frame assuming GSM carrier frequency and symbol rate for different mobile accelerations as a function of mobile speed. 130

4.13 The percentage normalized radio frame length as a function of carrier frequency. This is a fundamental result which is independent of the mobile speed, acceleration and the absolute time index n as long as these parameters are assumed to be the same for $f_c \neq 2$ GHz and $f_c = 2$ GHz. 131

4.14 The normalized percentage payload per second (after 1 sec) as a function of carrier frequency for different mobile accelerations assuming the symbol rate as that of GSM and mobile speed as 72 km/hr. 132

4.15 The instantaneous integrated radio frames per second for different frequencies and mobile accelerations. The symbol duration $T_s = 20$ micro second. 133
4.16 The percentage increase in integrated radio frames per second (assuming $nT_s = 1$ second) for different frequencies as compared to $f_c = 2$ GHz. The results are given for different accelerations as a function of mobile speed. The symbol duration $T_s = 20$ micro second. 134
4.17 The normalized integrated payload per second (after 2 sec) as a function of carrier frequency assuming the symbol rate as that of GSM and mobile speed as 50 km/hr. 135
4.18 The normalized percentage integrated frame overhead per second (after 2 sec) as a function of carrier frequency for different mobile accelerations assuming the symbol rate as that of GSM and mobile speed as 100 km/hr. 136

5.1 The transmitted frame format: T_s is the data symbol duration, T_p denotes pilot symbol insertion factor, the number of zeros (or, equivalently, unused *dof*) is equal to $\mathcal{M} - 1$ where the factor $\mathcal{M}$ is the upsampling factor. 142
5.2 The proposed scheme: The pilot symbols extracted from filtered sequence of received symbols are passed through Wiener smoother to get improved channel estimates at data symbol locations. 143
5.3 The spectra of the channel and the noise. We assume that the pilot symbols are all set to 1. 146
5.4 Impact of SNR and normalized fading rate on MMSE gain ($\mathcal{G}^U$) for different $\mathcal{M}$ 152
5.5 The plot of the difference in gains offered by the proposed scheme in uniform and Clarke's Doppler spectra as a function of SNR 153
5.6 MMSE gain for different $\mathcal{M}$ in low SNR regime with $f_{\mathrm{D}} = 0.005$ and $K = 1$ for uniform and Clarke's spectra. 154
5.7 Impact of oversampling factor K on MMSE gain for uniform Doppler spectrum with and without PE. Notice that increasing K shifts the MMSE peak towards lower SNR implying that using larger K, better MMSE performance can be achieved at lower SNR. Also observe that PE raises the peak gain by the same amount for all K. 155
5.8 Impact of normalized fading rate, f_{D} on MMSE gain ($\mathcal{G}$) with and without PE for $\mathcal{M} = 10$ when $\rho_p = \{-40, -15, 0\}$ dB. The Doppler spectrum is assumed to be uniform. 156

5.9 Impact of varying pilot insertion period T_p on MMSE gain with for different ρ_p when $f_{\mathrm{D}} = 0.005$ and $\mathcal{M} = 2$ both for uniform and Clarke's spectra. 156
5.10 Effective optimal μ and ζ for PE and DE assuming $\gamma_{opt} = 2\mathcal{M}f_{\mathrm{D}}$. The corresponding optimal μ and ζ for non-peaky signaling are also shown. 162
5.11 A comparison of Gaussian signaling capacity lower bound for the proposed schemes and NP scheme for $\mathcal{M} = 20$ and $f_{\mathrm{D}} = 0.005$. The perfect CSI capacity of Rayleigh fading channels is also shown as a benchmark. 164
5.12 The plot of $C_{lb}^{\mathrm{DE}} - C_{lb}^{\mathrm{NP}}$ for different $\mathcal{M}$. 165
5.13 The plot of $C_{lb}^{\mathrm{DE}} - C_{lb}^{\mathrm{NP}}$ for different f_{D} 166
5.14 A comparison of Gaussian signaling capacity lower bounds at low SNR. 167
5.15 The impact of $\mathcal{M}$ and SNR on the percentage rate gain $\mathcal{R}_g$ for NE, PE and DE cases. Note that absolutely optimal γ and corresponding μ have been considered. 168
5.16 C'_{lb} for PE and DE cases. Observe that, in general, the optimal γ is a vector where each element corresponds to a particular μ. 169
5.17 Optimal γ as a function of μ for PE and DE cases. 171
5.18 The percentage rate gain $\mathcal{R}_g$ as a function of optimal γ and μ for PE and DE schemes. 172
5.19 The impact of $\mathcal{M}$ on optimal γ and μ for PE and DE cases. The observed 'symmetry' across $\mu = 0.5$ is a result of very low SNR. 173
5.20 The impact of ρ on optimal γ and μ for PE and DE cases when $\mathcal{M} = 2$ and $f_{\mathrm{D}} = 0.01$. Observe that with an increase in ρ , the optimal γ for PE and DE tends to the minimum possible γ, *i.e.*, $2\mathcal{M}f_{\mathrm{D}}$ (for all μ) that satisfies the Nyquist criterion. The authors have verified that the value of ρ at which $\gamma_{opt} = 2\mathcal{M}f_{\mathrm{D}}$ is different for PE and DE cases, and is always greater for DE case. 174
5.21 The Monte Carlo simulation of the impact of normalized fading rate on percentage rate gain $\mathcal{R}_g$ for different ρ when $\mathcal{M} = 20$ (PE case). Notice that the gain offered by the proposed scheme is independent of f_{D} at very low SNR which verifies the analytical result obtained in (5.61). . . 176
5.22 The impact of $\mathcal{M}$ on percentage rate gain $\mathcal{R}_g$ for different f_{D} when $\rho = -15$ dB. We can observe that the gains offered by the proposed scheme depend on $\mathcal{M}$ and are different for different fading rates. 177
5.23 The impact of $\mathcal{M}$ on percentage rate gain $\mathcal{R}_g$ for different ρ when $f_{\mathrm{D}} = 0.001$. 178

6.1 A general scattering model for the frequency-selective SIMO system. $\psi(\widehat{\boldsymbol{\beta}}, \tau)$ is the random complex scattering gain for the waves arriving in direction $\widehat{\boldsymbol{\beta}}$ with delay τ at the receiver aperture. $\boldsymbol{x}_p$ is the location of the pth receive antenna relative to the receiver origin 'O' and $p = 1, \cdots, n_R$ and . $r_R \geq \max ||\boldsymbol{x}_p||$ is the radius of the sphere which encloses the receiver antennas. Scatters are distributed outside of the sphere with radius $r_{RS} > r_R$ and assumed they are in the farfield from the receiver antennas. 184

6.2 Absolute value of the space-frequency correlation function (6.11) across subcarriers on two receive antennas placed $d = 0.25\lambda$ apart for the IP uplink model (Fig. 3 in [4]). 192

6.3 Absolute value of the space-frequency correlation function (6.11) across subcarriers on two receive antennas placed $d = 0.25\lambda$ apart for the IP downlink model (Fig. 5 in [4]) 193

6.4 Absolute value of the space-frequency correlation function (6.11) across subcarriers on two receive antennas placed $d = 0.25\lambda$ apart for the elliptical scattering model (Fig. 5 in [5]) 194

6.5 Contour plot of the space-frequency correlation function shown in Fig. 6.2 for the uplink inverted-parabolic model. 195

6.6 The contour plot of the space-frequency envelope correlations for truncated-uniform and von-Mises (black lines) azimuth power distributions for broadside antenna orientation. The angular spread is assumed to be $5°$. . 198

6.7 The contour plot of the space-frequency envelope correlations for truncated-uniform and von-Mises azimuth power distributions for $\beta_0 = 45°$ assuming angular spread as $5°$. 199

6.8 The impact of angular spread of the scattering on the space-frequency correlation function for truncated-uniform distribution. The correlation contour value is assumed to be fixed at 0.5 and the mean scattering angle is $45°$. 200

6.9 The effect of changing mean scattering angle on space-frequency envelope correlation of von-Mises distribution. The correlation contour value is assumed fixed at 0.7 and the angular spread is assumed to be $5°$ that corresponds to $\kappa_r = 130$ for von-Mises distribution. 201

6.10 A comparison of space-frequency trade-off characteristics for truncated-uniform, Gaussian, Laplacian and von-Mises distributions 202

D.1 RHS of Eq. (D.20) as a function of ρ_p highlighting maximum of $\mathcal{G}^C$ (MMSE gain with Clarke's isotropic scattering model). It may be observed that $\rho_p = -4.65$ dB and -7.1 dB result in maximum MMSE gains respectively for $\mathcal{M} = 2$ and 6. 225

List of Tables

2.1 Scattering Coefficients γ_m for truncated-uniform, truncated-Gaussian, cosine, von-Mises and truncated-Laplacian power distributions. $|\beta - \beta_0| \leq \pi$ represents the support of AOA distribution for all scattering environments except the truncated-uniform environment. 37

3.1 Typical values of angular spread (Λ) at 1800MHz 64

3.2 Typical values of Λ at 900MHz 65

Chapter 1

Introduction

1.1 Background and Motivation

The mobile wireless communications lies at the helm of the explosive research in the field of telecommunications towards realizing the ultimate communications dream — the ubiquitous access to information, anywhere, anytime. The wireless communications offers many advantages over wired communications. One of the major advantages of wireless communications is the mobility — the communications source (the transmitter) and the destination (the receiver) can communicate while on the move. The realization of the communications dream, therefore, implicitly necessitates communications, at least somewhere in the system architecture, over wireless medium. Moreover, the simplicity and cost effectiveness in addition to the possibility of communications over longer distances make wireless communications really attractive as compared to wired communications. The wireless medium, however, is uncontrollable and unpredictable causing time-varying random attenuation (fading) of the transmitted signal. The reliability of the wireless link has to be improved with the help of different techniques like, for example, signal diversity, channel estimation, coding and equalization at the receiver.

The performance of different techniques to mitigate the random time-varying fading of the transmitted signal caused by the unpredictable wireless medium relies mainly on how good we know the instantaneous channel realization, *i.e.*, the channel state information (CSI). The availability of reliable CSI is of fundamental importance for the reliability of the communications system. The perfect knowledge of CSI, however, is practically impossible to obtain. There are many ways to facilitate the receiver in forming an estimate of CSI. The different techniques for CSI estimation can be broadly classified into blind, semi-blind and pilot-aided [6]. The blind CSI estimation technique relies solely on the channel statistics without using any pilot symbols. The pilot-aided channel estimation (PACE) uses known pilot symbols inserted in the transmitted stream to form

the channel estimate. The semi-blind estimation scheme is a combination of blind and pilot-aided techniques. The performance of PACE is superior to the other two techniques at the cost of system bandwidth and power that has to be allocated to pilot symbols. The channel estimates at pilot symbol instants obtained through PACE are interpolated to obtain estimates at data symbol instants. If the channel statistics are utilized in the process of interpolation, *e.g.*, using Wiener filter, the PACE scheme actually falls into the category of semi-blind estimation.

The emerging wireless communications standards specify higher carrier frequencies[1] with higher data rates in mobile environments. The communications at higher carrier frequencies is more sensitive to the the relative movement of user and the environment. As a possible remedy to this increased sensitivity, the emerging wireless standards specify shorter frame lengths over which the channel is assumed to be constant. The channel is estimated by sending pilot symbols resulting in reduced time for information transmission. Since the frame overhead and, perhaps, the number of pilots for channel estimation are to remain constant, communications at even higher carrier frequencies with mobility would require further reduction in the payload. The pilot-based technique of channel estimation might become infeasible in view of the promises of very high data rates in the future wireless communications systems. Such communications systems may have to rely on channel statistics and other redundancies in the transmissions to improve the overall performance of the communications systems. The channel statistics are a function of the structure of the propagation environment and the mobile dynamics [10–12]. The efficient utilization of channel statistics, therefore, depends strongly on the accuracy of the underlying mathematical model to describe the wireless propagation. However, the evaluation of the design of communications systems using computer simulations before its implementation has become a norm which requires the channel model to be of manageable computational complexity [13]. The accuracy of a particular channel model has, therefore, to be traded off with its computational complexity.

In most cases, it is desirable for a designed communications system to work in majority of all envisioned locations, not just in a single, specified place [14]. Statistical channel modeling is a preferred approach in such cases offering sufficient accuracy at significantly reduced complexity as compared to deterministic approaches. A well known statistical channel model is the classical Clarke model for single-input single-output (SISO) narrowband mobile radio reception [2] that models the channel process as a complex Gaussian channel process and, equivalently, its envelope as Rayleigh distributed. The main assumption of this model is the isotropicity of the scattering environ-

[1] 1The IEEE 802.16e standard also known as mobile *Worldwide Interoperability for Microwave Access* (WiMax) specifies mobile communications at carrier frequencies from 2-11 GHz in non-line-of-sight (NLOS) environments [7–9].

ment which implies a uniform probability distribution function (pdf) of angle-of-arrival (AOA) in the full azimuth and, hence, uniform azimuth (or angular) power distribution (APD). This model, applicable only to rich urban radio reception, is based on an over-simplification of the AOA probability and the scattering environment as has been argued and experimentally demonstrated (see [15] and references therein) that the scattering encountered in many suburban and rural environments is non-isotropic, *i.e.*, the pdf of AOA of waves is not always uniform as assumed in [2]. The use of a directional antenna with non-uniform gain pattern at the receiver also results in non-isotropic APD. The measurements have shown that scattering in vehicle-to-vehicle communication is also non-isotropic [16, 17]. Commonly non-isotropic APD has been shown to be well modeled by truncated-uniform (isotropic), truncated Laplacian [18], truncated Cosine, truncated Gaussian [19] and von-Mises distribution [15]. Several statistical models exist in literature, for SISO and multiple-input multipleoutput (MIMO) systems, modeling the non-isotropicity of the mobile radio reception where either the antenna or the scattering environment is non-isotropic (directional) and the probability of AOA is either uniform or non-uniform [1, 15, 20–29]. A generalization of the Clarkes model from narrowband to wideband was presented in [28]. Unlike Clarkes model where the scatterers are assumed to be uniformly distributed on a ring, it was assumed in [28] that the scatterers are uniformly distributed on an ellipse with the transmitter and the receiver positioned on the two foci of the ellipse. This structure of the scattering environment gave rise to non-uniform pdf of AOA over the whole azimuth. It may be emphasized that, in its current form, this model does not support scatterers distribution over a limited azimuth. Another generalization of [2] has been reported in [15] where the pdf of AOA is modelled as von Mises distribution. Yet another two somewhat similar generalizations of [2] to general 3D scattering environments (characterized by uniform or non-uniform pdf of AOA), which are related to our work, were recently presented in [1, 29, 30] based on spherical harmonics expansion of the plane wave propagating in 3D. These 3D generalizations do include SISO 2D scattering environments as special case but, however, the equivalent expressions obtained thus may be computationally expensive. In [1], for example, the following expression for 2D Doppler spectrum in isotropic scattering environment equivalent to Clarkes spectrum [2] was derived

$$\Phi(\omega) = \frac{\pi}{\omega_{\mathrm{D}}} \sum_{\theta=0}^{\infty} (2\theta + 1) \left(P_\theta(0)\right)^2 P_\theta\left(\frac{\omega}{\omega_{\mathrm{D}}}\right), \tag{1.1}$$

where $\omega_{\mathrm{D}} = 2\pi f_{\mathrm{D}}$ is the Doppler spread of the spectrum normalized to the symbol rate $1/T_s$, f_{D} is the normalized maximum Doppler frequency also known as *normalized*

fading rate and $P_\theta(x)$ is the Legendre polynomial of degree θ and argument x.

The equivalent Clarke's 2D Doppler spectrum defined in (1.1) (with $\theta \leq 10$) and original Clarke's 2D spectrum derived in [2] (Eq. (2.25)) have been plotted in Fig. 1.1. The computation time for the equivalent spectrum and the original Clarke's model was respectively 10.64 and 1.6 seconds. We, in this thesis, seek to develop a generalized Clarke model for SISO mobile radio reception assuming 2D scattering at the outset, to avoid increased complexity, rather than deriving it as a special case of 3D characterizations. We do this, firstly, because in many practical communications scenario, the waves can be safely assumed to be arriving only from the azimuth. Secondly, the spectral representations is useful for real-time estimation of the mobile to facilitate hand-off decisions [31] and mobility management in future ad hoc cellular networks [32]. It is therefore desirable to have spectral representation with less computational complexity.

The Clarke's 2D spectrum is obtained in its original form as a special case of the derived generalized 2D Clarke's model (Chapter 2). The generalized Clarke's model is then used to explore the impact of mobile direction of travel on channel statistics and overall system performance which has not been adequately addressed previously. To the best of authors' knowledge, there is no generalization of Clarke's model to constant mobile acceleration scenario which is becoming more relevant particularly, as we discuss in detail in Chapter 4, for future communications systems. Finally, the motivation behind our development of space-frequency cross correlation (SFCC) model (Chapter 6) for orthogonal frequency division multiplexing (OFDM) based space-frequency selective channels in general scattering environments is the fact that MIMO-OFDM has been specified as the technology of choice for most emerging wireless communications standards [7,33,34]. The SIMO-OFDM model derived in this thesis is easily extendable to MIMO-OFDM following the approach developed in [35].

Thus, on the basis of the preceding discussion we have identified the following basic questions not thoroughly addressed previously:

How to generalize the classical 2D Clarke model of narrowband mobile radio reception i) from isotropic scattering environment to general scattering environments and ii) from mobile motion with constant velocity to accelerating mobile scenario? How and when is it really important to have the perfect knowledge of the type of scattering environment and mobile dynamics? What impact will an accelerating mobile have on Rayleigh fading statistics and communications system performance?

Our approach to answer these questions is based on modal decomposition of the plane waves employed in [1,24,30,36] for 3D characterization of wireless channels. An important difference between previous 3D generalizations of Clarkes model discussed above and ours is that we use circular harmonics expansion for 2D plane wave propa-

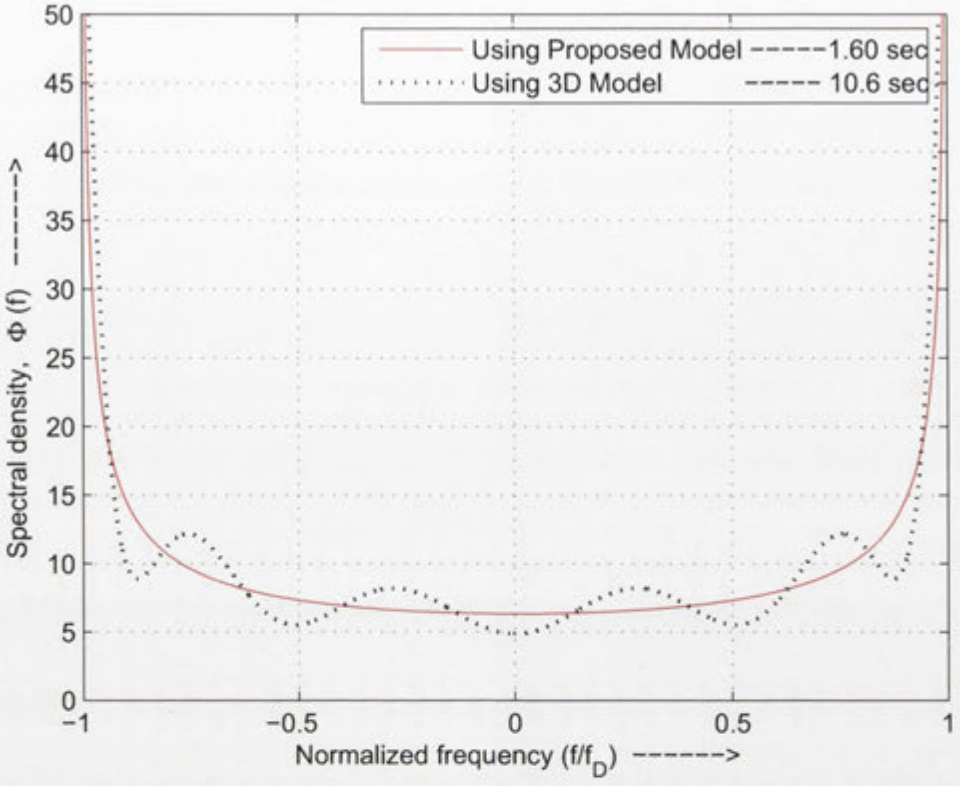

Figure 1.1: A comparison of computational complexity of the proposed 2D model and the one derived from 3D model [1]. The convergence of the latter model to the true Clarke's U-shaped spectrum [2] is not achieved even after 10.6 seconds.

gation as opposed to spherical harmonics expansion suitable for the expansion of plane waves propagating in 3D. The same modal decomposition technique is used to develop a SIMO-OFDM space-frequency selective model that is applicable in general scattering environments. We also study the impact of mobile velocity and non-isotropicity on channel statistics and system capacity — an important well known information theoretic measure with units of bits/sec—following the approach of [37]. The impact of mobile acceleration on the performance of communications systems is analyzed and a PACE based transmission scheme is developed which results in significant improvement in performance of PACE and communications systems. The most important assumption throughout this thesis is that we have the perfect knowledge of channel statistics and mobile dynamics. Therefore, the main theme of this thesis can be described as *the role of the knowledge of the scattering environment and mobile dynamics in communications over Rayleigh fading channels in general scattering environments.*

1.2 Radio Wave Propagation and Modeling: Preliminaries

In a wireless communications link, the transmitted radio frequency (RF) signal travels to the receiver along a number of different paths, collectively known as multipath, due to scattering, reflection and diffraction from different obstacles or refraction of the wireless medium itself [11].

Reflection

The reflection occurs when the propagating electromagnetic waves bounce off objects with dimensions larger than the wavelength of the wave, *e.g.*, the earth surface, buildings, walls etc.. The waves are perfectly reflected if such objects are perfect conductors. For objects with imperfect conduction property, the waves are partially absorbed and partially reflected resulting in a loss of wave energy. The electric field intensity of the reflected and absorbed waves is related to the incident waves through the Fresnel correlation coefficient which depends on the wave polarization, angle of incidence and frequency of the propagating wave [38].

Diffraction

The diffraction of electromagnetic waves can be be explained by the Huygens principle, which states that all points on a wavefront can be considered as point sources for the reproduction of secondary wavelets which combine to produce a new wavefront in the direction of propagation [38]. It is the diffraction phenomenon which allows the radio waves to propagate beyond the horizon and behind obstacles.

Scattering

It occurs when a radio waves impinges on objects with rough surface such as lampposts and trees. The incident energy on such objects is scattered (diffused) in all directions. It is the scattering phenomenon which explains stronger received signal strength than is predicted by the reflection and diffraction models alone.

1.2.1 Types of Fading

The reflection, diffraction and scattering of electromagnetic waves results in attenuation (fading) of the transmitted signal as it travels to the receiver. The signal fading as a

result of wireless transmission can be classified as path loss, long-term (slow) fading (also called shadowing) and short-term (fast) multipath fading.

Pathloss

The path loss is the reduction of radiated energy as a function of the distance between the transmitter and the receiver. In ideal free space propagation, the transmitted energy loss is proportional to the inverse square of the separation between transmitter and receiver so that the received signal power is given as [39], *i.e.*,

$$P_r = P_t \left(\frac{\lambda_c}{4\pi D_s} \right)^2 G_t G_r, \tag{1.2}$$

where P_r, P_t are the received and transmitted signal power, $\lambda_c = c/f_c$ is the carrier wavelength (f_c is the carrier frequency and c is the speed of light), D_s is the separation distance between the transmitter and the receiver, and Gt and Gr are the transmit and receive antenna power gains. In cellular environments, the path loss exponent is 4 implying a power loss of 40 dB/decade. In real world environments the path loss exponent may vary from 2.5 to 6 [11]. If the envelope (or squared-envelope) of the received signal is measured over a distance of several wavelengths, the mean envelope (or squared-envelope) can be obtained. This mean quantity is sometimes called local mean corresponding to a particular locality. If the local mean is averaged over sufficiently large spatial distances, the *area mean*(average signal strength) is obtained which is directly related to the path loss. The variation in the area mean is dictated by the path loss [40]. It may be mentioned here that the path loss in a wireless link is usually overcome by automatic gain control (AGC) [41] circuitry in the receiver.

Long-Term Fading

The long-term fading (also known as macroscopic fading and shadowing) which appears as a variation in the local mean is a result of shadowing of the receiver from the transmitter due to terrain and buildings. The shadowing is generally modeled as log-normally distributed [42] which implies that the received signal power in decibel (dB) is normally distributed, *i.e.*,

$$f(x) = \frac{1}{\sqrt{2\pi}\sigma} \exp\left(-\frac{(x-\mu)^2}{2\sigma^2} \right), \tag{1.3}$$

where x (in dB) is a random variable representing the long-term signal power fluctuation, μ and σ respectively are the mean and the standard deviation of x. The mean μ is, in fact, path loss. The time-scale of variation in long-term fading is much longer, typically on

the order of many seconds or even minutes, making it possible to be overcome through AGC system.

Short-Term Multipath Fading

The constructive and destructive interference of multipath signals with random amplitudes and phases results in short-term multipath fading [2, 11]. The time-scale of variation in multipath fading is much shorter, *e.g.*, of the order of a packet or even a single transmission symbol. Signal fluctuations due to multipath fading can be as large as 40 dB or more below the mean level with successive minima occurring every half a carrier wavelength or so. The short-term multipath fading effect is due to the scattering phenomenon.

1.2.2 Mathematical Modeling of Fading

There are three fundamental approaches to modeling the signal fading as a result of wireless propagationdeterministic, semi-deterministic and statistical.

Deterministic Models

The deterministic models incorporate the Maxwell's equations and all propagation mechanisms to give a very accurate description of the channel impulse response. One such approach known as 'ray tracing' is based on the fact that if we know the propagation environment exactly, it should be possible to trace paths emanating from the transmitter to the receiver to obtain the channel complex response from the amplitudes, delays, polarizations and phases of the incoming waves [43–45]. The cost which has to be paid for the high accuracy of deterministic techniques is very high computational complexity and the requirement of the physical environment data, *e.g.*, terrain and building databases. Other deterministic channel modeling techniques are based on the Uniform Theory of Diffraction and Geometric Theory of Diffraction [46].

Semi-Deterministic Models

Semi-deterministic modeling approach combines deterministic and statistical approaches to reduce the computational complexity of the determiniFstic models at the cost of some accuracy. COST231 Walfisch-Ikegami model [47] is one such semi-deterministic channel model used for path loss prediction in an urban environment. It uses site-specific data such as building height, street width, block size and direction of the streets to capture propagation effects.

Statistical Models

The statistical approach for channel modeling is more flexible and less complex than deterministic and semi-deterministic approaches providing sufficiently accurate channel information. These models attempt to generate artificial channel responses as representative of real world propagation channels. Such models assume that the signals arrive at the receiver according to a specific statistical distribution. The Okumura-Hata model for path loss calculation [47] and the Clarkes model for multipath fading [2] are two examples of statistical channel models. This thesis is devoted to statistical modeling of multipath fading and assumes that the path loss and long-term fading are perfectly compensated at the receiver through AGC and/or power control at the transmitter. We describe below a brief background on statistical modeling of multipath channel fading.

1.2.3 Statistical Modeling of Multipath Fading

The literature on statistical modeling of multipath fading is quite rich. Depending on the carrier frequency and propagation environment, several models exist for the statistical characterization of the impact of multipath fading on the envelope of the received signal, *e.g.*, Nakagami, Weibull, Rayleigh and Rician distributions [48]. However, Rayleigh and Rician fading models are more popular due to their mathematical tractability and conformance with the measurement data in sufficiently rich scattering environment. The definition of *sufficiently rich* scattering was investigated analytically by Beckmann in [49]. It was found that only a small number of arriving waves with their phases uniformly distributed over $[-\pi, \pi]$ and independent of their magnitudes is sufficient for the distribution of the received signal to be approximately complex Gaussian and its envelope to be approximated as Rayleigh distributed. This fact was substantiated by Jakes [39] who developed a deterministic model to simulate Rayleigh fading where only 9 waves were found to be enough for sufficient accuracy of the simulated Rayleigh fading. The accuracy of approximation improved as the number of arriving waves was increased.

Multipath Rayleigh Fading

The first statistical multipath fading model was presented in [50] for mobile radio reception in a suburban area with a line-of-sight (LOS) path between the transmitter and the receiver based on the reflection principle. Clarke [2] presented a more flexible statistical characterization of multipath fading based on scattering assuming sufficiently large (ideally infinite) number of equally strong 2-dimensional (2D) stationary scatterers around the mobile receiver moving with constant velocity v with no line of sight (LOS) path between the transmitter and the receiver. As discussed before, the probability of

angle-of-arrival (AOA) of scattered waves was assumed to be uniform over the whole azimuth which implies that the APD of the scattering environment is isotropic. It was further assumed that the phase of each impingent electromagnetic wave is independent of its magnitude and is uniformly distributed over $[-\pi, \pi]$. As a result of the central limit theorem (CLT), the in-phase (real) and the quadrature (imaginary) components of the received signal happened to be independent zero-mean stationary Gaussian processes with identical variances. Equivalently, the received signal was a zero-mean complex Gaussian process and the envelope $r \in \Re^+$ of the received signal was Rayleigh distributed (Fig. 1.2) [11], *i.e.*,

$$f(r) = \frac{2r}{\Upsilon} \exp\left(-\frac{r^2}{\Upsilon}\right) u(r), \tag{1.4}$$

where Υ is the average received power an $u(r)$ is the unit step function defined as

$$u(r) = \begin{cases} 1, & r \geq 0; \\ 0, & \text{otherwise.} \end{cases}$$

Multipath Rician Fading

If there is a LOS between the transmitter and the receiver in addition to diffuse scattering, the mean of the received complex Gaussian signal is non-zero resulting in Rician distributed envelope [11], *i.e.*,

$$f(r) = \frac{2r(K+1)}{\Upsilon} \exp\left(-K - \frac{r2(K+1)}{\Upsilon}\right) I_0\left(2r\sqrt{\frac{K(K+1)}{\Upsilon}}\right) u(r), \tag{1.5}$$

where K is the Rician factor — the ratio of the power of the LOS component to the power of the scattered component — and I_0 is the modified Bessel function of the first kind of order zero defined as

$$I_0 = \frac{1}{2\pi} \int_0^{2\pi} \exp\left(-x \cos\theta\right) d\theta \tag{1.6}$$

1.3 Multipath Rayleigh Fading: Dependence on Scattering Environment

The zero-mean complex Gaussianity of the channel process in sufficiently rich scattering environment allows the channel process to be fully described by its second order statistics which depend directly on the structure of the scattering environment [10–12].

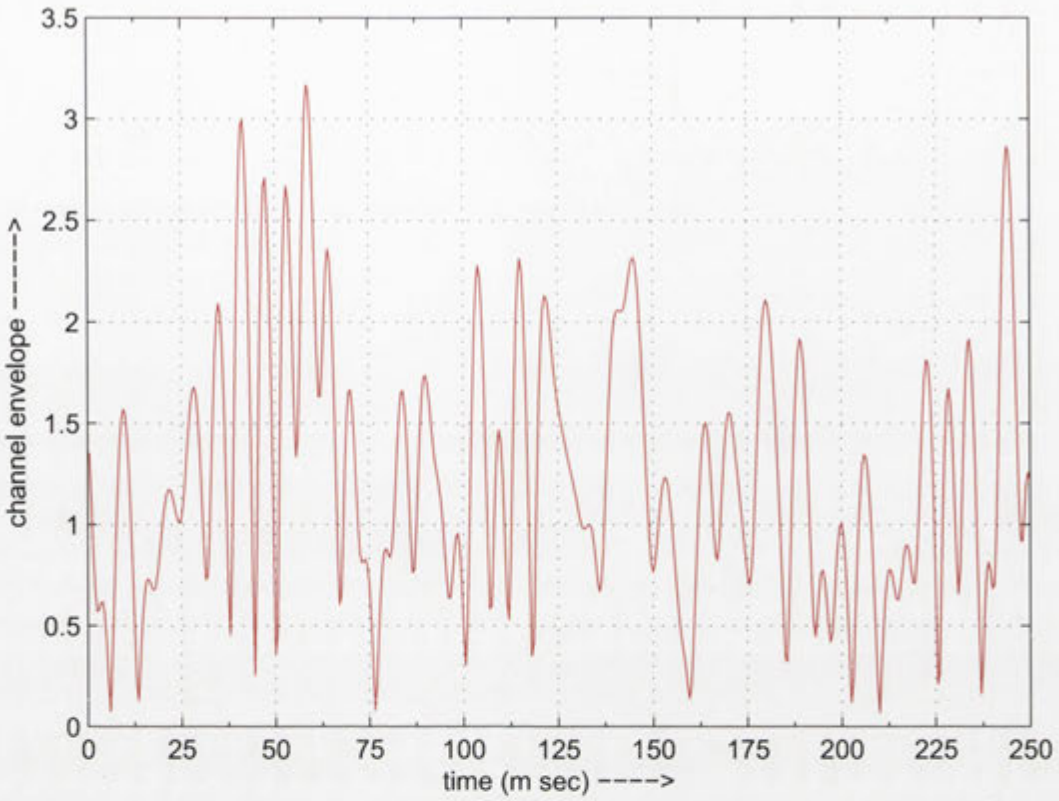

Figure 1.2: A Rayleigh distributed envelope of the time-varying complex Gaussian channel process when the highest Doppler frequency is 100 Hz.

Throughout this thesis (except in Chapter 4), we shall assume in general that the scattering, isotropic or non-isotropic, is *statistically homogeneous* [11] wide-sense-stationary uncorrelated, *i.e.*, WSSUS scattering [33]. The chapters in this thesis devoted to narrowband channel modeling do not require WSS part of the assumption. Notice that the statistical homogeneity implies that the scattering is uncorrelated in the angle domain, the WSSUS assumption implies that the channel is WSS in the time and frequency domains and uncorrelated scattering (US) assumption implies that the scattering is uncorrelated in the delay domain.

1.3.1 Isotropic Scattering: Uniform and Non-Uniform AOA

The two main assumptions in the Clarkes model [2] are that the scattering around the mobile receiver is isotropically random and, equivalently, the probability of AOA of waves impingent on the receive antenna is uniform over $[-\pi, \pi]$. Moreover, the scatterers are assumed static and time variation in the channel between transmitter and the receiver is due solely to the motion of the receiver. These assumptions result in a time-varying sta-

tionary Rayleigh fading channel with the following real-valued envelope autocorrelation

$$\Phi(\Delta t) = \Upsilon\ J_0(\omega_d \Delta t), \tag{1.7}$$

where Δt is the separation in time, $J_0(\cdot)$ is the Bessel function of the first kind and order zero, and ω_d is the Doppler spread (in radians per second) of the received signal Doppler spectrum

$$\omega_d = \eta|\boldsymbol{v}| = \frac{2\pi}{\lambda_c}|\boldsymbol{v}| = 2\pi\frac{f_c}{c}|\boldsymbol{v}|, \tag{1.8}$$

where f_c is the carrier frequency (in hertz (Hz)), λ_c is the carrier wavelength (in meters (m)), η is the free space phase constant of the electromagnetic wave, c is the speed of light and $|v|$ is the speed of the mobile receiver. The power spectral density (PSD), $\Phi(\omega)$, of the received baseband random complex Gaussian signal is related to the autocorrelation (Eq. (1.7)) through the Fourier transform (Wiener-Khintchine theorem [51]) as follows

$$\Phi(\omega) = \begin{cases} 2\left(\sqrt{\omega_d^2 - \omega}\right)^{-1}, & |\omega| \leq \omega_d; \\ 0, & \text{otherwise.} \end{cases} \tag{1.9}$$

Notice that $\Phi(\omega)$ is U-shaped symmetric about $\omega = 0$, which is a consequence of the real-valued autocorrelation. The extension of Clarkes model [2] to uniform scattering in 3D by the same author was presented recently in [52]. The channel autocorrelation function in 3D isotropic scattering is given by

$$\Phi_{iso}^{3D}(\Delta t) = \mathrm{sinc}(\omega_d \Delta t) \tag{1.10}$$

where $\mathrm{sinc}(\cdot)$ is defined as

$$\mathrm{sinc}(x) \triangleq \frac{\sin(x)}{x}. \tag{1.11}$$

The PSD of the received random signal in 3D isotropically random scattering is then given by the Fourier transform of (1.10) as

$$\Phi_{iso}^{3D}(\omega) = \frac{\mathrm{rect}(\omega)}{2\omega_d} \tag{1.12}$$

where $\mathrm{rect}(\cdot)$ is the rectangle function.

The assumption of uniform distribution of AOA of waves in the full azimuth was relaxed in [28] by allowing the scatterers to be uniformly distributed on an ellipse (instead of a circle) with the receiver and the transmitter positioned on the foci of the ellipse.

The resulting channel was time and frequency selective and the distribution of AOA of waves was non-uniform. As a consequence of non-uniform AOA distribution, the channel statistics were shown to depend on mobile direction of travel.

1.3.2 Non-Isotropic Scattering: Uniform and Non-Uniform AOA

It has been argued and experimentally demonstrated that the scattering encountered in many suburban and rural environments is non-isotropic [15, 18, 19, 53–55] and the distribution of AOA of waves is not always uniform [23, 28, 56–61]. The measurements have also shown that scattering in a vehicle-to-vehicle communication wireless link is also non-isotropic [16, 17]. The non-isotropicity of the scattering environment could well be due to the directionality of the mobile (smart) receive antenna [62, 63]. As pointed out earlier, only a small number of roughly equally strong arriving waves with phases uniformly distributed over $[-\pi, \pi]$ and independent from the magnitudes of arriving waves is sufficient for the channel process to be complex Gaussian and, equivalently, its envelope to be Rayleigh distributed. This implies that it is possible for the envelope to have Rayleigh statistics even when the scattering is non-isotropic (with either uniform or nonuniform AOA of waves). The assumption of isotropic scattering in the Clarkes model is, therefore, an oversimplification that simplifies the mathematical treatment of the subject. Commonly non-isotropic APD has been shown to be well modeled by truncated-uniform (isotropic), truncated Laplacian [18], truncated Cosine, truncated Gaussian [19] and von- Mises distribution [15]. Several other models exist in literature, for SISO and multiple-input multiple-output (MIMO) systems, which are based on the non-isotropicity of the mobile radio reception with either non-isotropic receive antenna or the scattering environment and the probability of AOA as either uniform or non-uniform [1, 20–27, 31].

To the best of authors knowledge, no unified framework exists for time-selective SISO (or MIMO) and OFDM based time-invariant space-frequency selective channels which could allow arbitrary APD (or AOA distribution of impingent waves) around the receiver. It is therefore of some interest, firstly, to develop such model for these channels which may be applicable in any scattering environment with arbitrary APD and, secondly, to know as to how much the knowledge of a particular scattering environment which improves the accuracy of the channel statistics adds to the overall performance of the non-coherent communications system (Chapter 3)? In communications systems where instantaneous CSI is unavailable, the statistics of the received signal are of fundamental interest for reliable demodulation and subsequent decoding of the received signal. Since the statistics of the channel are controlled by the scattering environment [64], the

knowledge of the non-isotropicity (or, equivalently, the angular spread[2](AS)) and the non-uniformity of the distribution of AOA are essential for better estimates of the channel process. This thesis in part is devoted to the development of SISO time-selective channel model (Chapter 2) and OFDM based space-frequency selective time-invariant channel models applicable in general scattering environments (Chapter 5).

1.4 Non-Stationary Mobile Rayleigh Fading Channels

The Clarkes model assumes that the mobile receiver has a constant mobile velocity. As a consequence of this assumption, the second order statistics of complex Gaussian channel process are time-invariant. In other words, the channel process is stationary when the mobile receiver has constant speed and the direction of mobile travel. The assumption of constant mobile velocity which obviously has limited validity is yet another idealization in the Clarkes model. A mobile moving with constant acceleration (or deceleration which is, in fact, negative acceleration) corresponds better to physical reality [66]. Therefore, it may be of some interest to explore the channel statistics when the assumption of constant mobile velocity is relaxed and the mobile is allowed to have constant acceleration implying a time-variant velocity and, hence, second order channel statistics. In other words, the motion of mobile with constant acceleration makes the channel process non-stationary. Chapter 4 in this thesis is devoted to the derivation of non-stationary channel statistics and its impact on the performance of non-coherent communications systems.

The mobile acceleration is taken due care of in the performance evaluation of ad hoc cellular networks because mobile acceleration affects many network parameters like the design of strategies for location updating and paging, quality-of-service (QoS), radio resource management (*e.g.*, dynamic channel allocation schemes), technical network planning and design (*e.g.*, cell and location area layout, network dimensioning). These sensitivities affect the performance of the network as a whole, and affect the ability to accomplish the mission assigned to a specific participant [67]. However, to the best of authors knowledge, the impact of mobile acceleration on channel statistics and, hence, on overall performance of single-user communications has not been studied so far in the literature. The reason behind this seems to be the fact that in the state-of-the-art communications systems the channel is estimated based on a very small segment of transmitted data frame typically of the order of a millisecond (msec) or less, *e.g.*, the channel estimates in a GSM system are refreshed every 577 micro-sec. Due to mass inertia effect, the change in acceleration for such very short bursts of transmission is negligibly small.

[2]Angular spread (AS) is defined as the standard deviation of APD of the scattering environment [65].

As discussed earlier, the emerging wireless communications standards specify higher carrier frequencies with higher mobility so that the duration of the transmission bursts has to be made even shorter. Such short duration bursts may not allow the transmission of known pilot symbols (as, for example, in GSM) to facilitate channel estimation at the receiver and, therefore, future designs may have to incorporate non-coherent channel estimation strategies which might require longer observation periods for sufficiently reliable channel estimates. In such scenarios, the impact of mobile acceleration on the performance of communications systems may be significant. In Chapter 4 we study the effects of mobile acceleration on mobile Rayleigh fading statistics and derive Wigner-Ville distribution (WVD) [68] and mean instantaneous power spectrum (MIPS) [69,70].

1.5 Mobile Rayleigh Fading Channels: Input-Output Model

The transmission of a communications signal through wireless medium suffers from frequency, time and angular dispersion. The dispersion in frequency (time-selectivity) is due to the Doppler effect as a result of motion of the mobile receiver. This implies that if a pure tone is transmitted, the received signal would have finite spectral bandwidth. The dispersion of the transmitted signal in the time domain (frequency selectivity) is due to the higher transmitted signal bandwidth than the channel coherence bandwidth[3]. Equivalently, if the signal bandwidth is sufficiently large as compared to the reciprocal of the root-mean-square (rms) delay spread[4] τ_{rms}, the signal spreads in time causing intersymbol interference (ISI). This implies that a single transmitted pulse looks like a series of pulses at the receiver. The angular spread at the receiver is due to physical scattering environment around the receiver. Mathematically, the standard baseband equivalent form of input-output (I/O) relationship in a wireless channel at time t is given as

$$r(t) = \sqrt{\rho}\, h(t,\tau) * s(t) + z(t), \tag{1.13}$$

$$= \sqrt{\rho} \int_{-\infty}^{\infty} h(t,\tau) * s(t-\tau) d\tau + z(t), \tag{1.14}$$

where $r(t)$ and $s(t)$ respectively are the channel output and input, and $h(t,\tau)$ denotes the channel response at time t and delay τ . The sign $*$ represents the linear convolution operator. Equations (1.13) and (1.14) are normalized such that channel, input and noise

[3]At this point, it suffices to mention that the channel coherence bandwidth is qualitatively defined as the frequency range over which the channel remains highly correlated.

[4]The rms delay spread τ_{rms} is defined as the standard deviation of the multipath power-delay profile which is defined as the distribution of power in the delay τ domain (see, for example, [71]).

processes are all of unit variance so that represents the signal-to-noise ratio (SNR). The main assumption underlying (1.13) and (1.14) is that the transmitted signal bandwidth is higher than the channel coherence bandwidth, *i.e.*, the transmitted signal is wideband which causes the signal spread in the delay domain. The frequency and angular dispersions[5] are implied in the notation $h(t,\tau)$ and would become evident later in the thesis. In fact, the angular (and time) dispersion shall be assumed to be time-invariant thereby implying that the time variation in the channel is only due to the Doppler effect, *i.e.*, the motion of the mobile receiver.

If, on the other hand, the signal bandwidth is less than the channel coherence bandwidth, *i.e.*, the signal is narrowband, the convolution operator in (1.13) and (1.14) becomes multiplication implying no spread of the signal in delay domain. Mathematically, the channel I/O relationship for narrowband transmission is then given as

$$r(t) = \sqrt{\rho}\, h(t)s(t) + z(t), \tag{1.15}$$

The discrete-time equivalents of narrowband and wideband I/O models shall be discussed respectively in Chapters 2 and 6.

1.6 Capacity of Mobile Rayleigh Fading Channels

As pointed out earlier, when no CSI is available at the receiver, it has to be estimated by the receiver on the basis of channel statistics which, in turn, depend directly on the scattering environment around the mobile receiver. We, in this thesis, claim that if the scattering around the mobile receiver is non-isotropic, the knowledge of the non-isotropicity of the scattering environment has quite noticeable impact on our knowledge of temporally correlated channel statistics. A comparison of two scattering scenarios based on channel statistics is obviously not as informative as their comparison on the basis of overall performance of the communications system. This is where an important information-theoretic function called capacity becomes useful. A better knowledge of channel statistics is translated into better channel estimation and, hence, higher achievable information communication rates. If we can derive the achievable rates for different scattering environments, a quite meaningful comparison in terms of channel capacity can be drawn.

The problem of Rayleigh fading channel capacity with no CSI has been studied for

[5]Sometimes the multipath powers in the angular and delay domain are jointly distributed, *i.e.*, there is a particular power-delay profile corresponding to a particular AOA [4, 5]. We shall use this joint angle-delay power distribution concept in Chapter 6 in the study of OFDM based space-frequency selective channel.

some simplified models *e.g.*, memoryless Rayleigh fading channel [72,73], block-fading Rayleigh fading channel [74, 75], block MPSK channels [76] and finite-state Markov channels [77]. The capacity achieving input signaling in noncoherent scenario has been shown to be discrete [72, 73, 78] which is in contrast to the perfect CSI scenario where continuous Gaussian inputs are optimal. The channel capacity for time-selective Rayleigh fading channels has been studied in [37, 79]. The impact of scattering environment on the Rayleigh fading capacity is captured in [79] through the rank of the channel covariance matrix without considering a specific scattering environment. In [37], the scattering environment is assumed to be isotropic and the achievable rates over the resultant Rayleigh fading channel are studied for two types of independent and identically distributed (i.i.d.) input signaling distributions: Gaussian and MPSK. The structure of capacity achieving input distribution is not studied in view of the difficulty of the problem and convenient upper and lower bounds to achievable rates are derived based on a no-CSI cost function.

1.6.1 No-CSI Cost Function

The results in [37] are based mainly on the evaluation of a (normalized) no-CSI cost (penalty) function for MPSK signaling, P_{δ}^{norm} — a function of the scattering environment and, equivalently, the eigenvalues of the channel covariance matrix — defined mathematically as (Section 3.3)

$$P_{\delta}^{norm} \leq \frac{1}{N} \sum_{i=1}^{N} \log\left(1 + \rho\lambda_i\right), \tag{1.16}$$

where N is the length of transmitted symbol sequence, log is the natural logarithm and λ_i is the ith eigenvalue of the channel covariance matrix. Notice that P_{δ}^{norm} represents an upper bound to no-CSI cost function which implies that no-CSI cost for Gaussian signaling is less than P_{δ}^{norm} [37]. Fig. 1.3 shows the behavior of no CSI cost function as a function of block length of transmission. The cost for unknown CSI is maximum when only one symbol is used which is in line with the intuition that the temporal correlation in the channel process is useless if a single symbol is considered. The penalty due to no CSI reduces by $\approx 77\%$, at $f_{\mathrm{D}} = 0.01$, when the channel is estimated on the basis of only 10 symbols. The reduction in no CSI cost is not significant for block lengths greater than 10 symbols.

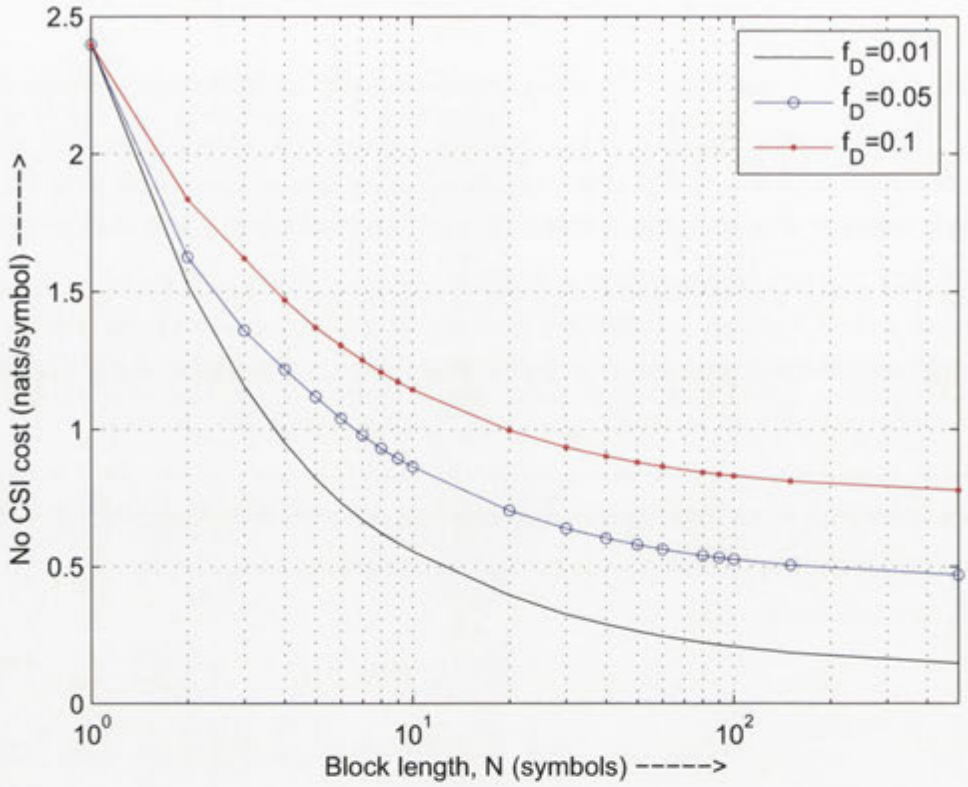

Figure 1.3: No CSI cost function as a function of block length of transmission.

1.6.2 Achievable Rates with Gaussian Signaling

The achievable information rates over mobile Rayleigh fading channels with Gaussian signaling $I_G(\mathbf{r}, \mathbf{s})$ are given as

$$I_G(\mathbf{r}, \mathbf{s}) \geq C_{\text{Rayleigh}}(\rho) - P_{\delta}^{norm}, \tag{1.17}$$

where $\mathbf{r}$ and $\mathbf{s}$ are the channel output and input vectors of length N, and $C_{\text{Rayleigh}}(x)$ is the ergodic Rayleigh capacity per symbol [80] with perfect CSI

$$C_{\text{Rayleigh}}(x) \triangleq \mathbb{E}_h \left\{ \log \left(1 + x|h|^2 \right) \right\} = -\exp\left(\frac{1}{\rho}\right) E_i\left(-\frac{1}{\rho}\right), \tag{1.18}$$

where $E_i(x)$ is the exponential integral defined as

$$E_i(x) \triangleq \int_{-\infty}^{x} \frac{\exp(u)}{u} du. \tag{1.19}$$

1.6.3 Achievable Rates with MPSK Signaling

The achievable rates for MPSK signaling, $I_C(\mathbf{r}, \mathbf{s})$, are given as

$$I_C(\mathbf{r}; \mathbf{s}) \leq C_{\text{AWGN}}(\rho) - P_\delta^{norm}, \tag{1.20}$$

where the AWGN capacity $C_{\text{AWGN}}(x)$ is defined as

$$C_{\text{AWGN}}(x) \triangleq \log(1 + x). \tag{1.21}$$

Notice that $I_C(\mathbf{r}, \mathbf{s})$ represents an upper bound to the achievable rates with MPSK signaling. The no-CSI cost function P_δ^{norm} and achievable rates for Gaussian and MPSK signaling in general scattering environments are studied in Chapter 3.

1.7 Pilot-Aided Channel Estimation for Mobile Rayleigh Fading Channels

The performance of a non-coherent communications system depends on the quality of CSI estimates. Traditionally, CSI is estimated by pilot-aided channel estimation (PACE) scheme in which known pilot symbols are multiplexed into the transmitted stream. At the receiver, these pilot symbols are demultiplexed out of the received symbol stream. The channel is estimated at pilot symbol instants which are then used to obtain estimates of CSI at data symbol locations through interpolation. Due to the presence of AWGN, CSI estimates at pilot symbols (and, hence, at data symbols) are imperfect. The quality of channel estimates at pilot symbol instants depends on SNR of pilot symbols. It is, therefore, always desirable to improve pilot symbol SNR either by enhancing power of pilot symbols or by reducing AWGN. Since power is a precious resource, we may not always have luxury to enhance power of the pilot symbols. So reducing noise to improve the quality of PACE is more desirable.

The optimal technique to reduce the impact of AWGN on CSI estimates at data symbol instants is to use Wiener interpolator which is optimal in the MMSE sense and requires the perfect knowledge of channel and noise statistics. The wiener interpolator effectively rejects out-of-band AWGN noise. It can be designed as an infinite impulse response (IIR) or finite impulse response (FIR) filter. In IIR realization, it requires the perfect knowledge of channel spectrum (or, equivalently, channel autocorrelation at infinite lags). For FIR Wiener filter implementation, however, the requirement is of finite but perfect autocorrelation samples. The complexity of Wiener interpolator is very large due to its requirement of large number of pilot symbols for sufficiently accurate channel

estimation making it impractical to implement. It is, however, very useful as a performance benchmark for PACE-based communications systems. Many suboptimal interpolating schemes have been proposed in the literature. One such approach that requires perfect knowledge of channel and noise spectra proposes to use Wiener filter to low pass filter the pilot symbol sequence but use a linear interpolator. There are simple interpolation schemes which do not require the knowledge of channel and noise spectra, *e.g.*, Gaussian, raised-cosine, low pass windowed sinc and frequency domain interpolation (see [81] and references therein).

A signal processing technique based on oversampling (or upsampling[6]) of the pilot symbols followed by filtering and subsequent downsampling was proposed and numerically analyzed in [82] in connection with Doppler frequency estimation. Assuming that the expected maximum Doppler frequency is known a priori, it was shown that the performance of Doppler frequency estimation is significantly improved because of noise reduction at the cost of increased complexity at the receiver. This popular technique of oversampling of channel samples to improve estimator performance has been adapted from the concept of fractionally spaced channel equalizations [83–85]. So if we can oversample or have oversampled channel process, we can improve the performance of PACE based channel estimator by incorporating a simple signal processing scheme at the receiver low pass filtering of the oversampled pilot sequence followed by downsampling. We describe this overall signal processing scheme as Oversample-Low pass filter-Downsample (OLD). The pilot symbol sequence thus processed is input to the interpolator to obtain CSI estimates at the data symbol instants.

While trying to develop some PACE scheme offering better quality of CSI estimates based on the perfect knowledge of channel statistics in general scattering environments, we came across the idea of so-called peaky signaling (also called flashy signaling) a type of signaling optimal in the low SNR regime that remains silent for most of the time and uses symbols of very large amplitude (approaching infinity as SNR tends to zero) when transmitting [78, 86, 87]. The peaky signaling, therefore, invariably results in a loss of useful degrees of freedom (*dof*). To find some way to utilize these unused degrees of freedom to enhance the overall performance of the system is obviously of some interest. In a recent contribution [78], the performance of peaky signaling over block-fading Rayleigh channels was shown to improve in conjunction with PACE in the low SNR regime. Chapter 5 in this thesis is devoted to the study of a modified peaky signaling in conjunction with PACE in time-selective Rayleigh fading channel (Fig. 5.1). The pilots are periodically inserted in the transmitted stream at least at the Nyquist rate

[6]Both upsampling and oversampling, sometimes defined differently in literature, are equivalent from the point of view of their impact on the spectrum of the sampled signal. In this thesis we shall be concerned with signal spectra and shall use the two terms interchangeably without causing confusion.

corresponding to the time rate of channel variation. The unused *dof* in the modified peaky signaling can equivalently be thought of as upsampling of the transmitted stream which can be effectively utilized by OLD scheme at the receiver to enhance SNR at pilot symbol instants by as much as the upsampling factor $\mathcal{M}$ — the number of unused *dof* . This pilot symbol SNR enhancement results in significant MMSE performance gain when the processed pilot symbol sequence is input to the wiener interpolator. Using improved CSI estimates, we optimize bandwidth and power allocation to pilot symbols following the approach of [88]. The results suggest that significant savings in power and bandwidth can be achieved with the proposed PACE scheme over time-selective Rayleigh fading channels.

1.8 Outline of Thesis

1.8.1 Overview

The primary motivation for this thesis has been to develop unified frameworks to assess the impact of perfect knowledge of a particular scattering environment, the carrier frequency, the mobile velocity and acceleration on the channel statistics and the performance of communications systems operating over mobile Rayleigh fading channels. The thesis can be broadly subdivided into two parts. The SISO time-selective Rayleigh fading channels are the subject of the first part. The space-frequency selective Rayleigh fading channels are considered in the second part.

SISO Time-Selective Rayleigh Fading Channels

The work on SISO time-selective Rayleigh fading channels can be further subdivided into twochannel modeling (and achievable information rates) and channel estimation. In the channel modeling part, we generalize the well known Clarkes mobile Rayleigh fading model [2] from two aspects. Firstly, the assumption of isotropic scattering environment around the mobile receiver in the Clarkes model is generalized to incorporate general scattering environments such that the Clarkes model is a special case of the generalized model. The impact of generalized Rayleigh fading on achievable information rates is also studied. Secondly, the assumption of constant mobile velocity in the Clarkes model resulting in stationary channel statistics is generalized to the case of a constant mobile acceleration which corresponds better to the physical reality. The implications of constant mobile acceleration on the performance of communications systems is also studied. We propose a PACE scheme for mobile Rayleigh fading channels based on OLD processing scheme at the receiver which utilizes the perfect knowledge of channel

statistics and the unused degrees of freedom in the peaky signaling [78] to significantly improve the system performance at low SNR. The scattering environment was assumed to be isotropic. We do not attempt to consider general scattering environments in view of the impossibility to obtain closed form solutions. However, as the results suggest, the proposed scheme would perform better in non-isotropic environments.

Space-Frequency Selective Rayleigh Fading Channels

The use of MIMO-OFDM in the future systems has been the motivation for us to develop a SIMO-OFDM framework for the calculation of channel statistics in general scattering environments. This SIMO-OFDM framework can be extended to the more general case of MIMO-OFDM. We also present a generalization of [19] to general scattering environments and give some useful results regarding space-frequency trade-off characteristics of different non-isotropic scattering distributions.

1.8.2 Questions to be Answered in this Thesis

In this section, we itemize some broad questions that would be answered in the following chapters of this thesis.

- Is it possible to develop a generalized SISO narrowband mobile Rayleigh fading model which may provide a unified framework to calculate and compare channel statistics in general scattering environments (with arbitrary APD)? How much difference does it make to the overall performance if a non-coherent communications system designed for one APD is operated in a different APD?

- The emerging wireless communications standards specify MIMO-OFDM as the technology of choice which has triggered recent interest in space-time coding for such systems. Can we develop a framework for calculating statistics of time invariant space-frequency selective channels in general scattering environments? Are different non-isotropic scattering distributions equivalent from the point of view of space-frequency trade-off?

- Generally, the literature on channel modeling is based on the assumption of constant mobile velocity. What happens to the channel statistics if the mobile has a constant acceleration? What are the implications of mobile motion with constant acceleration for future wireless communications systems?

- The peaky signaling results in a loss of useful *dof* . The use of PACE in conjunction with the peaky signaling results in better achievable rates than with the

peaky signaling alone. Is it possible to somehow make use of the unused *dof* to further improve the performance of PACE-based communications system that employs peaky signaling? How much bandwidth and power (that has to be allocated to the pilots symbols) can be saved when the desired performance is as good as achievable with non-peaky signaling?

1.8.3 Content and Contribution of Thesis

In the following, we summarize the contents of this thesis with emphasis on the contribution made within each chapter.

- Chapter 2 studies the mobile SISO Rayleigh fading modeling in general scattering environments. We develop a generalized Rayleigh fading model using the well known Jacobi-Anger plane wave expansion [89] assuming perfect knowledge of scattering environment and mobile dynamics. The Clarkes model [2] happens to be a special case of this model. The results suggest that the knowledge[7] of the degree of non-isotropicity and the mobile direction of travel with respect to the mean scattering angle can have significant impact on channel statistics. In particular, estimated channel statistics may have significant errors in more non-isotropic scattering environments if the degree of non-isotropicity and mobile direction of travel are unknown. We also compare channel statistics for common non-isotropic scattering distributions. The results suggest that common non-isotropic scattering environments are, to good approximation, equivalent for very small and large angular spreads. The difference for moderate angular spreads which may be significant depends on mobile direction of travel as well.

- Chapter 3 is, in fact, an application of the generalized Rayleigh fading model developed in Chapter 2. While comparing different scattering environments the statement like higher (or lower) correlation does not seem to be very useful one. This chapter gives a physical meaning to the impact of scattering environment on the overall performance of a communications system by quantifying differences in channel statistics due to different scattering scenarios in terms of an information theoretic quantity bits/sec. The results suggest that the perfect knowledge of mobile direction of travel and the degree of non-isotropicity may result

[7] It may be mentioned here that the channel estimator that we employ *does not* estimate the channel on the basis of individual realizations of the channel process. It forms the channel estimate on the basis of its autocorrelation function and power spectral density known *a priori*, which do require the knowledge of the degree of non-isotropicity and the mobile direction of travel with respect to the mean scattering angle. If we estimate the channel based on several realizations, the knowledge of channel statistics shall not be required.

in significantly higher achievable rates over isotropic scattering particularly for higher fading rates. This chapter also studies the impact of using a directional antenna (or beamforming) in isotropic scattering conditions. The results indicate that beamforming results in better performance only if mobility is very high. The poor performance of beamforming in low mobility applications is due to the fact that the use of directional antenna in isotropic scattering scenario results in poor SNR due to the rejection of useful power by the antenna resulting in overall performance loss as compared to isotropic antenna. The comparative study of different commonly used scattering distributions suggests that different scattering distributions are almost equivalent for sufficiently small and large angular spreads. The truncated-Laplacian,truncated-Gaussian and von-Mises distributions are almost equivalent for all angular spreads, mobile directions of travel and block lengths of transmission. The truncated-uniform distribution, however, results in better achievable rates than other distributions. We also present a practical example justifying the fact that the joint Gaussianity implies marginal Gaussianity but not vice versa. This confusion led authors in [90, 91] to incorrectly claim that the achievable rate with MPSK signaling derived by them was in fact the capacity of MPSK signaling. We dispel the confusion behind the arguments that led to such claim by giving mathematical and numerical results.

- Chapter 4 presents a generalization of the classical Clarke model that assumes constant mobile velocity to a mobile communications scenario where the mobile has constant acceleration. The assumption of constant velocity resulted in stationary Rayleigh fading statistics in the Clarkes model and its generalization in Chapter 2. The assumption of constant mobile acceleration renders the Rayleigh fading statistics time-varying, *i.e.*, non-stationary. It turns out that, under the assumptions of unbounded mobile velocity and infinite sampling rate, Wigner-Ville distribution (WVD) presents a natural extension of Clarkes model from stationary to non-stationary Rayleigh fading statistics. We also study the implications of constant mobile acceleration on the performance of emerging wireless communications systems in terms of frame overhead and payload. The impact of changes in carrier frequency on frame overhead and payload is also explored. The results show that, as compared to constant mobile velocity scenario, the mobile acceleration could result in significant increase in integrated frame overhead and decrease in useful integrated payload. Moreover, the impact of mobile acceleration is more when the initial mobile velocity is lower.

- Chapter 5 concerns the development of an improved MMSE performance of PACE

scheme in conjunction with peaky signaling for communication over mobile Rayleigh fading channels in isotropic scattering environment. We do not consider this problem of channel estimation in general scattering environments, firstly, because the results in Chapters 2 and 3 suggest that non-isotropicity of the scattering environment, in fact, 'slows down' the channel fading process so that the performance of a communications system in isotropic environment serves as a benchmark for general scattering environmentsthe performance of a communications system in general scattering environments is at least as good as in isotropic scattering if the observation period is infinite. Secondly, the channel spectrum in non-isotropic environments, in general, involves summation of product of functions. The use of this summation, therefore, allows only numerical evaluation of the performance of PACE in general scattering environments. The proposed scheme utilizes the idle *dof* in the peaky signaling to enhance MMSE performance of Wiener interpolation using OLD scheme by as much as the number of idle degrees of freedom. This translates into significant gains in achievable rates, particularly in the low SNR regime, over PACE-based Rayleigh fading channels consuming less resources than with conventional non-peaky signaling (that uses the same total average power) without OLD scheme at the receiver. We constrain the total average power in peaky and non-peaky to be the same. This constraint results in power savings as a result of idle *dof* in the peaky signaling giving rise to four possibilities. The power savings can be utilized in enhancing the power of the pilots symbols alone (pilot enhancement (PE)), data symbols alone (data enhancement (DE)), pilot and data symbols (pilot and data enhancement (PDE)). The fourth possibility is not to use these power savings, *i.e.*, no enhancement (NE). We mainly consider PE, DE and PDE choices and shall refer only to these unless otherwise stated. The results suggest that in the limit of zero SNR, all choices are equivalent irrespective of whether there is any constraint on pilot and data symbol powers. If the peakiness of the signaling is increased, we can get better performance (than NP scheme) with the proposed PE and DE schemes (allowing pilot and data symbol powers to be unequal) at even lower SNR but at the cost of deteriorated performance at moderately low SNR.

- Chapter 6 deals with the time-invariant space-frequency selective channels where we derive a general framework for the calculation of channel statistics for multicarrier modulation system in arbitrary scattering environments and antenna arrays. The proposed model of channel statistics gives SFCC between different subcarriers of OFDM signals at the two receive antennas. This SIMO-OFDM model can be extended to MIMO-OFDM which should be very useful for the performance

evaluation of MIMO-OFDM based system for any joint angle-delay power distribution. We apply the proposed model for the calculation of SFCC for inverted parabolic (IP) [4] and elliptical scattering (ES) [5] models with specified joint angle-delay power distributions. The results suggest that the ES results in less cross correlation between differen subcarriers as compared to IP model.

We also derive a generalization of [19] to general scattering environments. The results indicate that the variation of angular spread from 1° to 5° significantly changes the space-frequency trade-off behavior (mean scattering angle, $\beta_0 = 45.$). The variation of angular spread beyond 10°. doe not seem to have significant impact on trade-off characteristics. It turns out that, for a fixed correlation between envelopes at two antenna, different scattering distributions may have identical space-frequency trade-off characteristics for small antenna separations and significantly different characteristics when the antenna separation is large and, equivalently, the angular spread is small. If the correlation value and angular spread are fixed, the truncated-Laplacian distribution requires higher frequency separation for a given (sufficiently large) antenna spacing and vice versa. The question of as to if one scattering environment can be substituted for another depends on antenna spacing, angular spread and the mean scattering angle. When the antenna spacing is sufficiently small, angular spread is sufficiently large and antenna array orientation is more closer to being inline, such substitution may not matter. In other cases, however, such substitution deserves careful consideration of possible impacts on the design and analysis of the communications system.

Chapter 2

Generalized Clarke Model for Mobile Radio Reception

2.1 Background

In real world communication scenarios, the transmitter and/or the receiver may be in motion. In a mobile-radio situation in which the transmitter is fixed in position while the receiver is moving, the direct line between the transmitter and receiver may be obstructed. At ultra high frequencies and above, therefore, the mode of propagation of the electromagnetic energy from transmitter to receiver is largely by way of scattering [2]. Assuming that the scattering environment is 2D isotropic in this communication scenario, the amplitude fluctuations of the received signal were shown in [2] to follow Rayleigh distribution. The assumption of isotropic APD corresponds to uniform pdf of AOA of waves impingent on the omnidirectional antenna. The autocorrelation of the received signal happened to be strictly real valued and the resulting power spectral density (PSD) was U-shaped symmetric [2].

It has been argued and experimentally demonstrated (see [15] and references therein) that the scattering encountered in many suburban and rural environments is non-isotropic, *i.e.*, the distribution of AOA of waves is not uniform as assumed in [2]. The use of a directional antenna with non-uniform gain pattern at the receiver also results in non-isotropic APD as seen by the antenna. The measurements have shown that scattering in vehicle-to-vehicle communication is also non-isotropic [16, 17].

The assumption of uniform APD resulted in closed form expressions for the statistics of the channel in [2]. For non-uniform APD, the resulting expressions for the statistics of the channel are not in closed form [28]. A quadratic form for the probability distribution function (pdf) of the AOA proposed in [22] resulted in a closed form expression for the correlation of the complex envelope of the received signal in a non-isotropic scattering

environment. In [31], von Mises distribution (also known as *circular Normal distribution*) was used to model the pdf of AOA and effects of non-isotropic scattering on the correlation properties and velocity estimation in a Rician fading channel were discussed. In practice, APD under non-isotropic conditions has also been shown to be well modelled by truncated Laplacian, truncated Cosine, and truncated Gaussian distribution [36]. Some of the other work related to mobile fading channels are in [92–94].

The assumption of uniform APD introduces small errors on the first order statistics of the received signal but a significant error on the second order statistics [63], such as correlation function or, equivalently, PSD, and level crossing rates or, equivalently, the fading rate. There are certain communication system parameters like the estimation of vehicle velocity [31] for handoff decisions and the achievable information rates [37] without CSI that depend on the correlational properties of the received signal. It is, therefore, of some interest to develop a model that accurately models the statistics of the mobile Rayleigh fading channel in general scattering environments. In this thesis we shall use the term *generalized Rayleigh fading* to imply Rayleigh fading in general scattering environments.

As discussed in Section 1.1, many 3D generalizations of Clarke's model exist in literature which include 2D Clarke's model as a special case. However, these 3D generalizations do not reduce to the true Clarke's model but equivalent expressions which may be computationally expensive. Moreover, while such generalizations do suggest that the channel statistics in general scattering environments are affected by the mobile direction of travel with respect to the mean scattering direction, no detailed analysis of the impact of mobile direction of travel and non-isotropicity of the scattering environment on channel statistics and overall communications system performance is provided. This motivates us to, firstly, develop a model of the mobile radio reception in general 2D scattering environments which incorporates the true Clarke's 2D model as its special and, secondly, to explore the impact of mobile direction of travel on channel statistics in general scattering scenarios. This chapter therefore focuses mainly on the generalization of the Clarke's model of mobile radio reception in 2D scattering environment.

The chapter is organized as follows: The channel I/O model is described in Section 2.2 and the expressions for autocorrelation and PSD of the received signal are derived. Some common scattering distributions are also described. The Clarke's model is shown to be a special case of the derived model, and the impact of direction of mobile travel and the extent of non-isotropicity on channel statistics in truncated-uniform scattering environment is explored in Section 2.3. The comparative study of channel statistics for common scattering environments is performed in Section 2.4. Finally, we summarize the chapter highlighting specific contributions in Section 2.6.

2.2 Channel model

We consider a downlink transmission system where the transmitter is stationary while the receiver is moving with some speed[1] $|\boldsymbol{v}|$ at an angle of ϕ_v with respect to the x-axis, where $\boldsymbol{v} \equiv (|\boldsymbol{v}|, \phi_v)$ is the velocity of the mobile as shown in Fig. 2.1. We assume that the scatterers are statistically homogeneous and are distributed in the far-field from the omnidirectional receiver antenna. We also assume that the channel between the transmitter and the mobile receiver is a strictly bandlimited, flat-fading (frequency non-selective), wide-sense stationary, zero mean circularly symmetric Gaussian fading process. We have the following remarks:

1. Channel variations in the mobile fading channel under consideration are caused by the movement of the mobile. Since this movement is always limited due to physical limitations on the speed of the mobile, the channel process can be assumed to be frequency bandlimited.

2. The assumption of zero-mean complex Gaussian channel fading process implicitly assumes that the scattering is rich enough with *roughly equally* strong paths with independent phases rectangularly distributed on $[0, 2\pi)$, so that the central limit theorem applies. This assumption further implies that the scatterers have a fixed density, *i.e.*, the number of the scattered waves is constant and their amplitude and (uniform) phase distributions are i.i.d time-invariant. If the number of the scattered wave is random and the phases are non-uniformly distributed, the resulting complex process is no more Gaussian and the envelope of the process is Gamma distributed [96].

3. The assumption of circular symmetry of the channel fading process implies that the *pseudo-autocorrelation* [97] is identically zero, and , therefore, the fading process is completely characterized by its complex autocorrelation.

4. Our approach is similar to that employed in [98] for space-time MIMO channel model with some important differences. First, unlike [98] which considers continuous time fading process, we employ a discrete time channel model. Secondly, we assume that the channel fading process is wide-sense stationary which is a much milder requirement than the channel fading process to be ergodic as implicitly assumed in [98].

[1]Throughout this thesis, we shall assume that the scattering environment is fixed but the receiver is mobile. The impact of moving scatterers on channel statistics for a *fixed* receiver was studied recently in [95].

The baseband-equivalent received signal $r(t)$ at time t in *continuous-time* form is given as

$$r(t) = \sqrt{\rho}\, h_c(t)\, s(t) + z(t), \quad -\infty < t < \infty \tag{2.1}$$

where $s(t) \in \mathbb{C}$ and $r(t) \in \mathbb{C}$ denote the channel input and the corresponding output at time instant t, respectively. The additive noise $z(t)$ is modeled as a zero-mean circularly symmetric[2] complex Gaussian white noise process with $\mathbb{E}\{z(x)z^*(y)\} = \delta(x-y)$ where $\delta(\cdot)$ is Dirac's delta function. The fading process $h_c(t)$ is modeled as a wide-sense stationary zero-mean circularly symmetric complex Gaussian process and is given mathematically as (with respect to some arbitrary origin 'O' where we set $t = 0$)

$$h_c(t) = \oint \psi(\beta) \exp\left(i\eta t\, \boldsymbol{v} \cdot \widehat{\boldsymbol{\beta}}\right) d\beta, \tag{2.2}$$

where $\psi(\beta)$ is the time-invariant *complex scattering gain* from a particular AOA β, $i = \sqrt{-1}$ and $\eta = 2\pi/\lambda_c$ is the free space phase constant (λ_c is the wavelength). We further assume that $h_c(t)$ is of unit variance, *i.e.*, $\mathbb{E}\{h_c(t)h_c^*(t)\} = 1$. The channel input is also assumed to have unit variance, *i.e.*, $\mathbb{E}\{s(t)s^*(t)\} = 1$. With foregoing assumptions, equation (2.1) gets normalized such that ρ represents average SNR per symbol.

If the output $y(t)$ is processed through a matched filter[3], we get the following *discrete-time* model

$$r[j] = \sqrt{\rho}\, h_d[j]\, s[j] + z[j], \quad -\infty < j < \infty \tag{2.3}$$

where $\{z[j]\}$ is a sequence of samples of an i.i.d. zero mean[4] proper complex additive Gaussian noise process with unit variance, $\{h_d[j]\}$ is a sequence of zero-mean circular complex Gaussian channel process with unit variance and $\{s[j]\}$ is the input process of unit variance. In the sequel, for notational compactness, we shall use $\{h[j]\}$ instead of $\{h_d[j]\}$ to denote sampled channel process. Assuming that the symbol duration is T_s, the continuous-time and discrete-time models ((2.1) and (2.3) respectively) are related

[2]The circular symmetry of a complex random process implies that the real and imaginary parts of the random process are uncorrelated and zero-mean. In case of a circularly symmetric *Gaussian* random process, the circular symmetry also implies that the real and imaginary parts of the process have equal variances, are jointly Gaussian and, hence, are independent of each other [99, 100].

[3]The matched filter is optimal for a white Gaussian channel but is suboptimal, in general, for fading channels. We still have considered matched filter because it is commonly employed in many practical communication systems. We assume that the filter is matched to the symbol rate and the output of the filter is sampled at the end of the symbol period. Moreover, it is customary to normalize the filter response to have unit-energy over the duration of the symbol.

[4]If a circularly symmetric continuous-time random process is sampled, the sampled process is also circularly symmetric [99, 101] where circular symmetry implies that the process is zero-mean (see footnote 2).

through the following:

$$s[j] = \frac{1}{\sqrt{T_s}} \int_{jT_s}^{(j+1)T_s} s(t)\, dt, \tag{2.4}$$

$$r[j] = \frac{1}{\sqrt{T_s}} \int_{jT_s}^{(j+1)T_s} r(t)\, dt, \tag{2.5}$$

$$z[j] = \frac{1}{\sqrt{T_s}} \int_{jT_s}^{(j+1)T_s} z(t)\, dt, \tag{2.6}$$

$$h_{\mathrm{d}}[j] = \frac{1}{\sqrt{\int_0^{T_s}\int_0^{T_s} \Phi(x-y)\, dy\, dx}} \int_{jT_s}^{(j+1)T_s} h_{\mathrm{c}}(t)\, dy, \tag{2.7}$$

where $\Phi(\cdot)$ in (2.7) is the covariance of the continuous channel process, $h_{\mathrm{c}}(t)$. Equations (2.4)−(2.7) are based on the facts that matched filter is an integrator, the output of the filter is sampled at the end of the each symbol interval T_s and discrete-time input, output, noise and channel processes must be normalized to have the same (co)variances as their continuous-time counterparts. It is to be noted that while most of the material on channel modeling deals with continuous-time model, we have chosen to work in the discrete-time domain, firstly, because the two domains are equivalent as long as the sampling is performed at least at the Nyquist rate. Secondly, whenever it comes to practical implementation of the model, discrete-time models are computationally more efficient. There are some instances in literature of discrete-time modeling, *e.g.*, see [102] and references therein. Equation (2.3) can be obtained as a special case of the discrete-time triply (*i.e.*, time-frequency-space) selective model of [102].

With no loss of generality, let the mobile be at some arbitrary point 'O' at the signaling instant j'. Thus, at the signaling interval $j = j' + k$, the mobile will be at the point $(|\boldsymbol{v}|\eta k T_s, \phi_v)$ with respect to 'O', where T_s is the symbol duration and k is an integer, which represents the time lag. Assume that the scattered signals are impinging on the mobile receiver from all directions on the 2D (horizontal) plane. Let $\psi(\beta)$ be the scattering gain at the origin due to the signals arriving from the direction β with respect to the x-axis (see Fig. 2.1). Then we write the channel gain as

$$h[j] = \oint \psi(\beta) \exp\left(i\eta j T_s\, \boldsymbol{v} \cdot \widehat{\boldsymbol{\beta}}\right) \mathrm{d}\beta, \tag{2.8}$$

where $\widehat{\boldsymbol{\beta}} \equiv (1, \beta)$ represents a unit vector along the direction β, '$\cdot$' is the scalar product between two vectors and $i = \sqrt{-1}$. Note that the factor $\exp(i\eta j T_s \boldsymbol{v} \cdot \widehat{\boldsymbol{\beta}})$ in (Eq. (2.8)) reflects the phase delay of the incoming signal from the direction β at the mobile receiver with respect to the origin.

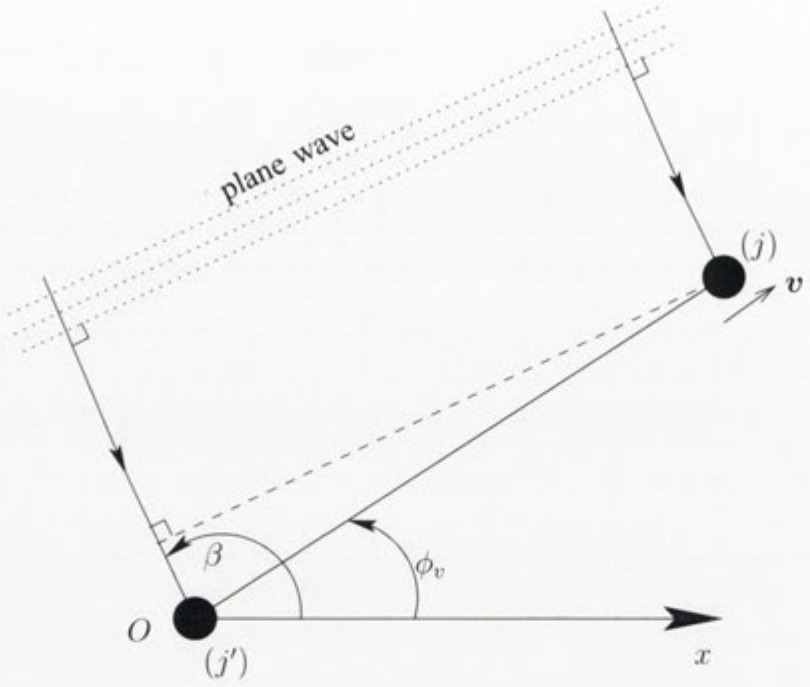

Figure 2.1: Illustration of the key parameters: direction of mobile travel ϕ_v, mobile velocity $\boldsymbol{v}$, direction of wave arrival β, time instances j' and j, and the origin 'O' of the co-ordinate system.

It is crucial to highlight an important conceptual difference between our approach and that used in [2] for modelling mobile radio reception. In [2], firstly, a probability of arrival of waves is associated with each direction in the azimuth implying that AOA are random. Secondly, the complex scattering gain, $\psi(\beta)$, from a certain direction of arrival is also random. In this contribution, we essentially assume that there is no probability distribution associated with AOA, *i.e.*, the waves are assumed to be impinging on the mobile receive antenna from all the directions in the azimuth. Only the complex random scattering gain, $\psi(\beta)$, is assumed to be random and has, associated with it, a probability distribution. An azimuth direction with zero associated probability of arrival of wave is *equivalent* to a direction with waves assumed to be impinging from that particular direction but zero complex scattering gain. In other words, our approach is a simplified yet equivalent form of that employed in [2] but proves more convenient, as we would see, for arriving at a generalized Rayleigh fading model for mobile radio reception.

2.2.1 Autocorrelation of the Channel Fading Process

Using (2.8) we write the correlation between the channel gain at the signaling intervals j' and j as

$$\begin{aligned}\Phi(j,j') &= \mathbb{E}\left\{h_j h_{j'}^*\right\} \\ &= \oint\oint \mathbb{E}\left\{\psi(\beta)\psi^*(\beta')\right\} \exp\left(i\eta T_s(j\,\boldsymbol{v}\cdot\widehat{\boldsymbol{\beta}} - j'\,\boldsymbol{v}\cdot\widehat{\boldsymbol{\beta}}')\right) \mathrm{d}\beta\mathrm{d}\beta', \end{aligned} \tag{2.9}$$

where $\mathbb{E}\{\cdot\}$ stands for the mathematical expectation. Assuming that the scattering gain from two distinct directions are uncorrelated [28], *i.e.*,

$$\mathrm{E}\left\{\psi(\beta)\psi^*(\beta')\right\} = \mathrm{E}\left\{|\psi(\beta)|^2\right\}\delta(\beta-\beta'), \tag{2.10}$$

where δ is the Dirac delta function. We have the following remarks:

1. The assumption of uncorrelated scattering (US) is a widely used assumption in the channel modeling literature [5, 36, 103–105]. This assumption is implicit in [4, 105–108] for the purpose of deriving the angular power spectrum in the frequency-flat fading scenarios as well as the joint angular power-delay profile in the frequency selective fading scenarios. This assumption has been verified by various measurement campaigns, including [59, 106, 109, 110]. However, this assumption is not strictly true for coherent sources in the adaptive beamforming literature [111, 112]. As a future research topic, one possible extension of the framework developed in this chapter is to take into account correlation among scatterers by following [113].

2. The assumption of US may not be realistic in view of the fact that the scattering objects can be buildings, trees, hills, etc. In order for scatterers to look like 'point scatterers' to the receiver so that the assumption of US is applicable, the dimensions of the physical scatterers have to be less than the receiver bandwidth [28,56]. In fact, behind the assumption of complex Gaussianity of the channel process lies this assumption of US.

Using(2.10) in (2.9) results in

$$\Phi(j,j') = \Phi(j-j') = \Phi(k) = \oint \Psi(\beta)\,\exp\left(i\eta T_s k\,\boldsymbol{v}\cdot\widehat{\boldsymbol{\beta}}\right)\mathrm{d}\beta \tag{2.11}$$

where $k = j - j'$ and

$$\Psi(\beta) = \mathrm{E}\left\{|\psi(\beta)|^2\right\}, \tag{2.12}$$

normally termed as the *angular (azimuth) power distribution* (APD) of the received signal. Thus, $\Psi(\beta)$ is the average power received from the direction β.

Notice that $\Psi(\beta)$ and $\exp\left(i\eta T_s k\, \boldsymbol{v}\cdot\widehat{\boldsymbol{\beta}}\right)$ are both periodic in β with period 2π. We can, therefore, express $\Psi(\beta)$ using the Fourier series as follows:

$$\gamma_m = \oint \Psi(\beta)\, e^{-im\beta}\, \mathrm{d}\beta, \tag{2.13a}$$

$$\Psi(\beta) = \frac{1}{2\pi}\sum_{m=-\infty}^{\infty} \gamma_m\, e^{im\beta}, \tag{2.13b}$$

where γ_m are the coefficients of the Fourier series expansion of $\Psi(\beta)$. Also, we can express the factor $\exp\left(i\eta T_s k\, \boldsymbol{v}\cdot\widehat{\boldsymbol{\beta}}\right)$ using Fourier series (also known as Jacobi-Anger expansion [89, page 67]) as

$$\exp\left(i\eta T_s k\, \boldsymbol{v}\cdot\widehat{\boldsymbol{\beta}}\right) = \sum_{m=-\infty}^{\infty} \underbrace{i^m\, J_m(\eta k T_s|\boldsymbol{v}|)\exp\left(-im\phi_v\right)}_{\xi_m} \exp\left(im\beta\right), \tag{2.14}$$

where ξ_m are the Fourier series coefficients and $J_m(\cdot)$ is the Bessel function of integer order m. Using (2.13), (2.14) and the convolution property[5] of the Fourier series, (2.11) can be written as

$$\begin{aligned}
\Phi(k) &= \frac{1}{2\pi}\oint \sum_{n=-\infty}^{\infty}\left(\sum_{m=-\infty}^{\infty}\gamma_m\,\xi_{n-m}\right)\exp\left(in\beta\right)\mathrm{d}\beta,\\
&= \frac{1}{2\pi}\sum_{n=-\infty}^{\infty}\left(\sum_{m=-\infty}^{\infty}\gamma_m\,\xi_{n-m}\right)\oint\exp\left(in\beta\right)\mathrm{d}\beta,\\
&= \sum_{m=-\infty}^{\infty}\gamma_m\xi_{-m}\\
&= \sum_{m=-\infty}^{\infty} i^{-m}\,\gamma_m\; J_m(\eta k T_s|\boldsymbol{v}|)\;\exp\left(im\phi_v\right),
\end{aligned} \tag{2.15}$$

where the inner summation in the first equality represents the convolution of the Fourier series coefficients γ_m and δ_m, the third equality is the result of the following fact:

$$\oint \exp\left(in\beta\right)\mathrm{d}\beta = \begin{cases} 2\pi, & n=0;\\ 0, & \text{otherwise.}\end{cases}$$

[5]The Fourier series coefficients of the product of two periodic functions are equal to the convolution of the coefficients of the Fourier series expansions of the individual functions [114].

and the relation $J_{-m}(\cdot) = (-1)^m J_m(\cdot)$. If we let $\omega_d = \eta|\boldsymbol{v}|$ be the maximum angular Doppler spread (maximum doppler frequency, $f_d = v/\lambda_c$), (2.15) can be rewritten as

$$\boxed{\Phi(k) = \sum_{m=-\infty}^{\infty} i^{-m}\, \gamma_m\, J_m(\omega_d k T_s)\, \exp\left(im\phi_v\right).} \tag{2.16}$$

Equation (2.16) is the complex autocorrelation function of the channel fading process as a function of time lag k. It is obvious from (2.16) that the autocorrelation of the fading process, in general, not only depends on the distribution of power (and, hence, mean scattering angle) but also on the direction of mobile travel, ϕ_v, maximum Doppler spread ω_d, and the symbol duration, T_s.

2.2.2 Spectral Density of the Channel Fading Process:

Using the well-known Wiener-Khintchine theorem [51], we obtain the PSD of the fading process by taking discrete-time Fourier transform (DTFT) of (2.16) as follows:

$$\Phi(\omega) = \sum_{m=-\infty}^{\infty} \gamma_m\, \exp(im\phi_v) \left\{ \sum_{p=-\infty}^{\infty} J_m(\omega_d p T_s) \exp\left(-i\omega p T_s\right) \right\}, \tag{2.17}$$

where $\omega \in [-\pi, \pi]$ is the continuous radian frequency variable. We simplify (2.17) in Appendix A.1 to obtain

$$\boxed{\Phi(\omega) = \frac{1}{\omega_D} \sum_{m=-\infty}^{\infty} \gamma_m\, \exp(im\phi'_v)\, F_m\left(\frac{\omega}{\omega_D}\right),} \tag{2.18}$$

where $\omega_D = \omega_d T_s = 2\pi f_{\mathrm{D}}$ is the normalized Doppler spread (f_{D} is the normalized fading rate) and $\phi'_v = \phi_v + \pi$. It is easy to see that (2.18) is equivalent to the following

$$\Phi(\omega) = \frac{1}{\omega_D} \left\{ \frac{2}{\sqrt{1-(\omega/\omega_D)^2}} + 2 \sum_{m=1}^{\infty} \Re\left(\gamma_m\, \exp(im\phi'_v)\right)\, F_m\left(\frac{\omega}{\omega_D}\right) \right\}, \tag{2.19}$$

where $\Re(\cdot)$ is the real part of the argument. Equation (2.19) clearly shows that the PSD is real-valued as expected.

2.2.3 Common Non-isotropic Scattering Distributions

A number of non-isotropic azimuthal power distributions have been proposed in the literature [15, 18, 53, 115] for modelling the non-isotropic scattering environments. Some commonly used non-isotropic scattering distributions include truncated-isotropic [53],

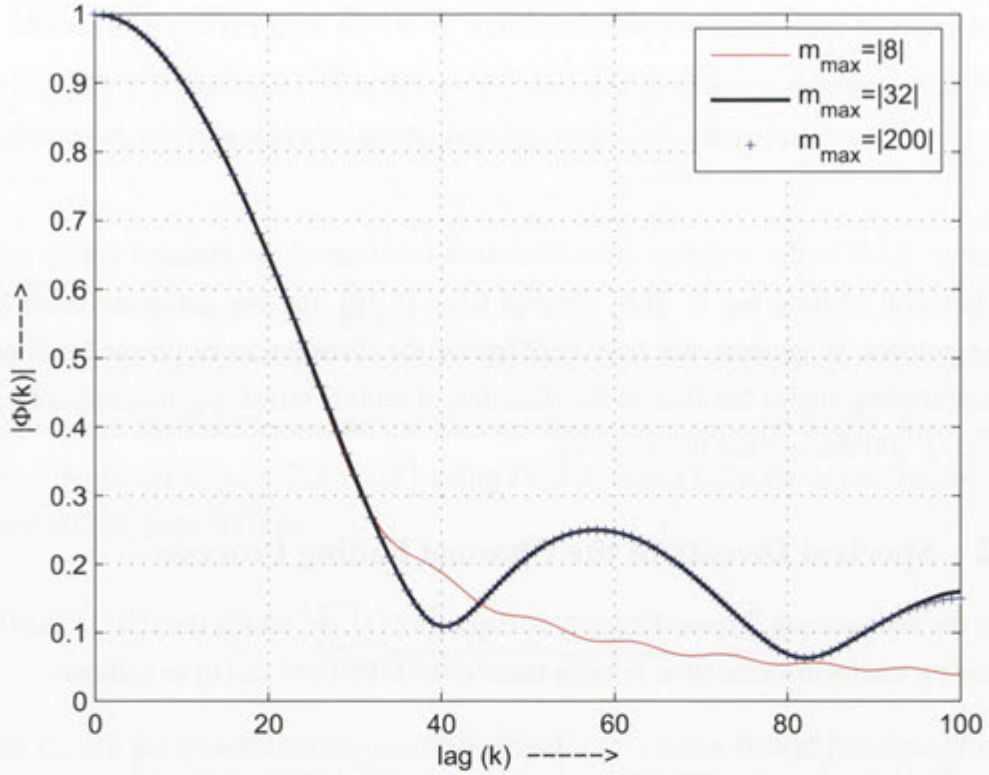

Figure 2.2: The truncation behavior of $\Phi(k)$: $\phi_v = 45$, $f_{\mathrm{D}} = 0.05$ and $\beta_0 = 90°$. The approximation based on the argument of the Bessel function proposed in [3] is quite good as the figure suggests only an insignificant increase in accuracy (at larger lags) as $|m_{max}|$ increases from 32 to 200.

truncated Gaussian [115], truncated Laplacian [18], cosine [53] and von-Mises [15,116]. These distributions were used to model the non-isotropic scattering environment surrounding either the receive or transmit antenna arrays. These distributions are characterized by the mean scattering angle β_0 and the angular spread Λ. Table-2.1 provides a summary of the distributions relevant for our work and gives the corresponding receiver scattering coefficients γ_m in closed-form.

2.2.4 Truncation of Series Expansions

Equations (2.16) and (2.19) involve summation over infinite number of terms. However, it is almost always possible in cases of practical interest to safely truncate the respective series up to a finite number of terms in the light of the following two facts:

i) For a fixed order m, $J_m(x)$ starts small and reaches its maximum at argument $x \approx O(m)$ before it starts decaying slowly. It was shown in [3] that $J_m(x) \approx 0$

PSD	Distribution Function $\Psi(\beta)$	$\gamma_m \times \exp(-im\beta_0)$
truncated-Uniform	$1/2\triangle_r$ $\beta \in (\beta_0 - \Delta_r, \beta_0 + \Delta_r)$	$\mathrm{sinc}(m\Delta_r)$
truncated-Gaussian	$K_G \exp\{-(\beta-\beta_0)^2/2\sigma_G^2\}$ $K_G = \frac{1}{\sqrt{2\pi}\sigma_G \mathrm{erf}(\pi/\sqrt{2}\sigma_G)}$ $\mathrm{erf}(x) = \frac{2}{\sqrt{\pi}}\int_0^x e^{-z^2}\mathrm{d}z$	$\exp(-im^2\sigma_G^2/2)$
truncated-cosine	$K_C \cos^2\left(\frac{\beta-\beta_0}{2}\right)$ $K_C = \frac{2^{2p_r-1}\Gamma^2(p_r+1)}{\pi\Gamma(2p_r+1)}$	$\frac{\Gamma^2(p_r+1)}{\Gamma(p_r-m+1)\Gamma(p_r+m+1)}$ $\Gamma(\cdot)$: Gamma function
von-Mises	$K_v e^{\kappa\cos(\beta-\beta_0)}$ $K_v = \frac{1}{2\pi I_0(\kappa)}$	$\frac{I_{-m}(\kappa_r)}{I_0(\kappa_r)}$ $I_m(\cdot)$: modified Bessel function
truncated-Laplacian	$K_L e^{-\sqrt{2}\lvert\beta-\beta_0\rvert/\sigma_L}$ $K_L = \frac{1}{\sqrt{2}\sigma_L(1-e^{-\sqrt{2}\pi/\sigma_L})}$	$\frac{(1-\xi(\sqrt{2}\cos m\pi - m\sigma_L \sin m\pi))}{\sqrt{2}(1-\xi)(1+m^2\sigma_L^2/2)}$ $\xi = \exp\left(\frac{-\sqrt{2}\pi}{\sigma_L}\right)$

Table 2.1: Scattering Coefficients γ_m for truncated-uniform, truncated-Gaussian, cosine, von-Mises and truncated-Laplacian power distributions. $|\beta - \beta_0| \leq \pi$ represents the support of AOA distribution for all scattering environments except the truncated-uniform environment.

for $|m| > 2\lceil x/2 \rceil + 1$ with $e = 2.7183\ldots$. Since the argument of $J_m(k\omega_\mathrm{D})$ depends on the lag variable k, the approximation would also depend on k for a fixed normalized fading rate.

ii) The Fourier coefficients γ_m must decay with m for Fourier series to be convergent (see, *e.g.*, [117]). The rate of decay depends on the smoothness of the function which is, in turn, related to the number of continuous derivatives of the function. In fact, the Fourier coefficients of an analytic (infinitely differentiable) function decay exponentially with m. Fourier coefficients of a Gaussian distribution, for example, decay exponentially with m, and decay polynomially for Laplace distribution [118]. The Fourier coefficients for a uniform distribution decay as $1/m$. In all these cases, the Fourier coefficients approach zero[6] with m. The faster the

[6]The Delta distribution is an exception to this behavior. The Fourier coefficients of a Delta distribution

decay of the Fourier series coefficients, the less the number of Fourier modes (γ_m) with significant contribution and vice versa.

For small k, the fact (i) above is useful in approximating (2.16) due to the presence of $J_m(k\omega_{\mathrm{D}})$. When $k = 0$, for example, $J_m(k\omega_{\mathrm{D}}) = 1$ for $m = 0$ and zero otherwise. In other words, none of the Fourier modes γ_m except $m = 0$ contribute to the autocorrelation of the channel process. For $k = 1$, $J_m(k\omega_{\mathrm{D}}) \approx 0$ after [7] $|m| > (2\lceil k\omega_{\mathrm{D}}/2 \rceil + 1)$. As k increases, the number of Fourier coefficients that are "allowed" to contribute also increases. In the limit $k \to \infty$, the number of Fourier modes that contribute to (2.16) also approaches infinity. This is where the fact (ii) comes into effect. Due to the decay (*e.g.*, exponential for a Gaussian distribution) of γ_m with m, the values of γ_m become increasingly small so that there must exist some finite m_0 such that $\gamma_m \approx 0$ for all $|m| > m_0$. We can , therefore, truncate the infinite summation in (2.16) to a summation over $|m| = m_0$ terms. The foregoing discussion implies that lesser Fourier modes are required in truncated-Gaussian, truncated-Laplacian and von-Mises distributions to achieve a particular accuracy as compared to truncated-uniform distribution. Fig.2.2 shows the impact of increasing number of modes in the summation in (2.16).

The approximation of the PSD of the fading process in (2.19) seems difficult due to the presence of the factor[8] $F_m(\omega/\omega_D)$ ((A.2) with $x = \omega/\omega_D$) which, for all m, sharply increases as ω approaches ω_D becoming infinite at ω_{D}. The approximation, therefore, would depend on the the decay of the Fourier coefficients of a particular scattering distribution. As long as the decay of γ_m is sufficiently fast, we can use the fact (ii) to approximate (2.19) to some finite $|m| = m_0'$ with the approximation error that approaches zero as m_0 approaches infinity. The accuracy of this approximation, however, depends on the angular spread of the scattering distribution and the mobile direction of travel. Again the faster decay of scattering coefficients of truncated-Gaussian, truncated-Laplacian and von Mises distributions as compared to the truncated-uniform distribution is due to their higher 'smoothness'. Fig. 2.3 shows PSD for different number of Fourier modes used in the summation in (2.19) for truncated-uniform distribution. The observed ringing effect is absent in other scattering distributions due to their 'smoothness'.

do not tend to zero at all, indicative of the fact that it is not an ordinary function and its Fourier series does not converge in the standard sense.

[7] For a normalized fading rate $f_{\mathrm{D}} = 0.05$ and a maximum time lag of $k = 10$ symbols, this approximation requires only $|m| = 3$ terms.

[8] Notice that the Fourier transformation of $J_m(k\omega_{\mathrm{D}})$ in (2.17), that gave rise to the factor $F_m(\omega/\omega_D)$, involves summation over $k = \pm\infty$ which implies that infinite number of modes are allowed to contribute to the PSD of the fading process.

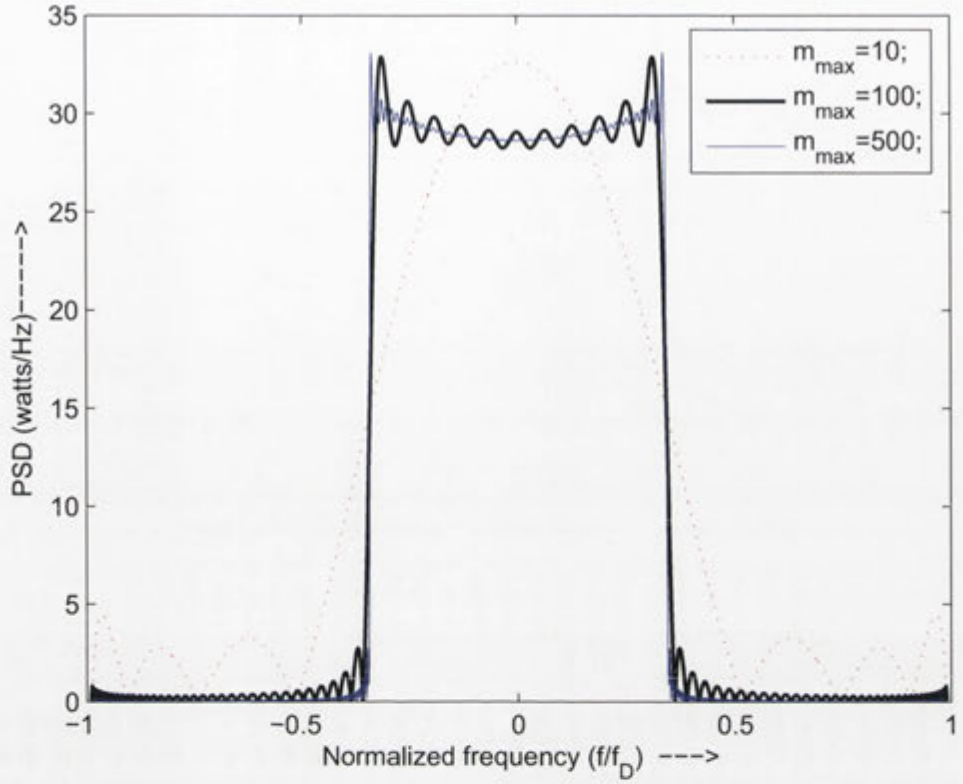

Figure 2.3: The truncation behavior of $\Phi(\omega)$: $\phi_v = 45$, $f_{\mathrm{D}} = 0.05$ and $\beta_0 = 90°$.

2.3 Effect of Non-Isotropicity and Mobile Velocity on Channel Statistics

Equations (2.16) and (2.19) describe the second order channel statistics, namely auto-correlation and power spectral density (PSD) for any 2D scattering environment around the receiver. For illustration purposes, throughout this section, we consider the so-called truncated uniform (uniform-limited [36]) scattering scenario, *i.e.*, scattered waves are arriving uniformly from an angular sector as shown in Fig. 2.4. For this case, we have

$$\Psi(\beta) = \begin{cases} 1/(2\triangle_r), & \text{if } |\beta - \beta_0| \leq \triangle_r \\ 0, & \text{otherwise} \end{cases} \tag{2.20}$$

where β_0 is the mean angle of arrival, β is any other angle of arrival, and $2\triangle_r$ is the angular spread of the truncated-uniform scattering arrival signals as illustrated in Fig. 2.4. The values of γ_m for some common scattering distributions were derived in closed form in [36] and are given in Table-2.1. The scattering coefficients for truncated-uniform

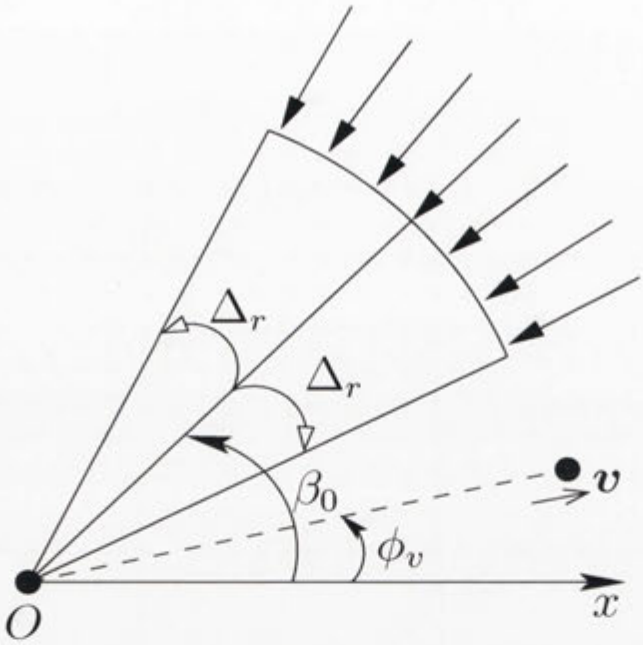

Figure 2.4: Illustration of an truncated-isotropic scattering scenario where the scattered power is uniformly distributed with magnitude $1/2\Delta_r$ over a part of the azimuth with a mean angle β_0 and a maximum deviation of Δ_r on each side of the mean. The direction of the mobile travel ϕ_v is also shown.

distribution are

$$\gamma_m = \exp(-im\beta_0)\,\mathrm{sinc}(m\Delta_r). \tag{2.21}$$

Degree of Non-isotropicity

We shall use the following definition throughout this thesis:

Definition 2.3.1 *If Λ denotes the angular spread, the degree of non-isotropicity, $\mathcal{D}$, is defined as*

$$\mathcal{D} = 1 - \frac{\Lambda}{103.9}, \tag{2.22}$$

where Λ is in degrees and 103.9° is the angular spread o the isotropic scattering environment [119]. Notice that $\mathcal{D}$ ranges from 1 (extremely non-isotropic) to 0 (isotropic) and is inversely related to angular spread.

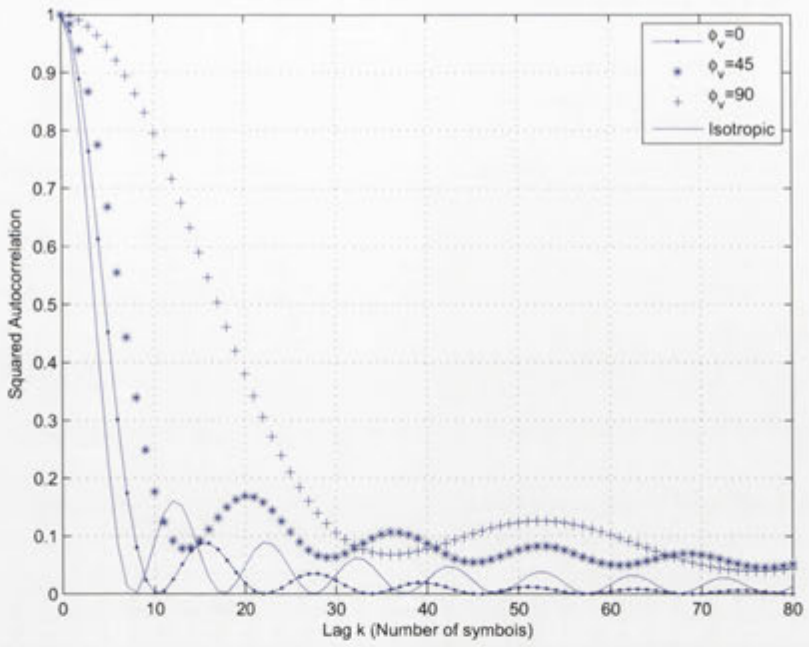

Figure 2.5: The plot of $|\Phi(k)|^2$ as a function of time lag k for different directions of mobile travel $\phi_v = 0°, 45°$, and $90°$, when $\beta_0 = 90°$, $\Delta_r = 60°$ and $f_{\mathrm{D}} = 0.05$. The autocorrelation for the isotropic case is also shown, which is independent of ϕ_v.

Autocorrelation and PSD in Truncated-Uniform Scattering

Using (2.21) in (2.16) and (2.18), we can write the autocorrelation and the PSD of the channel process respectively as follows

$$\Phi(k) = \sum_{m=-\infty}^{\infty} i^m \operatorname{sinc}(m\Delta_r)\, J_m(\omega_D k)\, \exp\left(-im\left(\beta_0 - \phi_v\right)\right), \tag{2.23a}$$

$$\Phi(\omega) = \frac{1}{\omega_D} \sum_{m=-\infty}^{\infty} \operatorname{sinc}(m\Delta_r)\, F_m\left(\frac{\omega}{\omega_D}\right) \exp\left(-im\left(\beta_0 - \phi_v'\right)\right). \tag{2.23b}$$

In the rest of this section we first show that the classical Clarke's model is a special case of the generalized Clarke's model introduced in this contribution. We then explore the effect of the degree of non-isotropicity and mobile velocity on channel autocorrelation and PSD.

2.3.1 Clarke's Model as a Special Case

When $\Delta_r = \pi$, *i.e.*, when the scattered power is uniformly distributed over the full azimuth plane around the mobile receiver, it can easily be verified that (2.23a) and (2.23b)

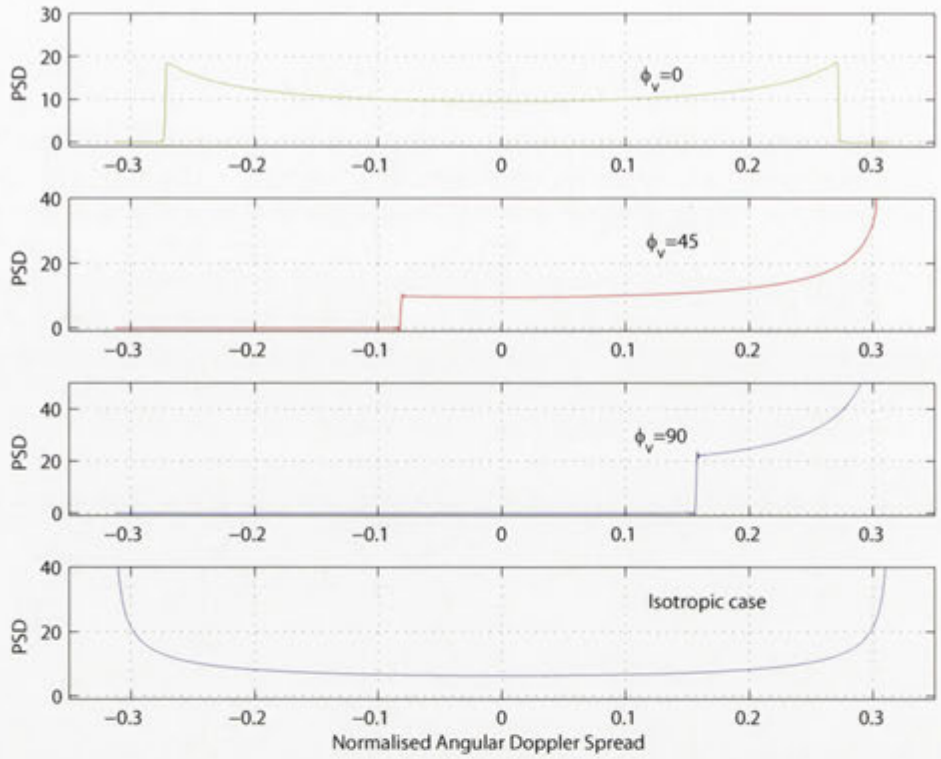

Figure 2.6: Effect of the mobile direction of travel $\phi_v = 0°, 45°$, and $90°$ on the Power Spectral Density (PSD) when $\beta_0 = 90°$, $\Delta_r = 60°$ and $f_D = 0.05$. The symmetric U-shaped PSD in case of isotropic scattering is also shown which is independent of the direction of travel.

collapse to the following equations for autocorrelation and PSD, respectively,

$$\Phi(k) = J_0(\omega_D k), \tag{2.24}$$

$$\Phi(\omega) = \frac{2}{\omega_D \sqrt{1 - (\omega/\omega_D)^2}}, \tag{2.25}$$

which is the well-known Clarke's description of channel statistics in 2D isotropic scattering around the receive antenna. Thus, Clarke's model is a special case of the generalized model developed in this contribution. Notice that, in general, the autocorrelation in (2.23a) is complex valued unlike that given in (2.24) for isotropic scattering environment which is strictly real valued.

2.3.2 Effect of Mobile Velocity

For a truncated-isotropic scattering scenario, the effect of changing the mobile direction of travel on the autocorrelation and PSD of the received signal has been shown in Figures

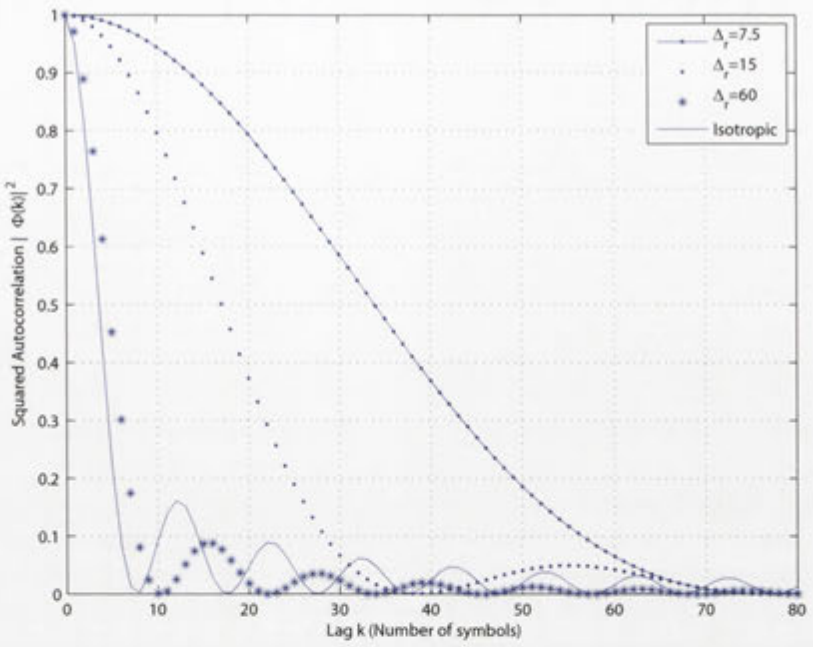

Figure 2.7: Effect of non-isotropicity on squared absolute autocorrelation as a function of time lag k when $\phi_v = 0°$, $\beta_0 = 90°$ and $f_{\mathrm{D}} = 0.05$. The autocorrelation for the isotropic case is also shown.

2.5 and 2.6 respectively. The autocorrelation and PSD for isotropic case have also been plotted for comparison. A marked deviation from the isotropic case can be observed. The skewness of the PSD is easily observed: If the mobile is moving into the non-isotropic scattering environment, the Doppler spectrum becomes (emphasized and) concentrated towards positive Doppler frequency axis. On the other hand, the Doppler spectrum is skewed towards negative Doppler frequency axis if the mobile moves away from the scatterers. The spectrum is symmetric about the mean only when the mobile moves at right angles to the mean scattering angle.

The above discussion of the autocorrelation and PSD *implicitly* assumes that the direction of mobile travel is perfectly known which is usually not the case in practice. It may be of some interest to find out the autocorrelation and PSD if the mobile direction of travel is unknown at the receiver. Suppose the mobile direction of travel is equiprobable in all directions, *i.e.*, $p\left(\phi_v\right) = 1/2\pi$, then, from (2.23a), the average autocorrelation, $\Phi_{\mathrm{avg}}(k)$ is given by

$$\Phi_{\mathrm{avg}}(k) = \sum_{m=-\infty}^{\infty} i^m \operatorname{sinc}(m\Delta_r)\, J_m(\omega_{\mathrm{D}} k) \exp\left(-im\beta_0\right) \int_0^{2\pi} \frac{\exp\left(im\phi_v\right)}{2\pi} \mathrm{d}\phi_v, \quad (2.26)$$

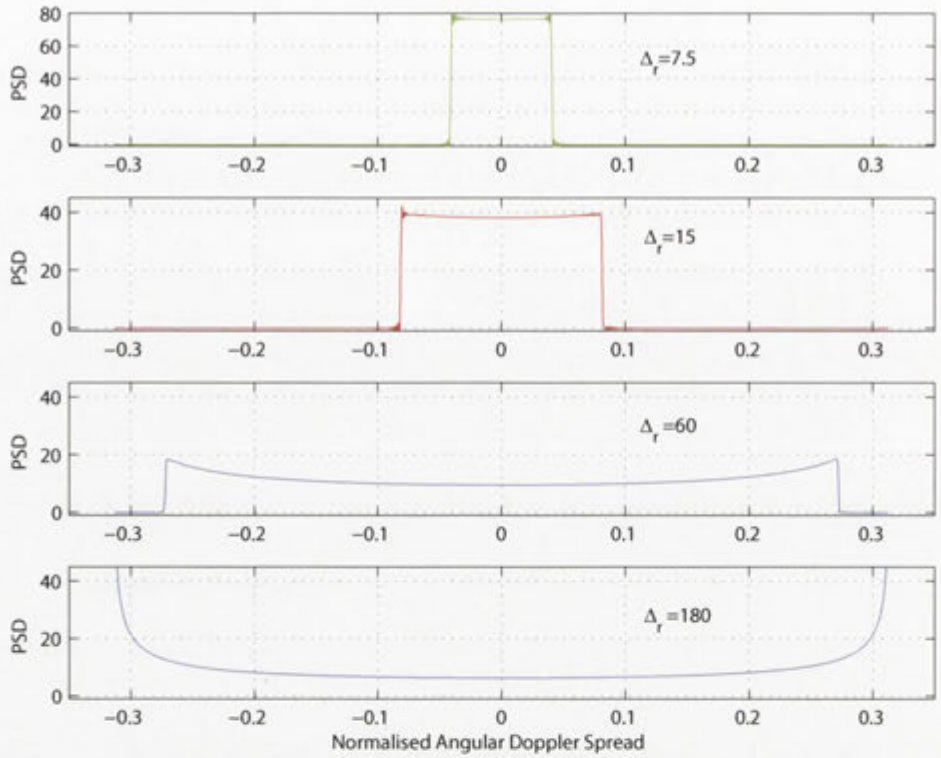

Figure 2.8: Effect of the degree of non-isotropicity on PSD when $\phi_v = 0°$, $\beta_0 = 90°$ and $f_D = 0.05$. The PSD for the isotropic case is also shown.

and using (2.23b), the average PSD, $\Phi_{\text{avg}}(\omega)$, is given by

$$\Phi_{\text{avg}}(\omega) = \frac{1}{\omega_D} \sum_{m=-\infty}^{\infty} \text{sinc}(m\Delta_r) F_m\left(\frac{\omega}{\omega_D}\right) \exp\left(-im\beta_0\right) \int_0^{2\pi} \frac{\exp\left(im\phi_v'\right)}{2\pi} \mathrm{d}\phi_v, \tag{2.27}$$

It is not hard to see that, irrespective of Δ_r and the β_0, the integrals in (2.26) and (2.27) are zero for all $m \neq 0$, and these two equations converge, respectively, to (2.24) and (2.25), *i.e.*, the Clarke's isotropic case. In other words, if the mobile direction of travel is equiprobable in all directions, a non-isotropic scattering environment on average is as good as an isotropic scattering environment.

2.3.3 Effect of Non-isotropicity

For a fixed direction of mobile travel, the effect of changing the degree of non-isotropicity on the autocorrelation and PSD of the fading process has been plotted in Figures 2.7 and 2.8 respectively. It can be seen from Fig. 2.7 that the channel fading process can have sig-

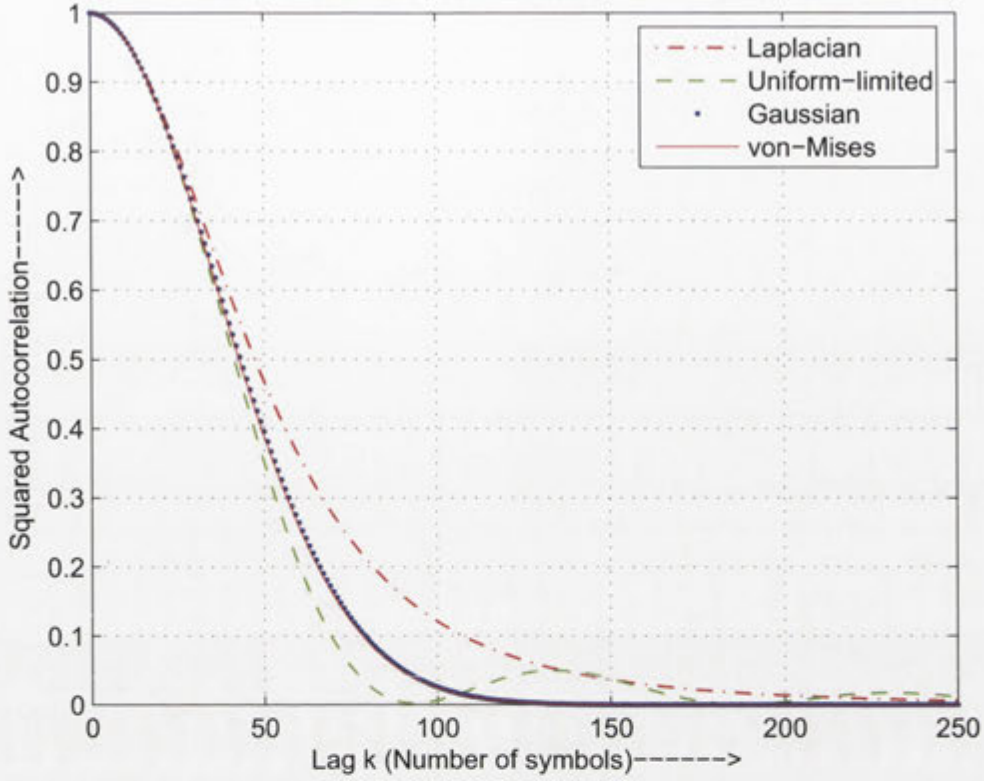

Figure 2.9: Autocorrelation of received signal envelope for different scattering environments when angular spread of the scattering is $5°$, $f_{\mathrm{D}} = 0.05$, $\phi_{\mathrm{v}} = 45°$ and $\beta_0 = 90°$.

nificantly higher correlation over time in non-isotropic scattering environments as compared to the isotropic scattering environment. With increasing Δ_r (or, in other words, decreasing the non-isotropicity) the correlation curves tend towards those of isotropic case.

Figure 2.8 shows the effect of changing the degree of non-isotropicity on the PSD of the channel process. The normalized Doppler spread seems to be directly proportional to Δ_r. For a fixed carrier frequency, f_{D} depends directly on the mobile speed. In our case none of the parameters, except the scattering environment (Δ_r), is being changed. It can, therefore, be concluded that changing the degree of non-isotropicity is actually equivalent to changing the normalized fading rate to some effective value, $f_{\mathrm{D}eff}$. In other words, the channel seems to have 'slowed down' as a result of non-isotropicity of the scattering environment. Similar 'slowing down[9]' of the channel is observed through beamforming, *i.e.*, using a non-isotropic antenna [120]. This 'slowing down' of channel rate of variation verifies the point of view of [63] that the assumption of isotropic

[9]This slowing down of the channel depends on the direction o mobile travel relative to the mean scattering angle an the degree of non-isotropicity as observed earlier in this chapter.

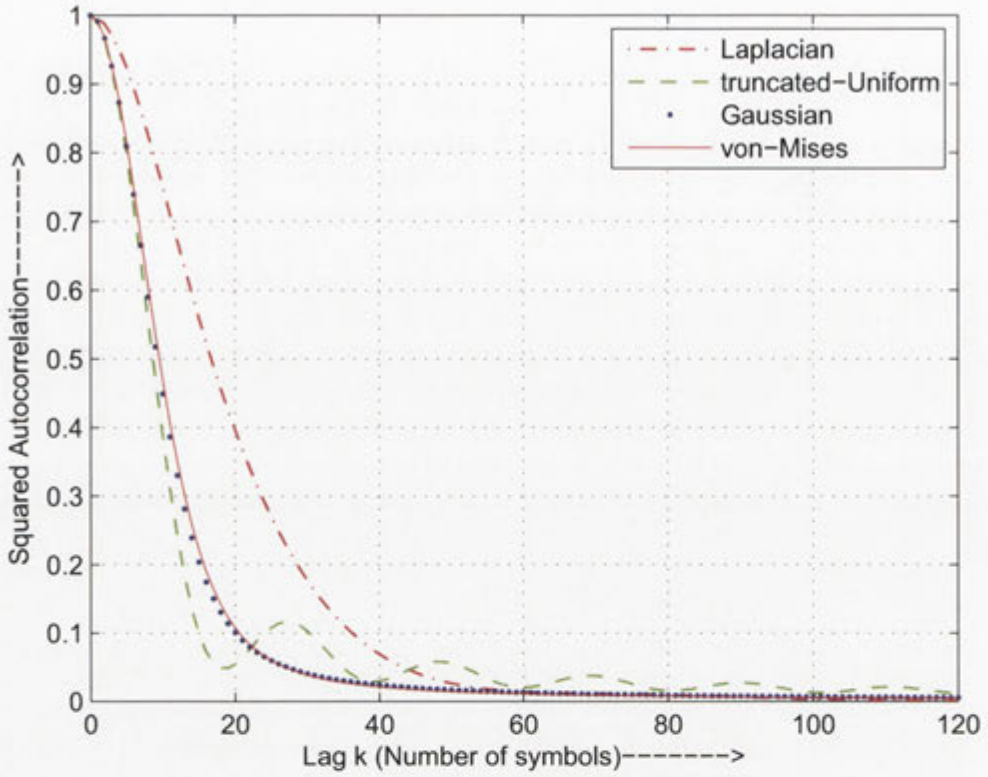

Figure 2.10: Autocorrelation of received signal envelope for different scattering environments when angular spread of the scattering is 25°.

distribution of scattered power when the power is actually non-isotropically distributed introduces significant errors in the second order statistics.

2.4 A Comparative Study of Non-isotropic Scattering Environments

It may be of some interest to investigate the impact on channel statistics of having different scattering distributions. In order to compare different scattering environments on a common basis, we have to fix all parameters and use the same angular spread for all scattering distributions. For that purpose, let us denote the angular spread of truncated-isotropic, truncated Laplacian, truncated Gaussian and von-Mises[10] distributions by $\sigma_{TU}, \sigma_L, \sigma_G$ and σ_V, respectively. The angular spread for truncated-isotropic

[10]The circular variance V_0 of the von-Mises distribution is defined as $V_0 = 2(1 - I_1(\kappa)/I_0(\kappa))$ [121]. The circular variance can be transformed to the standard deviation σ_V (or, equivalently, the angular spread) in the linear data sense using the transformation [122], $\sigma_V = (-2\log(1 - V_0))^{1/2}$.

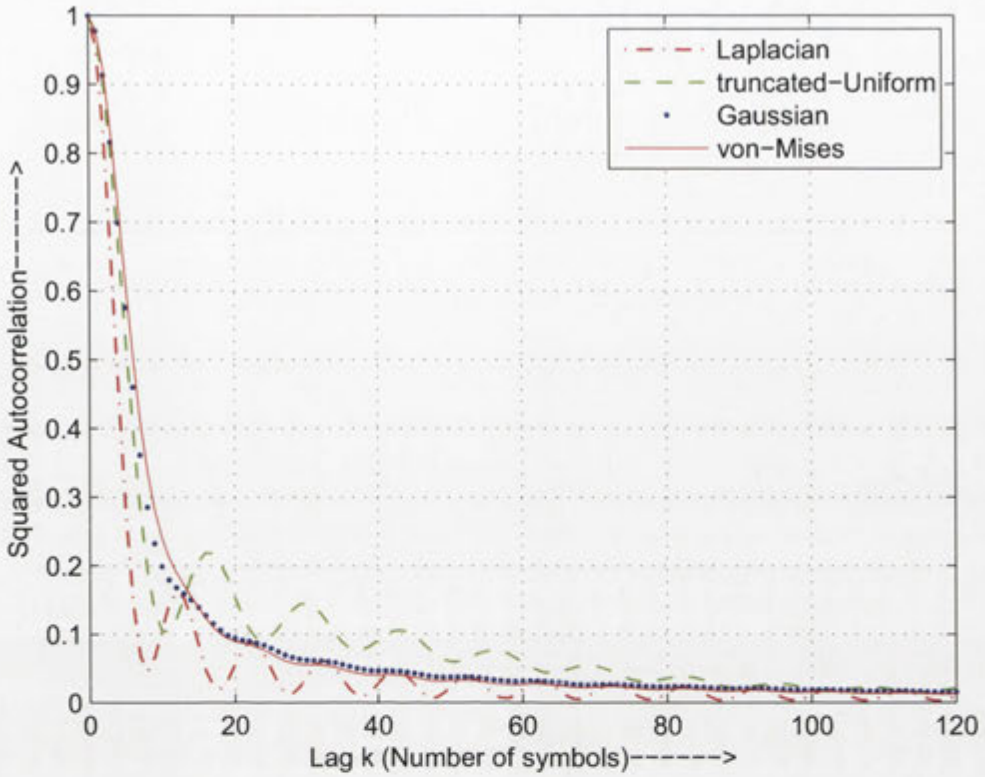

Figure 2.11: Autocorrelation of received signal envelope for different scattering environments when angular spread of the scattering is $45°$.

distribution is given by

$$\Lambda_{TU} = \Delta_r/\sqrt{3}. \tag{2.28}$$

For the truncated Laplacian distribution, the angular spread Λ_L is related to standard deviation σ_L of untruncated distribution as follows [20]

$$\Lambda_L = \sigma_L \sqrt{1 - \frac{e^{-\xi_l}}{1 - e^{-\xi_l}} \left[\frac{\xi_l^2}{2} + \xi_l\right]}, \tag{2.29}$$

where $\xi_l = \sqrt{2}\pi/\sigma_L$. For small angular spreads, $\Lambda_L \approx \sigma_L$ which is indicative of the fact that truncating the distributions' tails to $[-\pi, \pi]$ has negligible effect. The angular spread for the truncated Gaussian distribution Λ_G is related to σ_G as

$$\Lambda_G = \sigma_G \sqrt{1 - [2\xi_G \operatorname{erf}(\xi_G) \exp(\xi_G^2))]^{-1}}, \tag{2.30}$$

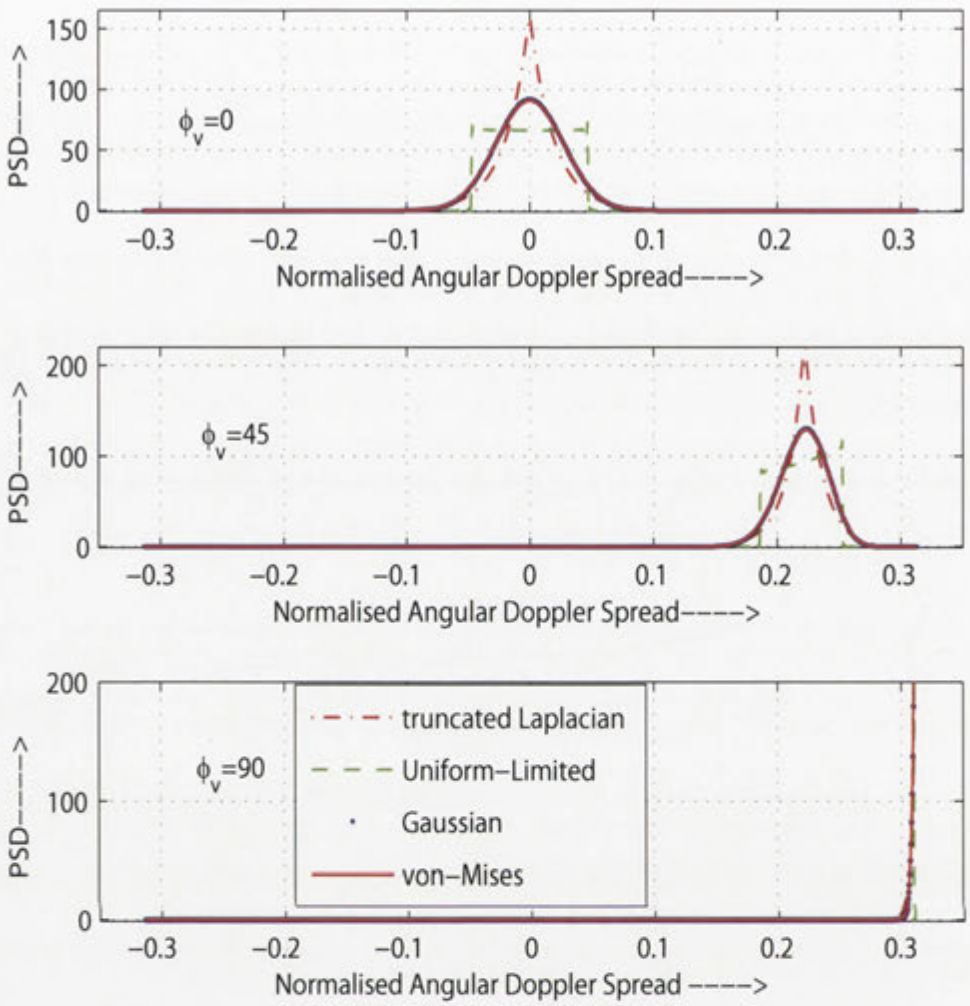

Figure 2.12: PSD of the received signal envelope for different scattering environments for different mobile directions of travel. The angular spread is 5°, $f_\mathrm{D} = 0.05$ and $\beta_0 = 90^\circ$.

where $\xi_G = \pi/(\sqrt{2}\sigma_G)$. For small angular spreads, $\Lambda_G \approx \sigma_G$.

2.4.1 Numerical Results and Discussion

In the light of foregoing discussion, we consider truncated-isotropic, truncated Gaussian, truncated Laplacian and von-Mises scattering distributions and explore their impact on channel statistics. An important assumption made throughout this chapter is that the received signal envelope follows Rayleigh statistics for all scattering environments. Figures 2.9–2.14 give simulation results.

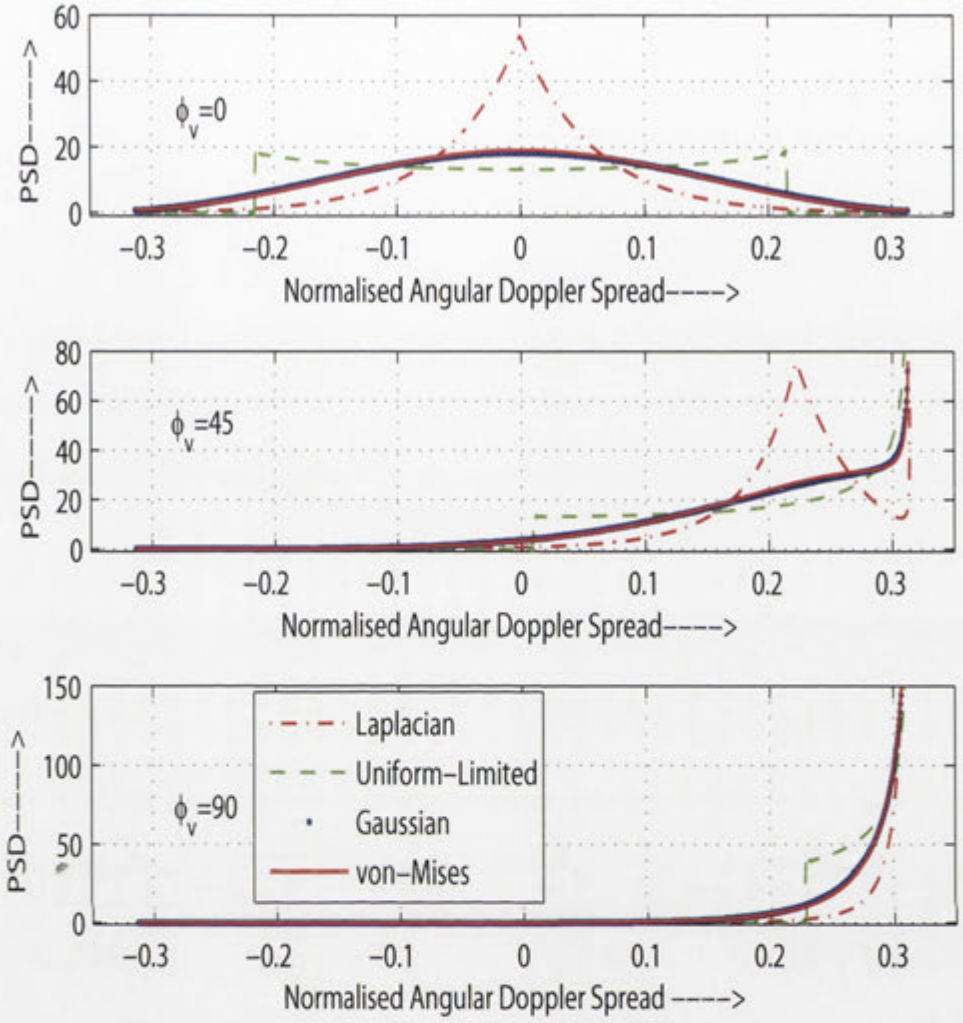

Figure 2.13: PSD of the received signal envelope for different scattering environments when angular spread is 25°.

Autocorrelation of received signal envelope has been plotted in Figures 2.9–2.11 for all four scattering distributions for different values of angular spread. The mobile direction of travel ϕ_v is fixed at 45°, mean scattering angle β_0 is taken as 90°. Normalized fading rate f_D chosen for simulations is 0.05. It can be observed from these figures that, firstly, truncated Gaussian and von-Mises distributions are identical for small angular spread (*e.g.*, 5° or less) and almost identical for moderate angular spread of 25°. The difference between the two distributions, though slight, appears when angular spread is 45°. Von-Mises and Gaussian distributions are usually considered equivalent for small angular spreads [123, 124]. The simulation results however confirm that this assumption remains true for moderate angular spreads. Secondly, no universal conclusion can be

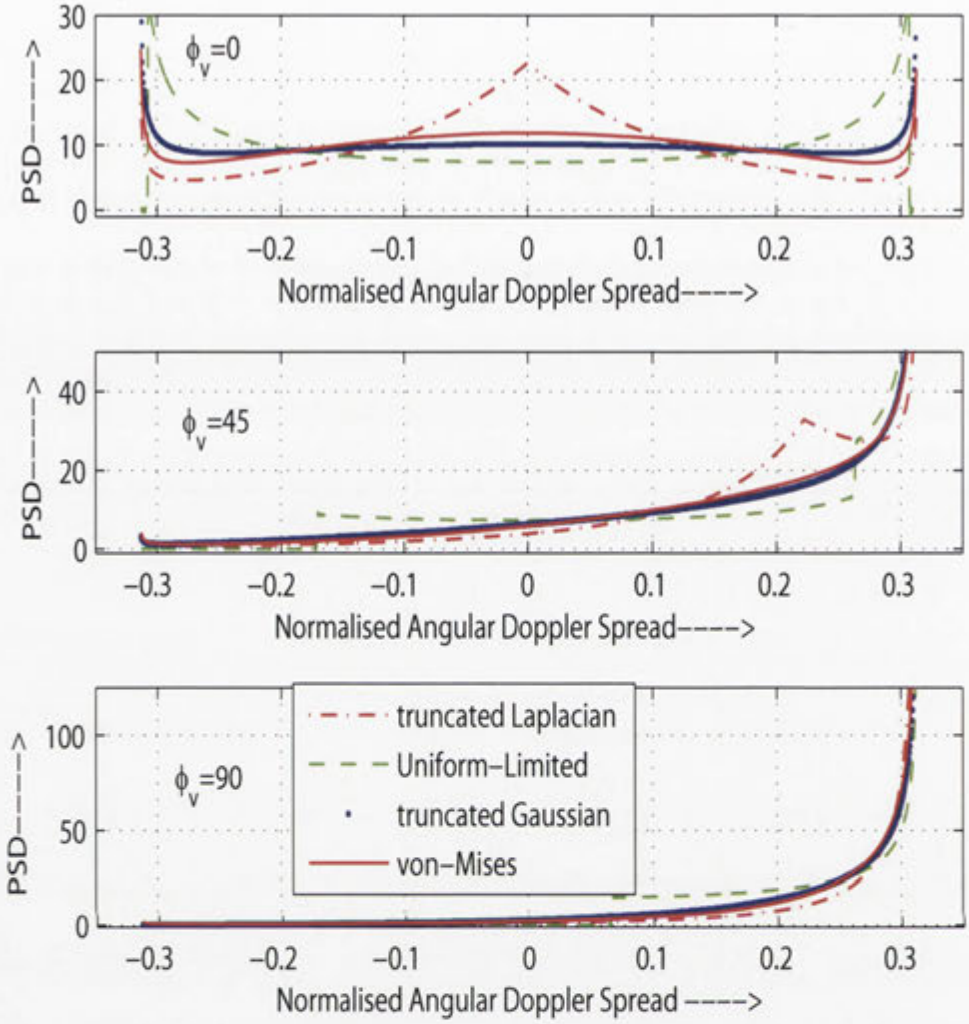

Figure 2.14: PSD of the received signal envelope for different scattering environments when angular spread is 45°.

drawn as to which scattering model has more favorable statistics (*i.e.*, higher correlation) than others. Any such conclusion would depend on observation length. The Laplacian model, for example, is "optimistic" (*i.e.*, has higher correlation) than others for angular spreads between 5° and 25° whereas it is "pessimistic" (*i.e.*, has lower correlation) than others when the angular spread is 45°. In the next chapter, we shall compare different scattering environments on the basis of a no-CSI cost function which depends on the channel statistics and translates differences in statistics into *bits* of information [125] thus giving a physical meaning to differences in scattering environments.

The comparison of PSD of received signal envelope is given in Figures 2.12−2.14. Normalized fading rate and mean scattering angle are the same as before. For each value

of angular spread, we give results for three different directions of mobile travel. We can observe from these figures that direction of mobile travel has significant impact on PSD (and, hence, autocorrelation) irrespective of the type of non-isotropic scattering environment. For $\phi_v > 0$, PSD for all scattering distributions is skewed unlike Clarke's [2]. PSD plots also confirm the observation that truncated Gaussian and von-Mises distribution are almost identical even for moderate angular spreads (*e.g.*, as large as $25°$).

From PSD plots (especially when $\phi_v = 0°$) we can see that the Doppler spread is directly proportional to the angular spread irrespective of the scattering model. As angular spread approaches 0, the Doppler spread would approach a single Doppler frequency for all scattering distributions which suggests that all scattering models are almost equivalent for very small angular spread. Similarly, as angular spread approaches $104°$ (maximum angular spread), all scattering models become equivalent.

2.5 Applications of the Generalized Clarke model

The generalized Clarke model presented in this contribution can be used for accurate performance evaluation and prediction of a communication system in Rayleigh fading under any scattering environment. Among many possible applications, following are some important applications of the generalized model:

- The modeling approach adopted herein to arrive at the generalized model lends itself easily to be extended to a generalized 3D Rayleigh fading environment.
- Most velocity and Doppler estimators are based on second order channel statistics. The performance of different velocity estimators in a non-isotropic Rician fading environment where the AOA distribution is modelled by Von-Mises distribution has been evaluated in [31]. The generalized Rayleigh fading model developed herein can be extended to include the Rician component and, then, it can be used to quantify the difference in performance of various velocity estimators (designed to operate in a particular environment) in general scattering environments.
- Blind and semi-blind channel estimation and equalization techniques based on second order channel statistics have been proposed in the literature [126]. The performance of these estimators and equalizers can be predicted accurately in Rayleigh fading in any scattering environment with the help of the proposed model.
- Second order statistics based blind and semi-blind channel identification techniques have been proposed in the literature [127]. The effect of having a different scattering environment on the performance of these identification techniques can be analyzed using the generalized model.

- The work of [37] on noncoherent communication over Rayleigh fading channel assumes isotropic scattering environment. Using the generalized model, we can extend this work to generalized Rayleigh fading with the results of [37] as a special case.

- Simulation model based on [2] was proposed in [39]. The generalized model presented here includes Clarke's model (and, hence, Jakes') as a special case which makes it possible to simulate Jakes' and non-Jakes' Doppler spectrum in a unified frame.

2.6 Summary and Contributions

A time-selective generalized Rayleigh fading model has been presented in this chapter that extends the Clarke's classical isotropic scattering model of mobile radio reception to general scattering environments. This model can be used to simulate non-Jakes' Doppler spectrum. It turned out that the statistics of a generalized Rayleigh fading channel depend on the direction of mobile travel and the mean angle of arrival, and can be significantly different from those in an isotropic environment. In general, the autocorrelation is complex-valued and the power spectral density is asymmetric. Moreover, if the mobile direction of travel is equiprobable in all directions and the mean angle of arrival is fixed, then a non-isotropic scattering environment, on the average, is identical to the isotropic scattering environment. The numerical results for truncated isotropic scattering environment verified that the assumption of isotropic scattering in a non-isotropic environment can introduce significant errors in the estimation of second order statistics. We also compared commonly used non-isotropic scattering distributions such as truncated-isotropic, truncated Gaussian, truncated Laplacian and von-Mises, on the basis of their Autocorrelation and PSD. Simulation results showed that truncated Gaussian and von-Mises distributions have almost identical second order statistics even for moderate angular spreads. Results for autocorrelation and PSD showed that the mobile direction of travel significantly affects second order channel statistics in a non-isotropic scattering environment irrespective of the type of scattering model. For small and large angular spreads, different scattering models have almost identical statistics. For moderate angular spreads, different scattering models can have different statistics and replacement of one scattering model by others will introduce errors in estimation of channel statistics.

Chapter 3

Achievable Information Rates Over Generalized Rayleigh Fading Channels

3.1 Background

In the previous chapter, we developed a generalized Clarke model to describe the Rayleigh fading statistics in general scattering conditions. We used generalized model to explore the impact of the extent of non-isotropicity and the mobile direction of travel on the channel statistics in different scattering environments. The comparative study of different scattering scenarios was done qualitatively using the terms like 'higher' and 'lower' correlation which may not be very useful from the point of view of system design. We, in this chapter, seek to quantify the impact of the degree of non-isotropicity and the mobile direction of travel with the help of some more meaningful measure. The difference between scattering conditions is reflected in different channel statistics which, in turn, implies a different channel quality. In this respect, the information theoretic measure of channel quality known as capacity [128] (the ultimate limit of achievable rates on a particular channel) seems to be the most suitable candidate which effectively translates differences in channel statistics into bits/sec — a useful term from the point of view of system design.

The capacity of wireless communication over fading channels have been explored in literature [129] for a variety of cases depending on channel models and availability of CSI at the transmitter and the receiver. It is well known that when CSI is perfectly known to the receiver, the channel capacity is achieved by i.i.d. Gaussian inputs [128]. If, in addition, CSI is available to the transmitter, Gaussian inputs are still optimal and the capacity is achieved by waterfilling the transmit power. However, the perfect CSI is not often available, for instance, due to the time variation of the channel as a result of the mobility of the sender or the receiver or both. Therefore, achieving reliable communication over

fading channels where CSI is not available at the transmitter and the receiver (but only channel statistics are known), is of particular interest. In such communications scenarios, the channel capacity problem has been studied for some simplified models, *e.g.*, a memoryless[1] Rayleigh fading channel [72,73], block-fading Rayleigh fading channel [74,75], block MPSK channels [76] and finite-state Markov channels [77]. The capacity achieving distribution in noncoherent scenario has been shown to be discrete [72–74] which is in contrast to the perfect CSI scenario where continuous Gaussian inputs are optimal. In non-coherent communications systems, the receiver has to form the estimate of CSI before demodulation of the data.

The CSI estimation techniques, in general, can be categorized into data-aided (pilot-assisted) and non-data-aided (blind). In data-aided channel estimation, known symbols are multiplexed into data stream. The receiver uses these known symbols to estimate the channel at pilot locations and then uses those estimates to form estimates of the channel at data symbol locations [130–132]. In non-data-aided channel estimation, no separate known symbols are transmitted along with data. Instead, channel statistics are used to estimate the channel (see for example [133] and references therein). In applications where mobility is moderate, data-aided channel estimation is employed due to its simplicity and superior performance. In the presence of additive noise, the estimates formed by receiver on the basis of noisy pilot symbols are imperfect. The performance of the receiver, therefore, depends on how good the channel estimate is [134, 135]. Capacities of systems with imperfect channel estimation have been studied in [88, 136–145].

Achievable rates over time-selective Rayleigh fading channel have been studied in [37, 79] assuming isotropic scattering environment. No specific signaling schemes and the type of scattering environment were considered in [79] and some general bounds on achievable rates were derived for block-fading model (where channel changes correlatively across each block of length T' symbols, and independently across blocks) and subblock-fading model[2] (where channel remains constant over a subblock and changes correlatively across subblocks). It was shown that when SNR is very large, the channel capacity grows logarithmically with SNR and this logarithmic growth is same for block-fading and subblock-fading channel models.

The work in this chapter is based[3] on [37] where achievable rates over continuously fading noncoherent Rayleigh fading channels were studied for Gaussian and constant

[1] A channel is memoryless if a symbol does not contain any information about any other symbol. More precisely, the channel is memoryless if its realizations are i.i.d..

[2] In subblock fading model, a block of length T' is subdivided into Q subblocks of length L' where Q is the rank of correlation matrix.

[3] The work presented in [37] is, in fact, a special case of [79]. While no particular scattering environment is assumed in [79], the results in [37] assume that the mobile receiver is surrounded by isotropically random scattering.

power (or MPSK) signaling schemes with scattering around the mobile receiver assumed to be isotropic. The assumption of isotropic scattering implies real valued correlation for the channel process and symmetric U-shaped Doppler spectrum [2]. Also channel statistics are independent of mobile direction of travel. We have observed in Chapter 2, Section 2.2 that, in general, autocorrelation of the channel fading process is complex valued and the Doppler spectrum is not symmetric. Moreover, channel statistics depend on the direction of mobile travel with respect to mean scattering angle. In this chapter we use the generalized mobile Rayleigh fading model and follow the approach of [37] to extend the available results to include non-isotropic communication scenarios. The numerical results suggest that the achievable rates depend on the angular spread, mobile direction of travel, normalized fading rate and the transmission block length. We also present comparative study for commonly employed non-isotropic scattering models from communication theoretical point of view with common assumptions and geometric references which gives new insights, which were not available before.

This chapter is organized as follows. The Section 3.2 describes the channel model. In Sections 3.3-3.5 we generalize the results of [37] by extending no-CSI cost function and information rates achievable in isotropic scattering environment to general scattering scenarios with uniform AOA distribution. We, in Section 3.6, discuss two specific non-isotropic communications scenario where either the antenna or the scattering environment is non-isotropic.In Section 3.7, we utilize the information rate *cost function* for unknown CSI introduced in Section 3.3 to compare and quantify the effect on no-CSI cost of having different non-isotropic scattering environments. These common non-isotropic scattering distributions are also compared with the isotropic environment. A practical example and implications of the fact that marginal Gaussianity does not imply joint Gaussianity is presented in 3.8. Finally, we summarize the chapter and emphasize specific contributions in 3.9.

3.2 Channel Model

We consider a downlink SISO transmission system where the transmitter is stationary while the receiver is moving with some velocity v (Fig. 2.4). A sequence of N symbols, $\mathbf{s} = [s_1, s_2, \cdots, s_N]^T$ is transmitted and the received $N \times 1$ vector $\mathbf{r}$ obtained by sampling the output of the matched-filter is given in complex baseband form as (Eq. (2.3))

$$\mathbf{r} = \sqrt{\rho}\,\mathbf{S}\mathbf{h} + \mathbf{z}, \tag{3.1}$$

where $\mathbf{S} = \text{diag}(s_1, s_2, \cdots, s_N)$ is the diagonal matrix of average power constrained ($\mathbb{E}\{|s_j|^2\} = 1$ for $j = 1, 2, \cdots, N$) transmitted symbols, $\mathbf{z} = [z_1, z_2, \cdots, z_N]^T$ is N-dimensional noise vector with zero mean vector and covariance matrix $\mathbf{I}$ and $\mathbf{h} = [h_1, h_2, \cdots, h_N]^T$ represents the samples of a band-limited, flat-fading (frequency non-selective) wide-sense stationary, zero-mean complex Gaussian process with Toeplitz positive semidefinite covariance matrix $\mathbf{C}_\text{h} \triangleq \mathbb{E}\{\mathbf{h}\mathbf{h}^*\}$.

Let $(j+k, j)$ entry of the channel covariance matrix be expressed as

$$[\mathbf{C}_\text{h}]_{j+k,j} = \mathbb{E}\left\{h_{j+k} h_j^*\right\} = \Phi(k), \tag{3.2}$$

where $\Phi(k)$ is the autocorrelation function of channel fading process. For an isotropic environment [37],

$$[\mathbf{C}_\text{h}]_{j+k,j} = J_0(2\pi f_\text{D} k), \tag{3.3}$$

where J_0 is the Bessel function of the first kind of order 0 and f_D is normalized fading rate. For a generalized Rayleigh fading environment with truncated-uniform APD, we have from (2.16), after some manipulation,

$$[\mathbf{C}_\text{h}]_{j+k,j} = \sum_{m=-\infty}^{\infty} i^m \, \gamma_m \, J_m(2\pi f_\text{D} k) \, \exp\left(im\phi_v\right), \tag{3.4}$$

where γ_m are the scattering coefficients, f_D is the normalized fading rate and ϕ_v is the mobile direction of travel with respect to the x-axis.

3.3 No-CSI Cost in Truncated-Uniform Scattering

In this section, we seek to generalize the results derived in [37] regarding achievable rates for Gaussian and MPSK signaling in isotropic scattering environment. We, therefore, consider a truncated-isotropic scattering model described in Section 2.3 and obtain the achievable rates in isotropic scattering scenario as a special case.

For length N sequence of input symbols, $\mathbf{s} = [s_1, s_2, \cdots, s_N]^T$, the (unnormalized) mutual information, $I(\mathbf{r}; \mathbf{s})$, between the output vector $\mathbf{r}$ received by the mobile receiver and the input vector $\mathbf{s}$ can be expressed using the chain rule as follows

$$I(\mathbf{r}; \mathbf{s}) = I(\mathbf{r}; \mathbf{s}, \mathbf{h}) - I(\mathbf{r}; \mathbf{h}|\mathbf{s}), \tag{3.5a}$$

$$= I(\mathbf{r}; \mathbf{s}|\mathbf{h}) - \{I(\mathbf{r}; \mathbf{h}|\mathbf{s}) - I(\mathbf{r}; \mathbf{h})\}, \tag{3.5b}$$

where the first term in (3.5b) is the mutual information with perfect CSI and, therefore,

$$P_\delta \triangleq I(\mathbf{r};\mathbf{h}|\mathbf{s}) - I(\mathbf{r};\mathbf{h}), \tag{3.6}$$

is the loss of information rate due to channel unpredictability when CSI is unknown. Since $I(\mathbf{r};\mathbf{h})$ is non-negative,

$$P_\delta \leq I(\mathbf{r};\mathbf{h}|\mathbf{s}). \tag{3.7}$$

Thus $I(\mathbf{r};\mathbf{h}|\mathbf{s})$ is the upper bound on the no-CSI cost. Making use of the Jensen's inequality and the determinant identity, $\det(\mathbf{I}+\mathbf{AB}) = \det(\mathbf{I}+\mathbf{BA})$, it can be shown that P_δ normalized by the sequence length denoted by P_δ^{norm} is given as

$$P_\delta^{norm} \leq \frac{1}{N}\text{logdet}(\mathbf{I}+\rho\mathbf{C}_\text{h}), \tag{3.8a}$$

$$= \frac{1}{N}\sum_{i=1}^{N}\log\left(1+\rho\lambda_i\right), \tag{3.8b}$$

where $\lambda_i, i = 1, 2, \cdots, N$, are the eigenvalues of the covariance matrix $\mathbf{C}$. In Appendix B.1 we show that P_δ^{norm} is maximum when channel fading process is uncorrelated, *i.e.*, $\lambda_1 = \lambda_2 = \cdots = \lambda_N$ and is minimum when all eigenvalues are equal to zero except one which is equal to N. This scenario corresponds to a perfectly correlated channel process. We have the following comments:

- The difference between non-isotropic and isotropic scattering models is reflected in eigenvalues of the correlation matrices. The different correlation matrices for non-isotropic and isotropic environment (Eqs. (3.4) and (3.3) respectively) imply different set of $\{\lambda_i\}$ which implies different information rate cost for unknown CSI (Eq. (3.8b)) and, hence, different achievable rates.

- The dependence of penalty (and, hence, achievable information rates) on eigenvalues $\{\lambda_i\}$ implies the dependence on the degree of non-isotropicity, normalized fading rate, mobile direction of travel and mean scattering angle.

- The equality holds in (3.8b) for MPSK signaling.

- Equation (2.23a) together with (3.8b) gives information rate loss due to unknown CSI in a truncated-isotropic scattering (with isotropic environment as a special case) for any block length N.

3.4 Achievable Information Rates: Gaussian and Constant Power Signaling

Let $I_C(\mathbf{r};\mathbf{s})$ and $I_G(\mathbf{r};\mathbf{s})$ denote the mutual information without CSI for constant power and Gaussian signaling, respectively. The following upper bound on the mutual information has been derived in [37] for MPSK (Eq. (1.20))

$$I_C(\mathbf{r};\mathbf{s}) \leq C_{\text{AWGN}}(\rho) - P_\delta^{norm},$$

At this point, it is important to refer to a recent work related to OFDM system capacity [90,91] where the authors have followed the approach of [37] to derive the achievable rates for an OFDM system. On the basis of incorrect arguments involving the concept of the Gaussianity of the channel output vector, they ended up with an exact information capacity expression. Since the information capacity of a system is an important benchmark that guides the coding community to devise codes that approach channel capacity, an erroneous capacity expression could lead to confusion about the performance of the codes. A code, for example, that may have performance close to the 'true' capacity might still be far behind the erroneous capacity which could lead the coding community into useless research efforts. Moreover, the constant power signaling [146] is one of the most widely-used signaling schemes among modern (state-of-the-art and future) digital modulation techniques mainly due to its relative robustness to noise and ease of implementation with inexpensive non-linear power amplifiers [147]. It is therefore of information-theoretic interest to have correct benchmarks for the performance of constant power signaling. We, in Section 3.8, therefore analyze the arguments that formed the basis of the inaccurate conclusion about constant power signaling capacity for OFDM based system in [90, 91] and numerically show that these achievable rates claimed to be exact capacity are, in fact, an upper bound to the capacity of OFDM system.

The Gaussian signaling lower bound in isotropic scattering environment as derived in [37] is given as (Eq. (1.17))

$$I_G(\mathbf{r},\mathbf{s}) \geq C_{\text{Rayleigh}}(\rho) - P_\delta^{norm},$$

where $C_{\text{Rayleigh}}(x)$ is the ergodic Rayleigh capacity per symbol [80] with perfect CSI defined in (1.18).

Equations (1.20) and (1.17) implicitly specify a trade-off between the degree of non-isotropicity (or, equivalently, eigenvalues) and SNR as we would discuss in Section 3.6.2.

3.5 Analysis of No-CSI Cost Function

We have observed from (3.8b) that information rate cost function, P_{δ}^{norm}, is a function of the block length, N, SNR and the spectrum of the channel fading process through eigenvalues, $\{\lambda_i\}$. It is of some interest to analyze the behavior of no-CSI cost function as a function of the degree of non-isotropicity, N and SNR which is the subject of this section[4]. In particular it is of interest from information theoretic perspective to analyze cost asymptotics for large (possibly infinite) block lengths and high (possibly infinite) SNR. For clarity of presentation, we in this section shall restrict ourselves to truncated-uniform scattering scenario.

3.5.1 No-CSI Cost for Infinite Block Length

Since the information rate loss, P_{δ} in (3.8b) is a non-increasing sequence of N (the block length), it has a limit as $N \to \infty$. The application of Szegö's limit theorem [148] to (3.8b) gives

$$\lim_{N\to\infty} P_{\delta}^{\mathrm{n}} = \frac{1}{2\pi} \int_{-\pi}^{\pi} \log\left(1 + \mathcal{E}_s\, \Phi(\omega)\right) d\omega. \tag{3.9}$$

Since $\Phi(\omega)$ (Eq. (2.23b)) involves summation, it is not possible to find a closed form solution for $\lim_{N\to\infty} P_{\delta}^{\mathrm{n}}$ due to that summation appearing within log in (3.9).

When $\Lambda \to 103.9^{\circ}$ (angular spread of an isotropic environment), we have [37]

$$\lim_{N\to\infty} P_{\delta\mathrm{Iso}}^{\mathrm{n}} = 2 f_{\mathrm{D}} \Theta\left(\frac{\mathcal{E}_s}{\pi f_{\mathrm{D}}}\right), \tag{3.10}$$

where

$$\Theta(g) = \begin{cases} 0, & \text{if } g = 0 \\ \frac{\pi}{2} g + \log\frac{g}{2} + \sqrt{1-g^2} + \log\left(\frac{1+\sqrt{1-g^2}}{g}\right), & \text{if } 0 < g \leq 1 \\ \frac{\pi}{2} g + \log\frac{g}{2} - 2\sqrt{g^2-1} + \tan^{-1}\left(\sqrt{\frac{g-1}{g+1}}\right), & \text{if } g > 1. \end{cases} \tag{3.11}$$

When $\Lambda \to 0^{\circ}$ (corresponding to a single point scatterer), it is shown in Appendix B.2 that for a given SNR

$$\lim_{N\to\infty} P_{\delta,0^{\circ}}^{norm} = 0, \tag{3.12}$$

[4] In this section, an important assumption is that SNR in truncated-uniform environment is the same as would be in isotropic environment.

which is independent of SNR. A natural question to ask here is: Even though the channel is perfectly correlated, why the penalty due to unknown CSI is non-zero for finite block lengths and is zero only when block length is infinite? An intuitive answer is that AWGN noise enters into the penalty expression through SNR (Eq. (3.8b)) and channel estimation on the basis of a finite observation length in the presence of noise can not be perfect even though channel gain has perfect correlation because the additive noise does not get perfectly averaged out. When observation length is infinite, noise would be averaged out and the estimate would be perfect resulting in zero penalty due to unknown CSI.

3.5.2 Factors Affecting Information Rate Loss

In addition to SNR and block length of transmission, the information rate loss in a truncated-isotropic environment depends on mean scattering angle, β_0, mobile direction of travel, ϕ_v and non-isotropicity. In the following, we shall use numerical means to evaluate the impact of each of these parameters on the no-CSI cost function.

Definition 3.5.1 *Suppose* $\mathrm{P}_{\delta}^{\mathrm{Iso}}$ *and* $\mathrm{P}_{\delta}^{\mathrm{NIso}}$ *respectively denote information rate loss in isotropic and a non-isotropic scattering scenarios. Let* I_{Iso} *and* I_{NIso} *respectively denote achievable rates in isotropic and non-isotropic environments. We define non-isotropicity gain,* NIgain, *as*

$$\mathrm{NIgain} = \mathrm{P}_{\delta}^{\mathrm{Iso}} - \mathrm{P}_{\delta}^{\mathrm{NIso}}, \tag{3.13}$$

$$= I_{\mathrm{NIso}} - I_{\mathrm{Iso}}. \tag{3.14}$$

A positive NIgain implies that loss due to unknown CSI is lower (and achievable rates are higher) in non-isotropic environment than in isotropic case and vice versa.

With no loss of generality, unless explicitly stated, we shall assume in the sequel that mean scattering angle, $\beta_0 = 90°$ and $\rho = 10$ dB both in isotropic and non-isotropic environments.

Impact of Mobile Direction of Travel

Unlike isotropic reception where the statistics of received signal (and, hence, information rate loss due to unknown CSI) are independent of mobile direction of travel, the information rate loss in a non-isotropic environment depends strongly on mobile direction of travel. Fig. 3.1 shows the effect of changing mobile direction of travel on information rate loss in truncated-isotropic environment. We can observe that there is a significant change in loss when mobile direction of travel changes from $0°$ to $90°$. Also information rate loss is maximum (at least for macro and microcellular environments) when the

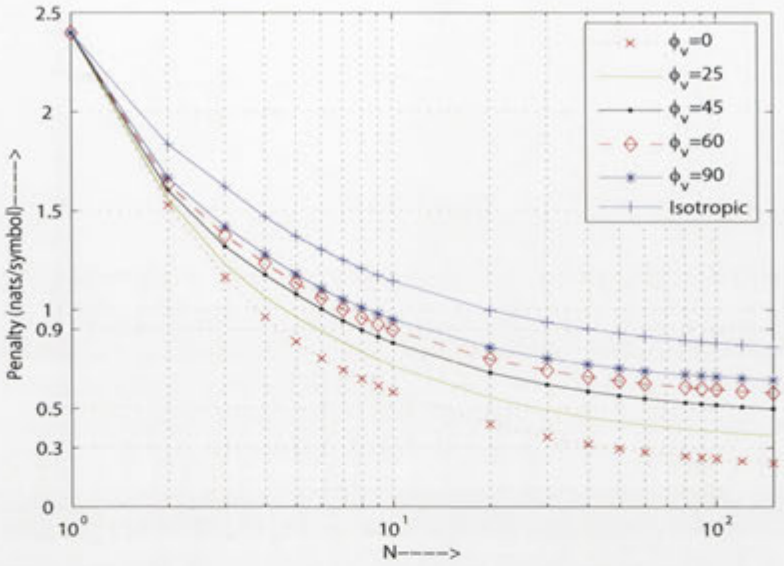

Figure 3.1: Effect of changing mobile direction of travel on information rate loss due to unknown CSI in truncated-isotropic environment when Δ_r=45° and f_D=0.1.

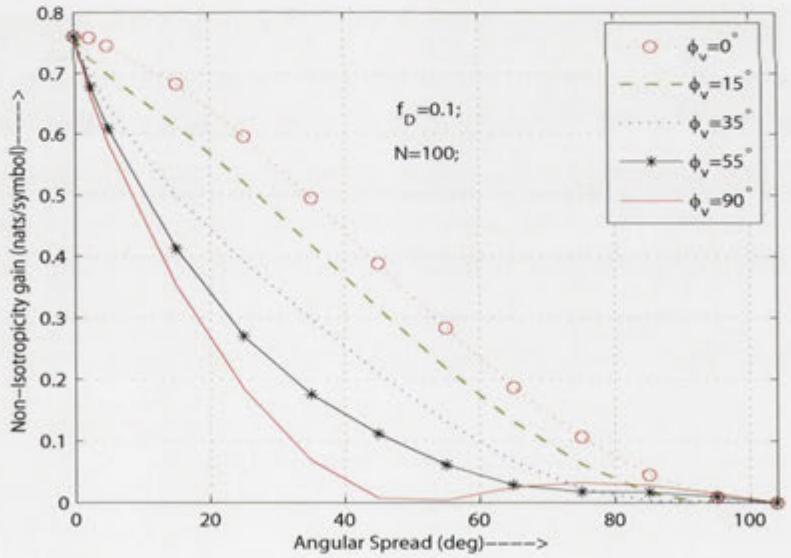

Figure 3.2: Impact of mobile direction of travel on non-isotropicity gain as a function of non-isotropicity when N=100 and f_D=0.1. For the limiting cases of $\Lambda \to 0$ and $\Lambda \to 104°$, non-isotropicity gain is not affected by direction of mobile travel.

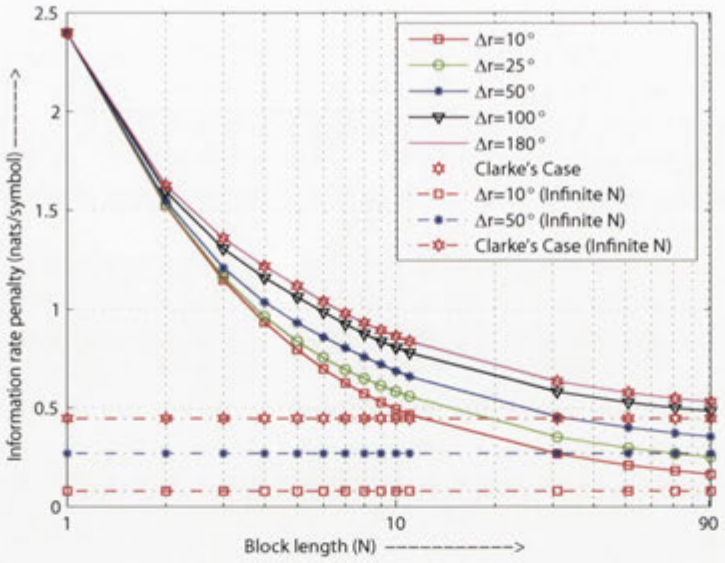

Figure 3.3: Non-isotropicity gain versus block length for different Δ_r when ϕ_v=0° and N=100. We can observe that penalty is less for smaller Δ_r (or in other words, higher degree of non-isotropicity).

mobile moves directly into the mean scattering angle, β_0.

We have plotted non-isotropicity gain, NIgain, against Λ for different ϕ_v in Fig. 3.2. We can observe that $\phi_v = 90°$ does represent a worst-case scenario for moderate angular spreads and $\phi_v = 0°$ corresponds to least information rate loss (and maximum correlation). These plots assume that mobile direction of travel is known *a priori* to the receiver. If mobile direction of travel is unknown to the receiver and is equally probable in all directions, it can be shown that truncated-isotropic environment, on average, is no different from isotropic case (Section 2.3.1). In other words, gain offered by non-isotropicity requires knowledge about the mobile direction of travel.

Impact of Transmission Block Length and Non-Isotropicity

P_δ^{norm} in (3.8b) is a non-increasing sequence in N which implies that with increasing block length of transmission, the loss in information rate due to unknown CSI can be reduced, with all other parameters fixed. Fig. 3.1 shows the effect of changing block length on penalty for different directions of mobile travel. We can observe a non-increasing behavior of cost function against increasing block length. Notice that at block length N=100, the information rate loss seems to have reached asymptotic value for all scattering scenarios which implies that increasing transmission block length in a non-coherent communication system beyond 100 reduces information rate loss by a very small amount

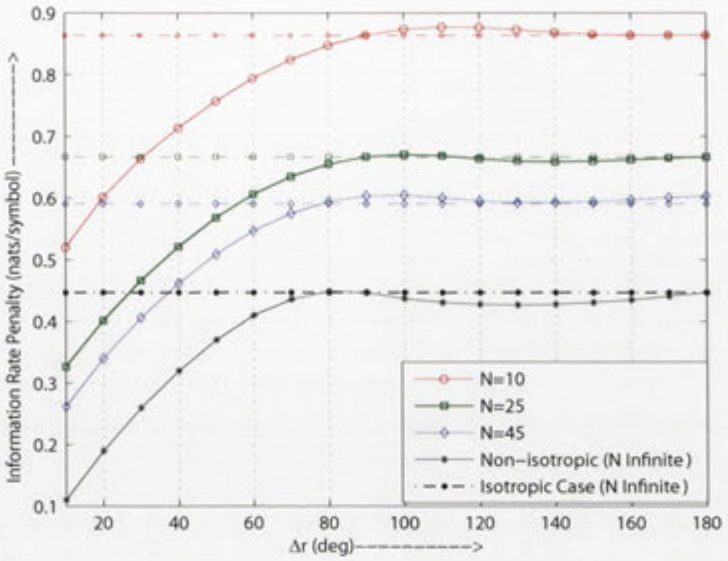

Figure 3.4: The penalty due to channel unpredictability because of no-CSI as a function of non-isotropicity for different transmission block lengths when f_{D}=0.05, ρ=10 dB and ϕ_v=90°. Though not shown for other ϕ_v, penalty remains less than or equal to that of isotropic environment when block length is infinite. The horizontal lines correspond to penalty in isotropic environment. An important observation is that penalty in a non-isotropic scenario is not, in general, monotonic in Δ_r (or Λ), *i.e.*, non-isotropicity.

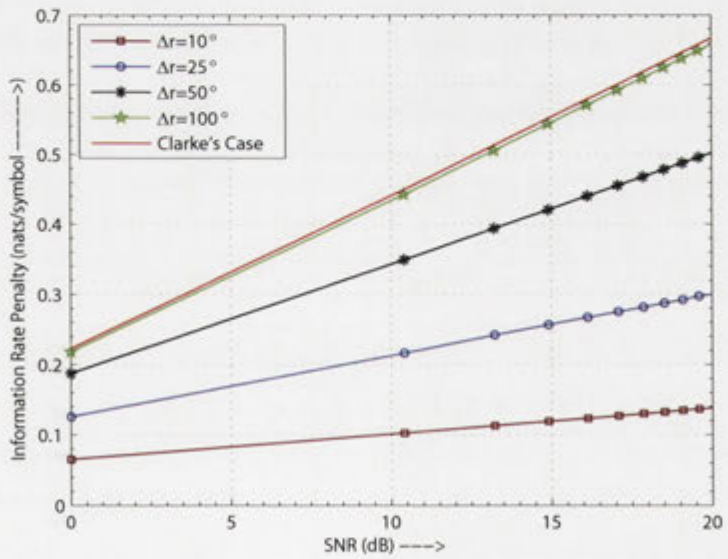

Figure 3.5: Effect of SNR and non-isotropicity on information rate cost for unknown CSI when ϕ_v=45°, f_{D}=0.05 and $N\to\infty$. The effect of changing non-isotropicity is to change the slope of penalty-ρ curve.

and there is no real temptation for making block lengths much larger than that.

Figs. 3.4 and 3.3 show the behavior of penalty for finite and infinite block lengths against non-isotropicity. Fig. 3.4 suggests that for finite block lengths, penalty in non-isotropic scenario can even be greater than in an isotropic environment. The intuition here is that for a certain block length, the correlation for a specific non-isotropic scattering scenario may remain higher than another scenario. However if block length is increased, the correlation in additional symbols could be lower for the first scenario than the second scenario (see correlation plot in [149], for example). An increase in block length might, therefore, have the net impact of lowering penalty for the second scenario in comparison to the first scenario. Fig. 3.4 confirms this intuition as we can see that for finite block lengths, information rate cost for non-isotropic scattering is higher than isotropic case for certain angular spreads. As the transmission block length is increased to infinity, isotropic penalty becomes an upper bound to the penalty in non-isotropic scenario. In other words, when transmission block length is infinite, isotropic scattering is worse than any truncated-uniform scenario. The same behavior can be shown for any ϕ_v and fading rate.

Table 3.1: Typical values of angular spread (Λ) at 1800MHz

Environment	Δ_r(deg)	Λ(deg)
Flat rural (Macro)	0.5	0.29
Urban (Macro)	10	5.77
Hilly (Macro)	15	8.66
Urban (Micro)	60	35
Indoor (Pico)	180	103.9

Impact of SNR

Fig. 3.5 shows the impact of varying SNR for different scattering scenarios when the block length is infinite. Observe that the effect of a change in non-isotropicity is to change the slope of penalty-ρ curve. We can observe a gradual decrease in the slope with increasing non-isotropicity. In the limiting case of $\Lambda \rightarrow 0°$, the penalty and the slope of penalty-ρ curve would be zero (Section 3.5.1) implying independence from SNR of information rate loss due to no-CSI. Similar reduction of slope can be observed in [37] as a result of changing fading rates in isotropic environment. The normalized fading rate is kept constant, and only degree of non-isotropicity is changed. This implies that changing non-isotropicity is tantamount to changing the effective fading rate f_{Deff}. We argue that $f_{\mathrm{Deff}} \leq f_{\mathrm{D}}$ when the transmission block length is infinite.

Table 3.2: Typical values of Λ at 900MHz

Environment	Δ_r(deg)	Λ(deg)
Flat rural (Macro)	2.5	1.44
Urban (Macro)	$2.5-5$	$1.44-2.9$
Suburban (Macro)	$2.5-5$	$1.44-2.9$
Micro	$20-45$	$11.54-25.98$
Indoor (Pico)	$45-180$	$25.98-103.9$

Impact of Fading Rate

As discussed in previous subsection, changing non-isotropicity is equivalent to changing fading rate. We can therefore argue that the impact of changing fading rate for a fixed non-isotropicity is equivalent to changing non-isotropicity for a fixed fading rate. Fig. 3.6 shows the impact of changing fading rate on non-isotropicity gain. We can observe that non-isotropicity gain is greater for higher fading rates and high degree of non-isotropicity. For small fading rates, non-isotropicity gain is nominal and remains almost insensitive to a change in non-isotropicity.

Definition 3.5.2 *Let* $\mathrm{NIgain}_{0^\circ}$ *and* $\mathrm{NIgain}_{90^\circ}$ *respectively denote the non-isotropicity gain for* $\phi_v = 0^\circ$ *and* 90° *assuming a fixed block length, SNR and mean scattering angle. We define sensitivity,* $\mathcal{S}$*, of non-isotropicity gain to a change in mobile direction of travel as*

$$\mathcal{S} = \mathrm{NIgain}_{90^\circ} - \mathrm{NIgain}_{0^\circ}, \tag{3.15}$$

where a large $\mathcal{S}$ would indicate a large swing in non-isotropicity gain due to a change in mobile direction of travel from 0° to 90° implying a greater sensitivity of non-isotropicity gain to mobile direction of travel.

Fig. 3.7 shows the effect of changing fading rate on $\mathcal{S}$ as a function of non-isotropicity. Note that non-isotropicity gain is more sensitive to a change in mobile direction of travel for moderate Λ and high fading rates. It means that in order to make use of gains offered by non-isotropicity at moderate angular spreads in high mobility applications, there is a greater need to have accurate knowledge of mobile direction of travel. The gain is less sensitive to a change in ϕ_v for small and large Λ irrespective of fading rate. We can observe that $\mathcal{S}$ is negative for a range of (large) angular spreads when $f_\mathrm{D} = 0.5$. We argue that this is again due to finiteness of block length and not due to any numerical approximation.

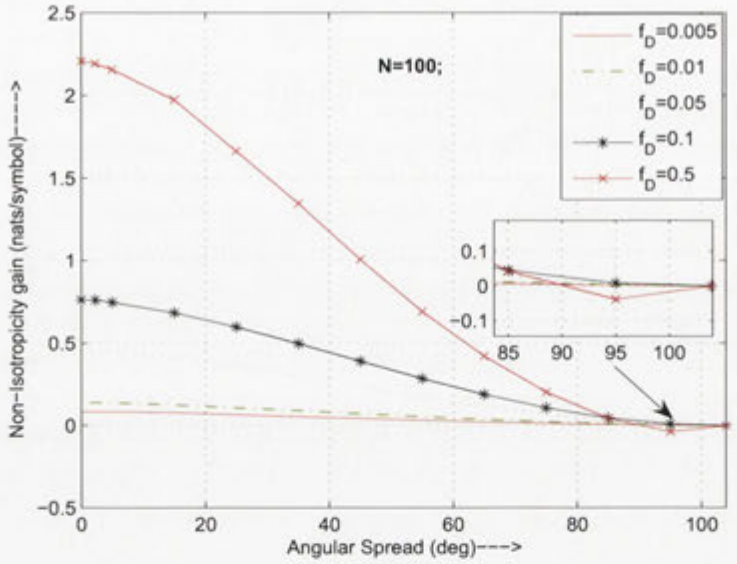

Figure 3.6: The non-isotropicity gain versus non-isotropicity for different normalized fading rates when ϕ_v=0° and N=100. We can observe that non-isotropicity gain is highest when scattering is most non-isotropic, *i.e.*, when $\Lambda \to 0$. And gains are higher for higher fading rates.

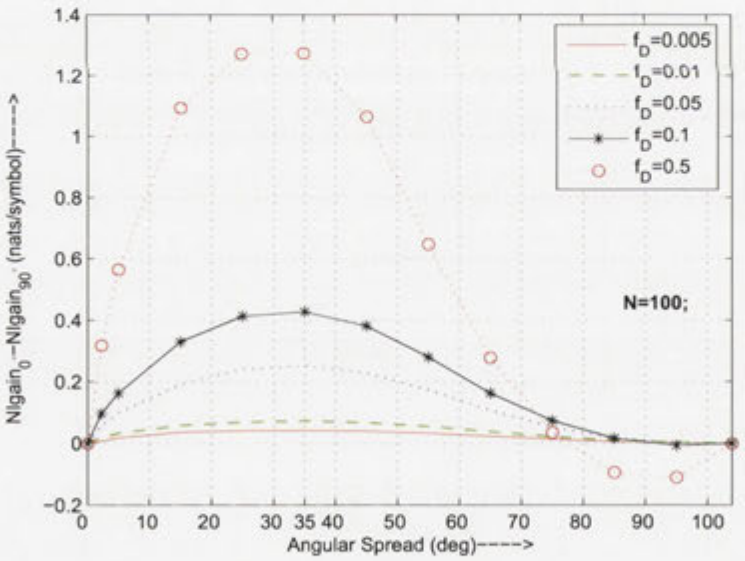

Figure 3.7: Sensitivity of non-isotropicity gain to mobile direction of travel as a function of angular spread for different normalized fading rates when N=100. We can observe that non-isotropicity gain is most sensitive to a change in mobile direction of travel for moderate angular spreads and higher fading rates, and is least sensitive when either $\Lambda \to 0$ or $\Lambda \to 104°$ and fading rates are small.

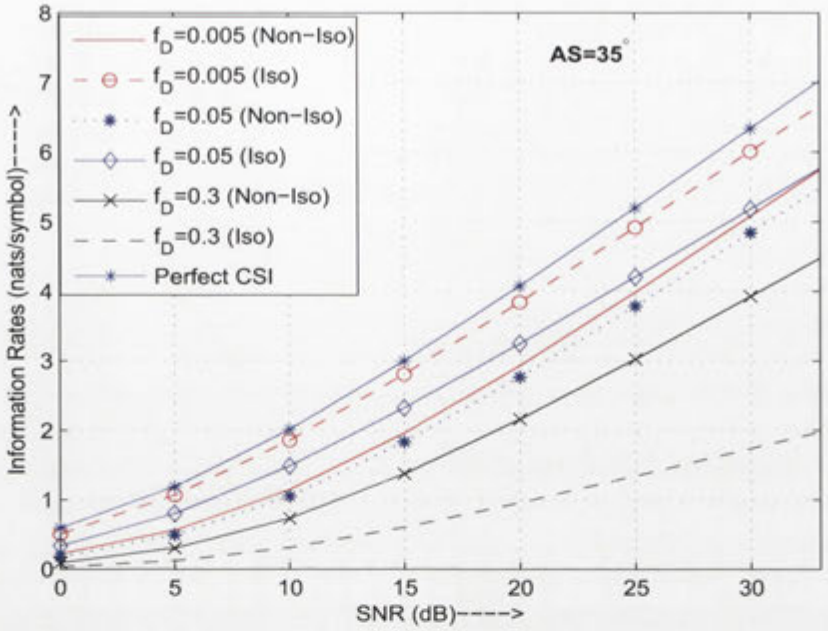

Figure 3.8: Impact of non-isotropicity on Gaussian signaling lower bound as a function of SNR for different fading rates when Λ=35° and ϕ_v=0°. It can be observed that use of a non-isotropic antenna in an isotropic scattering environment is useful only for high mobility applications.

3.6 Analysis of Two Non-Isotropic Communications Scenarios

This section is devoted to the analysis of two specific non-isotropic communications scenarios. In the first scenario the scattering is isotropic but the antenna is directional with uniform gain pattern (beamforming). On the other hand, the scattering is non-isotropic with uniform AOA but the antenna is isotropic in the second scenario. In both cases the scattered power is assumed to be the same. A directional antenna in the first case intercepts only a portion of the available scattered power. In the light of the discussion so far in this and the previous chapter, the use of directional antenna would result in better channel statistics at the cost of reduced SNR. On the other hand, the isotropic antenna in the second case implies that no useful scattered power is rejected. Our purpose in this section is to compare the performance of the communications system in these two scenarios to *isotropic scattering-isotropic antenna*.

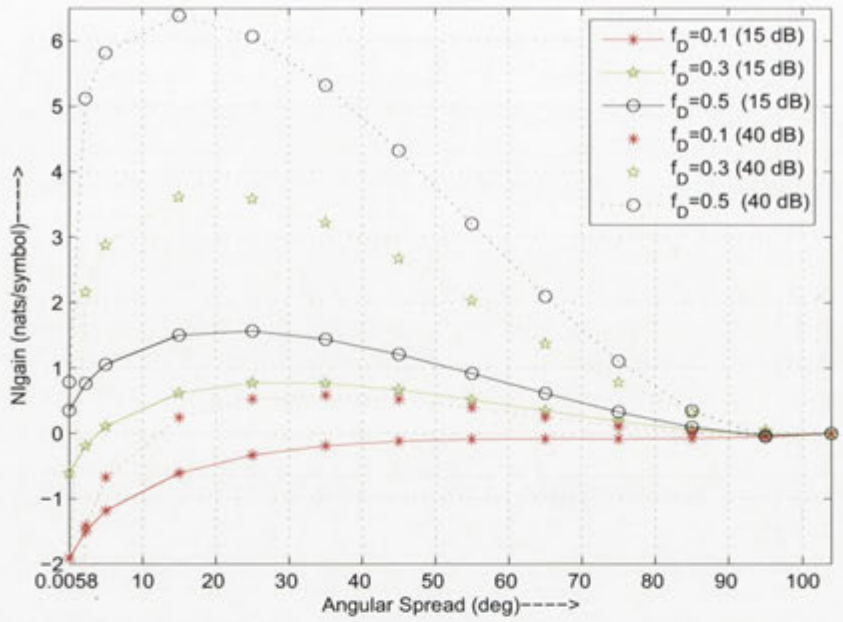

Figure 3.9: Non-isotropicity gain for Gaussian signaling versus angular spread for different normalized fading rates when a non-isotropic antenna is used at the mobile receiver in isotropic environment. ϕ_v=0° and N=100 and ρ=$\{15, 40\}$ dB. The figure suggests that a non-isotropic antenna offers significant gains as compared to an isotropic scattering environment when normalized fading rates are higher. Compare this figure to Fig. 3.6 which corresponds to isotropic antenna at the receiver in a non-isotropic environment assuming equal SNR in isotropic and non-isotropic scattering.

3.6.1 Non-Isotropic Scattering with Isotropic Receive Antenna

Using (1.20) and (1.17), the comparison of achievable rates with Gaussian and MPSK signaling for truncated-uniform and isotropic scattering models assuming equal SNR and large block length is given in Fig. 3.16. Significant gains in achievable rates with truncated-isotropic scattering can be observed. As we can see, the MPSK signaling upper bound is nearly 2.6 nats/symbol in case of truncated-uniform scattering ($\Delta_r = 10°$) for SNR of 12 dB which represents 30% increase over isotropic scattering model. For $\rho = 25$ dB, this gain rises to over 1 nat/symbol, an increase of 25% over isotropic case. These gains would be higher when ϕ_v=0°.

Similarly, Gaussian signaling lower bounds for truncated-uniform scattering are higher than in isotropic environment. At $\rho = 10$ dB, gain due to non-isotropicity is around 0.7 nats/symbol when $\Delta_r = 10°$ (which represents ≈47% gain over isotropic reception). When SNR is 25 dB, this gain rises to around 1.1 nats/symbol.

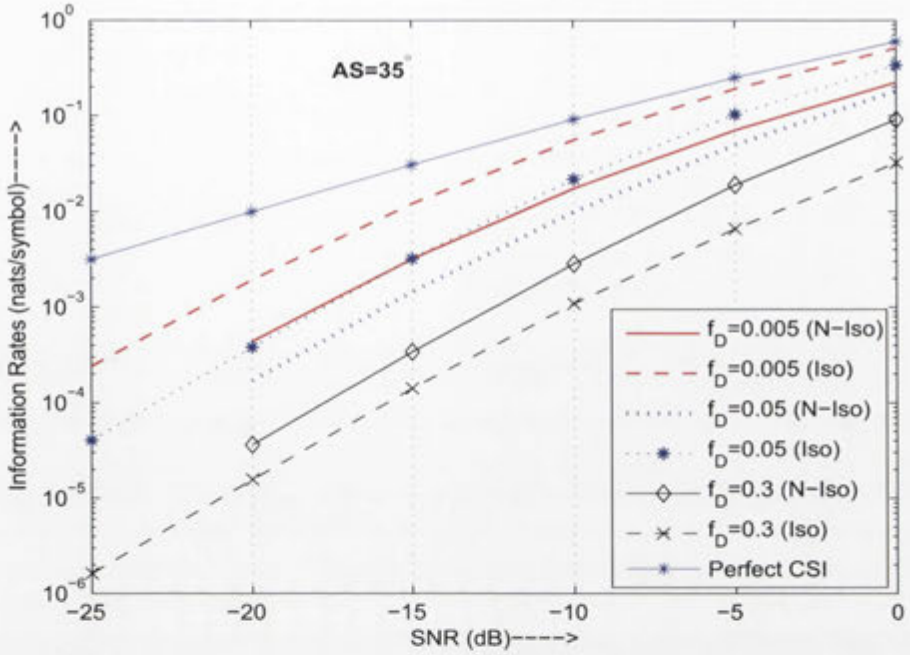

Figure 3.10: Impact of non-isotropicity on Gaussian signaling lower bound in the low SNR regime for different normalized fading rates when ϕ_v=0°, Λ=35° and N=100. The figure suggests that it is better to have a non-isotropic antenna in an isotropic scattering environment only when normalized fading rates are higher, *i.e.*, in very high mobility applications. At low to moderate fading rates, non-isotropic reception is counterproductive.

3.6.2 Isotropic Scattering with Non-Isotropic Receive Antenna

Equations (1.20) and (1.17) specify a trade-off between SNR and correlation (or eigenvalues). Notice that AWGN (or Rayleigh) capacity is a function of SNR while P_δ^{norm} is a function of SNR and eigenvalues $\{\lambda_i\}$. As we discussed before, changing the degree of non-isotropicity changes eigenvalues $\{\lambda_i\}$. If the degree of non-isotropicity is increased (or equivalently, angular spread is reduced), $\{\lambda_i\}$ change in a way to reduce P_δ^{norm} (see Fig. 3.3 for example). We, in this section, seek to find answer to the following question: Is it feasible to use a non-isotropic antenna in an isotropic environment? In other words, the question is of the feasibility of beamforming in isotropic environment? Obviously, the use of a non-isotropic antenna in an isotropic environment will result in reduced average received SNR due to a portion of useful available power being rejected. The non-isotropic reception would however result in increased correlation (if the block length is sufficiently large). SNR reduction and increased correlation both have the effect of reducing P_δ^{norm}. However, reduction in SNR reduces corresponding AWGN and Rayleigh capacity. Therefore, the use of a non-isotropic antenna results in a *trade-off*

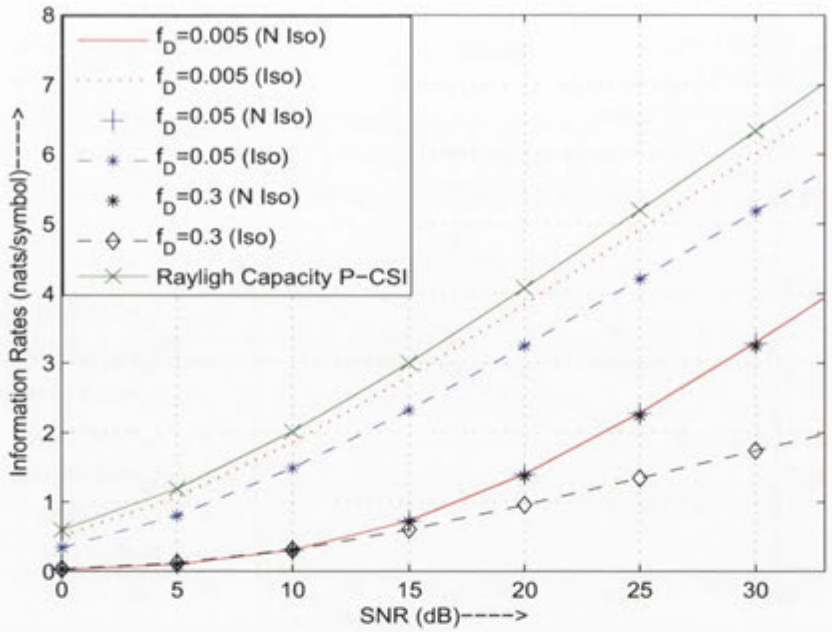

Figure 3.11: Impact of non-isotropicity on Gaussian signaling lower bound as a function of SNR for different fading rates when Λ=5° and ϕ_v=0°. It can be observed that use of a non-isotropic antenna in an isotropic scattering environment is useful only for high mobility applications. And lower bound is insensitive to a change in the fading rate.

between received SNR and correlation of the channel process. We intend to see if this trade-off can work in favor of a non-isotropic antenna in an isotropic environment.

The received SNR with an isotropic antenna is ρ. The SNR in case of a non-isotropic antenna, denoted by ρ' would be

$$\begin{aligned} \rho' &= \rho \frac{\Delta_r}{180}, \\ &= \rho \frac{\Lambda}{103.9}, \end{aligned} \tag{3.16}$$

where both Δ_r and Λ are in degrees. Note that $\rho' \leq \rho$ because a directional antenna in an isotropic scattering captures only a portion of the available power. The modified MPSK signaling upper bound and Gaussian signaling lower bound respectively become

$$I'_C(\mathbf{r}, \mathbf{s}) \leq C_{\text{AWGN}}(\rho') - P^{norm}_{\delta,\text{NA}}, \tag{3.17}$$

and

$$I'_G(\mathbf{r}, \mathbf{s}) \geq C_{\text{Rayleigh}}(\rho') - P^{norm}_{\delta,\text{NA}}, \tag{3.18}$$

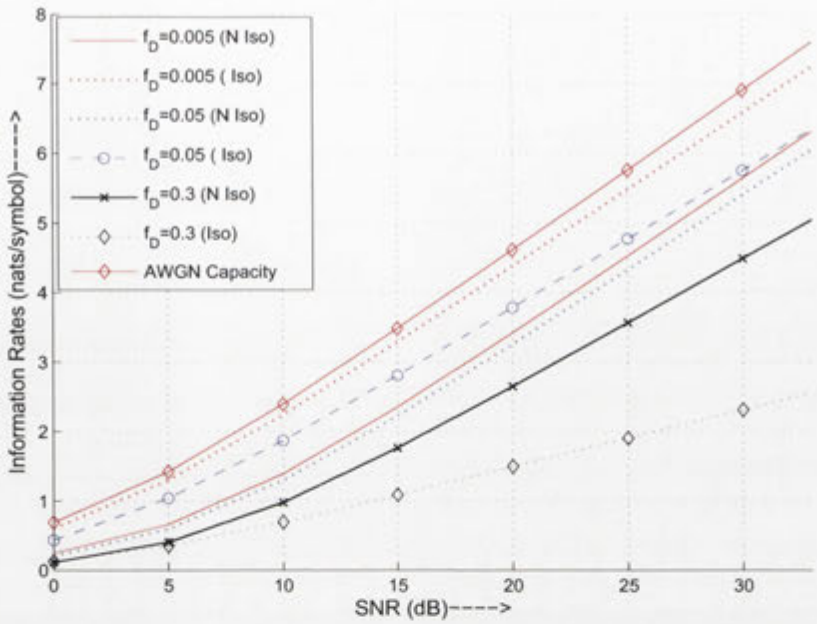

Figure 3.12: Impact of non-isotropicity on MPSK signaling upper bound as a function of SNR for different fading rates when Λ=35° and ϕ_v=0°. It can be observed that use of a non-isotropic antenna in an isotropic scattering environment seems useful only for high mobility applications. For low to moderate fading rates, isotropic reception performs much better than non-isotropic reception.

where $P_{\delta,\mathrm{NA}}^{norm}$ is the same as (3.8b) but the received SNR is ρ'.

We numerically evaluated (3.17) and (3.18) and plotted the results in Figures 3.8-3.12 along with Rayleigh and AWGN capacities for comparison. Observe from these plots that the non-isotropic antenna performs quite poorly as compared to isotropic reception for small fading rates for all SNR. It can also be observed that as SNR decreases below 0dB, penalty for unknown CSI increases. When SNR is 0dB, isotropic reception with f_{D}=0.005 almost achieves Rayleigh perfect CSI capacity. When SNR is -25dB, the difference between noncoherent isotropic reception and perfect CSI Rayleigh capacity is 0.00275 nats/symbol. Non-isotropic reception, however, outperforms isotropic reception when fading rate is high[5]. For $\rho = 33$ dB, achievable rates with Gaussian inputs with non-isotropic reception are higher than isotropic reception by ~ 2.5 nats/symbol. We can also observe that at small angular spread of 5°, Gaussian signaling lower bound is insensitive to a change in fading rate (Fig. 3.11). Similar behavior can be shown to exist for Λ<5°. This implies that at very small angular spreads, a change in fading rate

[5]Since $f_{\mathrm{D}} = \frac{vT_s}{\lambda}$, a high fading rate implies high mobility and/or high frequency of transmission and/or low symbol rate.

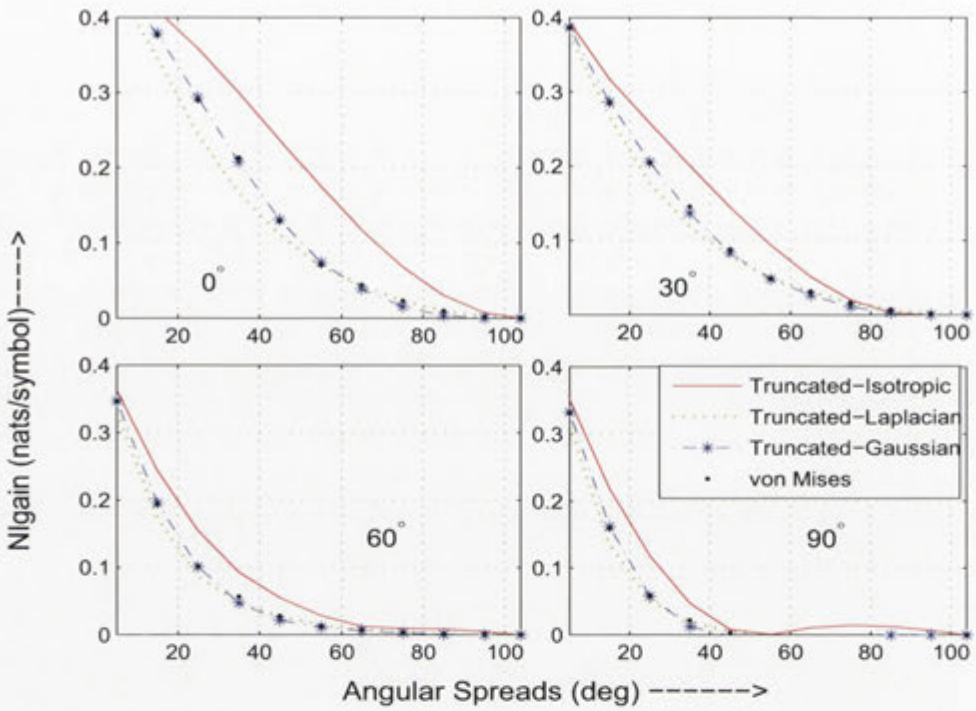

Figure 3.13: Comparison of non-isotropicity gain for different scattering environments as a function of angular spread, Λ, for $\phi_v = \{0°, 30°, 60°, 90°\}$, $f_{\mathrm{D}} = 0.05$ and $L = 100$.

does not alter channel statistics significantly.

3.7 Non-Isotropic Scattering Distributions: A Comparative Study

In Section 2.2.3, we briefly discussed commonly used non-isotropic scattering models and explored the impact of various scattering models on the channel statistics, *i.e.*, autocorrelation and PSD in Section 2.4. In this section, we use no-CSI cost function (which depends on the channel statistics) introduced in Section 3.3 (Eq. (3.8b)) to compare different non-isotropic scattering models. While looking at the autocorrelation and PSD plots in Chapter 2, we can only qualitatively describe the differences between different scattering models. By using no-CSI cost function, the difference in statistics is translated to nats/symbol thus specifying in information theoretic context the differences in statistics of different scattering models. In the subsequent analysis, we assume equal SNR for non-isotropic and isotropic scenarios.

For a fixed transmission block length and the normalized fading rate, Fig. 3.13 shows the comparison of the non-isotropicity gain for truncated-isotropic, Laplacian, Gaussian

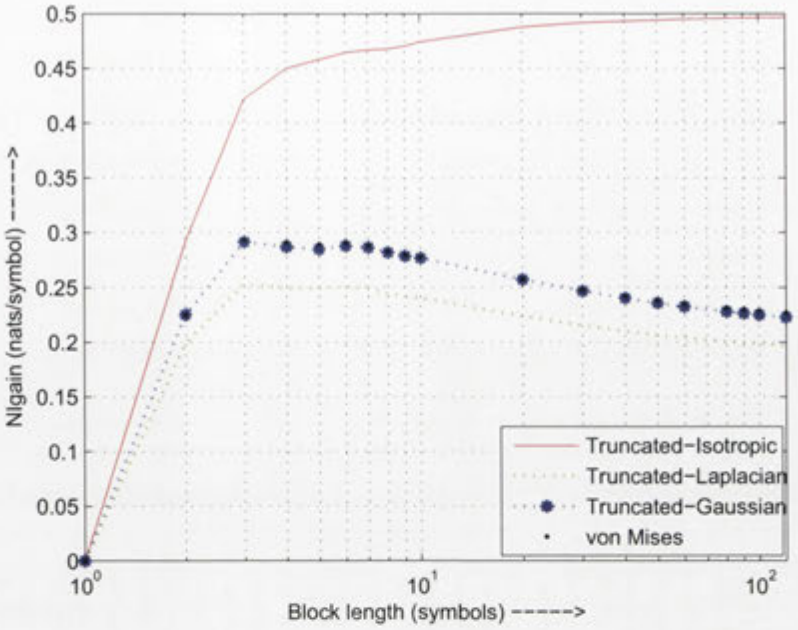

Figure 3.14: Comparison of non-isotropicity gain for different scattering distributions as a function of block length for ϕ_v=0°, $f_{\mathrm{D}} = 0.1$ and $\Lambda = 45°$.

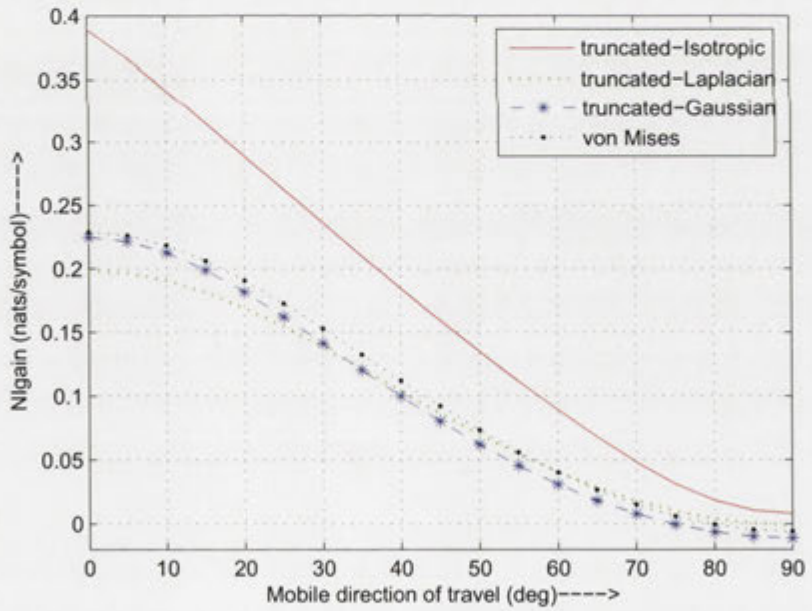

Figure 3.15: Comparison of non-isotropicity gain as a function of ϕ_v when $f_{\mathrm{D}} = 0.1$, $N = 100$ and $\Lambda = 45°$.

and von Mises scattering distributions as a function of the angular spread for different mobile directions of travel. No significant change in this behavior has been observed

if the block length is changed. Notice that for small and large angular spreads, different scattering distributions are almost identical. The difference among scattering distributions is noticeable for moderate angular spreads. Truncated-isotropic environment is "optimistic" (*i.e.*, it has higher correlation) as compared to other scattering models. Moreover, a Laplacian distribution is the "worst" among different models being studied for moderate angular spreads while Gaussian distribution becomes "worst" for large angular spread. It can also be observed that for ϕ_v=0°, the difference among scattering environments is more pronounced. Similarly while the pattern of behavior as a function of fading rate remains the same (with other parameters fixed) as in Fig. 3.13, the difference among scattering models in terms of nats/symbol becomes higher for higher fading rates. For the following analysis, unless explicitly stated, we therefore choose ϕ_v=0°, $f_{\mathrm{D}} = 0.1$ (very fast fading scenario) and moderate angular spread to highlight approximately worst case scenario.

For a fixed angular spread, mobile velocity and fading rate, the non-isotropicity gain for different scattering models has been plotted as a function of block length of transmission in Fig. 3.14. No significant change in this behavior has been observed if the angular spread is changed keeping the angular spread in the moderate range. Notice an upward trend (as a function of block length) in gain for truncated-uniform environment and a downward trend for Gaussian, Laplacian and von Mises distributions. An upward trend implies that every extra symbol carries more (incremental) information in truncated-isotropic case as compared to isotropic case. A downward trend for other scattering models indicates lesser information (than isotropic case) for every additional symbol. In this respect Gaussian, Laplacian and von Mises distributions are worse than isotropic environment. Notice that Gaussian and von Mises distributions are almost identical and Laplacian distribution is the "worst" of all scattering distributions. The truncated-uniform environment differs from other three distributions significantly. Therefore, assumption of truncated-isotropic environment could, in general, introduce significant errors in the analysis based on channel statistics if, in reality, scattering distribution is different.

As we discussed in Section 2.2, the channel statistics in a non-isotropic environment depend on the mobile direction of travel. Fig. 3.15 shows the behavior of non-isotropicity gain in common non-isotropic scattering scenarios as a function ϕ_v keeping block length of transmission, fading rate and the angular spread fixed. The sensitivity of non-isotropicity gain to mobile direction of travel is shown in Fig. 3.17 for different scattering distributions. Notice that all scattering distributions are almost equally sensitive to a change in mobile direction of travel. To be more precise, the truncated-Laplacian distribution is least sensitive to a change in ϕ_v when the angular spread is moderate. No

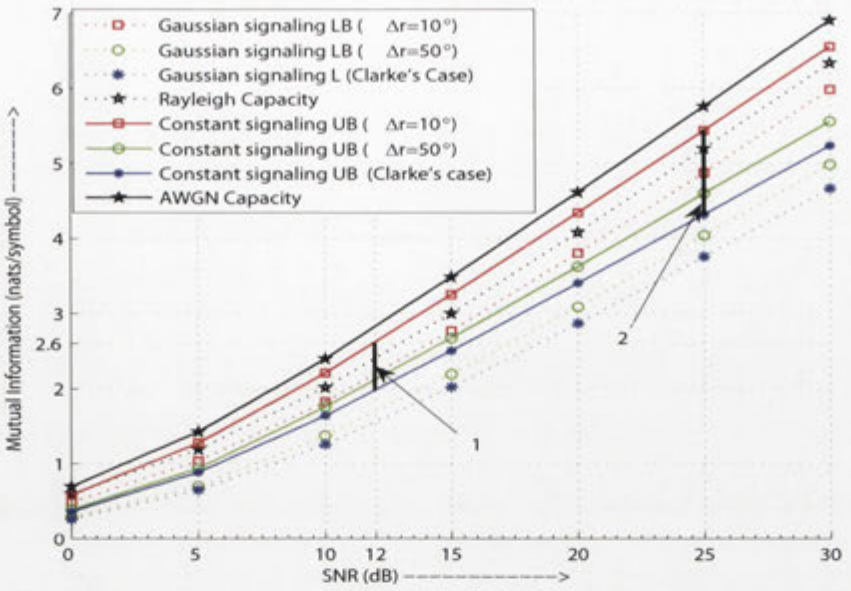

Figure 3.16: Achievable information rates as a function of SNR when the scattering distribution is truncated-isotropic for $\phi_v = 65°$ in case of different Δ_r. The potential gains for Gaussian signaling have been highlighted at two values of SNR.

significant change in this pattern of behavior has been observed as a result of a change in block length of transmission.

In the light of the preceding analysis, we can conclude that the truncated-uniform, truncated-Gaussian, truncated-Laplacian and von Mises distributions can be considered equivalent for small and large angular spreads, and small fading rates. Therefore, the replacement of one distribution for the other will not cause any significant errors in channel statistics and system analysis or design based on channel statistics. For moderate angular spreads and large fading rates, statistics of these distributions may differ significantly and replacement of one distribution for the other might introduce significant errors. Therefore, if the communications systems designer can have the perfect knowledge of the type of scattering environment and the mobile direction of travel (at the receiver[6]), the performance of the communications system can be enhanced Section 3.5.2.

[6]Throughout this thesis, we assume that the it is the receiver that knows the channel statistics. If, in addition, the knowledge of statistics is assumed at the transmitter as well, the overall performance of the system can be further improved by allowing the transmitter to adapt its transmissions according to the *expected* channel statistics.

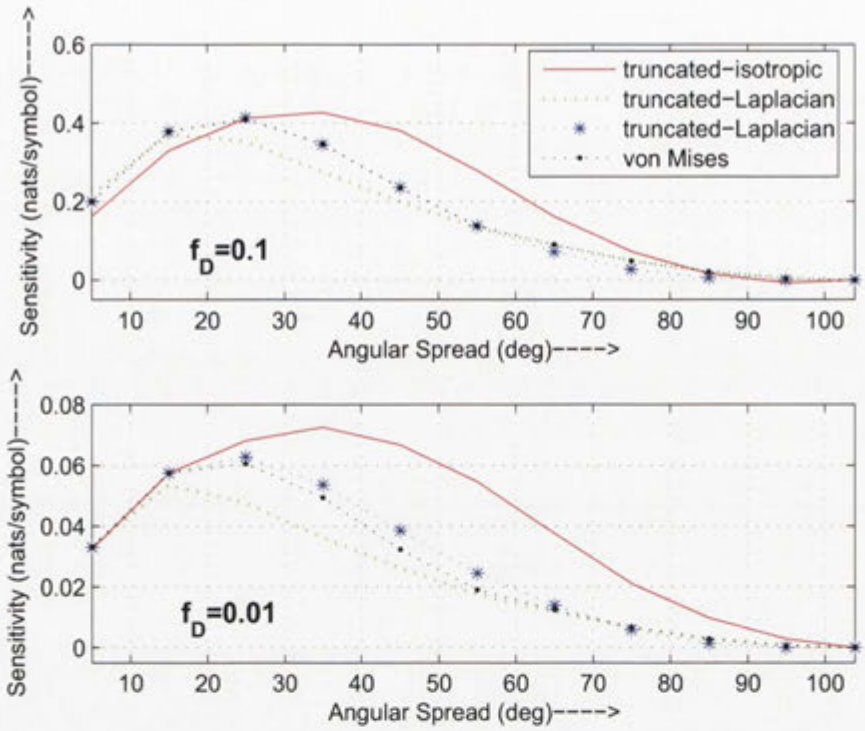

Figure 3.17: The gain sensitivity, $\mathcal{S}$, for different scattering environments as a function of angular spread for $f_{\mathrm{D}} = \{0.01, 0.1\}$ and $N = 100$.

3.8 Marginal Gaussianity does not Imply Joint Gaussianity: A Practical Example

The complex channel vector $\mathbf{h}$ in (3.1) is Gaussian (or equivalently jointly Gaussian) because it is obtained by sampling a complex Gaussian channel process $\{h\}$ where the complex Gaussianity of the channel process is due to the assumption of rich scattering with the phases of scattered electromagnetic waves uniformly distributed over $[-\pi, \pi]$. The question that we seek to answer in this section is the following: Given a Gaussian vector $\mathbf{h}$, is the output vector $\mathbf{r}$ in (3.1) in response to i.i.d. constant power signaling a Gaussian vector? The motivation behind the consideration of this problem lies in the recent contributions with contradictory results. In [90, 91], the authors claim to have derived exact OFDM channel capacity for constant power signaling arguing that the channel output is jointly Gaussian when the input is i.i.d. MPSK. In [37], on which the work in this chapter is mainly based, the authors are more cautious about the joint Gaussianity of the output vector and derive an upper bound on the capacity with i.i.d. constant power signaling (Eq. (1.20)).

The MPSK capacity upper bound (Eq. (1.20)) is correctly based on the premise that the entropy of any random process with a fixed covariance matrix is maximized when the process is jointly Gaussian. However, no comments have been made about the strictness of this upper bound in [37]. The *marginal* Gaussianity of the channel output in response to constant power signaling led authors in [90,91] to tacitly conclude that the channel output sequence is also *jointly* Gaussian and hence, to report an *exact* information rate for OFDM systems. In order to verify this claim, we propose to rigorously study the marginal and joint probability distributions of the channel outputs in response to i.i.d. MPSK in time-selective Rayleigh fading channels. This is carried out through mathematical analysis and computer simulations. We show that the system model under consideration is a clear example of the case where marginal Gaussianity does not imply joint Gaussianity. As a result, we show that the information rates reported in [90,91] are, in fact, strict upper bounds. We then examine the tightness of these bounds by comparing them with the perfect CSI upper bound for MPSK inputs. Interestingly, the comparison reveals that the perfect CSI upper bound can provide tighter bounds than those in [37,90] in slow fading channels and high SNR conditions, especially when the MPSK dimension is low (such as binary signaling).

Since the scattering environment has been assumed to be isotropic in [90, 91] and [37], the channel vector $\mathbf{h}$ has covariance matrix as defined in (3.3). To derive the marginal distribution of the channel output, we need to consider an arbitrary sample of the channel output at discrete time index ℓ, which is given as

$$r_\ell = \underbrace{s_\ell h_\ell}_{x_\ell} + z_\ell, \tag{3.19}$$

$$\begin{aligned} &= \sqrt{\rho}\, \exp(i\theta_\ell)\, |h_\ell|\, \exp(i\phi_\ell) + z_\ell, \\ &= \sqrt{\rho}|h_\ell|\, \exp(i(\theta_\ell + \phi_\ell)) + z_\ell, \end{aligned} \tag{3.20}$$

where fading amplitude $|h_\ell|$ is Rayleigh distributed and the fading phase ϕ_ℓ is uniformly-distributed over $[-\pi, \pi]$. $\sqrt{\rho}e^{i\theta_\ell}$ is the transmitted constant power signal. Because the additive noise is Gaussian and independent of $x_\ell = s_\ell h_\ell$, the Gaussianity (or non-Gaussianity) of the output vector is determined by x_ℓ. For MPSK, the signal phase can be one of the M possible phases as $\theta_\ell = 2\pi m/M$ for $m \in \{0, \cdots, M-1\}$. Since the transmitted signal has constant modulus, the distribution of $|x_\ell| = \rho|h_\ell|$ remains Rayleigh. To prove the Gaussianity of $x_\ell = s_\ell h_\ell$ (and hence marginal Gaussianity of r_ℓ), we only need to prove that the phase of x_ℓ (which is $(\theta_\ell + \phi_\ell)_{\otimes 2\pi}$) is uniformly distributed over $[-\pi, \pi)$. If the input phase was *continuously* uniform between $-\pi$ and π, one could show that $(\theta_\ell + \phi_\ell)_{\otimes 2\pi}$ remains uniform over $[-\pi, \pi]$ by invoking standard arguments in probability theory [150]. Intuitively, one expects that the distribution of $(\theta_\ell + \phi_\ell)_{\otimes 2\pi}$

remains uniform for MPSK signals with discrete distributions at $\theta_\ell = 2\pi m/M$. This intuitive reasoning has been used in [90] to show marginal Gaussianity of the output.

In fact, the following theorem from [151] provides even a stronger result.

Theorem 3.8.1 *If two processes $a(t)$ and $b(t)$ have the probability density functions $p_1(a,t)$ and $p_2(b,t)$, respectively, such that $a(t)$, modulo q, is statistically independent of $b(t)$ and uniformly distributed,* i.e.,

$$p_1(a_q,t) = \frac{1}{q}\left\{u(a) - u(a-q)\right\},$$

where $u(\cdot)$ is the unit step function, then the probability density function of $(a_q(t) \pm b(t))$, modulo q, is also uniformly distributed, regardless of the probability density function of $b(t)$. That is, if $w(t) = a_q(t) \pm b(t)$, then

$$p(w_q,t) = \frac{1}{q}\left\{u(w) - u(w-q)\right\}.$$

By directly applying the above theorem to the problem at hand, we formulate the following result:

Theorem 3.8.2 *The distribution of the phase process of the output $\{\Theta = (\phi+\theta)_{\otimes 2\pi}\}$, where ϕ and θ are statistically independent channel and input phase processes, is uniform over $[0, 2\pi)$ and is independent of the distribution of the input phase, θ.*

An immediate consequence of the second part of the theorem 3.8.2 is the following corollary.

Corollary 3.8.1 *The channel output r_ℓ in a time-selective Rayleigh fading channel is marginally Gaussian with zero-mean for any MPSK input distribution.*

3.8.1 Joint Distribution of the Output: Mathematical Analysis

In the previous section, we proved that each element x_ℓ of the vector $\mathbf{x}$ in (3.19) is zero-mean Gaussian. While joint Gaussianity implies marginal Gaussianity, the reverse is not necessarily true [152]. Therefore, $\mathbf{x}$ is not guaranteed to be multivariate Gaussian, although it is marginally Gaussian.

In the following, with the help of analytical arguments and numerical simulations we show that $\mathbf{x}$ is indeed jointly non-Gaussian and, hence, the output vector $\mathbf{r}$, which is the sum of independent non-Gaussian vector $\mathbf{x}$ and Gaussian vector $\mathbf{z}$, is non-Gaussian.

Firstly, we know that Gaussianity is preserved under invertible linear transformation [146]. Notice that if $\mathbf{S}$ were *known*, then $\mathbf{x} = \mathbf{Sh}$ would represent an invertible linear

transformation of the Gaussian random vector $\mathbf{h}$ and hence, would be jointly Gaussian. For example, in a pilot-aided data transmission scheme [153], $\mathbf{S}$ is known during the pilot transmission phase and the distribution of $\mathbf{x}$ and, hence, the output vector $\mathbf{r}$ in (3.1) is N-dimensional complex Gaussian. However, in the current scenario, $\mathbf{S}$ is the transmitted data, which is random and unknown. The product $\mathbf{Sh}$ therefore represents a linear and random non-invertible transformation. Thus, the output $\mathbf{r}$ can not be guaranteed to be Gaussian.

We construct the distribution of $\mathbf{r}$ using conditional distribution of $\mathbf{r}$ given $\mathbf{s}$. It can be noticed from (3.1) that the conditional distribution of $\mathbf{r}$ given $\mathbf{s}$, $f(\mathbf{r}|\mathbf{s})$, is $\mathcal{N}\left(\mathbf{0}, \mathbf{C}_{\mathbf{r}|\mathbf{s}}\right)$, where $\mathbf{C}_{\mathbf{r}|\mathbf{s}} = \mathbf{S}\mathbf{C}_{\mathbf{h}}\mathbf{S}^H + \boldsymbol{I}$ is the conditional covariance of $\mathbf{r}$ given $\mathbf{s}$. The distribution of $\mathbf{r}$, $f(\mathbf{r})$, is then given by

$$\begin{aligned} f(\mathbf{r}) &= \sum_{\mathbf{s}\in\chi^N} f(\mathbf{r}|\mathbf{s})\, p(\mathbf{s}), \\ &= \frac{1}{(M\pi)^N} \sum_{\mathbf{s}\in\chi^N} \frac{1}{|\mathbf{C}_{\mathbf{r}|\mathbf{s}}|} \exp\left[-\mathbf{r}^*\mathbf{C}_{\mathbf{r}|\mathbf{s}}^{-1}\mathbf{r}\right], \end{aligned} \tag{3.21}$$

where χ^N represents the N-dimensional probability space for $\mathbf{s}$, $p(\mathbf{s})$ is the probability mass function for discrete constant power input and M is the number of points in the MPSK constellation. Equiprobable i.i.d. MPSK inputs have been assumed to arrive at the second equality. Equation (3.21) shows that $f(\mathbf{r})$ is a summation of Gaussians and is, therefore, non-Gaussian. In the next subsection, we shall verify the non-Gaussianity of the output sequence with the help of numerical simulations.

3.8.2 Joint Distribution of the Output: Numerical Analysis

In order to prove that the output $\mathbf{r}$ is non-Gaussian, it is sufficient to show that $\mathbf{x}$ in (3.19) is non-Gaussian for $N = 2$. We proceed step-by-step as follows:

First, we generate a long sequence of channel fading process $\mathbf{h}$ according to the Clarke's model. This can be easily implemented using the L-th order autoregressive (AR) approximation of the process [154] with some high AR order such as $L = 500$. For notational simplicity, let us denote two consecutive channel realizations as h_1 and h_2. Since the fading process is marginally circularly symmetric complex Gaussian, the contour plot (2D-histogram) of $\Re(h_1)$ and $\Im(h_1)$ consists of concentric circles. This is not shown here for the sake of brevity. However, h_1 is correlated with h_2. Therefore, the contour plot of the joint distribution of $\Re(h_1)$ and $\Re(h_2)$ consists of concentric ellipses (the same statement applies to imaginary parts). Fig. 3.18 shows one such contour plot for a fading channel with the normalized Doppler frequency shift of $f_D T = 0.2$ and verifies the joint Gaussian distribution of $\Re(h_1)$ and $\Re(h_2)$. The number of samples

generated is $P = 10^6$ and the number of bins for each element is 62.

Second, we generate a long sequence of $\mathbf{x} = \mathbf{Sh}$ by multiplying $\mathbf{h}$ with i.i.d. realizations of input $\mathbf{S}$ from the MPSK constellation. For notational simplicity, let us denote two consecutive realizations of $\mathbf{s}$ as s_1 and s_2, given as follows

$$\mathbf{x}' = [x_1 x_2] = [\exp(i\theta_1)\, h_1 \;\; \exp(i\theta_2)\, h_2]^T. \tag{3.22}$$

Note that x_1 and x_2 are jointly Gaussian if and only if

$$\mathbf{x}'' = [\Re(\exp(i\theta_1)\; h_1) \;\; \Re(\exp(i\theta_2)\; h_2) \;\; \Im(\exp(i\theta_1)\; h_1) \;\; \Im(\exp(i\theta_2)\; h_2)]^T, \tag{3.23}$$

is jointly Gaussian [155]. Since any subset of a Gaussian vector is also jointly Gaussian, to prove that $\mathbf{x}''$ is not Gaussian, we only need to show that at least two elements of $\mathbf{x}''$ are jointly non-Gaussian. For example, it is sufficient to show that $\boldsymbol{w} = \left[\Re(e^{i\theta_1}\, h_1) \;\; \Re(e^{i\theta_2}\, h_2)\right]^T$ are jointly non-Gaussian.

Fig. 3.19 shows a contour plot of the joint distribution of $\boldsymbol{w}$ for $M = 2$ binary MPSK signaling and confirms its non-Gaussian joint distribution.

Fig. 3.20 shows a contour plot of the joint distribution of $\boldsymbol{w}$ for 16-PSK signaling. Compared with Fig. 3.20, the contour plot is somewhat more 'rounded'. Nevertheless, it is still not quite circular.

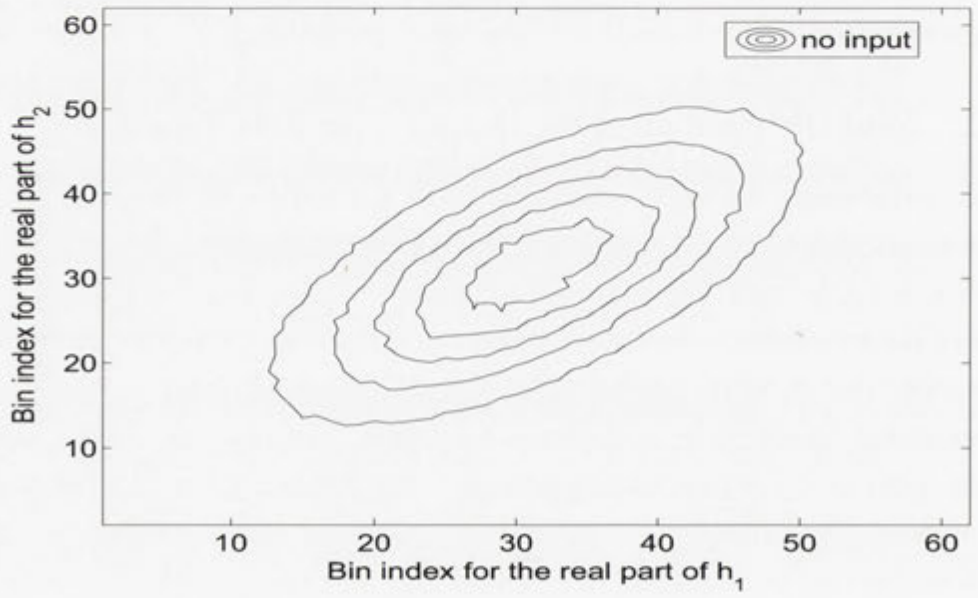

Figure 3.18: A contour plot of joint distribution of $\Re(h_1)$ and $\Re(h_2)$: $f_{\mathrm{D}} = 0.2$.

3.8.3 Implications of Non-Gaussianity of Channel Output on Information Rates

In Sections 3.8.1 and 3.8.2, we showed that a sequence of channel outputs of length N in response to MPSK signaling is jointly non-Gaussian. To see the consequence of this result on information rates, we first write an element of channel output covariance matrix at row k and column j as

$$[\mathbf{C_r}]_{k,j} = \mathbb{E}\left\{r_k r_j^*\right\} = \mathbb{E}\left\{h_k h_j^*\right\}\mathbb{E}\left\{s_k s_j^*\right\} + \delta_{k,j}, \tag{3.24}$$

which is a consequence of the independence between the input and channel processes. $\mathbb{E}\left\{h_{j+k}h_j^*\right\}$ was defined in (3.2). In (3.24), $\delta_{k,j} = 0$ for $j \neq k$. Therefore, we can upper bound the entropy rate of channel output sequence as follows

$$\begin{aligned}\frac{1}{N}h(\mathbf{r}) &< \frac{1}{N}\log\det(\pi e\mathbf{C_r}) \\ &\leq \frac{1}{N}\log\prod_{n=1}^{N}\pi e[\mathbf{C_r}]_{n,n} \\ &= \log(\rho+1),\end{aligned} \tag{3.25}$$

where $e = 2.718\cdots$, the first inequality holds because the entropy of any random vector is upper bounded by the entropy of a Gaussian random vector with the same covariance matrix. The second inequality follows from Hadamards inequality [156], with equality if and only if $[\mathbf{C_r}]_{k,j} = 0$, $k \neq j$, *i.e.*, if the input symbols are uncorrelated. The above procedure is correctly followed in [37]. We note from (3.24) that the output process becomes uncorrelated for i.i.d MPSK inputs, but since the output is not jointly Gaussian, one cannot conclude independence. The point of view of [90, 91] that i.i.d. constant power signaling *whitens* the channel process is not justified.

The mutual information rate $I(\mathbf{r};\mathbf{s})$ between the output $\mathbf{r}$ and the input $\mathbf{x}$ with no-CSI is given by

$$I(\mathbf{r};\mathbf{s}) = \frac{1}{N}(h(\mathbf{r}) - h(\mathbf{r}|\mathbf{s})). \tag{3.26}$$

Using (3.25), one can upper bound the information rate as

$$I(\mathbf{r};\mathbf{s}) < \log(\rho+1) - \frac{1}{N}h(\mathbf{r}|\mathbf{s}). \tag{3.27}$$

Therefore, the use of "capacity" in [90, 91] for the RHS of (3.27) is misleading and should be considered as a *strict upper bound* to the information rates achievable with M-

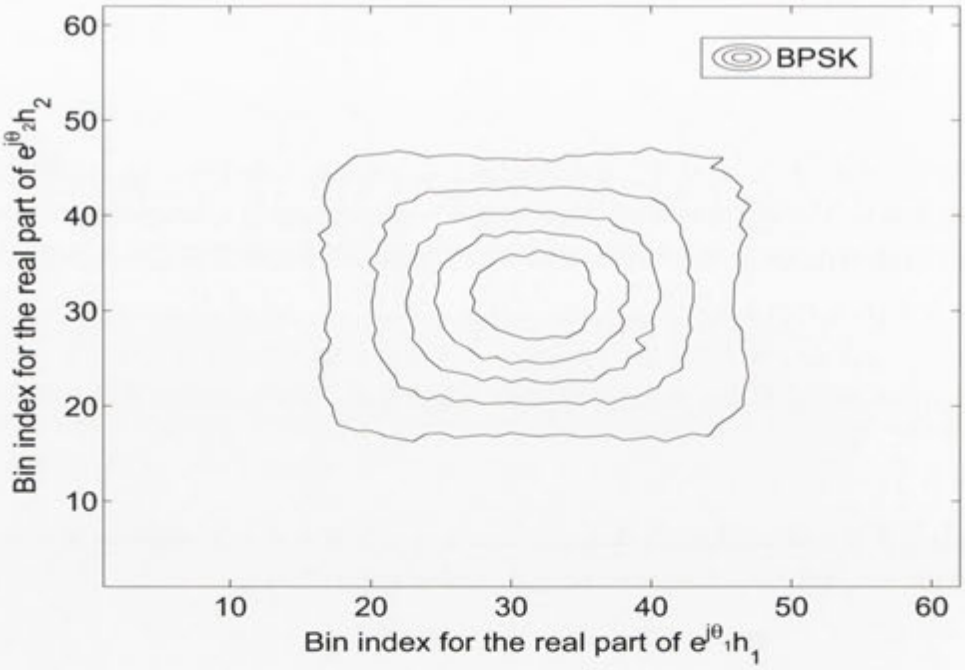

Figure 3.19: A contour plot of joint distribution of $\boldsymbol{w}$: BPSK signaling.

PSK signaling. Thus, we have shown, firstly, that the achievable rates derived in [90,91] for MPSK are an upper bound to the channel capacity. Secondly, the upper bound is strict in contrast to non-strict upper bound derived in [37].

It is reasonable to ask how tight the information rate upper bounds on the RHS of (3.27) are for practical MPSK schemes? We know trivially that $\log_2(M)$ bits per channel use is an upper bound for MPSK information rates. With this in mind, we compare (3.27) with the perfect CSI upper bound $I(\mathbf{r};\mathbf{s}|\mathbf{h}) = [h(\mathbf{r}|\mathbf{h}) - h(\mathbf{r}|\mathbf{s},\mathbf{h})]/N$. To compute the RHS of (3.27), we use a closed-form expression for $h(\mathbf{r}|\mathbf{s})/N$ provided in [37]. Fig. 3.21 shows two information upper bounds using (3.27) for normalized Doppler frequency shifts of $f_D T = 0.05$ and $f_D T = 0.2$. Relatively, we refer to the former as slow fading and the latter as fast fading. It is clear that for low MPSK dimensions (such as $M = 2$ or BPSK), (3.27) goes rapidly above the trivial upper bound of $\log_2(M) = 1$ bits per channel use. For slow fading channels, BPSK and 16-PSK CSI upper bounds provide tighter results for almost all SNRs. For the faster fading conditions, (3.27) provides relatively tighter bounds than the CSI upper bound for 16-PSK signaling for a wide range of SNR, but is still loose for BPSK signaling unless for very low SNR.

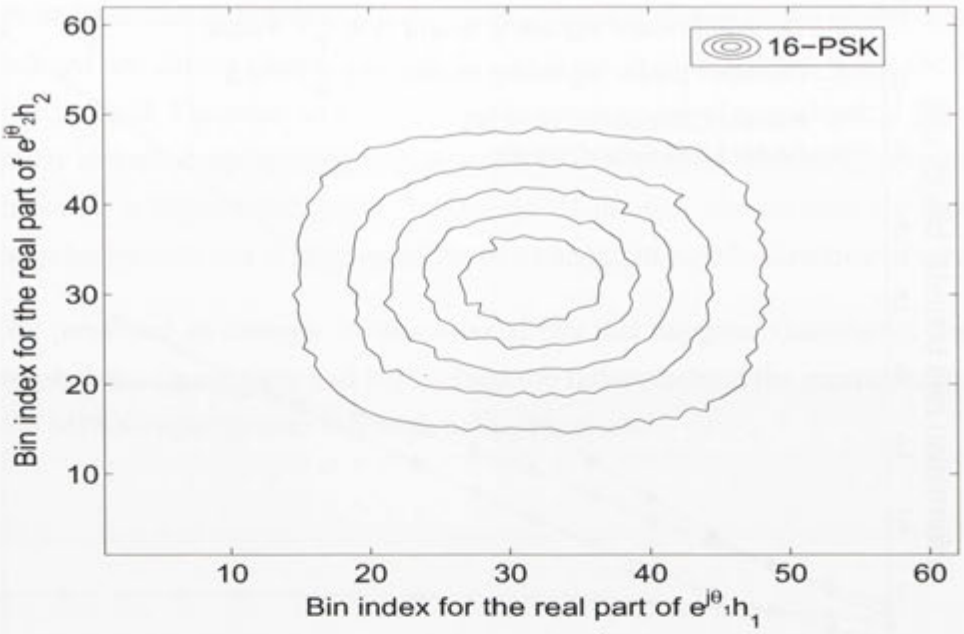

Figure 3.20: A contour plot of joint distribution of w: 16-PSK signaling.

3.9 Summary and Contributions

This chapter has investigated information rate penalty for unknown CSI and achievable rates for i.i.d. MPSK and Gaussian inputs over a noncoherent generalized time-selective Rayleigh fading channel. With the assumption of equal SNR for isotropic and non-isotropic scattering environments and an omnidirectional antenna at the receiver, the results suggested a significant reduction in information rate penalty for unknown CSI and gains in communication rates in a non-isotropic scattering scenario as compared to isotropic reception. We analyzed the impact of different parameters on information rate loss due to no-CSI and achievable rates. We also looked into the feasibility of a non-isotropic antenna in an isotropic environment taking into account the reduction in SNR due to the rejection of useful power by non-isotropic antenna. We compared common non-isotropic scattering environments using information rate penalty function, and explored the ways in which these distributions differ from the point of view of communication theory.

We investigated the statistical properties of the channel output in response to constant power signaling in Rayleigh fading channels. We showed that although the channel output at any given time is marginally Gaussian, a sequence of channel outputs are not jointly Gaussian. Therefore, one can only obtain upper bounds on the achievable information rates. We then compared these information rate upper bounds with the perfect CSI upper bound. The comparison showed that the obtained upper bounds from (3.27)

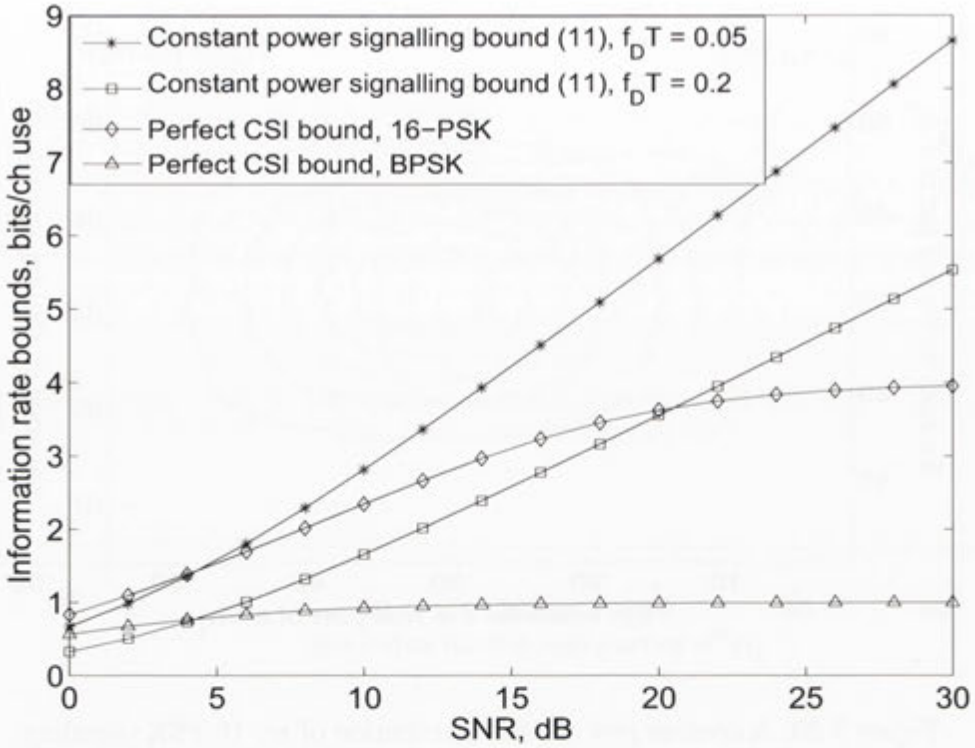

Figure 3.21: Comparison of information rate upper bounds.

become loose for high SNR and slow fading channels, especially for low-dimension MPSK signalling.

Some specific results of this chapter are as follows:

1. For infinite transmission block length, information rate loss due to unknown CSI in isotropic environment is an upper bound to the penalty in non-isotropic environments. For finite block lengths, however, a non-isotropic environment can have higher penalty than isotropic case.

2. Non-isotropicity gain is higher for small angular spreads and higher fading rates. In other words, communication in a non-isotropic environment offers gains over isotropic reception when both the mobility and the degree of non-isotropicity are high.

3. Non-isotropicity gain is more sensitive to a change in mobile direction of travel when normalized fading rates are higher and angular spread is moderate.

4. A non-isotropic antenna in isotropic environment outperforms isotropic antenna reception for high fading rates. For low fading rates, isotropic reception is much better than non-isotropic reception.

5. From information theoretic point of view, common non-isotropic scattering distributions are almost identical for small and large angular spreads when the fading rate is small. Gaussian and von Mises distributions are *almost* identical for all angular spreads keeping other parameters fixed. Moreover, truncated-isotropic distribution is significantly more "optimistic" than other distributions for moderate angular spreads and is more sensitive to a change in mobile direction of travel.

6. We presented an example of the classical fact that marginal Gaussianity does not imply joint Gaussianity and highlighted the fallacy behind the recent claim about the MPSK capacity over Rayleigh fading channels.

Chapter 4

Characterization of Rayleigh Fading Statistics with Constant Mobile Acceleration

4.1 Introduction and background

The Clarke's model of mobile radio reception and its generalization introduced in Chapter 2 are based on the assumptions of statistically homogeneous uncorrelated isotropically random scattering, independence between the magnitudes and phases of the arriving waves, uniform pdf of the distribution of AOA over $[-\pi, \pi]$ and constant mobile velocity. These assumptions gave rise to a zero-mean circularly symmetric WSS complex Gaussian fading process. Since the channel process is complex Gaussian, WSS implies strict sense stationarity of the channel process. The complex Gaussianity of the fading process implied that the zero-mean channel can be perfectly described by its autocorrelation (or, equivalently, its PSD). The stationarity of the complex Gaussian channel process imply that its autocorrelation (or PSD) is time-invariant. In this chapter, we retain all assumptions about the scattering and arriving waves but relax the assumption of constant mobile velocity allowing the mobile to have constant acceleration which corresponds better to the physical reality because a mobile user may experience changes in velocity caused by traffic lights or road conditions [66]. We seek to characterize the channel statistics under the assumption of constant mobile acceleration and its impact on the performance of communications systems.

4.1.1 Time-Varying Spectrum Due to Mobile Acceleration

For a fixed carrier frequency f_c, the Doppler spectrum of the channel fading process depends directly on the mobile velocity. In fact, we have the following relationship between a particular mobile velocity $\boldsymbol{v}$ and a particular Doppler frequency f_{d} present in the Doppler spectrum

$$f_{\mathrm{d}} = \frac{|\boldsymbol{v}|}{\lambda_c} \cos\,\gamma, \tag{4.1}$$

where $\lambda_c = c/f_c$ is the carrier wavelength (c is the speed of light), and γ is the angle between the scattering angle and the unit vector $\widehat{\boldsymbol{v}}$ (pointing in the direction of mobile movement). The maximum Doppler frequency, $f_d^{\max} = |\boldsymbol{v}|/\lambda_c$ corresponds to the wave impinging on the mobile receiver head-on. When the mobile receiver has constant acceleration α, the velocity of the mobile changes continuously with time. If, for example, $\boldsymbol{v}'$ denotes the mobile velocity at some time t', the velocity of the mobile at time $t > t'$ is given by

$$\boldsymbol{v}(t) = \boldsymbol{v}' + \alpha\,(t - t'). \tag{4.2}$$

The time-varying velocity would imply a time-varying PSD and, hence, autocorrelation. Equivalently, the channel would become a *non-stationary* complex process as a result of mobile acceleration and the estimation of the spectral contents of the non-stationary fading process based on stationarity assumption would be inaccurate [157–159].

4.1.2 Time-Varying Channel Coherence Time

The channel coherence, T_c, is an important design parameter in communication system design. It is a function of the maximum Doppler frequency (Doppler spread) in the channel Doppler spectrum and can qualitatively be considered as the time over which the channel fading process is highly correlated. Mathematically, as a rule of thumb [160]

$$T_c = \frac{0.423}{f_d}, \tag{4.3}$$

where f_d is the maximum Doppler frequency in the channel frequency response. Equation (4.3) gives T_c in units of time whereas T_c is given in terms of number of symbols as

$$T_c = \frac{0.423}{f_D}, \tag{4.4}$$

where f_D is the maximum Doppler frequency normalized by the symbol rate T_s, *i.e.*,

$$f_D = f_d T_s. \tag{4.5}$$

For a wide-sense stationary fading process, T_c is time-invariant and a fixed transmission scheme can be designed to maintain a constant *average* information transfer rate. For an accelerating mobile, on the other hand, T_c becomes time-variant as a result of time-variant Doppler spread and the instantaneous normalized fading rate is given as

$$f_D(t) = f_d(t)\, T_s. \tag{4.6}$$

4.1.3 A Brief Background on Non-Stationary Modeling

A non-stationary model was introduced in [161] which is, in fact, a 2-state model for land mobile satellite channels. This model can be generalized to an M-state model where each state is represented by a specific stationary process, *i.e.*, a non-stationary process can equivalently be represented by M stationary processes [162]. The impact of non-stationarity on the achievable rates over mobile Rayleigh fading channels has been considered in [163]. One part of this work addresses the problem of the instantaneous *mean* channel capacity of the frequency-selective channel at a fixed time with channel frequency response perfectly known, first, at the receiver and the transmitter and, then, at the receiver only. In the second part, an imperfect channel estimation is considered and assuming the estimation error to be additive Gaussian, capacity lower and upper bounds are shown for Global System for Mobile communications (GSM) in a hilly mobile environment. Though not explicitly stated, the plots suggest that a band of channel frequency spectrum where the frequency response is flat is considered. In other words, the capacity bounds with channel estimation errors correspond to frequency flat time-selective Rayleigh fading channels where the channel fading is implicitly assumed to be block-fading[1]. In other words, the channel gain is assumed to stay constant for the duration of the block of 142 symbols in a GSM time slot.

Recently, the impact of constant mobile acceleration has been discussed in [165] in relation to correlation based speed estimation for indoor positioning where the constant mobile acceleration introduced errors in speed estimation. The impact of mobile acceler-

[1]So far in this thesis we have assumed that the channel is time-selective and fades continuously. The block-fading model which assumes the channel gain to be *constant* over a block of transmitted symbols is a simplified version of the more general time-selective model. Let T_c denote the coherence time of the channel, *i.e.*, the time over which the channel fading is highly correlated, L_f be the length of the data frame transmitted and N_b be the number of coherence blocks in the data frame, *i.e.*, $N_b = L_f/T_c$. Now if $T_c = 1$, the channel is fast-fading (fully-interleaved). If $1 < T_c = L_f/N_b$, the channel is block-fading. And if $T_c = L_f$, the channel is said to be quasi-static [164].

ation on linear prediction (and subsequent equalization) of the envelope of frequency-flat complex Gaussian fading was investigated in [166]. The constant mobile acceleration was shown to have an impact on the choice of the adaptive prediction algorithm. For example, the linear prediction based on windowed recursive least squares (WRLS) algorithm performed better than the recursive least squares (RLS) algorithm for a mobile with constant acceleration.

To the best of our knowledge, the wireless channel statistics and the performance of a cellular wireless mobile communication system with accelerating (or decelerating) mobile receiver have not been analyzed in the literature as yet perhaps because, as we shall see in this chapter, the state-of-the-art wireless communication systems operate at frequencies of the order of 2 GHz and have sufficiently short transmission frame lengths. In such cases, the impact of mobile acceleration on the estimation of parameters of interest such as channel gain and maximum Doppler frequency, is not significant over the duration of the frame and can be ignored without significantly losing accuracy for all practical acceleration possibilities for mobile speeds as high as $\approx$ 200 Km/hr. At this point it should be emphasized that, unlike state-of-the-art cellular communication systems, peer-to-peer *ad hoc* networks (where the mobiles can communicate with each other like Motorola Talkabout Family Radio Service (FRS) and IEEE 802.11 wireless local area network (WLAN) mobile units [167], can act as routers and can share resources among them) are significantly affected by mobile speed and acceleration [66]. The reason for increased mobility impact on the *network performance* is due to the fact that, in addition to channel and Doppler estimation, network and application *protocols* are sensitive to route discovery and maintenance, which are strongly sensitive to mobility patterns. This is so because, in an *ad hoc* network, the participants move so that the network may not rely on static (or slowly changing) routing protocols to deliver information and must, therefore, adapt to changing connectivity. Moreover, mobility impacts the design of strategies for location updating and paging, quality-of-service (QoS), radio resource management (*e.g.*, dynamic channel allocation schemes), technical network planning and design (*e.g.*, cell and location area layout, network dimensioning). These sensitivities affect the performance of the network as a whole, and affect the ability to accomplish the mission assigned to a specific participant [67].

The future wireless communication systems, *e.g.*, cellular like mobile WiMax are expected to operate at much higher carrier frequencies[2] and would accommodate high mobility where the impact of mobile acceleration could not be ignorable. Therefore, it is of some interest to develop a framework to determine the impact of mobile acceleration

[2]The use of 62 GHz for future cellular communication with mobility has been suggested in [168] and experimental analysis of the propagation at this frequency has been reported in [169].

on the performance of wireless cellular communication systems which is the subject of this chapter.

This chapter is organized as follows. The Section 4.2 describes the channel model and communications scenario that we look into, and specifies different assumptions about various parameters involved. The instantaneous channel autocorrelation and corresponding PSD for continuous-time channel process are derived in the Section 4.3. The discretization of the non-stationary channel process is discussed in Section 4.4. The well known Wigner-Ville and instantaneous power spectra are derived for the non-stationary channel assuming infinite sampling rate and unbounded mobile velocity in Section 4.5. The implications of the assumption of bounded mobile velocity and finite sampling rate are discussed in Section 4.6. The impact of mobile acceleration on the design of the future mobile communication systems is discussed with numerical results in Section 4.7. Finally, the chapter summary and contributions are described in Section 4.8.

4.2 Problem Statement And Continuous-Time Channel Model

We consider a mobile communications scenario in which the transmitter is stationary while, at time t, the receiver equipped with an omni-directional antenna moving with initial velocity $\boldsymbol{v}$ and constant acceleration[3] α at angle ψ with respect to x-axis in a 2D scattering environment (Fig. 4.1). While mobile acceleration is normally assumed to be zero for mobile radio characterization, our intention here is to explore the impact of constant mobile acceleration on channel statistics.

We consider the baseband equivalent form of the I/O relationship defined in (2.1) with additional superscript 'ns' to denote non-stationarity

$$r(t) = \sqrt{\rho}\, h_c^{ns}(t)\, s(t) + z(t) \quad -\infty < t < \infty. \tag{4.7}$$

Assume that the accelerating mobile moving with initial velocity $\boldsymbol{v}_0$ is at some arbitrary origin 'O' at $t = 0$. The continuous-time non-stationary channel process $h_c^{ns}(t)$

$$h_c^{ns}(t) = \oint \psi(\beta) \exp\left(i\eta t\, \boldsymbol{v}(t) \cdot \widehat{\boldsymbol{\beta}}\right) d\beta, \tag{4.8}$$

where $\boldsymbol{v}(t)$ is the instantaneous velocity and η is the plane wave phase constant. We retain the assumptions underlying the circularly complex Gaussianity of the channel

[3]We assume that the mobile acceleration is aligned with velocity. The term 'acceleration' may, therefore, be interpreted as the magnitude of the acceleration.

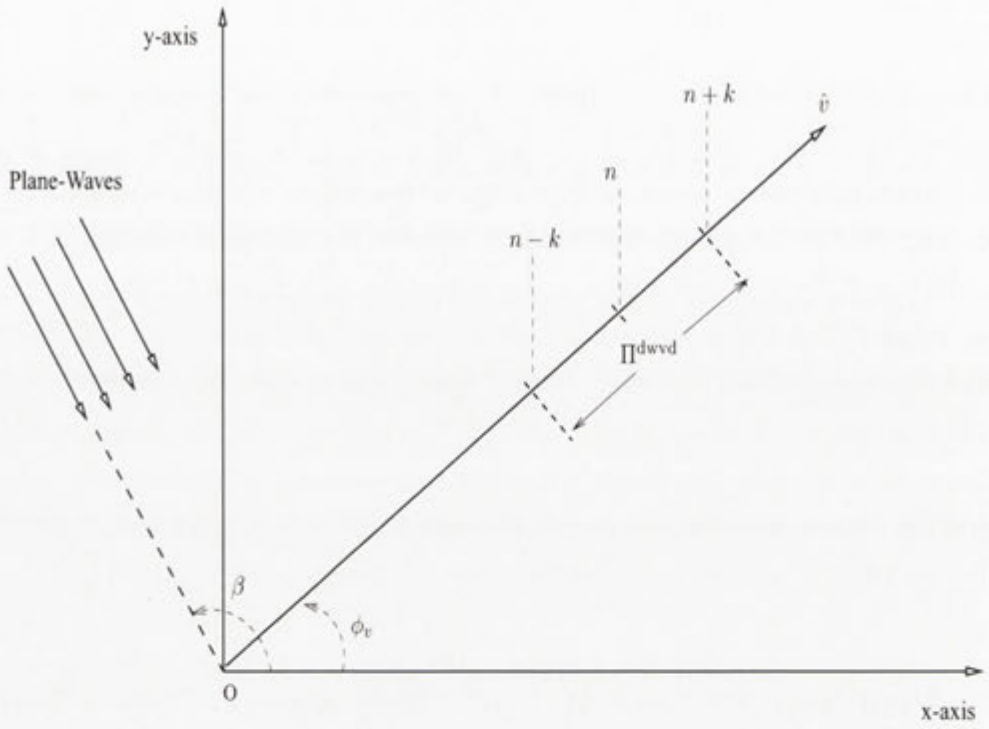

Figure 4.1: The mobile is moving at an angle ϕ_v with respect to x-axis with initial speed $|\boldsymbol{v}_0|$ and constant acceleration α in the direction of movement. A plane wave is shown incident on the receive antenna at an angle β and Π^{dwvd} defined in (4.69) is also depicted.

process so that the channel process at any arbitrary time t is circular complex Gaussian.

4.2.1 Types of Non-Stationary Gaussian Channel Processes

The Gaussianity of the channel process allows us to restrict our analysis of the impact of acceleration on the first two moments of the channel process, *i.e.*, the mean and the autocorrelation because a Gaussian process is completely characterized by its first two moments. Various types of non-stationarities in the Gaussian channel process are possible depending on whether mean, variance and/or covariance is time dependent. Usually, a sample record of a *composite* non-stationary continuous-time Gaussian channel process $h_{\text{c}}^{ns}(t)$ can be written as

$$h_{\text{c}}^{ns}(t) = A(t) + B(t)h_{\text{c}}^{s}(t), \tag{4.9}$$

where $A(t)$ and $B(t)$ are deterministic (or random) functions of time and $\left\{h_{\text{c}}^{s}(t)\right\}$ is a sample record from unit-variance zero-mean stationary random channel process which corresponds to a mobile moving with constant velocity (and zero acceleration) in rich

scattering environment. The different possibilities of non-stationarity in the Gaussian channel process $h_c^{ns}(t)$ can be classified as follows:

- If $B(t) = 1$, we can rewrite (4.9) as

$$h_c^{ns}(t) = A(t) + h_c^s(t), \tag{4.10}$$

which implies that for every t, a constant is added to the zero mean unit variance stationary process $h_c^s(t)$ so that

$$\mathbb{E}\left\{h_c^{ns}(t)\right\} = A(t), \tag{4.11}$$

implies that the mean of the channel process is time-varying and, hence, non-stationary. Because the variance and covariance of the random process are independent of the mean, $h(t)$ in (4.10) has stationary (*i.e.*, time-invariant) variance and covariance. Thus the channel process has non-stationary mean when $B(t) = 1$

- If $A(t) = 0$, equation (4.9) becomes

$$h_c^{ns}(t) = B(t)h_c^s(t), \tag{4.12}$$

which implies that for every t, if $B(t)$ is assumed to be deterministic, a time-dependent constant is multiplied with $h_c^s(t)$. Observe that

$$\mathbb{E}\left\{h_c^{ns}(t)\right\} = 0, \tag{4.13}$$

implying that the mean of the channel process $h(t)$ is zero and stationary. We know that multiplying a random variable by a constant increases the variance by the square of the constant, and the covariance of two random variables increases by the product of the two constants (if each random variable is multiplied by a different constant) [170]. Therefore, using (4.12) the variance and covariance of $h(t)$ are given respectively as

$$\mathbb{E}\left\{|h_c^{ns}(t)|^2\right\} = B^2(t)\mathbb{E}\left\{|h'(t)|^2\right\}, \tag{4.14}$$

$$\mathbb{E}\left\{h_c^{ns}(t_1)h_c^{*ns}(t_2)\right\} = B(t_1)B(t_2)\,\mathbb{E}\left\{h_c^s(t)h_c^{*s}(t-\tau)\right\}, \tag{4.15}$$

which imply that the random process has non-stationary variance and covariance.

- If $A(t), B(t)$ are deterministic and positive, in the light of above discussion, we can infer that the Gaussian process would have non-stationary mean, variance and covariance.

- If $B(t) = 1$ and $A(t)$ is random with time-varying mean and/or variance and covariance, the overall process $h_c^{ns}(t)$ shall have non-stationary mean and/or variance and covariance.

4.2.2 Is Non-Stationarity Due to Mobile Acceleration Separable from Stationary Statistics?

Firstly, we have to see what type of non-stationarity is caused by the mobile motion with constant acceleration. The assumptions of statistical homogeneity of the scattering environment and uniform distribution of AOA of arriving waves over $[-\pi, \pi]$ ensure that the non-stationary complex Gaussian channel process is zero-mean and has time-invariant variance. The mobile acceleration causes the mobile velocity to continuously change which implies a time varying autocorrelation function and PSD. Therefore, an accelerating mobile in sufficiently rich scattering environment results in a complex Gaussian channel process which has stationary mean and non-stationary covariance[4]. In the following we discuss if the non-stationary introduced due to the mobile acceleration is separable from stationary statistics.

Look at (4.9). A complex Gaussian process with stationary mean and variance but non-stationary covariance *may be* constructed if we assume that $A(t) = 0$ and $B(t)$ is a unit variance, not necessarily zero-mean, random rather than deterministic[5] function of time. Mathematically,

$$h_c^{ns}(t) = B(t)\, h_c^{s}(t), \tag{4.16}$$

This separability would allow us to write the autocorrelation of the composite process $h_c(t)$ as the product of individual autocorrelation functions of $B(t)$ and $h_c^s(t)$. However, the separability would be useful only if we know the covariances of individual component processes.

We know from the classical probability theory that the sum of two independent Gaussian random variables is Gaussian but the product of two (correlated or independent) random variables is non-Gaussian. Particulary, when the Gaussian random variables are zero-mean, the pdf of their product is a modified Bessel function of the second kind [172]. Therefore, since we have assumed $h_c^s(t)$ to be a zero-mean unit variance complex process, $B(t)$ obviously can not be Gaussian if $h_c(t)$ has to be Gaussian (again by assumption). While the product of a Gaussian random variable with a constant is

[4]Precisely speaking, the channel under consideration turns out to be a particular case of a *non-WSS* US channel [171].

[5]Assumption of deterministic $B(t)$ would result in a composite process with non-stationary variance (Eq. (4.9)) and will, therefore, be in contradiction with our assumption of homogeneous scattering.

Gaussian, we argue that the same is not true for the multiplication of a Gaussian random variable either by another dependent or independent non-Gaussian random variable. For any time $t = t_0$, equation (4.16) can be reduced to multiplication of a Gaussian random variable, *i.e.*, $h_c^s(t_0)$, by a constant *if and only if* $B(t_0)$ is known which is not the case. We therefore can assume the channel process $h_c(t)$ to be complex Gaussian as a whole which implies that the non-stationary and stationary channel statistics are not separable. Notice that the statistics of $B(t)$, in general, would be dictated by the mobile acceleration in addition to other transmission parameters, *e.g.*, the carrier frequency. We shall have more comments regarding the inseparability of stationary and non-stationary statistics in Section 4.5.2.

4.3 Joint Time-Frequency Analysis

Unlike stationary signals (and random processes), the structure of the non-stationary signals (and random processes), *e.g.*, a time-varying chirp signal, EEG signal, a wireless channel etc. is time-variant. The spectral contents of such time-varying signals change with time. The classical Fourier transform works well for the estimation of the spectral contents of the stationary processes because timing information is not important for such processes. However, for non-stationary signals and processes with time-varying spectrum, the timing information is very important for the analysis to be useful. The classical Fourier transform, therefore, fails for non-stationary signals and processes with time-dependent spectrum as was recognized by D. Gabor [173] who introduced the concept of time-frequency (TF) representation of the spectrum of non-stationary signals. However, TF representation of non-stationary signals (and processes) is not unique and, in fact, the number of valid[6] spectral representations is infinite which implies that one has a certain degree of freedom in non-stationary spectrum analysis. The joint TF representations are either parametric or non-parametric. We here assume the perfect knowledge of the parameters (*e.g.*, mean, variance, autocorrelation etc.) of the Gaussian channel process so that our approach is inherently parametric. The TF representations can be broadly classified into linear and quadratic distributions. In the following, we briefly describe a member of the linear TF distributions and then different quadratic TF distributions (relevant to our work) grouped into a single class, the Cohen's class [174].

[6] A spectral distribution is valid if it can be used to generate the signal or a random process.

4.3.1 Short-Time Fourier Transform (STFT)

The STFT is a linear technique that simply selects a segment of the data centered around the analysis time t, assumes data to be stationary over the selected segment and applies the classical Fourier transform to give a short-time Fourier transform of the signal $s(t)$. Mathematically, STFT is given in continuous form as

$$\text{STFT}\,(t,f) = \int_{-\infty}^{\infty} s(t)\, w(t-\tau) e^{-i2\pi f\tau} d\tau, \tag{4.17}$$

where $w(\cdot)$ is the window function used to select the length of the data segment to be Fourier transformed. The square of the absolute value of STFT is called spectrogram (a member of the Cohen's class of quadratic distributions discussed later), $\text{SPEC}\,(t,f)$, *i.e.*,

$$\text{SPEC}\,(t,f) = |\text{STFT}\,(t,f)|^2, \tag{4.18}$$

implying that the spectrogram gives the distribution of signal energy in the TF plane. Even though STFT and spectrogram are widely used due to their simplicity, they suffer from the so-called window effect, *i.e.*, the time and frequency resolutions of STFT and, the resulting, spectrogram are dictated by the Hiesenberg-Gabor uncertainty principle [173, 175] which states

$$\Delta t_w \Delta f_w \geq \frac{1}{4\pi}, \tag{4.19}$$

where Δt_w and Δf_w respectively are the average duration and average bandwidth of the analysis window. Equation (4.19) implies that it is not possible to simultaneously achieve very good time and frequency resolutions and, therefore, the window characteristics must be chosen taking into account the signal structure and the impact of time-variation on its components.

4.3.2 Cohen's Class Distribution Functions

In [176], Cohen formulated a generalized quadratic TF representation to give energy distribution of the non-stationary signal in TF plane. Most of the time-dependent spectra are a special case of the this class [157]. While there is no precise definition for the Cohen's class of distribution functions, it is usually defined as a set of all bilinear TF representations which are covariant under time and frequency translations. In general, the Cohen's class can be considered as a 2D filtering of the Wigner-Ville distribution (WVD) [68] (to be discussed later). Therefore, the cross-term interference which is

characteristic of WVD (and other quadratic TF representations) is less in Cohen's class distributions as compared to WVD due to the averaging. Mathematically, Cohen's class distribution function is given as

$$C_h(t,f) = \int_{-\infty}^{\infty}\int_{-\infty}^{\infty} \mathcal{A}_h(\varrho,\tau)\mathcal{K}(\varrho,\tau)\exp\left(i2\pi(\varrho t - \tau f)\right)\, d\varrho\, d\tau, \tag{4.20}$$

where $\mathcal{A}_h(\varrho,\tau)$ is the well-known ambiguity function (AF) defined as the following Fourier transform

$$\mathcal{A}_h(\varrho,\tau) = \int_{-\infty}^{\infty} \Phi_h(t,\tau)\exp\left(-i2\pi t\varrho\right) dt. \tag{4.21}$$

where $\Phi_h(t,\tau)$ is the instantaneous one-sample autocorrelation function and $\mathcal{K}(\varrho,\tau)$ is the kernel function which controls the characteristics of a particular distribution function of the Cohen's class.

A Correlation Approach to Quadratic TF Representations

A method called *Correlation Approach to TF Representations* (CATFRs) was put forward in [177] to explain various quadratic TF distributions based on the intuitive idea of non-stationary correlation. In view of the fact that the only non-stationarity in the Gaussian fading process under consideration is in the autocorrelation, CATFR provides a unified framework to analyze different TF representations of the non-stationary Gaussian channel process. For that purpose, we define a general instantaneous *temporal* ACF[7] of the channel process, $\Phi_h^g(t_1,t_2)$, as [177]

$$\Phi_h^g(t_1,t_2) = \mathbb{E}\left\{h(t_1)h^*(t_2)\right\}, \tag{4.22}$$

where the expectation is over the ensemble of the channel process. The corresponding TF energy distribution (TFED), $\mathcal{E}(t,f)$, is given as

$$\mathcal{E}(t,f) = \int_{-\infty}^{\infty} \Phi_h^g(t,\tau)\exp\left(-i2\pi f\tau\right) d\tau. \tag{4.23}$$

Notice the change of variables from t_1, t_2 in (4.22) to t, τ in (4.23). This change of

[7]Notice that we have emphasized that the ACF is *temporal*. The same ACF has been termed as *time-frequency* ACF (TFACF) in [177] which is inaccurate in view of the fact that we are considering samples of the channel process itself at two different times. The TFACF must have implied the multiplication of a sample of the channel process (at some time) and the magnitude of a particular frequency in its spectrum (at some other time). In fact, TFACF is commonly known as the ambiguity function, AF (Eq. (4.21)).

variables is governed by the following set of transformations, not necessarily linear [177]

$$\begin{aligned} t &= g_1(t_1, t_2) & t_1 &= g_3(t, \tau) \\ & \Longleftrightarrow & & \\ \tau &= g_2(t_1, t_2) & t_2 &= g_4(t, \tau) \end{aligned} \tag{4.24}$$

A TFED is said to satisfy marginals if the integration over all time t gives the signal energy density at frequency f, integration over all frequencies results in the signal's energy density at time t, and the integration of TFED over all time and frequencies gives the total energy Ξ_h of the process. Mathematically, [69]

$$\int_{-\infty}^{\infty} \mathcal{E}(t, f)\, dt = |H(f)|^2, \tag{4.25}$$

$$\int_{-\infty}^{\infty} \mathcal{E}(t, f)\, df = |h(t)|^2, \tag{4.26}$$

$$\frac{1}{2}\int_{-\infty}^{\infty} \mathcal{E}(t, f)\, dt\, df = \Xi_h, \tag{4.27}$$

where $H(f)$ is the Fourier transform of TFED at time t.

Remarks: It can also be observed that the ensemble averaging in (4.22) is equivalent to smoothing operation. This smoothing is possible only if the statistics of the channel process are known *a priori* which is what we assumed at the outset. However, as we shall see later, most of the proposed spectral estimation techniques to estimate the spectrum are based on only one sample of instantaneous ACF (or, equivalently, a single realization of the random process) which is the main reason behind very noisy spectral estimates [177]. Following are some important member distributions in the Cohen's class derived on the basis of CATFR.

Wigner-Ville Distribution (WVD)

The WVD (a special case of Cohen's class with $\mathcal{K}(\varrho, \tau) = 1$) is one of the most widely used TF methods [68]. This approach was developed by Wigner [178] in 1932 for use in Physics. Later Ville [179] introduced this technique to signal processing community in 1948. The classical method of determining the spectral contents of a random process is based on the well-known Wiener Khintchine theorem, *i.e.*, the spectrum of a random process equals the Fourier transform of the classical ACF which is a function of the lag variable, τ, only. The classical ACF is time-invariant because the time is integrated out of the result. The WVD is based on a variation of the classical ACF so that it retains time variable in the result. Such ACF is termed as *instantaneous* ACF, $\Phi_s^{wvd}(t, \tau)$ (assuming

a deterministic signal $s(t)$) given as

$$\Phi_s^{wvd}(t,\tau) = s\left(t+\frac{\tau}{2}\right) s^*\left(t-\frac{\tau}{2}\right), \tag{4.28}$$

which can be obtained from (4.24) through the following variable transformation

$$\begin{aligned} t &= \frac{t_1+t_2}{2} & t_1 &= t+\tau/2 \\ & \Longleftrightarrow & & \\ \tau &= t_1-t_2 & t_2 &= t-\tau/2 \end{aligned} \tag{4.29}$$

and corresponding TFED called WVD is then defined as

$$\begin{aligned} \mathcal{E}^{wvd}(t,f) &= \mathrm{WVD}\,(t,f), \\ &= \int_{-\infty}^{\infty} \Phi_s^{wvd}(t,\tau)\, \exp\left(-i2\pi f\tau\right) d\tau. \end{aligned} \tag{4.30}$$

Observe that the AF is the Fourier transform of the ACF with respect to t while WVD is the Fourier transform of ACF with respect to τ (Eqs. (4.21) and (4.30)). The WVD is, in fact, a distribution of the *mean instantaneous power* versus frequency, or equivalently, a distribution of the *mean energy* in the joint TF plane [159]. The WVD satisfies marginals but can be negative. However, the Gaussian smoothing implemented by convolving a Gaussian function with instantaneous ACF in (4.28), can ensure that it is always positive. Importantly, the smoothing makes WVD identical to a spectrogram [180] with reduced cross-term interference when multiple components are present in the signal, *e.g.*, a mobile radio signal. The smoothing operation in time results in a *smoothed* WVD, the smoothing in frequency results in *pseudo*-WVD and the smoothing in both time and frequency would result in *smoothed pseudo*-WVD [181, 182].

Equation (4.30) is valid for deterministic signal $s(t)$ (or a random process with only a single realization). Since we are dealing with a random channel process, we need to have a definition of WVD for random process with known statistics. The WVD for the random channel process $h_c^{ns}(t)$ is defined as the expectation of WVD (t,f) (Eq. (4.30)) over all possible realizations implied by the assumed channel statistics, *i.e.*,

$$\begin{aligned} \mathrm{WVD}\,(t,f) &= \mathbb{E}\left\{\int_{-\infty}^{\infty} \Phi_h^{wvd}(t,\tau)\, \exp\left(-i2\pi f\tau\right) d\tau\right\}, \\ &= \int_{-\infty}^{\infty} \mathbb{E}\left\{\Phi_h^{wvd}(t,\tau)\right\} \exp\left(-2\pi f\tau\right) d\tau, \end{aligned} \tag{4.31}$$

where $\mathbb{E}\left\{\Phi_h^{wvd}(t,\tau)\right\}$ represents the *average instantaneous* ACF for WVD. The inter-

change of the expectation and the integral in (4.31) is justified if the integral exists in the mean-square sense for which a necessary and sufficient condition is [183]

$$\int_{-\infty}^{\infty}\int_{-\infty}^{\infty} \mathbb{E}\left\{q_h(t,\tau_2)q_h^*(t,\tau_2)\right\}\, e^{-i2\pi f(\tau_1-\tau_2)} d\tau_1\, d\tau_2 < \infty. \tag{4.32}$$

Rihaczek Distribution

While most member energy distributions of the Cohen's class are real-valued, Rihaczek distribution, $\mathrm{RCK}(t,f)$, is a complex energy distribution [184] obtained from Cohen's class by setting $\mathcal{K}(\varrho,\tau) = \exp(-i\pi\tau\varrho)$. The real valued energy distributions describe the energy concentration in TF plane but do not carry any information about the phase of the deterministic (or random) signal which is exactly what Rihaczek distribution does. This distribution can be obtained from TFED by using the following variable transformation (Eq. (4.24))

$$\begin{array}{ccc} t = t_1 & & t_1 = t \\ & \Longleftrightarrow & \\ \tau = t_1 - t_2 & & t_2 = t - \tau \end{array} \tag{4.33}$$

for a deterministic signal $s(t)$ as follows (Eq. (4.23))

$$\mathrm{RCK}(t,f) = \int_{-\infty}^{\infty} s(t)s^*(t-\tau)\, \exp\left(-2\pi f\tau\right) d\tau, \tag{4.34}$$

$$= \int_{-\infty}^{\infty} \Phi_s^{rck}(t,\tau)\, \exp\left(-2\pi f\tau\right) d\tau, \tag{4.35}$$

$$= s(t)S^*(\omega)\, \exp\left(-2\pi ft\right), \tag{4.36}$$

where $\Phi_h^{rck}(t,\tau)$ is the unsymmetrical instantaneous ACF and $S(\omega)$ is the Fourier transform of $s(t)$. Equations (4.34)–(4.36) are different forms of the complex-valued Rihaczek distribution [22]. Notice that the Rihaczek distribution is essentially AF except that the latter is defined for the complex envelope of real signal $s(t)$ [184]. The Rihaczek distribution also turns out to be the complex conjugate of Levin's "complex instantaneous autocorrelation function" [70]. It satisfies the marginals (Eqs. (4.25)-(4.27)) and is useful to determine the phase coherence between two signals [185].

The Rihaczek distribution $\mathrm{RCK}^r(t,f)$ for the random (channel) process is defined in a manner similar to WVD, *i.e.*,

$$\mathrm{RCK}^r\left(t,f\right) = \mathbb{E}\left\{\mathrm{RCK}(t,f)\right\},$$

$$= \int_{-\infty}^{\infty} \mathbb{E}\left\{\Phi_h^{rck}(t,\tau)\right\} \exp\left(-2\pi f\tau\right) d\tau, \tag{4.37}$$

Instantaneous Power Spectrum (IPS)

The idea IPS was put forth by Page [69] as the rate of increase of the total energy (expended till any time t disregarding the future behavior of the *real* signal $s(t)$). Let IPS as defined by Page be denoted as $\mathrm{IPS}^{-}(t,f)$. Mathematically,

$$\begin{aligned}\mathrm{IPS}^{-}(t,f) &= \int_{-\infty}^{\infty} \mathcal{E}(t,f)\, df, \\ &= 2\,\Re\left\{\int_{-\infty}^{0} s(t)s(t+\tau)\, \exp\left(-2\pi f\tau\right)\, d\tau\right\},\end{aligned} \tag{4.38}$$

where $\Re\{\cdot\}$ is the real part operator. Equation (4.38) is a result of a change of variables (different from but equivalent to the one adopted in [69]). Notice that equation (4.38) is always positive as it should be to be a 'true' power spectrum [69].

Levin [70] disregarded the past values of $s(t)$ and derived an alternate IPS (also known as Levin's distribution[8] [180]) by considering only the future values of $s(t)$, *i.e.*,

$$\mathrm{IPS}^{+}(t,f) = 2\,\Re\left\{s(t)\, e^{i2\pi ft} \int_{t}^{\infty} s(x)\, \exp\left(-2\pi fx\right)\, dx\right\}, \tag{4.39}$$

$$= 2\,\Re\left\{\int_{0}^{\infty} s(t)\, s(t+\tau)\, \exp\left(-i2\pi f\tau\right) d\tau\right\}, \tag{4.40}$$

where (4.40) is a result of a simple change of variable approach similar to [69] that produced (4.38). Levin defined another IPS, $\mathrm{IPS}(t,f)$, by taking the average of two instantaneous power spectra defined earlier as follows

$$\begin{aligned}\mathrm{IPS}\,(t,f) &= \frac{1}{2}\left\{\mathrm{IPS}^{-}(t,f) + \mathrm{IPS}^{+}(t,f)\right\}, \\ &= \Re\left\{\int_{-\infty}^{\infty} s(t)\, s(t+\tau)\, \exp\left(-i\omega\tau\right)\right\}, \qquad (4.41) \\ &= \Re\Big(s(t)\, \exp\left(i2\pi ft\right)\, \mathrm{S}(\omega)\Big), \qquad (4.42)\end{aligned}$$

where we utilized (4.38) and (4.40) to arrive at (4.41). Equation (4.42) is a result of the application of time-shifting property of the Fourier transform [186]. Interestingly, $\mathrm{IPS}\,(t,f)$ turns out to be the real part of the Rihaczek distribution which allows us to imagine IPS as being the energy expended, till time t, by an ideal bandpass filter centered at the frequency f [187]. Notice that even though $\mathcal{E}(t,f)$ can be negative, its integral over all frequencies is always positive real implying that $\mathrm{IPS} > 0$. Moreover, like other

[8]The kernel function of the Levin's distribution in (4.20) is $\mathcal{K}\,(\varrho,\tau) = \exp(-i\pi|\tau|\varrho)$.

members of the Cohen's class, IPS also satisfies the marginals.

Making use of CATFR and *a priori* knowledge of the statistics of random channel process $h_c^{ns}(t)$, we can explicitly perform the ensemble averaging on (4.41) to get *mean* IPS (MIPS) representing an extension of IPS (Eq. [70]) from real deterministic signals to random processes as follows

$$\begin{aligned}
\mathrm{DMIPS}\,(t,f) &= \mathbb{E}\left\{\mathrm{IPS}\,(t,f)\right\}, \\
&= \mathbb{E}\left\{\Re\left\{\int_{-\infty}^{\infty} h_c^{ns}(t)\, h_c^{ns}(t+\tau)\, \exp\left(-i2\pi f\tau\right) d\tau\right\}\right\}, && (4.43)\\
&= \Re\left\{\int_{-\infty}^{\infty} \mathbb{E}\left\{h_c^{*ns}(t)\, h_c^{ns}(t+\tau)\right\} \exp\left(-i2\pi f\tau\right)\, d\tau\right\}, && (4.44)\\
&= \Re\left\{\int_{-\infty}^{\infty} \mathbb{E}\left\{h_c^{ns}(t)\, h_c^{*ns}(t-\tau)\right\} \exp\left(-i2\pi f\tau\right)\, d\tau\right\}, && (4.45)\\
&= \Re\left\{\int_{-\infty}^{\infty} \Phi_h^{mips}(t,\tau) \exp\left(-i2\pi f\tau\right)\, d\tau\right\}, && (4.46)
\end{aligned}$$

where (4.45) is a result of the following equivalent variable transformation

$$\begin{array}{ccc} t = t_2 & & t_2 = t \\ & \Longleftrightarrow & \\ \tau = t_1 - t_2 & & t_1 = t - \tau. \end{array} \qquad (4.47)$$

and $\Phi^{mips}(t,\tau)$ is defined as

$$\Phi^{mips}(t,\tau) = \mathbb{E}\left\{h_c^{ns}(t)\, h_c^{*ns}(t-\tau)\right\}, \qquad (4.48)$$

which is effectively the *average instantaneous* ACF for the Levin's IPS (Eq. (4.44)) obtained from (4.24) by transforming t_1 and t_2 as follows

$$\begin{array}{ccc} t = t_1 & & t_1 = t \\ & \Longleftrightarrow & \\ \tau = t_2 - t_1 & & t_2 = t + \tau, \end{array} \qquad (4.49)$$

Now that we have derived a number of quadratic TF distributions non-stationary channel process $h_c^{ns}(t)$, our next logical step is to describe these *continuous* TF distributions to discrete-time domain so that we may subsequently utilize important communication system design parameters like symbol rate and normalized fading rate, f_{D} to determine the impact of non-stationarity in the channel process due to mobile acceleration on the performance of future communication systems. In the next section, we first

study the discretization of random channel process $h_c^{ns}(t)$ followed by corresponding discrete-time TF distributions.

4.4 Discrete-Time Non-Stationary Channel Process and TF Distributions

The evaluation of non-stationary channel spectrum and its impact on communications system performance with the help of a computer necessitates the discretization of the continuous-time channel process and its corresponding TF distributions.

4.4.1 Discretization of Continuous-Time Channel Process

The discrete-time equivalent of the continuous-time input-output relationship is as follows (Eq. (4.7))

$$r[j] = \sqrt{\rho}\, h[j]\, s[j] + z[j], \quad -\infty < j < \infty \tag{4.50}$$

where, for simplicity of notation in the sequel, we have dropped the subscript 'd' (denoting discrete-time) and superscript 'ns' for discretized channel process. An important difference between the discrete-time models of (2.3) and (4.50) is in the sampling process. While the transmission and sampling rate are fixed in *stationary channel model* due to time-invariant spectrum of the channel fading process, we are at freedom either to fix or use variable transmission and sampling rates for *non-stationary channel model* (Eq. (4.50)).

Fixed Transmission and Sampling Rates

If the communication system designer can foresee the maximum time for which the mobile keeps on moving with the constant acceleration or, equivalently, the maximum Doppler spread is known at the transmitter *a priori*, it is possible to fix the transmission rate such that the channel is sampled at least at the Nyquist rate in worst channel conditions. As an example, let us assume that the maximum Doppler frequency is 200 Hz. The Nyquist rate corresponding to this rate of channel variation equals 400 Hz which implies that the channel samples required at the receiver to form CSI estimate must be furnished at least at the rate of 400 samples per second. This sampling rate, in turn, requires the symbol duration to be 2.5 msec. Since the symbol rate is fixed and the channel has to be sampled at symbol rate, at a time when the maximum Doppler frequency is 100 Hz, the channel would get oversampled at twice the Nyquist rate. In fact, when the transmission

rate is fixed according to worst channel conditions, the channel gets oversampled for almost the full duration of transmission. Therefore, the cost that has to be paid for keeping the transmission rate fixed is the added complexity due to oversampling of the channel process.

Adaptive Transmission and Sampling Rates

Equation (4.6) implies that the normalized fading rate f_{D} can be forced to be constant if we can change T_s or equivalently, the symbol rate at the transmitter. Equivalently, the transmission scheme should be adaptive to the instantaneous Doppler spread which requires *a priori* knowledge of the instantaneous channel spectrum at the transmitter. The receiver must also have the exact knowledge of the transmission rate implying that, in this adaptive transmission case, there may be more stringent adaptive synchronization requirements at the receiver as compared to the fixed transmission scheme.

4.4.2 Discretization of Continuous-Time TF Distributions

The extension of continuous-time TF representations to the discrete-time case may not always be straightforward even if the underlying random process has been sampled at the Nyquist rate, *e.g.*, aliasing problems appear if continuous-time WVD (Eqs. (4.30) and (4.31)) is extended to the discrete-time domain if the signal (or random process) has been sampled at the Nyquist rate [188]. In the following, we shall restrict our attention to the two widely used TF distributions, WVD and MIPS, the discretization of which is discussed below.

Discrete-time Wigner-Ville distribution (DWVD)

Assuming that the underlying Gaussian random channel process has been sampled at least at the Nyquist rate (using either a fixed or adaptive transmission scheme), the continuous-time WVD has the following logical extension to the discrete-time domain

$$\mathrm{DWVD}\,(nT_s, f) = \sum_{k=-\infty}^{\infty} \Phi'_h(n,k)\, \exp\left(-i2\pi f k T_s\right), \tag{4.51}$$

where $\Phi'_h(n,k)$ is the discrete-time equivalent of the continuous-time autocorrelation function $\Phi'_h(t,k)$ and is given as

$$\Phi'_h(n,k) = \mathbb{E}\left\{h(n-\frac{k}{2})h^*(n-\frac{k}{2})\right\}. \tag{4.52}$$

Notice that (4.51) requires samples of the channel process at non-integer instants which are not available if the channel process is sampled at the symbol rate. A number of different methods have been proposed in literature to overcome this problem [189]. Usual remedy to this problem is to oversample the channel process by a factor of 2, *i.e.*, twice the Nyquist rate so that the samples at non-integer sampling instants (otherwise unavailable) are made available [190]. Another method has been proposed in [191] which modifies the WVD kernel by inserting zeros at the non-integer sampling instants and an averaging operation is performed after taking the discrete Fourier transform (DFT). Yet another method that requires only Nyquist rate sampling is to use the analytic process corresponding to a real-valued non-stationary process so as to remove the negative frequencies in the spectrum of the process. The analytic processes, however, are in general improper so that this method can not be employed for the complex channel process under consideration which is by assumption a proper process. A comparative study of different discretizing functions was performed in [188] where it was concluded that the technique based on oversampling outperforms others. Therefore, we shall follow the technique based on oversampling and assume that the channel process is sampled at twice the Nyquist rate. This assumption enables us to write (4.51) as follows [190]

$$\mathrm{DWVD}\,(nT_s, f) = 2 \sum_{k=-\infty}^{\infty} \Phi_h^{dwvd}(n,k)\, \exp\left(-i2\pi f k T_s\right), \tag{4.53}$$

where

$$\Phi_h^{dwvd}(n,k) = \mathbb{E}\left\{h(n+k)h^*(n-k)\right\}. \tag{4.54}$$

Equation (4.54) gives DWVD for a general channel autocorrelation function $\Phi_h^{dwvd}(n,k)$. We shall later use it to describe Wigner-Ville spectrum of the Gaussian channel process, $h_c^{ns}(t)$.

Discrete-Time Mean Instantaneous Power Spectrum (DMIPS)

For the random channel process sampled at least at the Nyquist rate, the continuous-time MIPS spectra in (4.44)–(4.46) are logically extended to the discrete-time domain as

$$\mathrm{DMIPS}\,(nT_s, f) = \sum_{k=-\infty}^{\infty} \mathbb{E}\left\{h^*(n)\, h(n+k)\right\}\, \exp\left(-i2\pi f k T_s\right), \tag{4.55}$$

$$= \sum_{k=-\infty}^{\infty} \mathbb{E}\left\{h(n)\, h^*(n-k)\right\}\, \exp\left(-i2\pi f k T_s\right), \tag{4.56}$$

$$= \sum_{k=-\infty}^{\infty} \Phi_h^{dmips}(n,k)\ \exp\left(-i2\pi f k T_s\right), \tag{4.57}$$

where we have defined $\Phi^{dmips}(n,k)$ as

$$\Phi^{dmips}(n,k) = \mathbb{E}\left\{h^*(n)\, h(n+k)\right\}, \tag{4.58}$$

$$= \mathbb{E}\left\{h(n)\, h^*(n-k)\right\}, \tag{4.59}$$

where there is no $k/2$ factor in $\Phi^{dmips}(n,k)$ and, therefore, no spectrum foldover is observed in DMIPS if Nyquist rate sampling of the channel process is performed.

In the following section, we analyze the spectrum of the non-stationary Gaussian channel fading process in accelerating mobile environment by, first, formulating the instantaneous ACFs for DWVD and DMIPS and then using these ACFs respectively in (4.54) and (4.55)–(4.57) to obtain DWVD and DMIPS representations of the channel spectra.

4.5 Spectral Analysis of Non-Stationary Gaussian Channel Process

The evaluation of mobile channel spectra using DWVD and DMIPS techniques requires the formulation of instantaneous ACF, $\Phi^x(n,k)$ where x stands respectively for DWVD and DMIPS. In the following, we first derive $\Phi^x(n,k)$ and then determine the channel spectra taking discrete-time Fourier transform (DTFT) of the ACFs.

4.5.1 Formulation of Instantaneous Channel ACF

Let the mobile moving with initial velocity $\boldsymbol{v}_0 = |\boldsymbol{v}_0|, \phi_v$ and acceleration α be at an arbitrary origin O at the signaling instant 0 (Fig. 4.1). We can see from (4.54) and (4.58) that the formulation of ACFs for DWVD and DMIPS would require the determination of channel gains at instants n, $n-k$ and $n+k$ where k is the lag in number of symbols. At the signaling interval n, let the mobile be at the point (Π_n, ϕ_v) with respect to 0, where ϕ_v is the direction of the mobile with respect to x-axis. At the signaling interval $n-k$, the mobile is assumed to be at point (Π_{n-k}, ϕ_v). Similarly, at the signaling instant $n+k$, the mobile is assumed to be at (Π_{n+k}, ϕ_v). Using the fact that the mobile is accelerating in the direction of mobile travel, we have the following relationships for distances covered

by the mobile

$$\Pi_n = |\boldsymbol{v}_0| nT_s + \frac{1}{2}\alpha(nT_s)^2, \tag{4.60}$$

$$\Pi_{n-k} = |\boldsymbol{v}_0|(n-k)T_s + \frac{1}{2}\alpha\left((n-k)T_s\right)^2, \tag{4.61}$$

$$\Pi_{n+k} = |\boldsymbol{v}_0|(n+k)T_s + \frac{1}{2}\alpha\left((n+k)T_s\right)^2, \tag{4.62}$$

$$\tag{4.63}$$

and corresponding channel gains are

$$h[n] = \oint \psi(\beta) \exp\left(i\eta\Pi_n \widehat{\boldsymbol{v}} \cdot \widehat{\boldsymbol{\beta}}\right) d\beta, \tag{4.64}$$

$$h[n-k] = \oint \psi(\beta) \exp\left(i\eta\Pi_{n-k} \widehat{\boldsymbol{v}} \cdot \widehat{\boldsymbol{\beta}}\right) d\beta, \tag{4.65}$$

$$h[n+k] = \oint \psi(\beta) \exp\left(i\eta\Pi_{n+k} \widehat{\boldsymbol{v}} \cdot \widehat{\boldsymbol{\beta}}\right) d\beta. \tag{4.66}$$

Now that we have instantaneous channel gains, using (4.65) and (4.66), the instantaneous ACF for DWVD is given as (Eq. (4.54))

$$\Phi_h^{dwvd}(n,k) = \mathbb{E}\left\{h(n+k)h^*(n-k)\right\}, \tag{4.67}$$

$$= 2 \oint \oint \mathbb{E}\left\{\psi(\beta)\psi^*(\beta')\right\} \exp\left(i\eta\left(\Pi_{n+k}\widehat{\boldsymbol{v}} \cdot \widehat{\boldsymbol{\beta}} - \Pi_{n-k}\widehat{\boldsymbol{v}} \cdot \widehat{\boldsymbol{\beta}'}\right)\right) d\beta'\, d\beta,$$

$$= 2 \oint \Psi(\beta) \exp\left(i\eta\Pi^{dwvd}\, \widehat{\boldsymbol{v}} \cdot \widehat{\boldsymbol{\beta}}\right) d\beta, \tag{4.68}$$

where (4.68) is the result of assumption of statistically homogeneous scattering and

$$\Pi^{dwvd} = \left(\Pi_{n+k} - \Pi_{n-k}\right),$$

$$= 2\, kT_s \left(|\boldsymbol{v}_0| + \alpha(nT_s)\right), \tag{4.69}$$

is the distance covered by the mobile at signaling instant $n+k$ with respect to the signaling instant $n-k$ (Fig. 4.1).

Similarly, using (4.64) and (4.65), the ACF for DMIPS as defined by (4.58) can be shown to be

$$\Phi_h^{dmips}(n,k) = \mathbb{E}\left\{h(n+k)h^*(n)\right\}, \tag{4.70}$$

$$= \oint \Psi(\beta) \exp\left(i\eta\Pi^{dmips}\, \widehat{\boldsymbol{v}} \cdot \widehat{\boldsymbol{\beta}}\right) d\beta, \tag{4.71}$$

where we have defined Π^{dmips} as

$$\begin{aligned}\Pi^{dmips} &= (\Pi_{n+k} - \Pi_n)\,, \\ &= |\boldsymbol{v}_0| k T_s + |\boldsymbol{v}_0| k T_s \left(\frac{\alpha T_s}{|\boldsymbol{v}_0|}(n + 0.5k)\right). \end{aligned} \tag{4.72}$$

Equations (4.68) and (4.71) respectively represent channel ACFs for DWVD and DMIPS in general scattering environments. It can be observed that unlike WSS channel process where the phase of the plane wave in autocorrelation expression turns out to vary linearly with lag k, the mobile acceleration causes a time-dependent non-linear plane wave phase variation with k.

The APD $\Psi(\beta)$ and the plane wave $\exp\left(i\eta\Pi^x\,\widehat{\boldsymbol{v}}\cdot\widehat{\boldsymbol{\beta}}\right)$ (where the superscript x stands for either DWVD or DMIPS) are periodic in β. We follow the approach adopted in Chapter 2, firstly, to represent $\Psi(\beta)$ in circular Fourier series form by the following pair of equations (Eqs. (2.13a) and (2.13b)), *i.e.*,

$$\begin{aligned}\gamma_m &= \oint \Psi(\beta)\,\exp(-im\beta)\,\mathrm{d}\beta, \\ \Psi(\beta) &= \frac{1}{2\pi}\sum_{m=-\infty}^{\infty}\gamma_m\,\exp(im\beta)\,,\end{aligned}$$

where m is an integer, γ_m are Fourier series coefficients. Secondly, we invoke the well-known Jacob-Anger expansion of the plane wave (2.14) to decompose $\exp\left(i\eta\Pi^x\,\widehat{\boldsymbol{v}}\cdot\widehat{\boldsymbol{\beta}}\right)$ into its modes as follows

$$\exp\left(i\eta\Pi^x\,\widehat{\boldsymbol{v}}\cdot\widehat{\boldsymbol{\beta}}\right) = \sum_{p=-\infty}^{\infty} i^p\,J_p(\eta\Pi^x)\exp(-ip\phi_v)\,\exp(ip\beta)\,. \tag{4.74}$$

Equations (4.68) and (4.71) involve the product of two periodic functions, $\Psi(\beta)$ and $\exp\left(i\eta\Pi^x\,\widehat{\boldsymbol{v}}\cdot\widehat{\boldsymbol{\beta}}\right)$. The representation of these periodic functions by their respective Fourier series would result in their Fourier series coefficients to be convoluted (see footnote 5 in Chapter 2). Using (2.13) and (4.74) and following the steps taken in the Chapter 2 (Eqs. (2.11)–(2.16)), we can rewrite equations (4.68) and (4.71) respectively in the following form

$$\Phi_h^{dwvd}(n,k) = 2\sum_{m=-\infty}^{\infty} i^m\,\gamma_m\,J_m(\eta\Pi^{wvd})\,\exp(im\phi_v)\,, \tag{4.75}$$

$$\Phi_h^{dmips}(n,k) = \sum_{\nu=-\infty}^{\infty} i^\nu\,\gamma_\nu\,J_\nu(\eta\Pi^{ips})\,\exp(i\nu\phi_v)\,, \tag{4.76}$$

where ν is an integer. It is easily verified that if the mobile were moving with constant velocity ($\alpha = 0$), (4.75) and (4.76) would collapse to (2.16) and the channel process would therefore be WSS. For all $\alpha > 0$, (4.75) and (4.76) are not only a function of the lag k but also the absolute time index n implying a non-WSS channel process.

Let us define the initial time-invariant Doppler spread as

$$\omega_{d,0} = \eta|\boldsymbol{v}_0|, \tag{4.77}$$

so that the normalized initial Doppler spread $\omega_{D,0}$ shall be given by

$$\omega_{D,0} = \frac{\omega_{d,0}}{(1/T_s)}. \tag{4.78}$$

We also define the normalized mobile acceleration α^N as

$$\alpha^N = \frac{\alpha}{|\boldsymbol{v}_0|\,(1/T_s)}, \tag{4.79}$$

where the normalization is by the initial velocity v_0 and the symbol rate $1/T_s$.

Using (4.69), (4.72) and (4.77)-(4.79), we can rewrite (4.75) and (4.76) respectively as follows

$$\Phi_h^{dwvd}(n,k) = 2\sum_m i^m\,\gamma_m\,J_m\Big(\omega_{D,0}\,k + \omega_{D,0}\,k\big(1+2\alpha^N n\big)\Big)\,\exp\left(im\phi_v\right), \tag{4.80}$$

$$\Phi_h^{dmips}(n,k) = \sum_\nu i^\nu\,\gamma_\nu\,J_\nu\Big(\omega_{D,0}\,k + \omega_{D,0}\,k\Big(\alpha^N(n+0.5\,k)\Big)\Big)\,\exp\left(i\nu\phi_v\right), \tag{4.81}$$

where each subscript with the summation sign indicates summation over that subscript from $-\infty$ to ∞. Notice that the stationary and non-stationary parts of the ACFs in (4.80) and (4.81) are not separable. The best thing we can do to show stationary and non-stationary parts apart is the use of the Bessel function addition theorem [192]

$$J_p(x_1+x_2) = \sum_{k=-\infty}^{\infty} J_k(x_1)J_{p-k}(x_2), \tag{4.82}$$

which obviously does not indicate separability.

ACFs for DWVD and DMPIS Spectra in Isotropic Scattering Environment

While equations (4.80)−(4.81) represent average instantaneous ACF for DWVD and DMIPS in a general scattering environment, more intuition behind the impact of non-

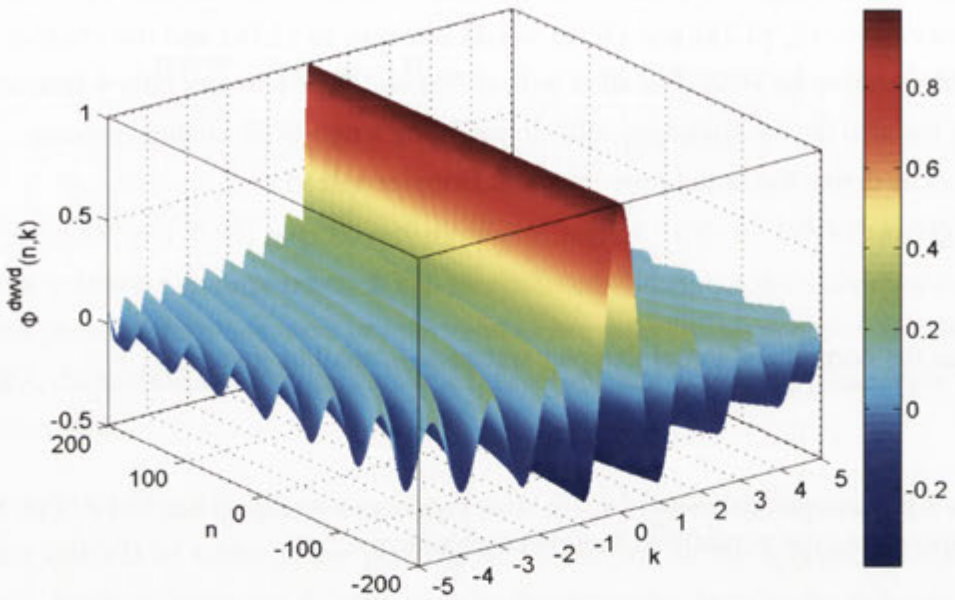

Figure 4.2: The ACF of DWVD as a function of the lag k and absolute time index n: $|\boldsymbol{v}_0| = 20$m/sec, $\alpha = 10$m/sec^2, f_c =2GHz and $T_s = 5$msec. Increasing τ and n have the effect of reducing the autocorrelation faster.

stationarity due to mobile acceleration on channel ACF can be obtained if these equations are specialized to the case of isotropic scattering (see Chapter 2, Section 2.3.1). When the scattering power is isotropically distributed over the azimuth, equations (4.80) and (4.81) respectively become

$$\Phi_{iso}^{dwvd}(n,k) = 2J_0\Big(\omega_{D,0}\,k + \underbrace{\omega_{D,0}\,k\Big(1+2\alpha^N n\Big)}_{\text{Due to Non-Stationarity}}\Big), \tag{4.83}$$

$$\Phi_{iso}^{dmips}(n,k) = J_0\Big(\omega_{D,0}\,k + \underbrace{\omega_{D,0}\,k\Big(\alpha^N(n+0.5\,k)\Big)}_{\text{Due to Non-Stationarity}}\Big). \tag{4.84}$$

We can make the following observations regarding ACFs for DWVD and DMIPS in isotropic scattering environment

1. The unsymmetrical ACF formulation in DMIPS results in quadratic dependence of non-stationary ACF on the lag variable k as can be observed in (4.84). The symmetrical ACF formulation for DWVD, on the other hand, depicts a linear dependence of non-stationary ACF on k (Eq. (4.83)). However, a slight manipulation of (4.83) reveals that the symmetrical ACF introduces a factor 2 in the argument

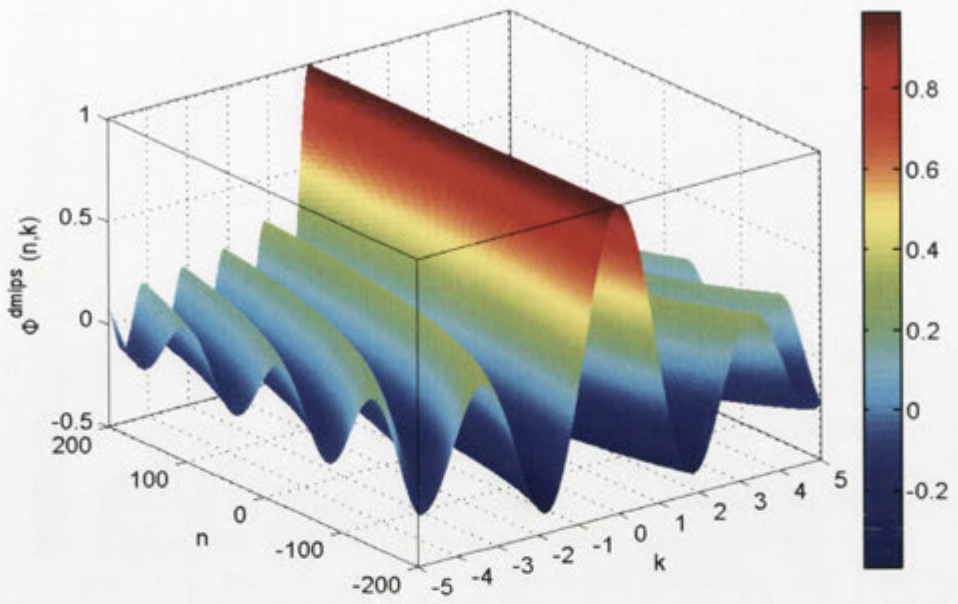

Figure 4.3: The ACF of DMIPS as a function of the lag k and absolute time index n: $|\boldsymbol{v}_0| = 20$m/sec, $\alpha = 10$m/sec^2, f_c =2GHz and $T_s = 5$msec. Increasing τ and n have the effect of reducing the autocorrelation faster.

of the Bessel function which can be considered as having the impact of doubling the *effective* mobile speed.

2. The non-stationarity impact due to a constant mobile acceleration not only depends on the absolute time index n but also on the lag variable k, the initial velocity $\boldsymbol{v}_0$ and the symbol rate.

3. As long as n and k are finite, ACFs corresponding to DWVD and DMIPS are in closed-form which is due to the presence of the Bessel functions (see Chapter 2).

4.5.2 Formulation of Non-Stationary Spectra: DWVD and DMIPS

The substitution of the instantaneous ACF for DWVD (Eq. (4.81)) in (4.54) gives the DWVD of the non-stationary channel process which is, in fact, the DTFT of the ACF with respect to k thereby giving the PSD of the channel process in the *conventional* sense (Wiener-Khintchine theorem [51])

$$\begin{aligned}&\text{DWVD}\,(nT_s, f)\\ &= \sum_{k=-\infty}^{\infty} \Phi_h^{dwvd}(n,k)\,\exp\left(-i2\omega kT_s\right),\end{aligned}$$

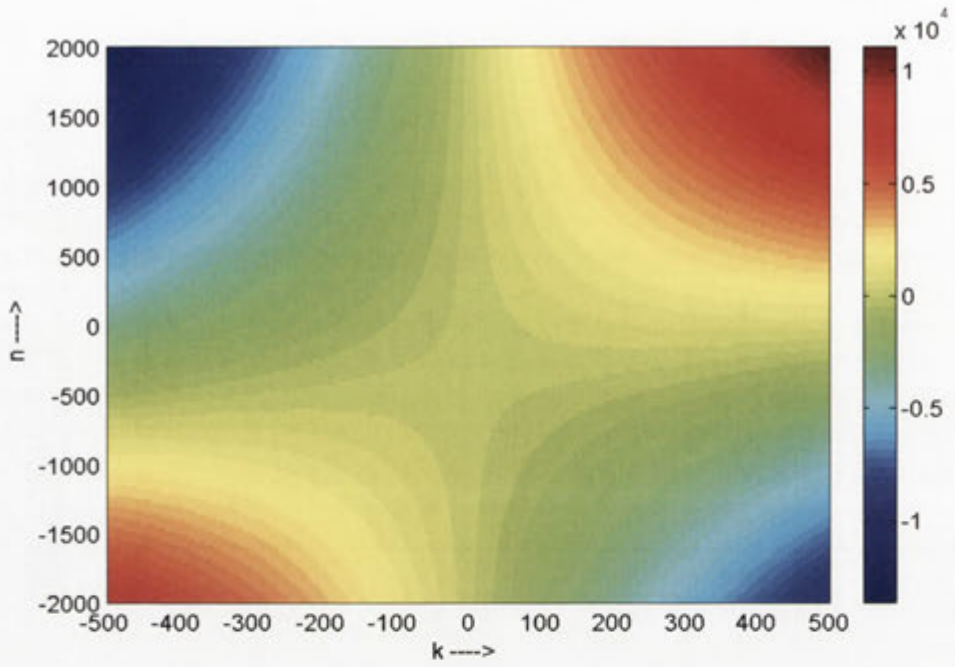

Figure 4.4: The 2D view of the $\mathrm{Arg}_{\mathrm{DVWD}} - \mathrm{Arg}_{\mathrm{DMIPS}}$: $|\boldsymbol{v}_0| = 20$m/sec, $\alpha = 10$m/sec^2, f_c =2GHz and $T_s = 5$msec.

$$= 2 \sum_{m,p,k} i^m \, \gamma_m \, \exp\left(im\phi_v\right) \, J_p\left(\omega_{D,0}\, k\right) J_{m-p}\left(\omega_{D,0}\, k\big(1 + 2\alpha^N n\big)\right) \exp\left(-i\omega k T_s\right), \tag{4.85}$$

where (4.85) is a result of the application of the Bessel function addition theorem defined in (4.82). Observe that (4.85) involves a product of two functions. We know that the multiplication of functions in the time-domain implies convolution of their spectra in the frequency domain [114]. We have, therefore, to define the following DTFTs

$$\frac{1}{T_s} \sum_{k=-\infty}^{\infty} J_p\Big(\omega_{D,0}\, k\Big) \, \exp\left(-i\omega k T_s\right) \triangleq \mathrm{DTFT}_k(\omega), \tag{4.86}$$

$$\frac{1}{T_s} \sum_{k=-\infty}^{\infty} J_{m-p}\Big(\omega_{D,0}\, k\big(1 + 2\alpha^N n\big)\Big) \, \exp\left(-i\omega k T_s\right) \triangleq \mathrm{DTFT}_n^{dwvd}(\omega), \tag{4.87}$$

the use of which along with the fact that DTFT is linear, we can rewrite Wigner-Ville spectrum in (4.85) as follows

$$\mathrm{DWVD}\left(nT_s, f\right) = T_s \sum_{m,p} i^m \, \gamma_m \, \exp\left(im\phi_v\right) \Big(\mathrm{DTFT}_k^{dwvd}(\omega) \odot \mathrm{DTFT}_n^{dwvd}(\omega)\Big), \tag{4.88}$$

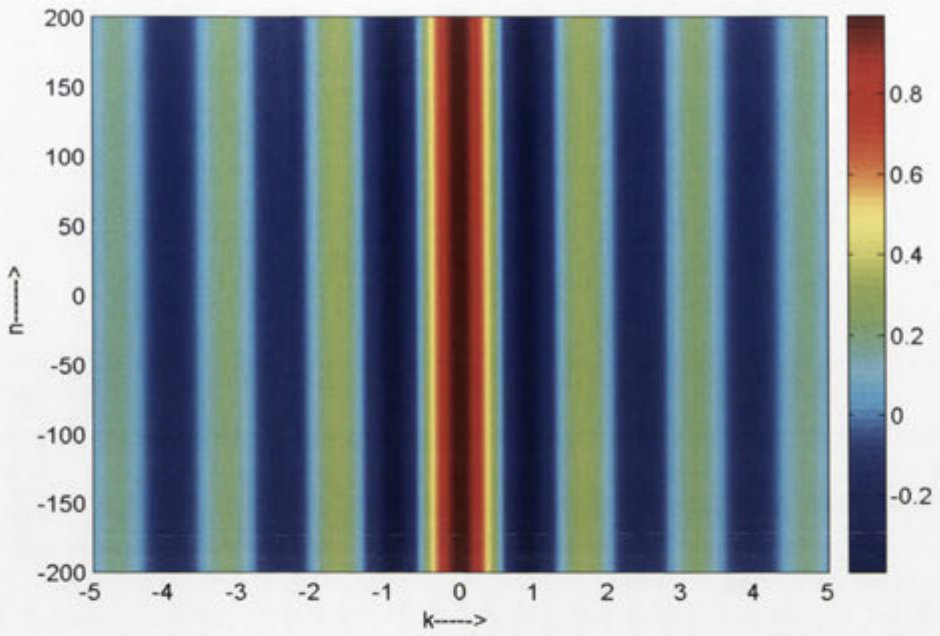

Figure 4.5: The 2D view of ACF for zeroth order Bessel function of the first kind as a function (Clarke's model) as a function of the lag k and absolute time index n: $|\boldsymbol{v}_0| =$ 20m/sec, $\alpha = 10\text{m/sec}^2$, f_c =2GHz and $T_s = 5$msec. Observe that the absolute time does not change the ACF.

The convolution of the stationary and non-stationary spectra again implies that non-stationarity is not separable from stationary statistics of a complex Gaussian channel with a mobile receiver moving with constant acceleration. Similarly, DMIPS spectrum is obtained by substituting the corresponding instantaneous channel ACF (Eq. (4.71)) in (4.57) as follows

$$\begin{aligned}
&\text{DMIPS}\,(nT_s, f) \\
&= 2\sum_{\nu,p,k} i^{\nu}\,\gamma_{\nu}\,J_p\Big(\omega_{D,0}k\Big)\,J_{\nu-p}\Big(\omega_{D,0}k\Big(\alpha^N(n+0.5\,k)\Big)\Big)\;\exp\left(i\nu\phi_v\right)\,\exp\left(-i\omega kT_s\right), \\
&= T_s\sum_{\nu,p} i^{\nu}\,\gamma_{\nu}\,\exp\left(i\nu\phi_v\right)\,\Big(\text{DTFT}_k^{dmips}(\omega)\odot\text{DTFT}_{n,k}^{dmips}(\omega)\Big), \qquad (4.89)
\end{aligned}$$

where we have defined $\text{DTFT}_{n,k}^{dmips}$ as

$$\text{DTFT}_{n,k}^{dmips}(\omega) = \frac{1}{T_s}\sum_{k=-\infty}^{\infty} J_{\nu-p}\Big(\omega_{D,0}k\Big(\alpha^N(n+0.5\,k)\Big)\Big)\,\exp\left(-i\omega kT_s\right), \qquad (4.90)$$

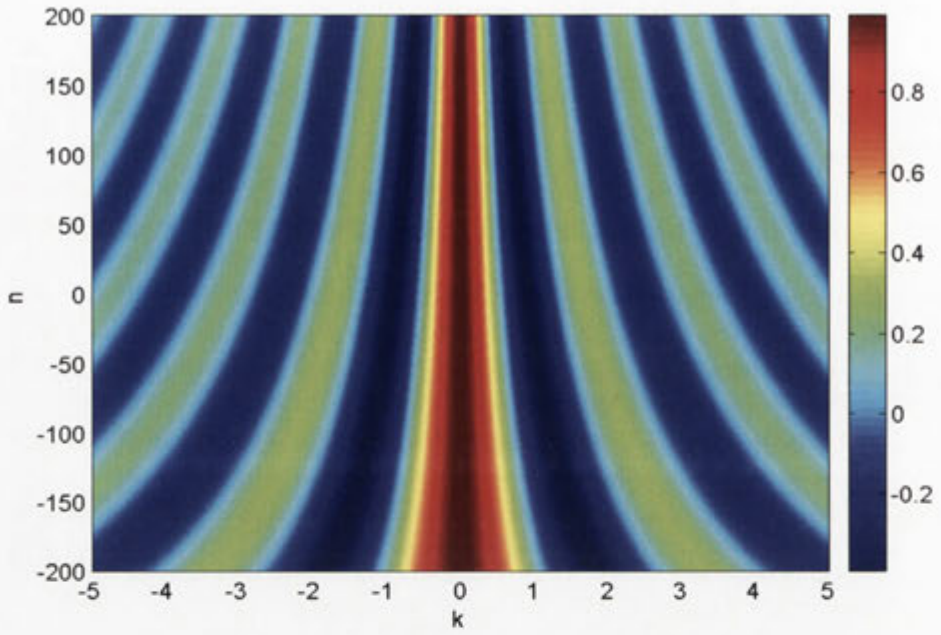

Figure 4.6: The 2D view of ACF for DWVD (isotropic scattering) as a function of the lag k and absolute time index n: $|\boldsymbol{v}_0| = 20$m/sec, $\alpha = 10$m/sec^2, $f_c = 2$GHz and $T_s = 5$msec. Increasing τ and n have the effect of reducing the autocorrelation faster.

and

$$\mathrm{DTFT}_k^{dmips}(\omega) = \mathrm{DTFT}_k^{dvwd}(\omega). \tag{4.91}$$

2D DWVD and DMIPS Spectra

The Wigner-Ville and instantaneous power spectra considered so far describe the spectral contents of the underlying channel process as a function of time in the conventional sense, *i.e.*, the time-varying spectral contents are obtained by taking DTFT with respect to lag k. Sometimes it is of some interest to determine the spectrum of time-variation (SOTV) of this conventional spectrum. The SOTV, in fact, is a joint spectrum of time n and lag k domains. Such spectrum which was derived in [193] is obtained by taking DTFT of the conventional time-dependent spectrum with respect to the time index n. The SOTV of DWVD (Eq. (4.88)) is given as

$$\mathrm{SOTV}^{dvwd}(g,f) = \sum_{m,p} i^m \gamma_m \ \exp(im\phi_v) \left(\mathrm{DTFT}_k^{dvwd}(\varrho,\omega) \odot \mathrm{DTFT}_n^{dwvd}(\varrho,\omega)\right), \tag{4.92}$$

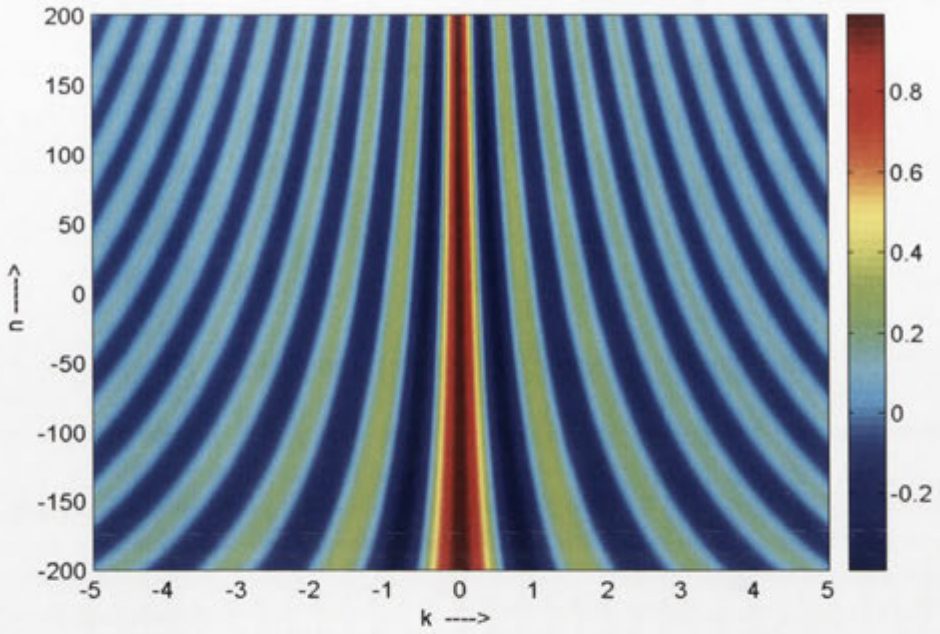

Figure 4.7: The 2D view of ACF for DMIPS (scattering environment) as a function of the lag k and absolute time index n: $|\boldsymbol{v}_0| = 20$m/sec, $\alpha = 10$m/sec^2, f_c =2GHz and $T_s = 5$msec. Increasing τ and n have the effect of reducing the autocorrelation faster.

where $\varrho = 2\pi g$ is frequency in radians and g is the frequency variable in Hz, and

$$\mathrm{DTFT}_k(g,f) \triangleq \frac{1}{T_s^2} \sum_{n,k} J_p\Big(\omega_{D,0}\, k\Big)\, \exp\left(-iT_s\left(n\varrho + \omega k\right)\right), \tag{4.93}$$

$$\mathrm{DTFT}_n^{dwvd}(g,\omega) \triangleq \frac{1}{T_s^2} \sum_{n,k} J_{m-p}\left(\omega_{D,0}\, k\big(1+2\alpha^N n\big)\right)\, \exp\left(-iT_s\left(n\varrho + \omega k\right)\right), \tag{4.94}$$

and for DMIPS (Eq. (4.89)), we have

$$\mathrm{SOTV}^{dmips}(g,f) = \sum_{\nu,p} i^{\nu}\, \gamma_{\nu}\, \exp\left(i\nu\phi_v\right)\, \Big(\mathrm{DTFT}_k^{dmips}(\varrho,\omega) \odot \mathrm{DTFT}_{n,k}^{dmips}(\varrho,\omega)\Big), \tag{4.95}$$

where we have defined

$$\mathrm{DTFT}_{nsp}^{dmips}(g,f) = \frac{1}{T_s^2} \sum_{n,k} J_{\nu-p}\Big(\omega_{D,0} k\Big(\alpha^N (n+0.5\,k)\Big)\Big)\, \exp\left(-iT_s\left(n\varrho + \omega k\right)\right). \tag{4.96}$$

Equations (4.88) and (4.89) respectively describe the instantaneous channel spectra according to WV and IPS definitions whereas (4.92) and (4.95) represent SOTV of the

instantaneous conventional spectra of the channel process. An alternative formulation of all these equations which does not involve any convolution of spectra is possible if we do not make use of the Bessel function addition theorem in the formulation of ACFs and derive the DVWD and DMIPS spectra based on (4.67) and (4.58) respectively. These alternative relations respectively for DVWD, DMIPS and their corresponding SOTV are given as

$$\begin{aligned}&\text{DWVD}\,(nT_s, f)\\&= 2\sum_m i^m\,\gamma_m\,\exp\left(im\phi_v\right)\left(\frac{1}{T_s}\sum_k J_m\Big(2\omega_{D,0}\,k\,\left(1+\alpha^N n\right)\Big)\exp\left(-i\omega k T_s\right)\right),\end{aligned} \tag{4.97}$$

$$\begin{aligned}&\text{DMIPS}\,(nT_s, f)\\&= \sum_\nu i^\nu \gamma_\nu \exp\left(i\nu\phi_v\right)\left(\frac{1}{T_s}\sum_k J_m\Big(\omega_{D,0}k+\omega_{D,0}k\Big(\alpha^N(n+0.5\,k)\Big)\Big)\exp\left(-i\omega k T_s\right)\right),\end{aligned} \tag{4.98}$$

$$\begin{aligned}&\text{SOTV}^{dvwd}(g, f)\\&= \sum_m i^m\gamma_m\,\exp\left(im\phi_v\right)\left(\frac{1}{T_s^2}\sum_{n,k} J_m\Big(2\omega_{D,0}\,k\,\left(1+\alpha^N n\right)\Big)\,\exp\left(-iT_s\left(n\varrho+\omega k\right)\right)\right),\end{aligned} \tag{4.99}$$

$$\begin{aligned}&\text{SOTV}^{dmips}(g, f)\\&= \sum_\nu i^\nu\gamma_\nu\,\exp\left(i\nu\phi_v\right)\times\frac{1}{T_s^2}\sum_{n,k} J_m\Big(\omega_{D,0}k\,\left(1+\alpha^N n+0.5k\alpha^N\right)\Big)\,\exp\left(-iT_s\left(n\varrho+\omega k\right)\right),\end{aligned} \tag{4.100}$$

which are all applicable in general scattering environments.

DWVD, DMIPS and Corresponding SOTV in Isotropic Scattering Environment

Equations (4.97)-(4.100) describe DWVD, DMIPS and their corresponding SOTV in arbitrary scattering environments. These equations respectively reduce to the following set of equations when the scattering environment is isotropic[9]

$$\text{DWVD}_{\,iso}(nT_s, f) = \frac{1}{T_s}\sum_k J_0\Big(\overbrace{2\omega_{D,0}\left(1+\alpha^N n\right)}^{\widetilde{\omega}_{D,n}}\,k\Big)\exp\left(-i\omega k T_s\right), \tag{4.101}$$

$$\text{DMIPS}_{\,iso}(nT_s, f) = \frac{1}{T_s}\sum_k J_0\Big(\overbrace{\omega_{D,0}\left(1+\alpha^N n+0.5k\alpha^N\right)}^{\widehat{\omega}_{D,n,k}}\,k\Big)\Big)\exp\left(-i\omega k T_s\right), \tag{4.102}$$

[9]When scattering is isotropic, these equations are non-zero only for $m = 0$.

$$\mathrm{SOTV}_{iso}^{dvwd}(g,f) = \frac{1}{T_s^2}\sum_{n,k} J_0\left(\widetilde{\omega}_{D,n}\, k\right) \exp\left(-iT_s\left(n\varrho + \omega k\right)\right), \tag{4.103}$$

$$\mathrm{SOTV}_{iso}^{dmips}(g,f) = \frac{1}{T_s^2}\sum_{n,k} J_0\left(\widehat{\omega}_{D,n,k}\, k\right) \exp\left(-iT_s\left(n\varrho + \omega k\right)\right), \tag{4.104}$$

where $\widetilde{\omega}_{D,n}$ and $\widehat{\omega}_{D,n,k}$ respectively are *instantaneous normalized Doppler spread* for DWVD and DMIPS spectra. Mathematically,

$$\widetilde{\omega}_{D,n} = 2\omega_{D,0}\left(1+\alpha^N n\right), \tag{4.105}$$

$$= 2\frac{|\boldsymbol{v}_0|T_s}{\lambda_c}\left(1+\frac{\alpha n T_s}{|\boldsymbol{v}_0|}\right) \tag{4.106}$$

and

$$\widehat{\omega}_{D,n,k} = \omega_{D,0}\left(1+\alpha^N n + 0.5k\alpha^N\right), \tag{4.107}$$

$$= \frac{|\boldsymbol{v}_0|T_s}{\lambda_c}\left(1+\frac{\alpha T_s}{|\boldsymbol{v}_0|}\left(n+0.5k\right)\right), \tag{4.108}$$

where (4.106) and (4.108) shall be particularly useful in Section 4.7 for the analysis of the impact of mobile acceleration, initial velocity, symbol rate and carrier wavelength (or, equivalently, carrier frequency) on time-varying DVWD and DMIPS spectra of the channel process. The instantaneous normalized Doppler spreads for DVWD and DMIPS, $\widetilde{\omega}_{D,n}$ and $\widehat{\omega}_{D,n,k}$, are fundamentally related to the channel coherence time T_c through the following relations (Eq. (4.4))

$$\widetilde{T}_{c,n} = \frac{2.6578}{\widetilde{\omega}_{D,n}}, \tag{4.109}$$

$$\widehat{T}_{c,n,k} = \frac{2.6578}{\widehat{\omega}_{D,n,k}}, \tag{4.110}$$

where $T_{c,n}$ denotes channel coherence at time n. Equations (4.109) and (4.110) are obviously useful for analyzing the impact mobile acceleration, initial velocity, symbol rate and carrier wavelength on the channel coherence time and functions thereof. Notice that $\widehat{T}_{c,n}$ is implicitly dependent on the lag variable k which is a result of unsymmetrical ACF formulation for DMIPS (Eq. (4.59)).

4.5.3 Analysis of DWVD and DMIPS Channel Spectra in Isotropic Scattering

Equations (4.101) and (4.102) respectively describe DVWDD and DMIPS channel spectra when the mobile receiver equipped with omnidirectional antenna moves with constant

acceleration in isotropic scattering environment. At this point it is instructive to observe that the instantaneous normalized Doppler spread for DVWD, $\widetilde{\omega}_{D,n}$, is a function of time variable n only and for DMIPS, $\widehat{\omega}_{D,n,k}$, is not only a function of the time index n but also the lag k — the variable in Fourier transformation.

DWVD

We consider the following DTFT relationship for the Bessel function of the first kind of integer order z with linear argument (Eq. (A.4)) [194, 195]

$$\sum_{\ell=-\infty}^{\infty} J_z(\widetilde{\omega}_{D,n}\ell)\ \exp\left(-i\omega\ell T_s\right) = \frac{F_z\left(\omega/\widetilde{\omega}_{D,n}\right)}{i^z\ \widetilde{\omega}_{D,n}}, \tag{4.111}$$

where F_z is given in (A.2). Using (4.101) and (4.111) and discarding all terms except corresponding to $z = 0$, we can write DWVD in isotropic scattering environment as

$$\mathrm{DWVD}\left(nT_s, f\right) = \frac{2\,\widetilde{\omega}_{D,n}}{\sqrt{\widetilde{\omega}_{D,n}^2 - \omega^2}}, \tag{4.112}$$

which is true for $\omega \leq \widetilde{\omega}_{D,n}$. A comparison of (4.112) with the Clarke's model of stationary channel statistics ((2.25)) suggests that DWVD represents a natural *generalization* of channel spectrum from stationary to non-stationary scenario. We emphasize that in order to arrive at the DWVD spectrum (Eq. (4.112)) we have had to assume that the lag k is allowed to approach infinity as required by the definition of DTFT. By allowing k to approach infinity for any $n < \infty$, we are in fact assuming that the transmission frame is of infinite length and the mobile velocity is allowed to increase without bound becoming infinite when k is infinity. Moreover, the discretization of the continuous-time Bessel function of the first kind of order zero with linear argument without aliasing requires infinite sampling rate[10] [196]. The assumption of infinite sampling rate is obviously a convenient mathematical construct rather than a physical reality in view of the fact that nothing can move faster than the speed of the light [197] and only finite sampling rate is possible. To be more relevant, the maximum speed of vehicles is only a few hundred Km/hr, *i.e.*, only a very slight fraction of the speed of the light and a vehicle can keep on

[10]Our assumption of the availability of infinite sampling rate removes the need for an analog prefilter before analog-to-digital converter (ADC) used to limit the bandwidth of infinite-bandwidth AWGN noise. A consequence of infinite sampling rate is that the discrete-time AWGN in (4.50) is truly white. The usual bandlimitation of AWGN using analog prefilter results in colored AWGN noise. We had to allow infinite noise bandwidth into the digital receiver because our useful channel spectrum assumed to be known also extends to infinity due to unbounded mobile velocity. The use of an analog prefilter to limit the undesired AWGN noise may also result in a loss useful signal information . In this section, we restrict ourselves to the case of an analog prefilter with infinite bandwidth (or, equivalently, no prefilter).

accelerating only for a finite time. Both of these real-world facts imply that neither n nor k can approach infinity. The finiteness of n and k would require finite-length windows in the time n and lag k domains in the DTFT representation defined in (4.111). An important implication of (4.112) is that, for a finite n, the channel process has a bandlimited representation.

DMIPS

The argument of the zeroth order Bessel function in DMIPS representation ((4.102)) is quadratic in k. In order to give an idea of what this quadratic dependence on k could mean for the DMIPS spectrum, we have plotted $J_0(a\,k)$ and $J_0(a\,k^2)$ in Fig. 4.8 assuming $a = 1$. Unlike $J_0(a\,k)$, the quadratic argument causes $J_0(a\,k^2)$ to oscillate faster and faster without bound with increasing k in a chirp-like behavior [198]. As we have assumed an infinite sampling rate, the chirp-like behavior due to the Bessel function with quadratic argument causing the spectrum to extend to infinity is not a problem in the derivation of discrete-time MIPS.

Using (4.105), we use the following equivalent form of (4.102)

$$\text{DMIPS}_{\,iso}(nT_s, f) = \frac{1}{T_s}\sum_k J_0\Big(0.5\,\widetilde{\omega}_{D,n}\,k + 0.5\omega_{D,\alpha}\,k^2\Big)\exp\left(-i\omega k T_s\right), \quad (4.113)$$

$$= T_s \sum_p \text{DTFT}_n^{dmips}(\omega) \odot \text{DTFT}_\alpha^{dmips}(\omega), \quad (4.114)$$

where we have defined acceleration-dependent normalized Doppler spread

$$\omega_{D,\alpha} = \alpha^N\,\omega_{D,0}, \quad (4.115)$$

and the following DTFTs

$$\text{DTFT}_n^{dmips}(\omega) \triangleq \frac{1}{T_s}\sum_k J_{-p}\Big(0.5\,\widetilde{\omega}_{D,n}\,k\Big)\,\exp\left(-i\omega k T_s\right), \quad (4.116)$$

$$\text{DTFT}_\alpha^{dmips}(\omega) \triangleq \frac{1}{T_s}\sum_k J_p\Big(0.5\omega_{D,\alpha}\,k^2\Big)\,\exp\left(-i\omega k T_s\right), \quad (4.117)$$

The $\text{DTFT}_n^{dmips}(\omega)$ which involves the $-p$th order Bessel function of the first kind with linear argument can be obtained using (4.111) as follows

$$\text{DTFT}_n^{dmips}(\omega) = (-1)^p \frac{F_p\left(\omega/0.5\widetilde{\omega}_{D,n}\right)}{i^p\,\widetilde{\omega}_{D,n}}, \quad (4.118)$$

where we have used the relation $J_{-p}(y) = (-1)^p J_p(y)$. In the Appendix C.1, we show

that $\mathrm{DTFT}_{\alpha}^{dmips}(\omega)$ involving pth order Bessel function of the first kind with *quadratic* argument is given by

$$\begin{aligned}\mathrm{DTFT}_{\alpha}^{dmips}(\omega) &\triangleq \mathrm{DTFT}\left\{J_p(\omega_{d,\alpha}\,(kT_s)^2)\right\} \\ &= (1+\exp(i\,p\,\pi))\ \mathrm{BMFC}_{dtft},\end{aligned} \tag{4.119}$$

where BMFC_{dtft} — Bessel-Modulated discrete-time Fourier Chirp transform — is defined as

$$\mathrm{BMFC}_{dtft} \triangleq \frac{1}{2\pi}\int_{-\omega_{D,\alpha}}^{\omega_{D,\alpha}} \frac{\exp(i\,p\ \arcsin(\mu_N/\omega_{D,\alpha}))}{\sqrt{\omega_{D,\alpha}^2-\mu_N^2}}\ \mathrm{DTFT}_{chirp}^{\mu_N}(\omega)\,d\mu_N. \tag{4.120}$$

where $\mathrm{DTFT}_{chirp}^{\mu_N}(\omega)$ is the DTFT of the discrete-time Chirp ($\exp(i\mu_N\,kT_s)$) defined as

$$\begin{aligned}\mathrm{DTFT}_{chirp}^{\mu}(\omega) &\triangleq \frac{1}{T_s}\sum_{k=-\infty}^{\infty}\exp\left(i\,\mu(kT_s)^2\right)\exp(-i\omega kT_s), \\ &= \left(i\frac{\pi}{\mu_N}\right)^{1/2}\exp\left(-i\,\frac{\omega^2}{4\,\mu_N^2}\right),\end{aligned} \tag{4.121}$$

which implies that a linear chirp in time-domain is Fourier transformed to a linear chirp in the frequency domain.

4.6 Bounded Mobile Velocity and Finite Sampling Rate

So far in this chapter we assumed that the mobile velocity could be unbounded resulting in a channel process with spectrum extending over the whole real line. The infinite bandwidth necessitated infinite sampling rate for discretizing of the channel process without aliasing. However, in reality neither mobile velocity can increase without bound nor we can have infinite sampling rate capability at our disposal. One of the immediate implications of a bounded mobile velocity is that we can not transmit a frame of data of infinite length without violating our main assumption of bounded mobile. Secondly, since the resulting channel process is bandlimited, we do not need to employ infinite sampling rate to sample the channel.

4.6.1 Analog Prefilter Bandwidth

In the previous section, since we allowed the mobile velocity to increase without bound, we had assumed an infinite bandwidth analog prefilter before ADC so as to pass the infinite-bandwidth channel undistorted. Since the channel process is always going to be

a bandlimited process in view of physical limitations to the mobile velocity, an analog prefilter with finite bandwidth would suffice. Usually, the spectrum of the *stationary* channel process is much narrower as compared to the signal of interest, *e.g.*, the maximum frequency in the channel spectrum for radio reception in a vehicle with speed of 500 km/hr would be $\approx$ 926Hz for a carrier frequency of 2GHz which is $\approx$ 22 times less than the maximum frequency in an audio signal. In other words, the channel is narrowband as compared to the signal. In communications scenario with accelerating mobile, the spectrum widens with time which gives rise to the possibility of the narrowband channel becoming wideband. Since the channel spectrum is our useful signal[11] in addition to the transmitted signal, the prefilter bandwidth has to be dictated by the maximum of the channel and transmitted signal bandwidth. Now the amount of noise that enters into the receiver is also proportional to the filter bandwidth with more noise implying reduced SNR. Our interest in allowing the channel to pass through to the receiver system undistorted is that we wish to estimate the channel based on its known spectrum. These CSI estimates would then be used for transmitted signal demodulation. One of communications system design priorities, on the other hand, is to limit the white noise that enters the receiver. As long as our channel is narrowband as compared to the useful transmitted signal, we can choose the prefilter bandwidth based on useful signal bandwidth without losing channel information. However, when the channel is wideband and we opt to allow channel spectrum which is wider than the useful signal spectrum, we are in fact allowing extra than necessary noise in the receiver. We, therefore, have to keep in view the detrimental effects of the excess noise. There seems to be a trade-off between extra knowledge that we obtain by allowing full channel spectrum and the excess noise that degrades the SNR. The bandwidth of the analog prefilter, therefore, has to be optimized taking into account the impact of additional channel knowledge and excess noise. While we do not attempt to address this question in this thesis, this optimization problem seems to be worth scrutinising in later research.

4.6.2 Windowing

The spectrum of the channel is directly proportional to the observation time (or the transmission frame length) we select. Fortunately, in a wireless environment with accelerating mobile, increasing observation time may not be desirable in most instances of practical interest in view of the fact that larger lags contain increasingly less information due to faster and faster decorrelation with time (see Fig. 4.8 for example) which suggests

[11] In the present non-coherent communication scenario, the knowledge of channel statistics is all what we have about the channel. If the channel gets distorted as a result of bandlimitation of the receiver, we are supposed to lose information about the channel that could otherwise be useful.

shorter transmission frame lengths for higher accelerations. As we have discussed before, under the assumption of constant mobile acceleration, the transmission length has to be finite in view of bounded mobile velocity. When the data are finite, the need for the use of windowing[12] naturally arises as a way to control the resolution, bias and variance of the spectral estimates. In a wireless communication environment, we may be more interested in the width, *i.e.*, the maximum frequency of the spectrum instead of the shape of the spectrum in view of the fact that the shape of the spectrum does not significantly affect the quality of the channel estimation[13] based on the knowledge of channel statistics [199, 200] which implies that we might be more interested in reducing bias in the estimated spectrum rather than the resolution while making a choice about the window.

There is a great deal of literature on the design of windows with scores of windows proposed [198, 201–205]. The most popular among the proposed windows are rectangular (Boxcar or Dirichlet window), Hamming, Hann, Kaiser, Blackman windows etc., with each window having some merits and demerits representing some sort of trade-off between bias and resolution of the estimated spectrum. The length and the type of the window used affects the resolution and bias of the estimated spectrum. A window with infinite length (providing least time resolution) does not alter the DTFT spectrum (providing maximum resolution in the spectrum). We do not intend to go into the details about the design of the windows. Rather we shall qualitatively describe the impact of the use of a *general* window on the channel ACF and its spectrum (in DMIPS formulation).

Recall that, irrespective of a particular non-stationary spectral estimation technique, the ACF has been formulated as the *ensemble average* of the instantaneous ACF. It is important to answer the question of as to how does the ensemble averaging of the instantaneous ACF affect the non-stationary spectral estimation? The ensemble averaging is in fact ideal averaging so that the ACF samples thus obtained are free from any noise due to estimation error. The use of a window in connection with DMIPS is to limit the span of the lag domain at any time n. No weighting of the ACF samples is required in view of the fact that all ACF samples are noiseless and equally reliable. The rectangular window (also called the Boxcar or Dirichlet window) which gives equal weightage to all samples seems to be a logical choice. However, the use of rectangular window in the time domain results in ripples in the convoluted spectrum of the signal and the window,

[12]Recall that the DWVD is always a bandlimited process as long as the current time index $n < \infty$ whereas DMIPS spectrum is never bandlimited, irrespective of the current time index n if the lag domain is allowed to extend to infinity. While the discussion here about windowing applies to Wigner-Ville spectrum as well, we shall, for the purpose of brevity, explicitly discuss DMIPS spectrum which inherently needs windowing in the lag domain in order to be bandlimited.

[13]This must be true for channel spectra which are symmetric about $\omega = 0$. In Chapters 2 and 3, we have observed that when the channel spectra are asymmetric, the shape of the spectrum does affect the autocorrelation properties of the channel to an extent that the shape of the spectrum does matter for correlation based channel estimation and functions thereof.

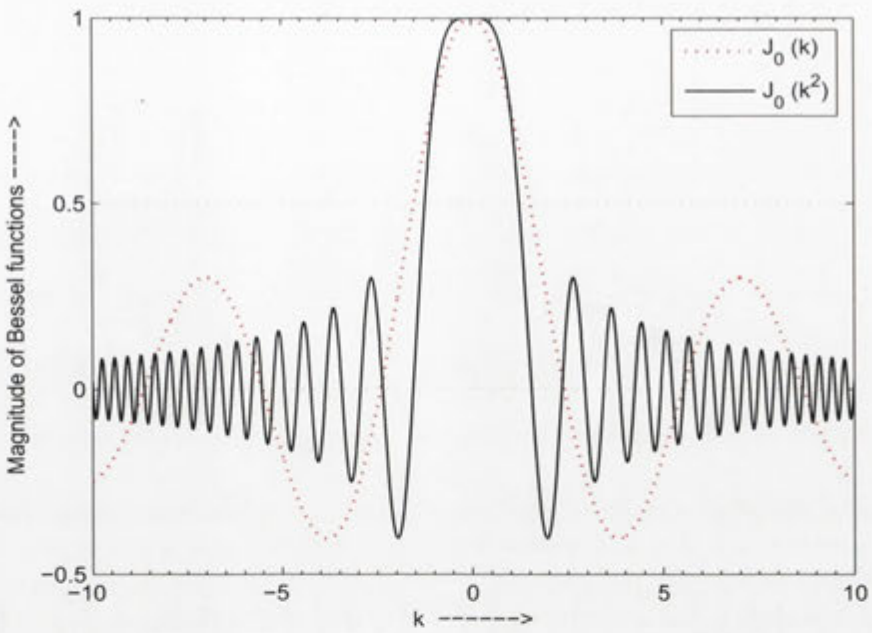

Figure 4.8: The plot of $J_0(a\ k)$ and $J_0(a\ k^2)$. We can observe the quadratic argument makes the Bessel function non-stationary so that its spectrum is lag-dependent. $J_0(a\ k^2)$ oscillates faster with lag k implying that it is no more a bandlimited like $J_0(a\ k)$ which is limited to $|\omega| \leq a$.

due to unwanted side lobes in the window's spectrum. On the other hand, the use of any window with unequal weights for spanned ACF samples, *e.g.*, Hamming, Hanning, Bartlett and Gaussian windows, would introduce unnecessary bias in the ACF samples and, hence, the spectrum but ,however, such windows would improve the ripple effect due to smooth transition of these windows to zero at the edges. Such windows with unequal weights across the length of the window can really be useful when we do not have ensemble averaged ACF samples. In fact, in most instances we have only noisy estimates of ACF samples and the use of windows with unequal weights is warranted. The process of windowing in the lag domain consists of multiplication of the window function with the ACF. The multiplication of the channel ACF in (4.113) by the window would result in convolution of Fourier spectra of the window and the channel.

4.6.3 Windowed DMIPS spectrum

The DMIPS spectrum obtained by windowing ACF using a length $(2K+1)$ symmetric window $\mathcal{W}_K(k)$ in the lag domain (resulting in windowed DTFT) is given as

$$\overline{\mathrm{DMIPS}}_{iso}(nT_s, f)$$

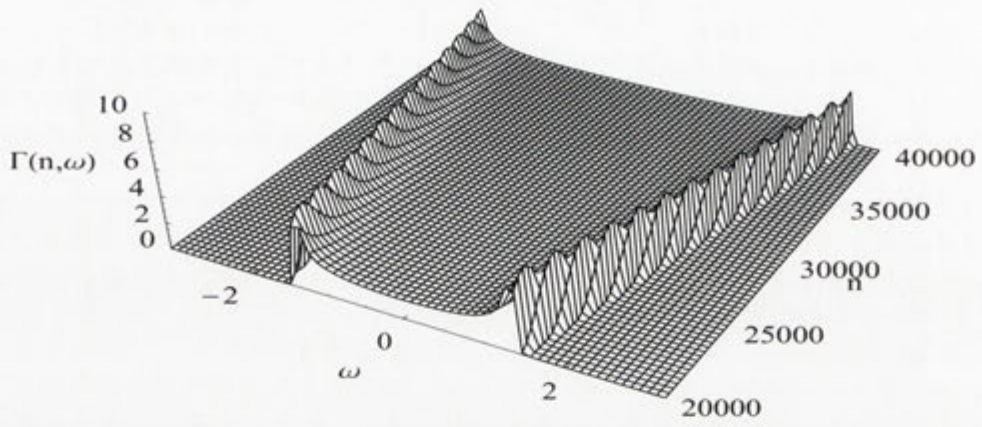

Figure 4.9: Non-stationary DMIPS spectrum by Blackman-Tukey method. The finite window length is assumed to be 51 samples in the lag domain. We assume that the carrier frequency is 2GHz, $T_s = 2.65$msec, $|\boldsymbol{v}_0| = 20$m/sec and the acceleration $\alpha = 10\text{m/sec}^2$. As can be observed, the instantaneous Doppler spread increases linearly with n exhibiting the same U-shaped behavior characteristic of the Clarke's model. Notice that the poor resolution in the frequency domain is due to the finiteness of the window function.

$$= \frac{1}{T_s} \sum_k \underbrace{\mathcal{W}_K(k) J_0\Big(0.5\,\widetilde{\omega}_{D,n}\,k + 0.5\omega_{D,\alpha}\,k^2\Big)}_{\text{Windowed Instantaneous ACF}} \exp\left(-i\omega k T_s\right), \tag{4.122}$$

$$= \frac{1}{T_s} \sum_k \mathcal{W}_K(k) \sum_p \Big(J_p\Big(0.5\,\widetilde{\omega}_{D,n}\,k\Big)\, J_{-p}\Big(0.5\omega_{D,\alpha}\,k^2\Big)\Big) \exp\left(-i\omega k T_s\right), \tag{4.123}$$

$$= T_s^2 \sum_{p=-P_0}^{P_0} \text{DTFT}_{\mathcal{W}}(\omega) \odot \text{DTFT}_n^{dmips}(\omega) \odot \text{DTFT}_\alpha^{dmips}(\omega), \tag{4.124}$$

where we have defined the following DTFTs in the last equation

$$\text{DTFT}_{\mathcal{W}}(\omega) \triangleq \frac{1}{T_s} \sum_k \mathcal{W}_K(k)\, \exp\left(-i\omega k T_s\right), \tag{4.125}$$

$$\text{DTFT}_n^{dmips}(\omega) \triangleq \frac{1}{T_s} \sum_k J_p\Big(0.5\,\widetilde{\omega}_{D,n}\,k\Big)\, \exp\left(-i\omega k T_s\right), \tag{4.126}$$

$$\text{DTFT}_\alpha(\omega) \triangleq \frac{1}{T_s} \sum_k J_{-p}\Big(0.5\omega_{D,\alpha}\,k^2\Big)\, \exp\left(-i\omega k T_s\right). \tag{4.127}$$

Notice that the summations in (4.122)-(4.123) are always finite because of the finite window. These summations can be taken as zero beyond the length of the window. The

summation in (4.124) is finite due to the presence of the Bessel function(s) (see discussion on Bessel function approximation in Section 2.2.4 in Chapter 2). This summation can be taken as zero beyond $|p| > P_0(n, K)$ where $P_0(n, K)$ is given as

$$P_0(n, K) \triangleq \min \left\{ \arg \left(J_p \left(0.5 \, \widetilde{\omega}_{D,n} \, K \right) \right), \arg \left(J_{-p} \left(0.5 \omega_{D,\alpha} \, K^2 \right) \right) \right\}, \tag{4.128}$$

where $\arg(y)$ represents the argument of y. Notice that (4.122) is essentially the Blackman-Tukey method of estimating the spectrum of a random process and (4.123) is a result of the application of Bessel function addition theorem. It may be emphasized that the DMIPS spectrum obtained by windowing in the lag domain is no more a true DMIPS spectrum. Instead, it is a *psuedo* DMIPS. The true DMIPS spectrum can be obtained using an infinite length of the window.

Asymptotic Analysis of DMIPS Spectrum

Since the quadratic argument in the Bessel functions in DMIPS spectrum causes the channel to decorrelate faster and faster with increasing lag k, the length of the window has to be time-dependent (irrespective of transmission strategy) so as to limit the inclusion of highly oscillatory and increasingly less useful lags. To appreciate this point, we consider the asymptotic behavior of the channel ACF, *i.e.*, when lag k and n are such that the argument of the Bessel function in the DMIPS spectrum is either very small or very large. The following asymptotic relationships[14] for Bessel function of order zero with argument x exist [206]:

$$J_0(x) \approx \begin{cases} 1, & x \ll 1 \\ \sqrt{\frac{2}{\pi x}} \cos(x - \frac{\pi}{4}), & x \gg 1, \end{cases} \tag{4.129}$$

where we can observe that for zeroth order Bessel function argument much smaller than unity, the value of the Bessel function is 1. The DTFT[15] of 1 is $2\pi\delta(\omega)$ implying that for sufficiently small n and k (and in fact for sufficiently small symbol rate, mobile initial velocity and the carrier frequency), the channel process is essentially a non-random (or, more precisely, a constant gain) process with no time-variation. If it is just the lag k that

[14]These relationships are of no concern if the channel has stationary statistics because these special cases are taken care of in the evaluation of stationary channel spectrum. In the non-stationary scenario, these asymptotic relationships become important because we are less concerned about the average spectrum. Rather we need to know the instantaneous spectrum.

[15]We know that the evaluation of DTFT involves infinite k. The DTFT of 1 must therefore involve infinite k. But we can not allow infinite k in view of the constraint on Bessel function argument $x << 1$ which implies that it is grossly inaccurate to use the term DTFT for the asymptotics applicable over only a certain range of the argument x. However, we shall continue to make use of the concept of DTFT here as it matches with the intuitive expectations about the spectrum of the Bessel function asymptotics.

we can control assuming all other parameters fixed, the behavior of Bessel function at small arguments suggests keeping the maximum transmission block length such that the argument of the Bessel function remains much less than 1. This discussion implies that we should use sufficiently small transmission block length if we want the channel gain to remain constant during the whole transmission.

The Bessel function asymptotics for arguments much larger than 1 suggest that it behaves like a damped cosine (or, equivalently, sine) function for sufficiently large arguments. As x approaches infinity, the correlation approaches zero implying that the channel process gets fully decorrelated with no correlation between two consecutive symbols. In the context of DMIPS spectrum, infinite Bessel function argument in (4.84) can be achieved even if the current time index $n = 0$. The channel decorrelation at infinite k implies that transmission frame length can be made very large if the current time-index is sufficiently small. And if the current time index n is itself infinite, looking for channel correlation even at lag $k = 1$ is useless because the channel would have fully decorrelated. This suggests that the transmission block length has to be made increasingly smaller as the current time index n increases. Therefore, a time-dependent window length is to be used to reduce the complexity at the receiver.

4.7 Mobile Acceleration Impact on Non-Coherent Mobile Communications

We have so far been concerned with the effect of mobile acceleration on the statistics of Rayleigh fading, *i.e.*, the ACF and the spectral density of the channel process. We observed that the impact of mobile acceleration on channel statistics strongly depends on a particular formulation of the instantaneous channel autocorrelation. The symmetrical ACF formulation in the Wigner-Ville spectrum results in a time-variant channel Doppler spectrum that is only a function of the time index n. The unsymmetrical channel ACF formulation underlying instantaneous power spectrum technique results in time-varying channel spectrum that is not only a function of time index n but the lag k as well. In this section we seek to explore the impact of mobile acceleration on the overall performance of the wireless communications system. We also investigate the role played by the carrier frequency and initial mobile velocity on the channel coherence time T_c with accelerating mobile receiver.

In the non-stationary channel under consideration, T_c which is directly related to the Doppler spread of the channel also turns out to be time-varying. Using (4.106), (4.108), (4.109) and (4.110), we get the following relationships between T_c (in number

of symbols) and instantaneous Doppler spread respectively for WVD and MIPS

$$\widetilde{T}_{c,n} = 1.3289\,\lambda_c \left(|\boldsymbol{v}_0| T_s \left(1 + \left(\frac{\alpha n T_s}{|\boldsymbol{v}_0|} \right) \right) \right)^{-1}, \tag{4.130}$$

$$\widehat{T}_{c,n} = 2.6578\ \lambda_c \left(|\boldsymbol{v}_0| T_s \left(1 + \frac{\alpha T_s\,(n + 0.5\,k)}{|\boldsymbol{v}_0|} \right) \right)^{-1}, \tag{4.131}$$

where $|\boldsymbol{v}_0| > 0$.

The knowledge of T_c enables the communication system designer to design the basic transmission unit at the physical layer commonly called radio frame [207] (or a time slot). We denote the duration of the radio frame as T_{rf}. A generic radio frame with dedicated portions for overhead (including channel estimation, channel signaling) and payload is shown in Fig. 4.10. Usually the radio frame has to perform the following tasks [208]:

- Time structuring of the radio interface,
- To provide the receiver with updated channel estimates so as to assist the receiver with power control
- To assist receiver synchronization,
- Transportation of signaling and user data (payload).

The assumption of quasi-static fading[16] is true only if the radio frame duration is much smaller than T_c. In other words, for stable channel estimation and, hence, reliable information transmission, the size of the radio frame must be adapted to the time-varying T_c in accelerating mobile environment. One of the design goals in communication system design is to keep the signaling and channel estimation overhead to as small a fraction of the radio frame as possible because the time slots used up by overhead do not carry any payload. However, the overhead provides the receiver with useful information to facilitate the receiver with auxiliary information for proper decoding the received payload. While the optimal design of the frame duration must depend on the particular application requirements, we shall follow [208] to assume that the radio frame duration is 10% of T_c, *i.e.*,

$$T_{rf} = 0.1\,T_c, \tag{4.132}$$

[16]Precisely speaking, the assumption of quasi-static fading is not applicable in time (and/or frequency selective) channels. However, by keeping the length of the radio frame sufficiently smaller than T_c, the channel fading can approximately be assumed as quasi-static. The wireless communication systems are always designed to transmit data in short frames to optimize the sharing of available resources and to provide the receiver with regular auxiliary information in the form of overhead and coded user data to facilitate reliable decoding of the received information.

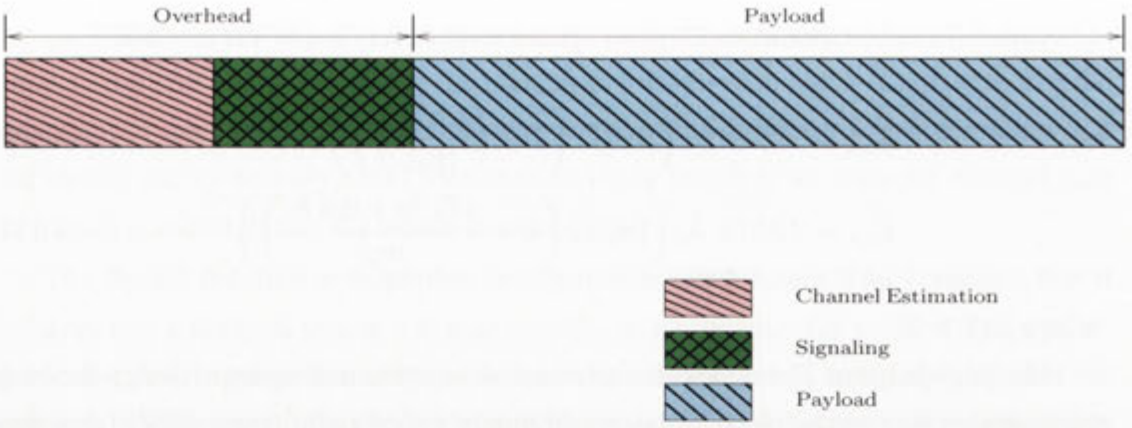

Figure 4.10: The general structure of a transmission frame.

where T_c (in number of symbols) is given (4.109) and (4.110) respectively for WVD and MIPS spectra. While it is possible to adapt the frame overload to the prevailing channel conditions[17] provided that certain parameters are known a priori at the transmitter, we shall assume [208] that the frame overload is $1/4$ of the frame length at 6 GHz and $|\boldsymbol{v}_0| = 250$ km/hr, and remains constant as the channel dynamics change over time implying that the receiver can have the knowledge of the instantaneous channel statistics (and hence the fading rate) but the transmitter may not so that no overhead adaptation is possible. An implication of the assumption of fixed frame overhead is that any channel dynamics affecting the channel coherence time T_c and, therefore, T_{rf} would result in a change in the size of the useful payload.

4.7.1 Numerical Analysis and Discussion

In this section, we aim to give quantitative impact of mobile acceleration as a function of carrier frequency and the initial velocity of the mobile on channel coherence time and, in fact, the radio frame in the context of some state-of-the-art and future communication systems. Since the channel gain is assumed to be constant over the duration of the radio frame, the mobile acceleration would not affect the quality of estimation within one frame. However, any (possibly adaptive[18]) channel estimation strategy that takes into account the channel gains over multiple frames (destined for the same user) for prediction or interpolation of channel estimates would obviously be affected by the mobile acceleration. For the sake of brevity and simplification, we shall consider only the channel coherence dynamics for WVD as defined in (4.130).

[17] When the channel fading is quite slow, for example, it may be possible to reduce the training bits (and hence the frame overhead) in the radio frame so as to include more user data.

[18] Such scheme corresponds to adaptive overhead scenario. This scheme may not use equal number of pilots in all frames destined for the same user.

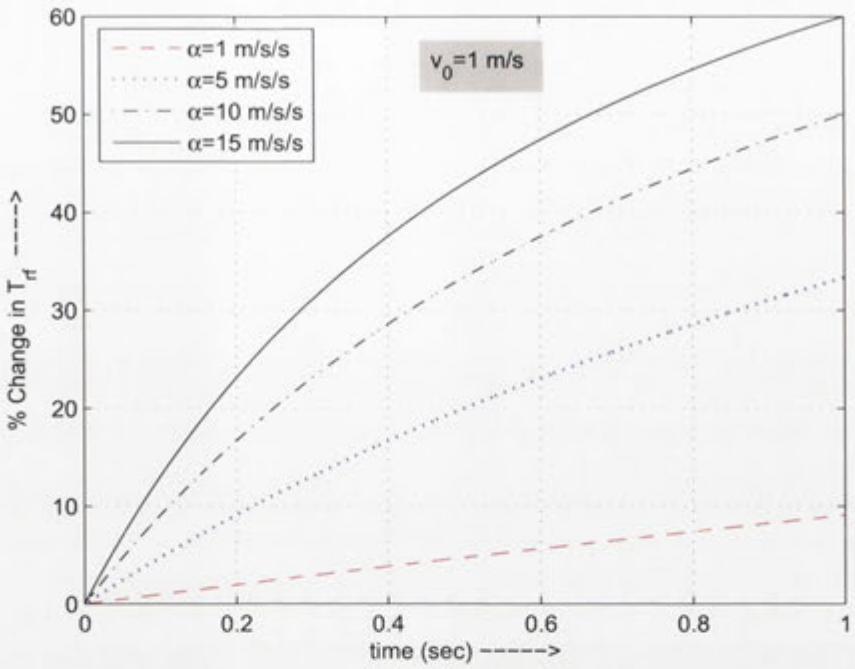

Figure 4.11: The instantaneous percentage decrease in the duration of radio frame (with respect to $\alpha = 0$m/sec) for different mobile accelerations assuming mobile speed of 1 m/s, $T_s = 3.69$ micro second and $f_c = 2$ GHz. Notice that the carrier frequency and the symbol duration correspond to GSM communications.

Equations (4.130) suggests that the change in channel coherence due to mobile acceleration is dependent on

- the absolute time index n
- the initial mobile speed $|\boldsymbol{v}_0|$
- the carrier wavelength λ_c (or, equivalently, carrier frequency)
- the symbol rate.

As the time progresses, the accelerating mobile gains more speed so that the channel coherence time being a function of mobile speed becomes dependent on the absolute time index n. In Fig. 4.11, we have plotted instantaneous percentage decrease in radio frame duration T_{rf} for different accelerations[19]. The percentage decrease in T_{rf} has been

[19]The accelerations below or equal to 1 m/sec^2 are representatives of the pedestrian (or vehicle) acceleration whereas the acceleration between 1-5 represent the vehicle accelerations. The accelerations beyond 5m/sec^2 have been chosen for our model calculations.

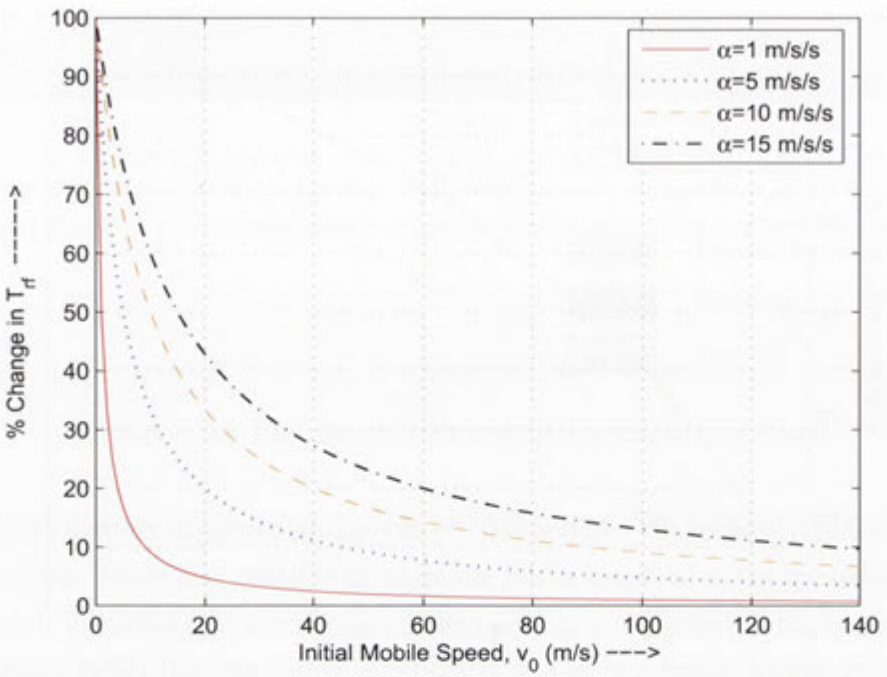

Figure 4.12: The percentage change in the duration of radio frame assuming GSM carrier frequency and symbol rate for different mobile accelerations as a function of mobile speed.

defined with respect to $\alpha = 0\text{m/sec}^2$. Mathematically,

$$\%\ \text{Decrease in } \mathrm{T_{rf}} \triangleq \frac{T_rf\Big|_{\alpha} - T_rf\Big|_{\alpha=0}}{T_rf\Big|_{\alpha=0}} \times 100 \tag{4.133}$$

where $T_rf|_{\alpha}$ indicates the radio frame duration for a particular $\alpha > 0$. The figure suggests a linear percentage decrease in T_rf for smaller α whereas the decrease becomes increasingly non-linear for larger α. The instantaneous radio frame duration for $\alpha = 15$ m/sec^2 decreases by $\approx 60\%$ after just 1 second of mobile movement. Similarly, Fig. 4.12 depicts the percentage decrease in T_rf with acceleration as a function of the initial mobile speed. Notice that the mobile acceleration impact is more pronounced for smaller $|\boldsymbol{v}_0|$ (*i.e.*, for slow to moderate fading channels). At higher $|\boldsymbol{v}_0|$ (*i.e.*, for faster fading channels), the decrease in T_rf turns out to be $\leqslant 10\%$. This implies that the communication schemes exploiting slow fading character of the wireless channel by sending data in large blocks seem to have greater need to take the mobile acceleration into account.

The future wireless communications standards specify the use of higher carrier frequencies for wireless communications. The WiMax standard, for example, proposes the use of 5-10 GHz as carrier frequency. In [208], the feasibility of higher carrier frequen-

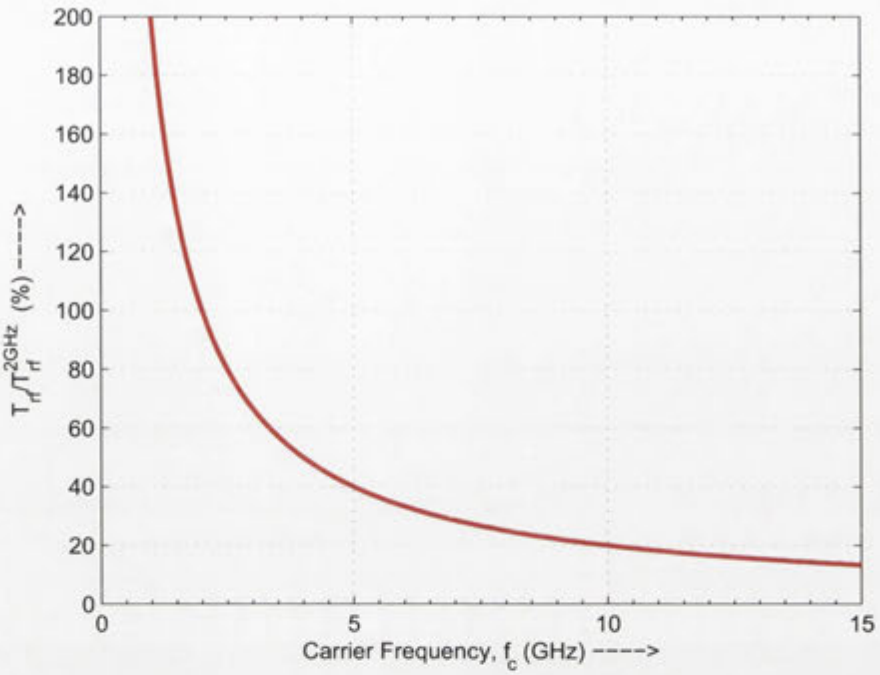

Figure 4.13: The percentage normalized radio frame length as a function of carrier frequency. This is a fundamental result which is independent of the mobile speed, acceleration and the absolute time index n as long as these parameters are assumed to be the same for $f_c \neq 2$ GHz and $f_c = 2$ GHz.

cies as compared to 2 GHz has been discussed assuming constant mobile velocity. It was concluded that the the suitable spectrum should be chosen as close as possible to the state-of-the-art mobile communication systems. The maximum tolerable frequency was argued to be around 6 GHz. It is of some interest to see as to what impact the mobile acceleration may have on mobile communications at higher carrier frequencies? The Fig. 4.13 shows a fundamental result quantifying the effect of changing carrier frequency on the duration of radio frame normalized[20] to the radio frame length at $f_c = 2$ GHz. This result is independent of mobile velocity, acceleration and, even, the absolute time index n as long these parameters are kept to be the same for $f_c = 2$ GHz and any other frequency being compared. Using (4.130) and (4.132), it is easily shown that normalized percentage radio frame duration denoted by T_{rf}^N is given as

$$T_{rf}^N\Big|_{f_c} \triangleq \left(\frac{T_{rf}\Big|_{f_c}}{T_{rf}\Big|_{f_c=2\text{G}}} \right) \times 100,$$

[20]In the sequel, unless otherwise specified, we use the term *normalized* to mean normalization of a particular parameter to its value at $f_c = 2$ GHz.

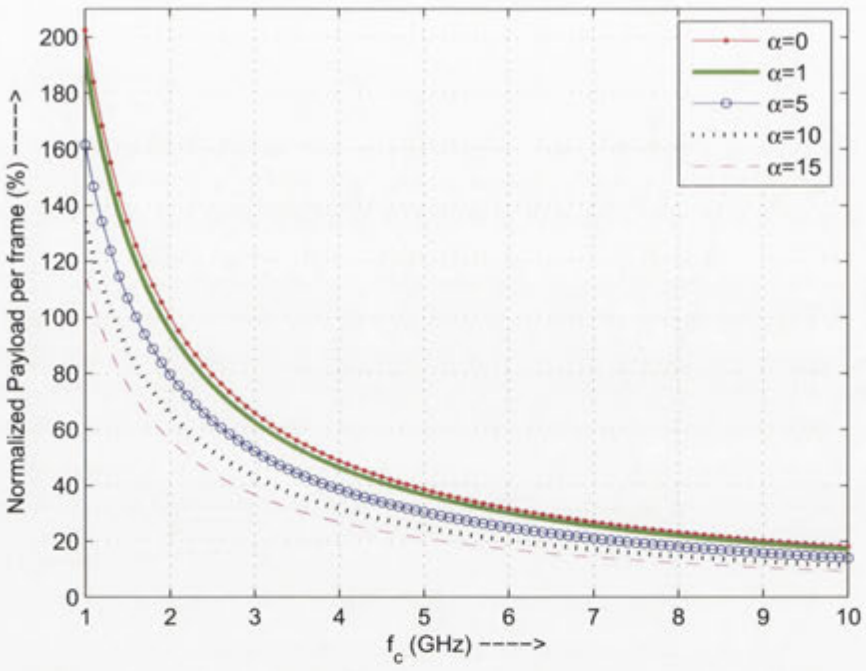

Figure 4.14: The normalized percentage payload per second (after 1 sec) as a function of carrier frequency for different mobile accelerations assuming the symbol rate as that of GSM and mobile speed as 72 km/hr.

$$= \frac{\lambda_c}{\lambda_c^{2G}}, \tag{4.134}$$

where λ_c^{2G} is the carrier wavelength at 2 GHz. Fig. 4.13 is simply a plot of (4.134) suggesting that T_{rf} at 10 GHz reduces to just 20% of that at 2 GHz.

The normalized payload per frame after 1 second of mobile movement is shown in Fig. 4.14 as a function of carrier frequency. Notice that the effect of acceleration is emphasized at lower carrier frequencies. At an acceleration of 5 m/sec^2 and 2GHz carrier frequency, the payload per frame is 20% lower than without acceleration at the same frequency. At 6GHz, the payload per frame with acceleration of 5 m/sec^2 reduces by just over 75% which is quite significant.

Since we have assumed the frame overhead to be constant, any changes in coherence time (or radio frame duration) due to mobility must be at the cost of payload. It may be of interest to have an idea of the mobile acceleration impact on the *integrated* number of frames, overhead and payload for wireless transmission spanning 1 second. Fig. 4.15 shows the instantaneous integrated number of radio frames that can be transmitted at different frequencies and accelerations. When $\alpha = 1$ m/sec^2, the number of transmittable frames is approximately insensitive to a change in time for different frequencies whereas rise in umber of frames is noticeable when $\alpha = 5$ m/sec^2. It may be empha-

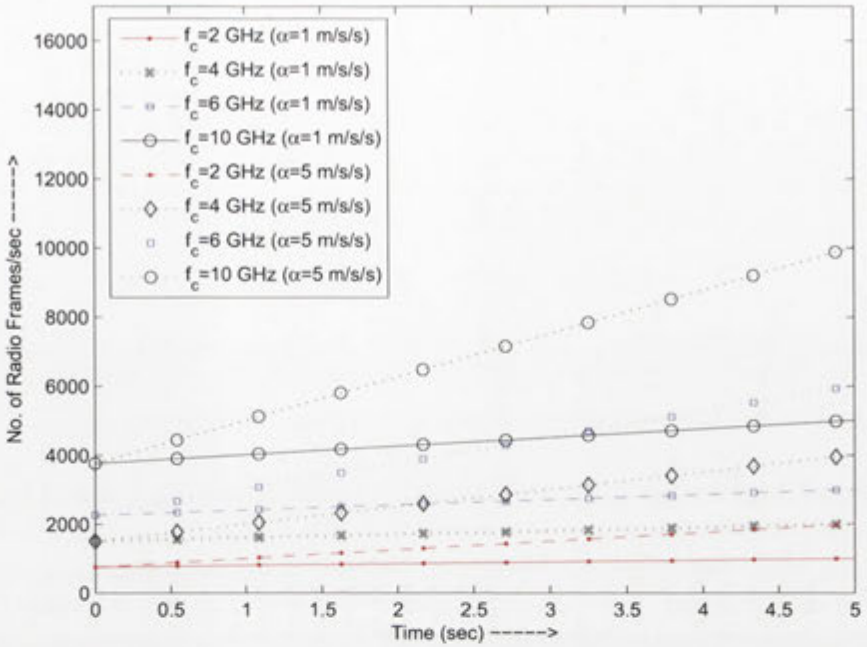

Figure 4.15: The instantaneous integrated radio frames per second for different frequencies and mobile accelerations. The symbol duration $T_s = 20$ micro second.

sized again, however, that being able to send more frames per second is not beneficial here. In fact, adding more frames per second is adding to the integrated frame overhead and reducing the integrated payload per second. Fig. 4.16 depicts the integrated number of frames per second as a percentage of the number of frames for $f_c = 2$ GHz as a function of mobile speed. Again, we can observe that low mobile speeds are more sensitive to a change in mobile acceleration. Fig. 4.17 shows the reduction in integrated payload as compared to payload at $f_c = 2$ GHz as a function of carrier frequency for different mobile accelerations. We have also plotted integrated payload per second for stationary channel ($\alpha = 0$) assuming mobile speed of 250 km/hr. In 2 seconds, the mobile moving with initial speed of 50 km/hr and acceleration 15 m/sec^2 would have attained speed of 158 km/hr. Observe that for $f_c < 4$ GHz, the accelerating mobile scenario where the mobile achieves speed of 158 km/hr behaves worse than the stationary channel case with mobile speed 250 km/hr. Similarly, the normalized integrated overhead per second shown in Fig. 4.18 suggests a linear increase in overhead with increasing carrier frequency. The figure shows that a mobile moving with initial speed of 100 km/hr and acceleration of 15 m/sec^2 supposed to achieve speed of 208 km/hr is worse than a mobile moving with no acceleration but speed of 250 km/hr (which is obviously greater than 208 km/hr). At 6 GHz, the normalized integrated overhead per second rises to 400% for mobile acceleration of 5 m/sec^2.

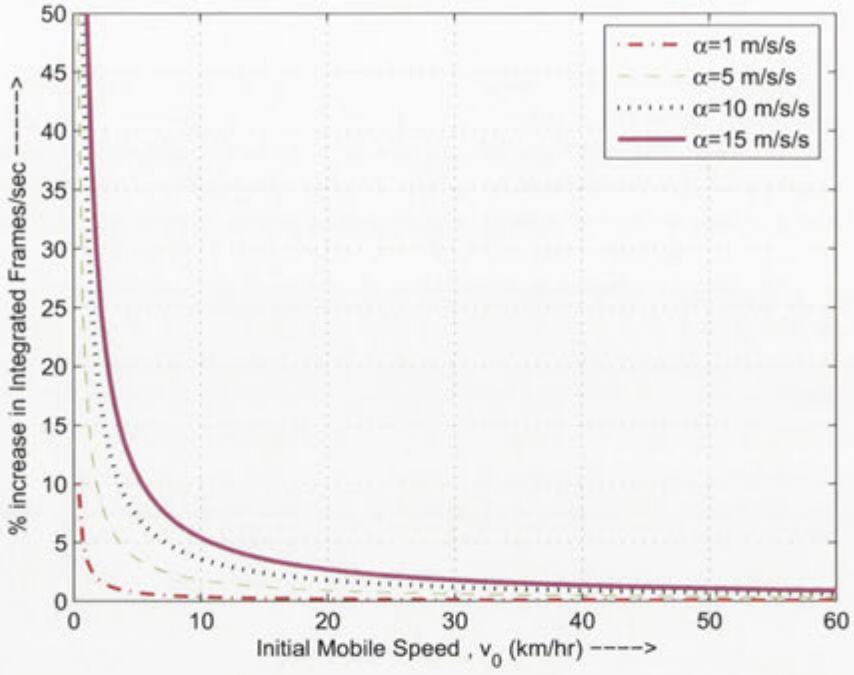

Figure 4.16: The percentage increase in integrated radio frames per second (assuming $nT_s = 1$ second) for different frequencies as compared to $f_c = 2$ GHz. The results are given for different accelerations as a function of mobile speed. The symbol duration $T_s = 20$ micro second.

The results suggest that the performance of a communication system in terms of data rate is more (less) sensitive to acceleration at lower (higher) mobile velocities. Finally, the calculations in this chapter have been based on the Doppler spectrum of the SISO channel. The overall performance of emerging wireless networks might depend on channel dynamics in more complicated ways and the results could be different. In Chapter 2, we observed a significant slowing down of the channel dynamics with non-isotropic reception. We argue that the use of a directional antenna in accelerating mobile case would lead to significant reduction in dependence of channel dynamics (and, therefore, channel coherence) on mobile acceleration.

The numerical results presented here taking into account the mobile acceleration reinforce the conclusion drawn in [208] that the spectrum of future wireless mobile communications systems should be chosen as close as possible to the state-of-the-art systems. The mobile acceleration renders the channel dynamics even worse resulting in less overall data rate. The rise of integrated overhead per second to 400% at 6 GHz significantly adds to the complexity (and hence power requirements) at the mobile receiver which is of course not desirable for power-limited mobile terminals suggesting the use of lower carrier frequencies. While the use of lower carrier frequencies might result in en-

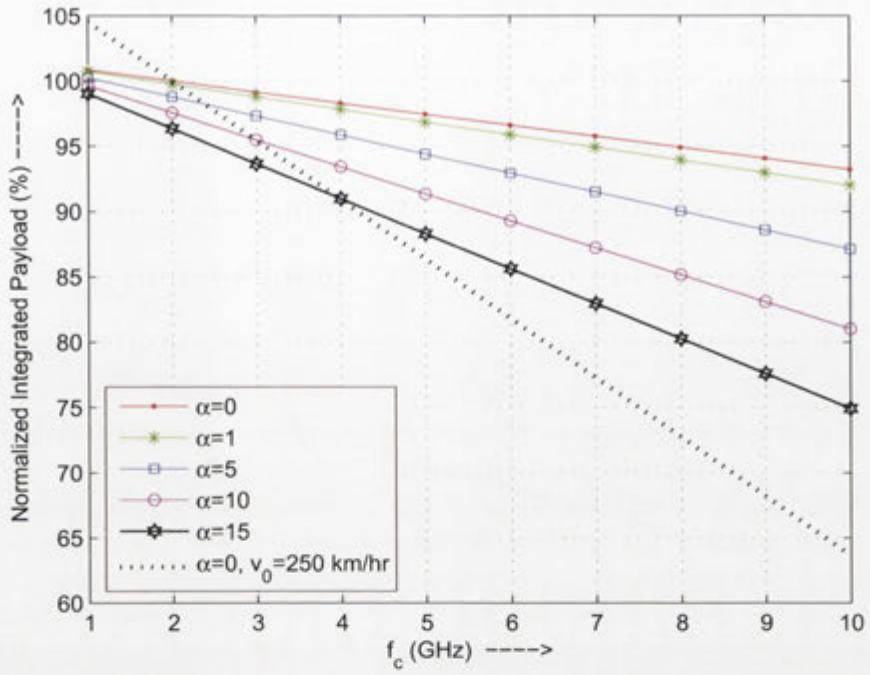

Figure 4.17: The normalized integrated payload per second (after 2 sec) as a function of carrier frequency assuming the symbol rate as that of GSM and mobile speed as 50km/hr.

hanced transmission efficiency, less cost of the semiconductor devices and components, reduced complexity and decreased power consumption at the mobile receiver, there are many merits of choosing a higher carrier frequency for wireless communication, *e.g.*, as the carrier frequency is raised [208]

- more spectrum becomes available in view of the fact that spectrum allocations are usually in direct proportion to the frequency of the band which implies availability of higher data rates (capacity).

- it is possible to employ low order modulation schemes (*e.g.*, instead of 8-PSK we might be able to use 4-PSK or even BPSK) yet maintaining the same system capacity by using large bandwidth resulting in reduced carrier to noise and interference requirements for the system which actually enhances the range of the wireless communications systems.

- the financial cost of licensing is significantly reduced in view of the fact that higher frequencies are considered less 'favorable' and the optimized frequency bands are very expensive due to higher demand.

- the gain of the (dish) antennas being employed is expected to be higher since, in general, antennas have higher gain at higher frequencies. This merit though may

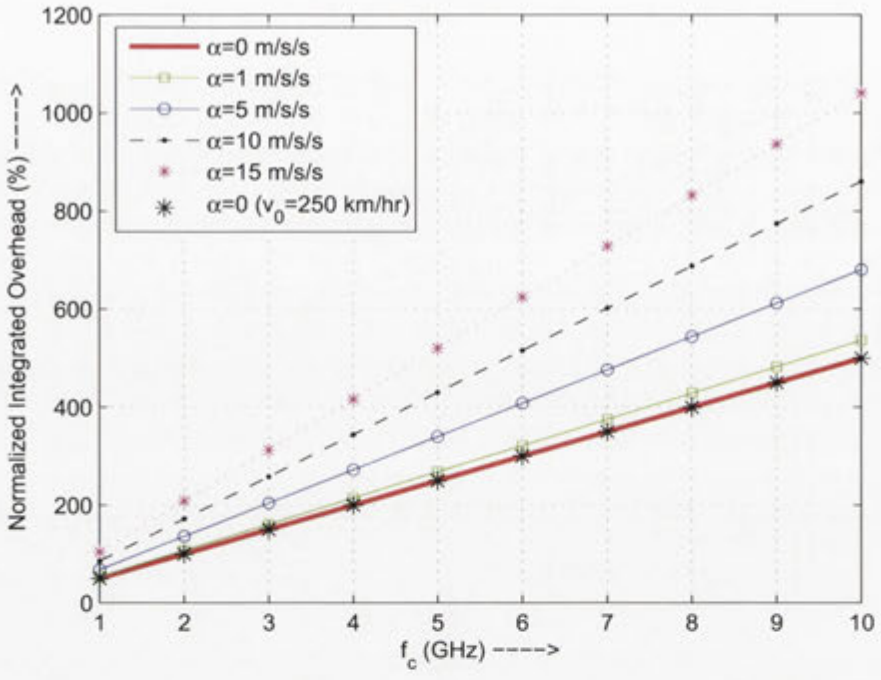

Figure 4.18: The normalized percentage integrated frame overhead per second (after 2 sec) as a function of carrier frequency for different mobile accelerations assuming the symbol rate as that of GSM and mobile speed as 100 km/hr.

not be very attractive because the mobile communication devices use dipole antenna which exhibit a different performance as compared to a dish antenna. Moreover, an increase in antenna gain inherently makes antenna directional which necessitates some sort of dynamic controlling of the directivity for correct alignment of the antennas. It may here be pointed out that the discussion on the directional antenna and scattering in Chapter 2 naturally applies to wireless communications at higher carrier frequencies due to antenna directivity.

- it becomes possible to make mobile terminals based on multiple-input multiple-output (MIMO) technology (which is an integral part of any future communications system) more compact because at higher frequencies the size of antennas and the displacement between antennas is reduced.

- the use of relaying and adaptive antennas in future communications systems can overcome the inherent problem of short range while communicating at higher frequencies.

4.8 Summary and Contributions

This chapter presents a generalization of Clarke's model from mobile motion with constant velocity to constant acceleration. The mobile motion with constant acceleration through sufficiently rich statistically homogeneous scattering environment renders the channel process non-stationary assuming unbounded mobile velocity and infinite sampling rate. We derived Wigner-Ville distribution (VWD) and instantaneous power spectrum (IPS) for the non-stationary complex Gaussian process. It turned out that DWVD represents a natural generalization of the Clarke's model and retains the U-shaped characteristic of the spectrum. On the other hand, IPS spectrum representation is more involved as a result of ACF involving Bessel function with quadratic argument. The effect of bounded mobile velocity and finite sampling rate is also discussed. The impact of mobile acceleration on the performance of communications systems was also discussed. The results suggest that the acceleration affects the performance when the initial mobile velocity and the carrier frequency are low. The non-coherent communications at higher carrier frequencies is infeasible if the mobile moves with constant acceleration.

The specific contributions of this chapter are summarized below.

- We generalize the Clarke's well known model of mobile radio reception which assumes the mobile motion with constant velocity to mobile motion with constant acceleration. The expressions for VWD and IPS are derived for the non-stationary complex Gaussian channel process under the assumptions of unbounded mobile velocity and infinite sampling rate. The VWD turns out to be a natural generalization of the Clarke's stationary model to non-stationary scenario.

- We discuss the impact of mobile acceleration when the mobile velocity remains bounded and the channel sampling rate is finite.

- The impact of mobile acceleration on the performance of communications systems is explored in terms of frame overhead and payload. The results suggest that it is more infeasible to communicate at higher carrier frequencies if the mobile moves with constant acceleration.

Chapter 5

Improved MMSE Performance of PACE over Rayleigh Fading Channels Using Modified Peaky Signaling

5.1 Introduction

A wide variety of digital communication systems (particularly in wireless, satellite, deep-space, and sensor networks) operate in the power-limited (or, equivalently, wide-band) region [209] where the so-called *peaky signaling* is known to achieve capacity of a noncoherent average power constrained Rayleigh fading channel. The pilot-aided channel estimation (PACE) in conjunction with peaky signaling results in improved performance over Rayleigh fading channel at low signal-to-noise ratio (SNR) [78]. Since the peaky signaling remains silent most of the time, a significant number of *dof* may be lost. It is therefore of some interest to make use of the unused degrees of freedom to enhance the performance of the communication systems operating at very low SNR. In this chapter, we seek to answer three questions regarding a PACE based system over continuously fading Rayleigh channel employing peaky signaling. Firstly, how to make use of the unused degrees of freedom in the peaky signaling to improve minimum mean square error (MMSE) performance of PACE scheme? Secondly, how does improved MMSE performance affect the optimum resource allocation between pilot/data symbols? Thirdly, what is the impact of any change in the optimum resource allocation on overall gains in communication system performance?

The accurate knowledge of channel state information (CSI) quite significantly affects the performance of wireless communication systems because it permits the realization of coherent demodulation. In PACE, pilot symbols are time-multiplexed into the data stream [140]. The channel estimates obtained at pilot symbol locations are then used to

predict or interpolate the channel estimates at data symbol locations for demodulation. The channel estimates thus obtained and subsequent demodulation, is imperfect due to the presence of noise and, therefore, the performance of the communication system is directly affected by the level of noise that corrupts pilot symbols [136, 210]. The pilot symbol SNR can be enhanced either by allocating more power to pilot symbols or by reducing the noise. Since power is a precious resource, it may not be feasible in most instances to allocate more power to pilot symbols. It is, therefore, of fundamental interest to devise some method to mitigate the degrading noise.

Generally speaking, PACE is based on either the least squares (LS) or the linear MMSE (LMMSE) technique (an approximation of MMSE[1]) [211–214]. The essential difference between these two types of techniques is that the channel coefficients are treated as deterministic but unknown constants in the former, and as random variables of a stochastic process in the latter. Compared with LS-based techniques, LMMSE-based techniques yield better performance because they additionally exploit and require prior knowledge of the channel correlation.

A technique based on oversampling of the pilot symbols followed by filtering and subsequent downsampling was proposed in [82] in connection with Doppler frequency estimation. We describe this overall signal processing scheme as Oversample-Low pass filter-Downsample (OLD). With an ideal low pass filter, the technique offered significant performance improvement for slow fading scenarios at low SNR. Though it was not explicitly mentioned in [82], we shall later show that ideally, at low SNR, this scheme can improve performance by as much as the *oversampling factor* by enhancing SNR by the same factor. This SNR enhancement can be explained if we consider the fact that the process of oversampling reduces the required filter bandwidth to pass the useful signal intact thus reducing the output noise by decreasing the noise bandwidth [8]. The obvious cost for the improved performance of Doppler frequency estimator proposed in [82] was increased complexity at the receiver end necessitated by oversampling of pilot symbols in addition to the filtering. We, in this chapter, propose a PACE based transmission scheme that works in conjunction with the *modified* peaky signaling which consists of unused *dof* resulting in pilots-plus-zeros stream at the receiver. The pilots-plus-zeros stream effectively represents an oversampled pilot sequence which is low pass filtered and then downsampled to obtain pilots-only sequence. Thus, the explicit oversampling as required by OLD scheme is avoided at the cost of inherent oversampling of the pilot sequence due to the peakiness of the signaling.

The peaky signaling has been well researched in literature from the point of view of

[1] If the observation process and the the parameter to be estimated are jointly Gaussian [132], MMSE and LMMSE are equivalent.

its design and performance over fading channels. With a fourthegy (a fourth-order cost function related to the number of diversity paths) constraint, it was confirmed in [215] that signals need to be peaky in time (and/or frequency) to be able to achieve constant information rates per unit power over very-wide-band wide-sense stationary uncorrelated scattering (WSSUS) fading channels [216]. Non-peaky signals like those used in direct-sequence (DS) spread-spectrum systems do not have enough fourthegy per unit energy to achieve significant values of reliably communicated bits per unit energy for a WSSUS fading channel. The performance of peaky signaling was analyzed with an average power constraint for noncoherent bandlimited multipath fading channels in [217] and lower and upper bounds to the error probability were derived. In [218], the peaky signaling was considered for fading relay channels with memory. The performance of peaky Gaussian signaling was studied for Rayleigh fading channels in the low SNR regime in [78]. The channel was assumed to remain constant over the length of the block of symbols and a lower bound to the capacity of Gaussian peaky signaling was proposed in terms of peakiness and coherence time. A comparison was also made between the peaky and non-peaky (NP) signaling schemes. We emphasize that, unlike [78], we do not make block fading assumption in this chapter. Rather, we allow the channel to continuously fade across the block of symbols.

The performance of PACE technique for non-peaky signaling over continuously fading Rayleigh channel without proposed additional filtering of pilot symbols has been considered in [88] (this work shall be taken as representative of the non-peaky signaling over time-selective rayleigh fading channels for the sake of comparison). The optimal resource allocation for pilot and data symbols was determined by maximizing the *Gaussian signaling* Rayleigh capacity lower bound. Our approach in the second part of this chapter closely follows [88, 210] to determine optimal resource allocation to pilot/data symbols in order to ascertain the impact of improved MMSE performance of the proposed scheme. To the best of our knowledge, the results reported in this chapter are not available in literature in connection with PACE based peaky signaling over time-selective fading channels.

The rest of the chapter is organized as follows. In Section 5.2 we describe the discrete time Rayleigh fading model on which the subsequent analysis is based. We also describe the proposed peaky signaling scheme. In Section 5.3 we derive an expression for MMSE assuming an infinite number of pilot symbols. The results of Section 5.3 are used in Sections 5.4-5.6 to optimize the allocation of resources to pilot and data symbols for transmission over Rayleigh fading. Finally, the chapter is summarized and specific contributions are highlighted in Section 5.7.

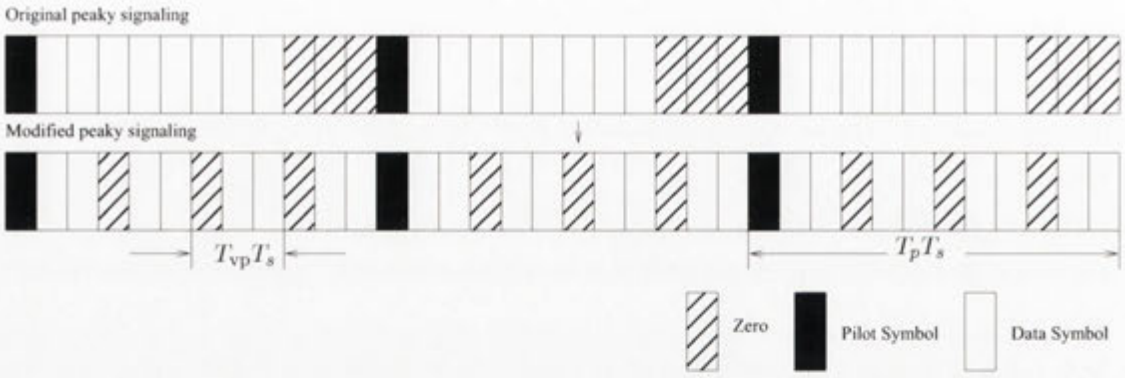

Figure 5.1: The transmitted frame format: T_s is the data symbol duration, T_p denotes pilot symbol insertion factor, the number of zeros (or, equivalently, unused *dof*) is equal to $\mathcal{M}-1$ where the factor $\mathcal{M}$ is the upsampling factor.

5.2 Channel Model and Signaling Scheme

5.2.1 Channel Model

The channel between the transmitter and the mobile receiver is modeled as a stationary, frequency non-selective circularly-symmetric complex Gaussian random process. At this point, we do not make any assumption about the scattering environment around the receiver. We use the following I/O model

$$r[m] = \sqrt{\mathcal{E}_s}\ h[m]\, s[m] + \ z[m], \tag{5.1}$$

where $r[m]$, $s[m]$, $h[m]$ and $z[m]$ respectively are the samples of complex channel output, input , gain and discrete AWGN at signaling interval m. Equation (5.1) is normalized such that $\mathbb{E}\{|s[m]|^2\} = 1$, $\mathbb{E}\{|h[m]|^2\} = 1$, $\mathbb{E}\{|z[m]|^2\} = N_0$ so that $\mathcal{E}_s\,/N_0$ represents the average received SNR per data symbol. We also assume that the data, channel and noise sequences are independent processes and channel statistics are perfectly known to the receiver. Notice that the I/O models described by (5.1) and (2.1) differ in the normalization of the noise process.

5.2.2 Modified Peaky Signaling Scheme

We consider a slight *modification*[2] of the original peaky signaling scheme with $\mathcal{M}-1$ unused degrees of freedom of the original peaky signaling rearranged as shown in Fig. 5.1 where the factor $\mathcal{M}$ can be considered as *upsampling factor* [114]. It is assumed that

[2]This modification is assumed to facilitate the process of demultiplexing at the receiver. If we are to use the conventional peaky signaling, a little thought would reveal that we shall need to incorporate a more complex demultiplexer (Fig. 5.1).

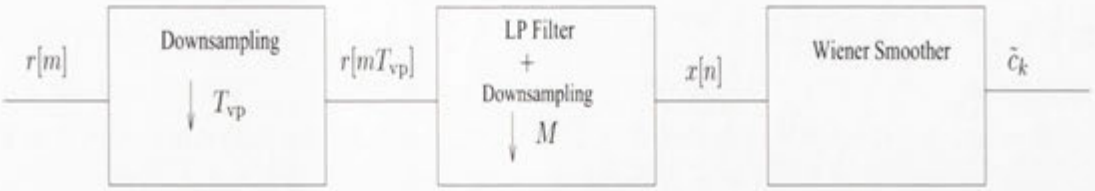

Figure 5.2: The proposed scheme: The pilot symbols extracted from filtered sequence of received symbols are passed through Wiener smoother to get improved channel estimates at data symbol locations.

the pilot symbols are inserted in the transmitted stream at least at the Nyquist rate, *i.e.*, $2f_{\mathrm{D}}$ where f_{D} is the channel fading rate normalized to the symbol rate, $1/T_s$.

Traditionally, as we know, the received pilots-plus-data symbols stream is downsampled to separate pilot and data streams. The pilot symbol sequence is first used to estimate the channel gains at pilot symbol instants. These channel estimates are then interpolated to obtain channel estimates at data symbol locations. The use of OLD processing scheme requiring an oversampled pilot symbol stream improves the performance of PACE [82]. In this chapter, we propose a scheme (Fig. 5.2) which is based on the same OLD processing scheme but does not require explicit oversampling of the pilot observation process at the receiver. This scheme makes use of the unused *dof* in the transmitted stream to obtain improved channel estimates at the receiver. In the proposed scheme, the symbol stream to be transmitted consists of pilot and data symbols, and, in addition, $\mathcal{M}-1$ zeros[3] multiplexed between two consecutive pilot symbols in the stream. If we assume that the total available power is $T_p\mathcal{E}_s$, the unused *dof* result in savings in transmitted power corresponding to zeros giving rise to the following four possible transmission schemes.

No Enhancement (NE) Scheme

One of the possibilities is not to use savings in power implying that the average pilot symbol power and data symbol powers are equal. Though the total power used by this scheme is less than that of NP scheme, the performance of this scheme is intuitively inferior to that of NP scheme which utilizes more power. From the point of view of data transmission, NE signaling scheme can be considered as *pseudo-peaky* because in this scheme only the silent period changes while the average power during the data transmission remains *fixed*.

[3]Notice that $2\leq\mathcal{M}\leq T_p-2$ is an integer where T_p is the spacing in number of symbols between two successive pilot symbols. Also, the zeros occupy data symbol locations, *i.e.*there is no bandwidth expansion, as compared to the traditional schemes, due to the insertion of zeros.

Pilot Enhancement (PE) Scheme

The second possibility is to use the power savings to enhance the power of the pilot symbols only. When the number of unused *dof* is $\mathcal{M}$, the pilot symbol power in PE scheme would be, *i.e.*:

$$\mathcal{E}_p^{\mathrm{PE}\dagger} = \mathcal{M}\mathcal{E}_s\,, \tag{5.2}$$

and the data symbol power $\mathcal{E}_d = \mathcal{E}_s$. This scheme can also be considered as *pseudo-peaky*.

Data Enhancement (DE) Scheme

The DE scheme uses savings in power to increase the power of data symbols by distributing the power savings equally over all data symbols in a transmission block. When the number of unused *dof* is $\mathcal{M}$, the number of data symbols in the block would be $T_p - M$ and the each data symbol would have the following average power

$$\mathcal{E}_d^{\mathrm{DE}\dagger} = \left(1 + \frac{\mathcal{M}-1}{T_p - \mathcal{M}}\right)\mathcal{E}_s\,, \tag{5.3}$$

and the pilot symbol power remains unaltered, *i.e.*, $\mathcal{E}_p = \mathcal{E}_s$. As the peakiness of the signaling increases, this scheme concentrates more and more power in time. The DE scheme therefore can be considered as peaky in the usual sense.

Pilot and Data Enhancement (PDE) scheme

This scheme uses the power savings to enhance power of the pilot and data symbols by distributing the power savings equally over the non-zero symbols in the transmission block. The resulting data symbol power would be

$$\begin{aligned}\mathcal{E}_d^{\mathrm{PDE}\dagger} &= \left(1 + \frac{\mathcal{M}-1}{T_p - \mathcal{M}+1}\right)\mathcal{E}_s\,, \\ &= \mathcal{E}_p^{\mathrm{PDE}\dagger}\,.\end{aligned} \tag{5.4}$$

The PDE scheme, like DE scheme, can be considered as peaky signaling in the true sense.

In this chapter, we shall extensively compare the performances of PE, DE and PDE schemes with non-peaky[4] (NP) signaling scheme and appropriate subscripts (or super-

[4]Unless otherwise specified, wherever in the sequel we refer to the performance of non-peaky (NP) signaling, we would imply the work of [88].

scripts) shall be used to identify a particular scheme.

5.2.3 Specification of Transmission Parameters

We assume the following (Fig. 5.3)

$$\frac{1}{T_s} = N\, 2f_{\mathrm{d}}, \tag{5.5}$$

where f_{d} is the maximum Doppler frequency in the Doppler spectrum of the channel and N is an integer. Equation 5.5 implies that *symbol rate* sampling results in channel being oversampled by the integer factor $N > 1$. Assuming that all pilot symbols are set equal to one, pilot symbols and zeros are time-multiplexed into data symbols at regular intervals and pilot symbols are obtained by 2-stage downsampling as shown in Fig. 5.3, following relationships hold:

$$\mathcal{M} = \frac{T_p}{T_{\mathrm{vp}}}, \tag{5.6}$$

where T_{vp} is the spacing between a pilot symbol and the succeeding zero, and

$$\frac{1}{T_p} = K 2f_{\mathrm{D}}, \tag{5.7}$$

where integer $K \geq 1$ is the channel oversampling factor at pilot symbol rate and f_{D} is the channel fading rate normalized by the symbol rate. Equations (5.5)-(5.7) imply that

$$\begin{aligned} \frac{N}{K} &= \frac{T_p}{T_s}, \\ &> 1, \end{aligned} \tag{5.8}$$

implying that $N > K$. Using (5.6) in (5.8) implies $N < K\mathcal{M}$.

5.2.4 Process of Downsampling and Problem Statement

The received symbol stream downsampled by a factor[5] T_{vp} is, in fact, an 'upsampled' pilot sequence with $\mathcal{M} - 1$ zeros between two consecutive pilot symbols. This pilot sequence is passed through an ideal low pass filter with cut-off frequency $\omega''_N = f_{\mathrm{D}} \frac{T_p}{\mathcal{M}}$ to remove out-of-band white noise thus improving SNR at pilot symbol instants. After low pass filtering, the "upsampled" pilot symbol sequence is downsampled by a factor

[5]The subscript '*vp*' stands for *virtual pilots* with transmitted pilots-cum-zeros considered as virtual pilot sequence (because the zeros do not convey any data but facilitate channel estimation at the receiver). T_{vp}, therefore, stands for the pilots-cum-zeros insertion period.

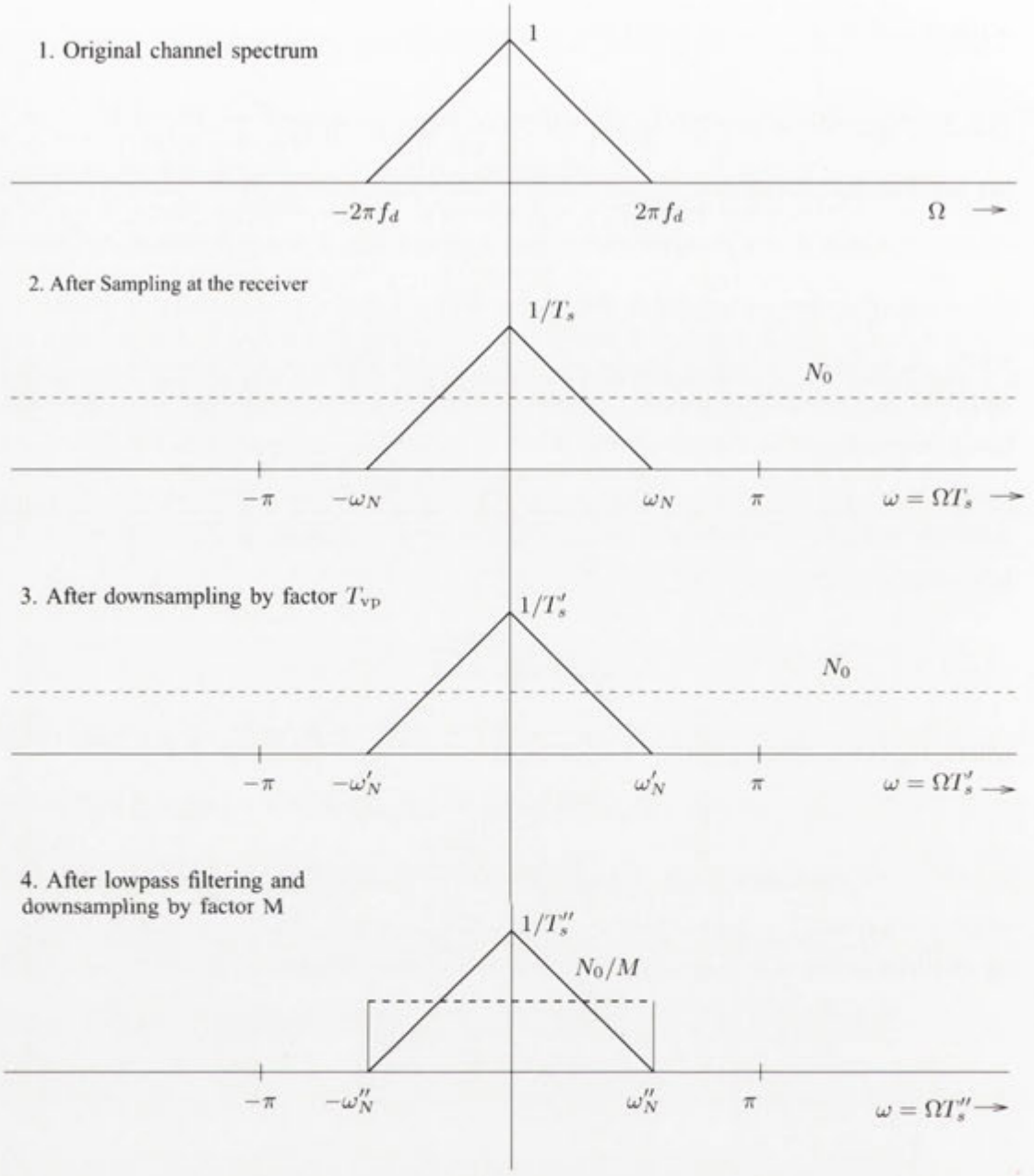

Figure 5.3: The spectra of the channel and the noise. We assume that the pilot symbols are all set to 1.

$\mathcal{M}$ to get actual pilot symbol sequence without any zeros. If $x[n]$ is the output during pilot symbol at nth pilot symbol instant, we have

$$x[n] = r[nT_p] = \sqrt{\mathcal{E}_p}\ h[nT_p] + z[nT_p], \tag{5.9}$$

where $\mathcal{E}_p$ is the average energy per pilot symbol. Since we wish to obtain MMSE estimate at data symbol locations which are shifted with respect to pilot symbol locations,

we need to define the following shifted and sampled channel process

$$c_k[n] = h[nT_p + k], \qquad 0 \leq k \leq T_p - 1 \tag{5.10}$$

where $c_k[\cdot]$ represents the *channel gain* at delay of k symbols from the pilot symbol at instant nT_{p}. Obviously, when $k = 0$, the shifted channel process $\{c_k\}$ is identical to the original channel process $\{h\}$.

Remarks

1. Notice that the filtering has been proposed for the pilots-plus-zeros symbol stream. This filtering is in addition to the analog prefiltering of the received symbol stream before the sampler at the receiver. Since the symbol stream consists of data-plus-pilot symbols (along with zeros) at the input of the analog prefilter, the cut-off frequency of the analog prefilter has to be much larger than the channel spectrum because the cut-off frequency of the analog prefilter has to be ideally equal to (or greater than) the highest frequency in the convoluted spectrum[6] of the spectra of data and channel so as not to lose any useful information of the data or the channel. Since the bandwidth of the mobile channel is not more than few hundred Hz in the worst case, from the channel estimation point of view, the unavoidable out-of-band noise allowed into the receiver by analog prefilter significantly reduces SNR at pilot symbol instants. The same SNR degradation would result if we opt to perform proposed (digital) filtering before downsampling by the factor T_{vp}. It may also be observed that the PSD of white noise after downsampling by T_{vp} remained unaltered which is due to the fact that previously white noise remains white (with identical variance) after downsampling [219].

2. The downsampling by factor $\mathcal{M}$ in Fig. 5.3 does not improve SNR because the power of neither the noise nor the useful channel signal changes. However, this downsampling operation is required to get rid of the unused *dof* in the symbol stream before pilot symbols are input to the Wiener filter. More importantly, this operation brings the factor $\mathcal{M}$, which is a measure of peakiness of the signaling, into the final MMSE expression.

[6] It is well known that the multiplication of two functions in the time domain is equivalent to convolution in the frequency domain and vice versa [114].

5.3 Derivation of Optimal Wiener Smoother and MMSE

While the analysis can be carried out for finite pilot symbols in a finite transmission block length, we assume, in an information theoretic context, that the transmission block length is infinite and so are the pilot symbols. Fig. 5.3 shows the channel Doppler and noise spectra at different stages in the proposed scheme. Using (5.5), (5.6) and (5.8), we can see that

$$\omega_N = \frac{\pi}{N} = 2\pi f_{\mathrm{D}},\ \omega'_N = 2\pi f_{\mathrm{D}} \frac{T_p}{\mathcal{M}},\ \omega''_N = 2\pi f_{\mathrm{D}} T_p,$$

and

$$T'_s = T_s T_{\mathrm{vp}},\ T''_s = T_s \frac{T_p}{\mathcal{M}N}.$$

In order to explore the limiting performance of the proposed scheme, we input noisy pilot sequence $x[n]$ to the Wiener filter (Fig. 5.2) which is optimal in the mean-squared error sense. We know from classical Wiener filter theory [220] that the transfer function of optimal infinite impulse response (IIR) MMSE Wiener filter $W_{o,k}$ is given in frequency domain as

$$W_{o,k}(\omega) = \frac{\mathcal{S}_{c_k x}(\omega)}{\mathcal{S}_{xx}(\omega)}, \tag{5.11}$$

where $\mathcal{S}_{c_k x}(\omega)$ is the cross-spectral density of the pilot observation process and channel gain at data symbol shifted k symbols from the pilot symbol, and $\mathcal{S}_{xx}(\omega)$ is the spectral density of the pilot observation process. In the Appendix D.1, we show that the optimal Wiener filter and the corresponding MMSE, σ_ϵ^2 for the proposed scheme are given respectively as

$$W_{o,k}(\omega) = \exp(i\omega k)\, \frac{1}{T_p} \frac{\sqrt{\mathcal{E}_p}\, \mathcal{S}_h\left(\frac{\omega}{T_p}\right)}{\left(\frac{N_0}{\mathcal{M}} \operatorname{rect}\left(\frac{\omega}{4\pi f_{\mathrm{D}} T_p}\right) + \frac{\mathcal{E}_p}{T_p} \mathcal{S}_h\left(\frac{\omega}{T_p}\right)\right)}, \tag{5.12}$$

$$\sigma_\epsilon^2 = \frac{1}{2\pi} \int_{-2\pi f_{\mathrm{D}}}^{2\pi f_{\mathrm{D}}} \mathcal{S}_h(\omega) \left(1 - \frac{\mathcal{E}_p\, \mathcal{S}_h(\omega)}{T_p \left(\frac{N_0}{\mathcal{M}} + \frac{\mathcal{E}_p}{T_p} \mathcal{S}_h(\omega)\right)}\right) d\omega, \tag{5.13}$$

where the factor $\exp(i\omega k)$ in (5.12) is due to the cross-spectral density, $\mathcal{S}_{c_k x}(\omega)$. Equation (5.12) implies that the spectral characteristics of the Wiener filter are the same for each k except a relative phase shift proportional to k. Notice the presence of additional

(downsampling) factor $\mathcal{M}$ in the magnitude of the optimal Wiener filter and MMSE which is absent in [221] where OLD processing scheme is not employed.

There are few important questions that could be asked here: Firstly, is it not possible to obtain the same MMSE as with the proposed scheme by simply low pass filtering the received pilot symbol sequence when no zeros are transmitted, *i.e.*, the signaling is non-peaky? The answer to this question is 'No' which is, however, not quite obvious. Notice that the computation of MMSE (Eq. (5.13)) involves integration of the *ratio* of PSDs with respect to ω from $-2\pi f_{\mathrm{D}}$ to $2\pi f_{\mathrm{D}}$, *i.e.*, over the support of the original sampled channel spectrum[7]. Now if there were no zeros transmitted, we would have obtained a noisy pilot symbol sequence at the receiver by downsampling the received pilot-plus-data symbol stream by factor T_p. If this (infinite) pilot symbol sequence were passed through an ideal low pass filter, out-of-band noise would have been removed reducing the noise power (and, thus, improving the SNR) at the output of the low pass filter (Fig. 5.3). However, the noise PSD would have remained unchanged in the interval of integration. Interestingly, however, this filtering operation has no impact on the MMSE of the optimal Wiener filter and MMSE in this case is identical to MMSE given in [136,221] (where no additional filtering prior to Wiener interpolator is assumed), *i.e.*,

$$\sigma^2_{\epsilon,\mathrm{NPwF}} = \frac{1}{2\pi}\int_{-2\pi f_{\mathrm{D}}}^{2\pi f_{\mathrm{D}}} \frac{1}{2f_{\mathrm{D}}}\left(1 - \frac{\rho_p}{2f_{\mathrm{D}}T_p + \rho_p}\right) d\omega, \tag{5.14}$$

$$= \sigma^2_{\epsilon,\mathrm{NP}}, \tag{5.15}$$

where $\sigma^2_{\epsilon,\mathrm{NPwF}}$ and $\sigma^2_{\epsilon,\mathrm{NP}}$ respectively indicate MMSE for NP schemes with and without filtering. The comparison of (5.14) with (D.13) clearly shows the effect of filtering followed by downsampling. As long as the overall downsampling factor is T_p, the interval of integration and the channel PSD would be identical for all schemes. It is, then, the noise PSD that carries the difference among different schemes.

Secondly, is it not possible to first upsample (or, equivalently, oversample) the received pilot symbol sequence at the receiver by factor $\mathcal{M}$, low pass filter it and then downsample by factor $\mathcal{M}$ to obtain the same MMSE performance as with the proposed scheme, *i.e.*, enhancement of pilot symbol SNR by $\mathcal{M}$? Though not established in the literature to the best of the authors' knowledge, the answer to this question in view of foregoing explanation is 'yes'. This is the same technique that has been employed in [82]. However, as mentioned in remarks before, the complexity of the receiver would be significantly increased due to the oversampling involved. We have utilized the unused degrees of freedom in the signaling to avoid the oversampling required otherwise at the receiver.

[7]The interval of integration for NP schemes [136,221,222] and ours turns out to be the same.

5.3.1 MMSE for uniform and Clarke's Doppler Spectra

In this subsection, we specialize MMSE derived in the preceding section to two most widely used bandlimited (sampled) channel Doppler spectra. The uniform spectrum, $\mathcal{S}_{hh}^{U}(\omega)$, results when the mobile receiver is surrounded by isotropic 3D scattering

$$\mathcal{S}_{hh}^{U}(\omega) = \begin{cases} \frac{1}{2f_{\mathrm{D}}}, & |\omega| \leq 2\pi f_{\mathrm{D}}; \\ 0, & \text{otherwise.} \end{cases} \tag{5.16}$$

and classical U-shaped Clarke's spectrum, $\mathcal{S}_{hh}^{C}(\omega)$, which results when there is isotropic scattering in 2D around the mobile receiver

$$\mathcal{S}_{hh}^{C}(\omega) = \begin{cases} 2/\left(\omega_{\mathrm{D}}\sqrt{1-(\omega/\omega_{\mathrm{D}})}\right), & |\omega| \leq 2\pi f_{\mathrm{D}}; \\ 0, & \text{otherwise.} \end{cases} \tag{5.17}$$

In the Appendix D.2, we show that the MMSE for the uniform and Clarke's Doppler spectra are given respectively as

$$\sigma_{U,\epsilon}^{2} = \frac{2f_{\mathrm{D}}T_p}{2f_{\mathrm{D}}T_p + \mathcal{M}\,\rho_p}, \tag{5.18}$$

$$\sigma_{C,\epsilon}^{2} = 1 - \frac{4\chi}{\pi\sqrt{1-\chi^2}}\mathrm{arctanh}^{-1}\left(\sqrt{\frac{1-\chi}{1+\chi}}\right), \tag{5.19}$$

where $\chi := \mathcal{M}\,\rho_p/(\pi f_{\mathrm{D}}T_p)$.

5.3.2 MMSE Performance: Proposed Signaling versus Non-Peaky Signaling Scheme

In order to draw a comparison of the MMSE performance of the proposed scheme with NP scheme, we define the following:

$$\mathrm{MMSEgain} = \mathcal{G} = \sigma_{\epsilon,\mathrm{NP}}^{2} - \sigma_{\epsilon,\mathrm{PwF}}^{2}, \tag{5.20}$$

$$> 0 \tag{5.21}$$

where we have used $\sigma_{\epsilon,\mathrm{NP}}^{2}$ and $\sigma_{\epsilon,\mathrm{PwF}}^{2}$ respectively to indicate MMSE for NP scheme and the proposed schemes (the subscript 'PwF' indicates peaky signaling with filtering), and the last inequality is true for $\mathcal{M} \geq 2, 0 < \rho < \infty$ which implies that, for the proposed schemes, *it is always advantageous for signaling to be more peaky from the point of view of channel estimation*. In the Appendix D.3, we show that $\mathcal{G}^{U}$ is maximum when SNR is

given as

$$\rho_p^{\mathrm{U\,max}} = \frac{2f_{\mathrm{D}}T_p}{\sqrt{\mathcal{M}}}. \tag{5.22}$$

In case of Clarke's spectrum, however, we have to resort to numerical means in order to determine $\rho_p^{\mathrm{C\,max}}$. Fortunately, however, the numerical results suggest $\rho_p^{\mathrm{C\,max}}$ does not differ from $\rho_p^{\mathrm{U\,max}}$ by a large amount and, as a rule of thumb, we can write

$$\rho_p^{\mathrm{U\,max}} \approx \rho_p^{\mathrm{C\,max}}, \tag{5.23}$$

where the approximation is found to be more accurate for smaller $\mathcal{M}$.

5.3.3 Numerical Analysis of $\mathcal{G}$

With the analytical MMSE results outlined before, we perform numerical analysis of the gains in MMSE performance achievable with the proposed scheme. The performance of the proposed scheme depends on ρ_p, normalized fading rate, the pilot-insertion period (T_p) and the number of zeros ($\mathcal{M}-1$) transmitted between two consecutive pilot symbols. The behavior of $\mathcal{G}^U$ function against ρ_p and f_{D} for $\mathcal{M}=100$ and $T_p=200$ has been plotted in Fig. 5.4 with and without PE. It can be observed that there is no use of investing power savings in enhancing pilot symbol SNR if we are operating at, at least, around -20dB. However, if the operating SNR is very low, channeling more power to pilot symbols is highly feasible. Fig. 5.5 shows the difference plot of MMSE gains in uniform and Clarke's Doppler spectra, *i.e.*, $\mathcal{G}^C-\mathcal{G}^U$ for $\mathcal{M}=\{2,25,50\}$ for fixed block length of $T_p=200$. No significant difference in MMSE gains can be observed as a function of either SNR or f_{D}. However, more precisely, Clarke's spectrum offers higher MMSE gains at low SNR for large $\mathcal{M}$. The uniform channel spectrum, on the other hand, may lead to higher MMSE gain if the operating SNR is roughly between -8dB and -30dB. These results imply that the two Doppler spectra can roughly be considered equivalent.

The impact of changing the oversampling factor K (for fixed $\mathcal{M}=10$) on MMSE gain is shown in Fig. 5.7 as a function of SNR. Qualitatively speaking, the effect of increase in K is to shift the MMSE gain curve to -SNR axis that results in better MMSE performance at low SNR. However, non-peaky schemes can fill the performance gain at moderate to high SNR when oversampling factor is high resulting in lower MMSE gain at moderate to high SNR for greater K. The effect of PE is to raise MMSE peak along with a small shift towards -SNR axis, and peak shift is equal for all K in Fig. 5.7.

The impact of normalized fading rate and pilot enhancement on MMSE performance

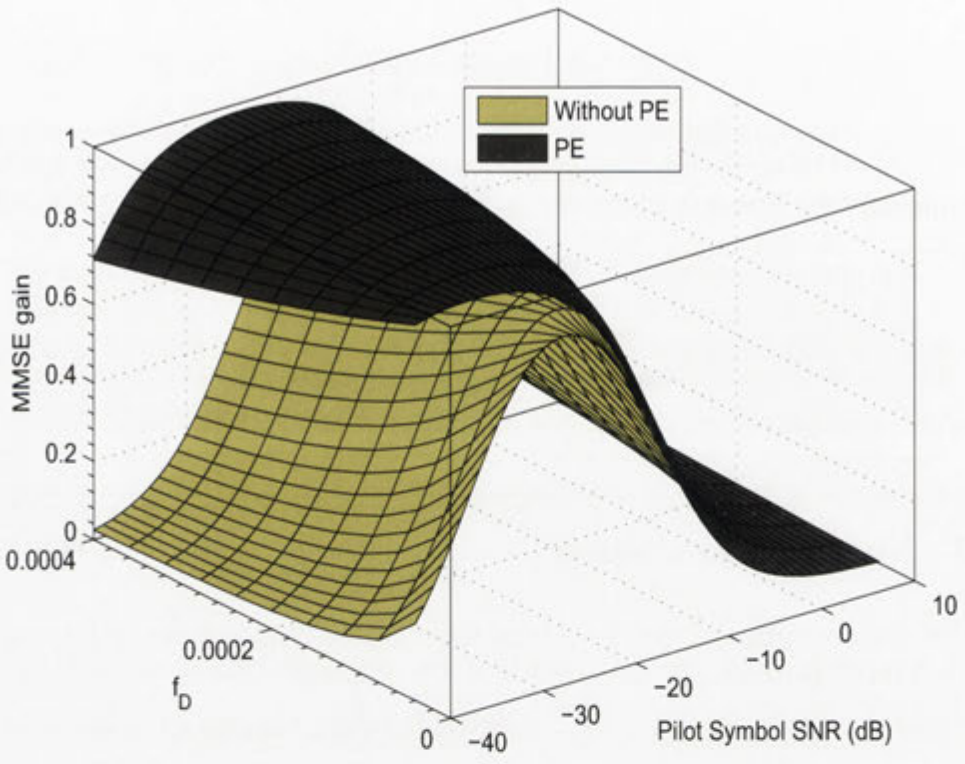

Figure 5.4: Impact of SNR and f_{D} on $\mathcal{G}^U$ with and without pilot enhancement (PE) for uniform Doppler spectrum: $\mathcal{M} = 100$ and $T_{\mathrm{p}} = 200$. Observe that PE significantly improves MMSE gain at very low SNR. However, there is almost no gain in MMSE performance for SNR $\gtrsim -20$ dB.

in a scattering environment characterized by uniform Doppler spectrum has been plotted in Fig. 5.8 assuming $\mathcal{M} = 10$, $T_p = 40$ and SNR$= \{-40, -15, 0\}$ dB. It may be observed that the behavior of MMSE gain as a function of f_{D} is strongly dependent on SNR. At SNR$= -40$ dB, MMSE gain is a decreasing function of f_{D} implying that the optimal $f_{\mathrm{D}} \approx 0$ and pilots sent more often than the Nyquist rate are desirable. The behavior does not seem to have changed with PE. The MMSE gain at SNR$= -15$ dB is maximum around $f_{\mathrm{D}} \approx 0.0013$ which shifts to $f_{\mathrm{D}} \approx 0.004$ when pilot symbols are enhanced with power savings. The MMSE gain is an increasing function of f_{D} for SNR$= 0$dB (and, in fact, for all SNR> 0) which implies that pilots which are being sent more often than the Nyquist rate are infeasible. The gain function is almost unchanged after PE suggesting that power savings due to unused degrees of freedom in the peaky signaling should be invested elsewhere for operating SNR greater than about 0 dB. This behavior of MMSE gain can be explained in view of the fact that we have assumed low pass filtering of noisy pilot symbols such that the channel spectrum is unaltered

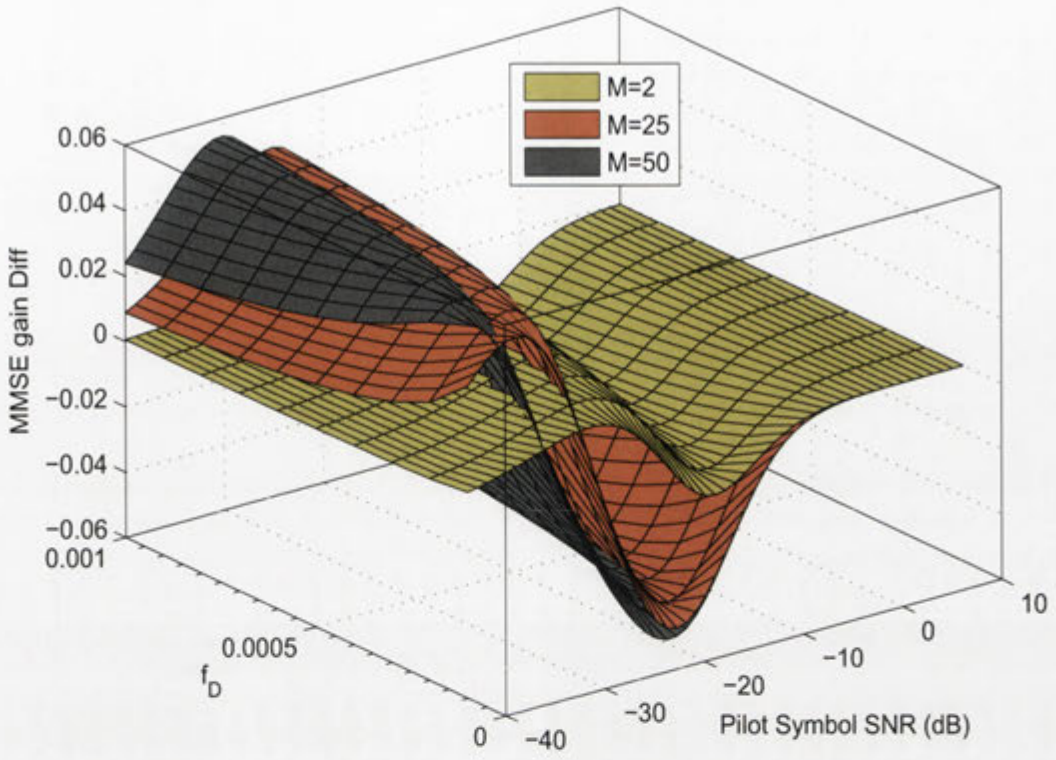

Figure 5.5: The plot of $\mathcal{G}^C - \mathcal{G}^U$ as a function of SNR and f_{D} where $\mathcal{M} = \{2, 25, 50\}$ and $T_p = 200$. It can be noticed that $\mathcal{G}^C$ and $\mathcal{G}^U$ are approximately equal. However, to be more precise, Clarke's spectrum offers higher MMSE gain at very low SNR.

which implies that the filtering (and downsampling) operation does not alter power of the channel process. However, the noise power is altered in inverse proportion to f_{D} (Fig. 5.3). In other words, a change in f_{D} does not change the (useful) signal power but changes the noise power thus changing ρ_p. Therefore, a change in f_{D} is equivalent to changing ρ_p and the impact of change in ρ_p can be observed in Fig. 5.4 for uniform Doppler spectrum. The pilot insertion period (T_p) is an important design parameter in the design of systems based on pilot-aided channel estimation. It is, therefore, of some interest to look at the behavior of MMSE gain function, $\mathcal{G}$, against a change in T_p. Fig. 5.9 shows the behavior of $\mathcal{G}$ as a function of T_p for uniform and Clarke's Doppler spectra assuming $\mathcal{M} = 2$. It can be observed that the behavior of $\mathcal{G}$ against T_p depends on ρ_p. At $\rho_p = -20$ dB, optimal T_p is the smallest possible value, *i.e.*, the Nyquist period, whereas for $\rho_p = -10$ dB the optimal insertion period is 14. The figure suggests that the optimal value of T_p for $\rho_p > 0$ dB seems to be $\gg 100$ which implies that sending pilot symbols less often would be optimal.

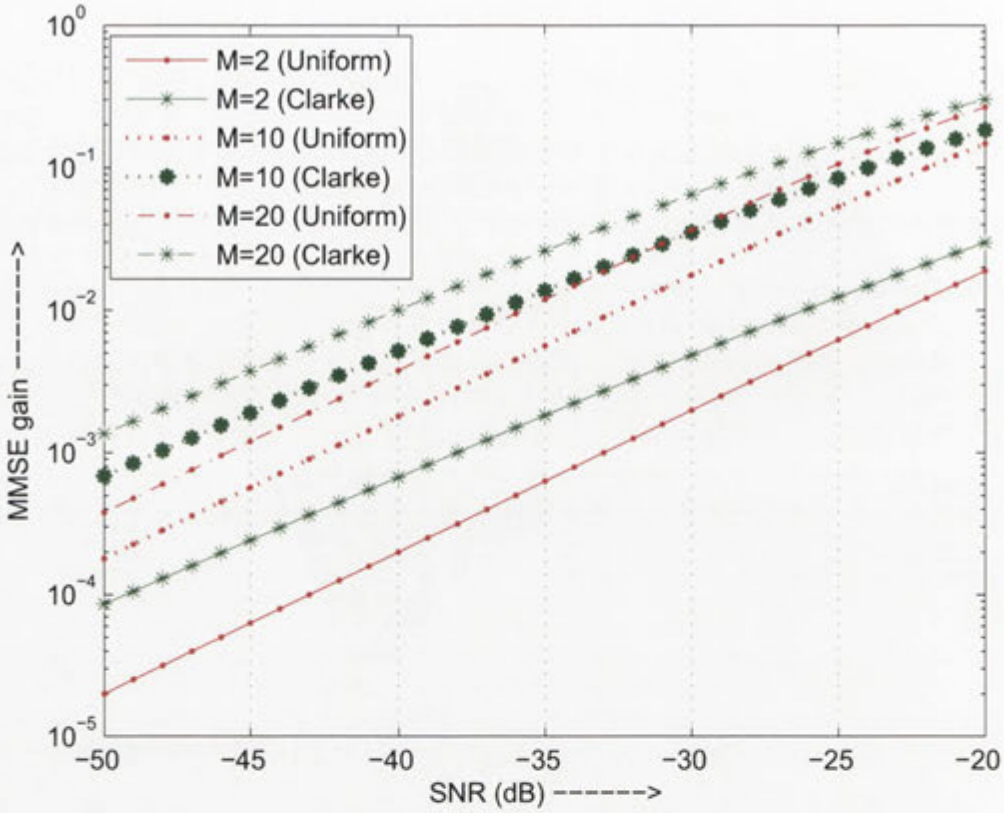

Figure 5.6: MMSE gain for different $\mathcal{M}$ in low SNR regime with $f_{\mathrm{D}} = 0.005$ and $K = 1$ for uniform and Clarke's spectra.

5.4 Optimal Resource Allocation: Mathematical Problem Formulation

5.4.1 Expressions for Pilot and Data Symbol Powers

Consider the transmitted frame format as shown in Fig. 5.1 and assume that the channel Doppler spectrum is uniform (Eq. (5.16)). For the sake of simplicity in the subsequent analysis, we would confine our attention to PE and DE schemes in this section. We consider a block of T_p symbols and make the assumption that the total power is constrained to be equal to $T_p\mathcal{E}_s$. Let γ be the fraction of bandwidth allocated to pilot symbols plus $\mathcal{M} - 1$ zeros so that

$$\gamma = \frac{\mathcal{M}}{T_p}, \tag{5.24}$$

and let μ be the fraction of power of $T_p - \mathcal{M} + 1$ symbols in the block allocated to the pilot symbol for channel estimation. The average pilot symbol power for PE scheme,

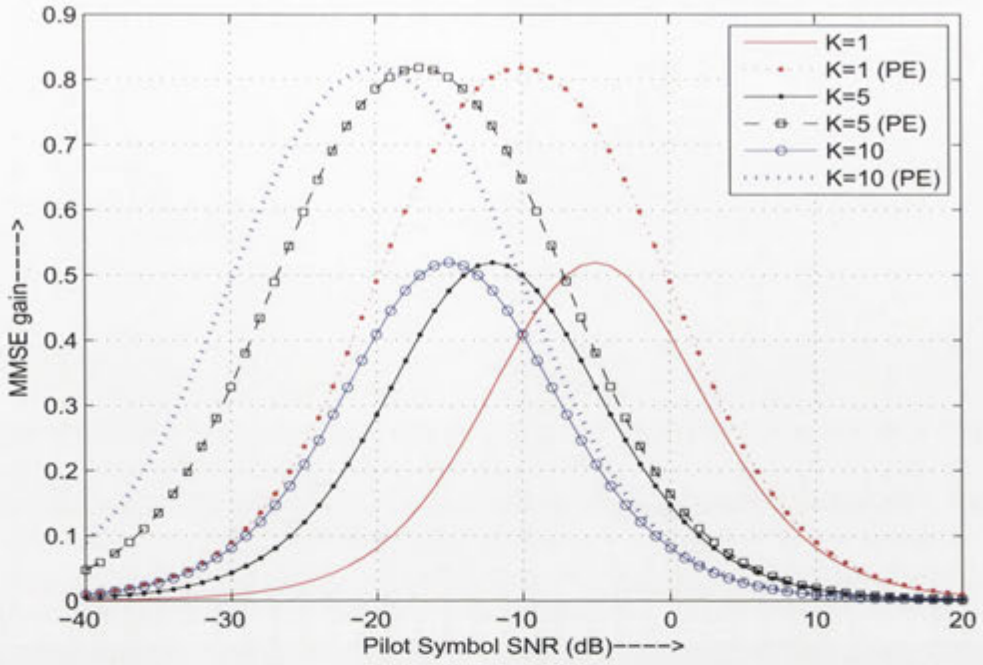

Figure 5.7: Impact of oversampling factor K on MMSE gain for uniform Doppler spectrum with and without PE. Notice that increasing K shifts the MMSE peak towards lower SNR implying that using larger K, better MMSE performance can be achieved at lower SNR. Also observe that PE raises the peak gain by the same amount for all K.

$\mathcal{E}_p^{\mathrm{PE}}$, is then given as

$$\begin{aligned}\mathcal{E}_p^{\mathrm{PE}} &= \mu(T_p - \mathcal{M} + 1)\mathcal{E}_s + (\mathcal{M}-1)\mathcal{E}_s\,, \\ &= \left(\frac{\mathcal{M}\mu + (\mathcal{M}-1)\gamma(1-\mu)}{\mathcal{M}}\right)\mathcal{E}_s\,, \qquad (5.25)\\ &= \mu_e^{\mathrm{PE}}\, T_p \mathcal{E}_s\,, \qquad (5.26)\end{aligned}$$

where μ_e^{PE} is given as

$$\mu_e^{\mathrm{PE}} = \left(\frac{\mathcal{M}\mu + (\mathcal{M}-1)\gamma(1-\mu)}{\mathcal{M}}\right), \qquad (5.27)$$

is the so-called *effective* μ for PE scheme that represents the fraction of total available power $T_p\mathcal{E}_s$ allocated to pilot symbols. The data symbol power, $\mathcal{E}_d^{\mathrm{PE}}$, would then be given by

$$\mathcal{E}_d^{\mathrm{PE}} = \frac{1-\mu}{1-\gamma} G\mathcal{E}_s\,,$$

where $G = \mathcal{M} - (\mathcal{M}-1)\gamma$.

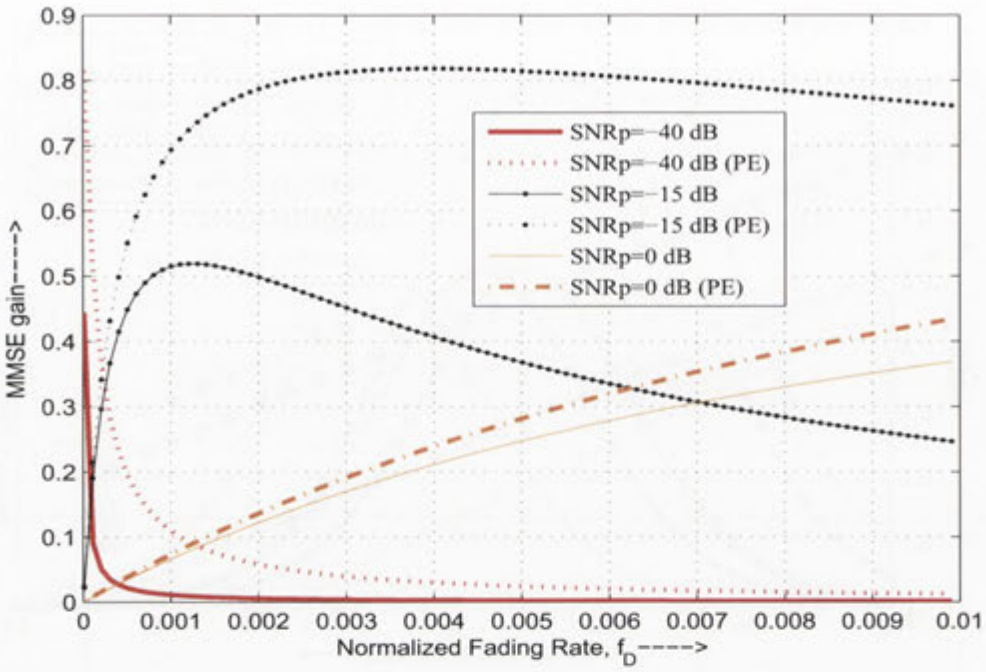

Figure 5.8: Impact of normalized fading rate, f_{D} on MMSE gain ($\mathcal{G}$) with and without PE for $\mathcal{M} = 10$ when $\rho_p = \{-40, -15, 0\}$ dB. The Doppler spectrum is assumed to be uniform.

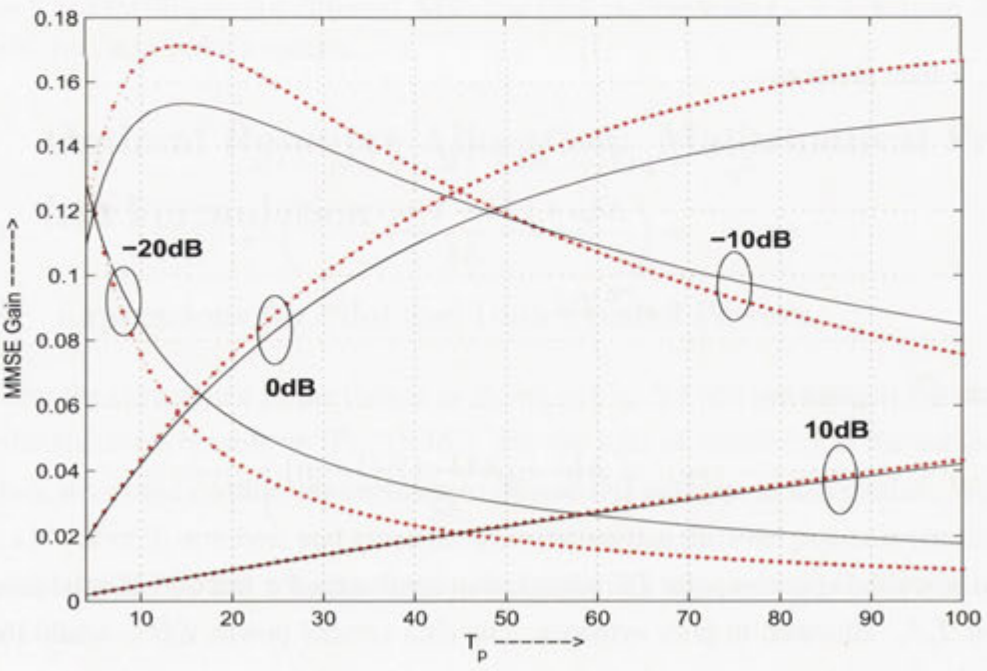

Figure 5.9: Impact of varying pilot insertion period T_p on MMSE gain with for different ρ_p when $f_{\mathrm{D}} = 0.005$ and $\mathcal{M} = 2$ both for uniform and Clarke's spectra.

Similarly, the average pilot symbol power for DE scheme, $\mathcal{E}_p^{\mathrm{DE}}$, is given as

$$\begin{aligned}\mathcal{E}_p^{\mathrm{DE}} &= \mu(T_p - \mathcal{M} + 1)\mathcal{E}_s\,, \\ &= \frac{\mu}{\gamma}\left(\mathcal{M} - (\mathcal{M}-1)\gamma\right)\mathcal{E}_s\,, \\ &= \mu_e^{\mathrm{DE}}\, T_p \mathcal{E}_s\,,\end{aligned} \tag{5.28}$$

where

$$\mu_e^{\mathrm{DE}} = \mu\left(1 - \frac{(\mathcal{M}-1)\gamma}{\mathcal{M}}\right), \tag{5.29}$$

is the effective μ for DE scheme. The data symbol power, $\mathcal{E}_d^{\mathrm{DE}}$, would then be

$$\begin{aligned}\mathcal{E}_d^{\mathrm{DE}} &= \frac{(1-\mu)(T_p - \mathcal{M} + 1) + (\mathcal{M}-1)}{T_p - \mathcal{M}}\mathcal{E}_s\,, \\ &= \left(\frac{\mathcal{M}(1-\mu) + \gamma\mu(\mathcal{M}-1)}{\mathcal{M}(1-\gamma)}\right)\mathcal{E}_s\,.\end{aligned} \tag{5.30}$$

With no loss of generality, we would suppress the time index in the sequel. The channel gain, h is normally modeled as the sum of the estimate, $\widehat{h}$, and the error in estimate, $\breve{h}$ [210] as

$$h = \widehat{h} + \breve{h}, \tag{5.31}$$

so that the received data symbol (Eq. (5.1)) would be given as

$$\begin{aligned}r &= \sqrt{\mathcal{E}_s}\, s\widehat{h} + \overbrace{\sqrt{\mathcal{E}_s}\, s\breve{h}c + z}, \\ &= \sqrt{\mathcal{E}_s}\, s\widehat{h} + w,\end{aligned} \tag{5.32}$$

where w is assumed to be the zero-mean AWGN [88, 210]. The effective received SNR for the scheme[8] x, ρ_e^x is given by

$$\rho_e^x = \frac{\mathcal{E}_d^x\,(1 - \sigma_{U,\epsilon}^2)}{\mathcal{E}_d^x\,\sigma_{U,\epsilon}^2 + N_0}, \tag{5.33}$$

$\sigma_{U,\epsilon}^2$ is the MMSE given in (5.18). Using (5.18), (5.25)-(5.30) and (5.33), we can write after some straightforward manipulation

$$\rho_e^x = \zeta^x\,\rho\,, \tag{5.34}$$

[8]The superscript or subscript x may be appropriately modified to indicate a particular scheme

where we have defined $\rho = \mathcal{E}_s / N_0$ as average symbol SNR and

$$\zeta^x = \frac{Y_x}{X_x}, \tag{5.35}$$

where we have the following for PE and DE, respectively

$$\begin{aligned} Y_{\mathrm{PE}} &= DE\mathcal{M}\rho\,, \\ Y_{\mathrm{DE}} &= FG\mathcal{M}\mu\rho\,, \\ Y_{\mathrm{NP}} &= (1-\mu^{\mathrm{NP}})\mu^{\mathrm{NP}}\rho\,, \end{aligned}$$

where the constants $D = \mathcal{M}\mu + \gamma(1-\mu)(\mathcal{M}-1)$, $E = \mathcal{M}(1-\mu) - \gamma(1-\mu)(\mathcal{M}-1)$, $F = \mathcal{M}(1-\mu) + \gamma\mu(\mathcal{M}-1)$. It can be verified that when no zeros are transmitted, all ζ^x are identical implying that the proposed schemes collapse to NP scheme.

5.4.2 Optimality Criterion

Our purpose is to determine the *optimal* allocation of resources — bandwidth and power — to pilot and data symbols. Before we can proceed we have to fix the criterion for optimality. There can be different criteria for the allocation of resources to pilot and data symbols. An allocation which is optimal against one criterion may not necessarily be optimal against other criteria.

We choose to follow the approach of [88, 210] to obtain optimal resource allocation between pilot and data symbols and consider the Rayleigh capacity lower bound (Eq. (5.37)) (described below) so as to make it possible to compare the results of the proposed peaky signaling scheme with those of NP schemes. Therefore, an allocation of resources between pilot and data symbols shall be optimal if it maximizes the Rayleigh Capacity lower bound for Gaussian signaling. There are two possibilities to be considered: Firstly $\mathcal{E}_p$ and $\mathcal{E}_d$ can be allowed to be unequal, and secondly, $\mathcal{E}_p$ and $\mathcal{E}_d$ can be constrained to be equal.

Rayleigh Fading Capacity Lower Bound for Gaussian Signaling

The capacity of time-selective Rayleigh fading channel is still an open problem. However, it is possible to derive a useful lower bound on the capacity by assuming Gaussian signaling [88,210]. In order to optimize the resource allocation to pilot and data symbols for the proposed PACE scheme and for subsequent comparison with the NP scheme, we follow the approach of [88,210] and consider the following Gaussian signaling Rayleigh

capacity lower bound [88, 129]

$$C \geq C_{lb}^{x} \triangleq \frac{T_p - \mathcal{M}}{T_p} C_{\text{Rayleigh}}(\zeta^x \rho), \tag{5.36}$$

$$= (1-\gamma) C_{\text{Rayleigh}}(\zeta^x \rho), \tag{5.37}$$

where $C_{\text{Rayleigh}}(y)$ is the ergodic capacity per symbol of the Rayleigh fading with perfect CSI and average received SNR, y, and is given as [37, 80, 88]

$$C_{\text{Rayleigh}} \triangleq \mathbb{E}_{\mathcal{C}} \{\log(1 + y\mathcal{C})\}, \tag{5.38}$$

where $\mathcal{C} = |c|^2$ is an exponentially distributed random variable with mean 1. Equation (5.37) implies that the capacity of a system with PACE is equivalent to that of a system with perfect CSI but with a loss in bandwidth and power.

5.5 Optimal Resource Allocation: Unequal Pilot and Data Symbol Powers

We follow the approach of [88, 137] and determine the optimal γ by first examining the first derivative of the capacity lower bound, C_{lb}^{x}, with respect to γ

$$\begin{aligned}
\frac{\partial C_{lb}^{x}}{\partial \gamma} &= -C_{\text{Rayleigh}}(\zeta^x \rho) + (1-\gamma)\frac{\partial}{\partial \gamma} C_{\text{Rayleigh}}(\zeta^x \rho), \\
&= \mathbb{E}_{\mathcal{C}} \left\{ -\log(1 + \zeta^x \rho \mathcal{C}) + \frac{\rho \mathcal{C}}{1 + \zeta^x \rho \mathcal{C}} (1-\gamma) \frac{\partial \zeta^x}{\partial \gamma} \right\}, \\
&= \mathbb{E}_{\mathcal{C}} \left\{ -\log(1 + \zeta^x \rho \mathcal{C}) + \frac{\rho \mathcal{C}}{1 + \zeta^x \rho \mathcal{C}} \underbrace{(1-\gamma)(\ell_1 x + \ell_2 x)} \right\},
\end{aligned} \tag{5.39}$$

where, for PE

$$\begin{aligned}
\ell_{1\text{PE}} &= \frac{-\mathcal{M}(\mathcal{M}-1)(1-\mu) D\rho + \mathcal{M}(\mathcal{M}-1)(1-\mu) E\rho}{Y_{\text{PE}}}, \\
\ell_{2\text{PE}} &= -\frac{(-2f_{\text{D}} + \mathcal{M}(1-\gamma))\, \mathcal{M}(\mathcal{M}-1)(1-\mu)\rho - \mathcal{M}^2(2f_{\text{D}} + D\rho)}{X_{\text{PE}}},
\end{aligned} \tag{5.40}$$

and for DE

$$\ell_{1\text{DE}} = \frac{G\mathcal{M}(\mathcal{M}-1)\mu^2\rho - \mathcal{M}(\mathcal{M}-1)\mu F\rho}{Y_{\text{DE}}},$$

$$\ell_{2\mathrm{DE}} = -\frac{2f_{\mathrm{D}}\mathcal{M}(\mathcal{M}-1)\mu\rho \; - \mathcal{M}^2(\mathcal{M}-1)(1-\gamma)\mu\rho \; - \mathcal{M}^2(2f_{\mathrm{D}} + \mu G\rho\,)}{X_{\mathrm{DE}}},$$

where

$$X_{\mathrm{PE}} = 2f_{\mathrm{D}}E\mathcal{M}\rho \; + \mathcal{M}^2(1-\gamma)(2f_{\mathrm{D}} + D\rho\,),$$
$$X_{\mathrm{DE}} = 2f_{\mathrm{D}}F\mathcal{M}\rho \; + \mathcal{M}^2(1-\gamma)(2f_{\mathrm{D}} + \mu G\rho\,),$$

Notice that in (5.39), it is the presence of the factor $(1-\gamma)(\ell_1 x + \ell_2 x) < 1$ (with $\mathcal{M} = 1$) in [88] which made it possible to analytically show that the derivative of C_{lb}^{NP} with respect to γ^{NP} was always nonpositive for $\rho > 0$, $f_{\mathrm{D}} > 0$ and $0 < \mu^{\mathrm{NP}} < 1$. It was also shown that the capacity derivative was a decreasing function of γ^{NP}. Hence, irrespective of μ^{NP}, the optimal γ^{NP} was equal to the minimum possible as required by the Nyquist criterion, *i.e.*, $2f_{\mathrm{D}}$. This fact allowed the authors in [88] to optimize μ^{NP} independently of γ^{NP}. For the proposed scheme, in general, the factor $(1-\gamma)(\ell_1 x + \ell_2 x) \not< 1$. However, there are certain scenarios depending on $\mathcal{M}$, operating SNR and f_{D} where $(1-\gamma)(\ell_1 x + \ell_2 x) < 1$ for the proposed signaling and, therefore, $\gamma_{opt} = 2\mathcal{M}f_{\mathrm{D}}$, *i.e.*, the optimal pilot insertion rate equals Nyquist rate which is always the case when non-peaky signaling is employed. The above discussion implies that the optimal pilot insertion frequency may not always be equal to Nyquist rate. We therefore have two distinct possibilities, *i.e.*, the optimal pilot insertion frequency is either equal to or greater than the minimum Nyquist rate.

5.5.1 Case 1: Optimal Pilot Insertion Rate Equals Nyquist Rate

For sufficiently large $\mathcal{M}(\rho\,, f_{\mathrm{D}})$ and $\rho\,(\mathcal{M}, f_{\mathrm{D}})$, and sufficiently large $f_{\mathrm{D}}(\mathcal{M}, \rho\,)$ the factor $(1-\gamma)(\ell_1 x + \ell_2 x) < 1$ for all γ and μ in (5.39) implying that the optimal pilot insertion frequency is equal to the Nyquist rate. In such a scenario, we can write

$$\frac{\partial}{\partial\gamma}C_{lb}^{x} < \mathbb{E}_{\mathcal{C}}\left\{-\log(1+\zeta^x\,\rho\,\mathcal{C}) + \frac{\rho\,\mathcal{C}}{1+\zeta^x\,\rho\,\mathcal{C}}\right\},$$
$$\leq 0,$$

where the second inequality is a result of the fact that

$$\log(1+y) \geq \frac{y}{1+y},$$

for all nonnegative y. This implies that the optimal γ reduces to the minimum possible, *i.e.*, $2\mathcal{M}f_{\mathrm{D}}$ for all μ, and the optimal μ can be found independently of optimal γ as in [88, 137]. It is of some interest to find the optimal μ in such scenarios where the

optimal $\gamma = 2\mathcal{M}f_{\mathrm{D}}$ is for all μ.

Notice that the optimal μ must maximize ζ^x (Eq. (5.37)). We can rewrite (5.35) as

$$\zeta^x = \frac{1}{Q_x}\frac{Y_x}{\mu + \xi_x}, \tag{5.41}$$

where

$$\begin{aligned} Q_{\mathrm{PE}} &= \mathcal{M}^2(1-\gamma) - 2f_{\mathrm{D}}G - \mathcal{M}(\mathcal{M}-1)\gamma(1-\gamma), \\ \xi_{\mathrm{PE}} &= \frac{2f_{\mathrm{D}}\mathcal{M}\left(\mathcal{M}(1-\gamma) + G\rho\right) + J_{\mathrm{PE}}}{Q_{\mathrm{PE}}\rho}, \end{aligned} \tag{5.42}$$

$$\begin{aligned} Q_{\mathrm{DE}} &= Q_{\mathrm{PE}}, \\ \xi_{\mathrm{DE}} &= \frac{J_{\mathrm{DE}}}{\rho\, Q_{\mathrm{DE}}}, \end{aligned} \tag{5.43}$$

where $J_{\mathrm{PE}} = \mathcal{M}^2(\mathcal{M}-1)\gamma(1-\gamma)\rho$ and $J_{\mathrm{DE}} = 2\mathcal{M}^2 f_{\mathrm{D}}\rho$.

Notice that ζ^x must be nonnegative which requires that f_{D} must be less than[9] $1/8$ in (5.41) and allowed maximum (see footnote 3) $\mathcal{M}$ is a decreasing function of f_{D} so that $\mathcal{M}$ must not be higher than 2 when $f_{\mathrm{D}} \lesssim 1/8$. With this constraint on f_{D}, ξ_x is positive and μ_{opt}^x is given by

$$\mu_{opt}^x = \mathcal{K}(\xi_x), \tag{5.44}$$

where the function $\mathcal{K}(\xi_x)$ is respectively given for PE and DE cases as

$$\mathcal{K}(\xi_{\mathrm{PE}}) = -\xi_{\mathrm{PE}} + \sqrt{\xi_{\mathrm{PE}}^2 + \mathcal{Q}(\xi_{\mathrm{PE}})}, \tag{5.45}$$

$$\mathcal{K}(\xi_{\mathrm{DE}}) = -\xi_{\mathrm{DE}} + \sqrt{\xi_{\mathrm{DE}}^2 + \mathcal{Q}(\xi_{\mathrm{DE}})}, \tag{5.46}$$

where the function $\mathcal{Q}(\xi_x)$ has been defined in the Appendix D.4. It is easy to verify that when $\mathcal{M} = 1$, μ_{opt}^x collapse to $\mu_{opt}^{\mathrm{NP}} = \mathcal{K}(\xi_{\mathrm{NP}})$ where

$$\mathcal{K}(\xi_{\mathrm{NP}}) = -\xi_{\mathrm{NP}} + \sqrt{\xi_{\mathrm{NP}}^2 + \mathcal{Q}(\xi_{\mathrm{NP}})}. \tag{5.47}$$

Using (5.27) and (5.29) the effective μ_{opt}^x is given respectively for PE and DE schemes

[9] In [88], the fading rate f_{D} was assumed to be less than $1/4$. Our assumption of $f_{\mathrm{D}} < 1/8$ still covers most channels that may be of practical interest.

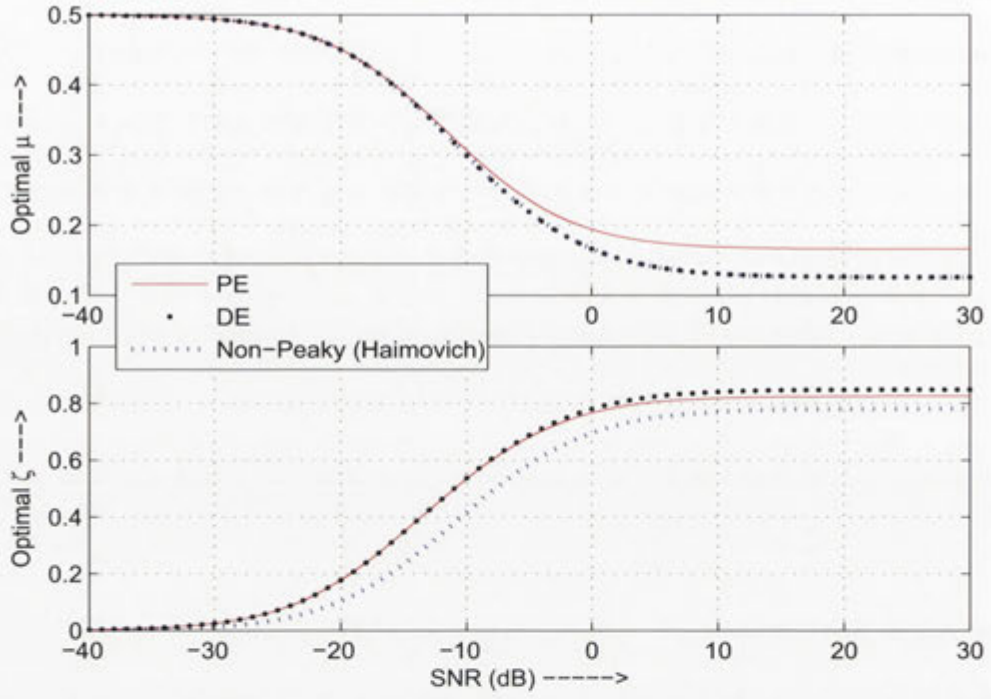

Figure 5.10: Effective optimal μ and ζ for PE and DE assuming $\gamma_{opt} = 2\mathcal{M}f_{\mathrm{D}}$. The corresponding optimal μ and ζ for non-peaky signaling are also shown.

as

$$\mu_{opt,e}^{\mathrm{PE}} = \mu_{opt}^{\mathrm{PE}} + (\mathcal{M}-1)(1-\mu_{opt}^{\mathrm{PE}})2f_{\mathrm{D}}, \tag{5.48}$$

$$\mu_{opt,e}^{\mathrm{DE}} = \mu_{opt}^{\mathrm{DE}}\left(1-(\mathcal{M}-1)2f_{\mathrm{D}}\right), \tag{5.49}$$

and the effective ζ_{opt}^{x} is obtained by substituting μ_{opt}^{x} in (5.41). The following statements can be verified for $\rho > 0$, $f_{\mathrm{D}} < 1/8$, $\mathcal{M} \leq \mathcal{M}_{\max}(f_{\mathrm{D}})$:

1. For a fixed $\mathcal{M}$, ξ_x is positive, an increasing function of f_{D} and a decreasing function of ρ. This implies that μ_{opt}^{x} is an increasing function of f_{D} and a decreasing function of ρ. Moreover, ζ_{opt}^{x} increases with increasing ρ and decreases with increasing f_{D}. In other words, for slower fading and high ρ, lesser fraction of power needs to be allocated to pilot symbols and vice versa. This implies that the use of pilots to estimate the channel becomes more efficient.

2. For a fixed ρ and f_{D}, μ_{opt}^{PE} is an increasing function of $\mathcal{M}$ whereas μ_{opt}^{DE} is a decreasing function of $\mathcal{M}$.

3. In the low SNR regime, the optimal μ^{x}_{opt} and $\mu^{\mathrm{x}}_{opt,e}$ are given as

$$\lim_{\rho \to 0} \mu^{\mathrm{PE}}_{opt} = \frac{1 - 2(\mathcal{M}-1)2f_{\mathrm{D}}}{2\,(1-(\mathcal{M}-1)2f_{\mathrm{D}})}, \tag{5.50}$$

$$\lim_{\rho \to 0} \mu^{\mathrm{PE}}_{opt,e} = \frac{1}{2}, \tag{5.51}$$

$$\lim_{\rho \to 0} \mu^{\mathrm{DE}}_{opt} = \frac{1}{2\,(1-(\mathcal{M}-1)2f_{\mathrm{D}})}, \tag{5.52}$$

$$\lim_{\rho \to 0} \mu^{\mathrm{DE}}_{opt,e} = \frac{1}{2}, \tag{5.53}$$

which are true for all $\mathcal{M} \leq \mathcal{M}_{\max}(f_{\mathrm{D}})$ and $f_{\mathrm{D}} < 1/8$. This implies that *effectively* it is optimal to use half of the available power for pilot symbols in the limit of zero SNR. This result is the same as in the non-peaky case [88].

4. For a fixed $\mathcal{M}$, ζ^{x}_{opt} is an increasing function of ξ_x.

5. In the Appendix D.5 we show that $\mu^{x}_{opt,e} > 2f_{\mathrm{D}}$ which implies that the optimal power allocated to pilot symbols is always greater than the average symbol power. This is the same result as obtained for non-peaky signaling [88]

Fig. 5.10 shows the effective μ_{opt} and ζ_{opt} for PE, DE and NP cases. Notice that, at high SNR, the PE scheme optimally uses more power than DE scheme but its corresponding ζ is less than that for DE[10] which implies that priority should be given to DE scheme if the operating SNR is going to be greater than 0 dB. However, at low SNR both PE and DE have almost identical effective μ_{opt} and corresponding ζ_{opt}. It may be observed that, like NP scheme, the effective optimal μ^{x} approaches $1/2$ which verifies the low SNR asymptotic result for optimal μ (equations (5.51) and (5.53)). It can also be noticed that DE scheme optimally requires as much power as NP scheme, but results in higher corresponding ζ. This suggests that it is better to invest power savings in data symbols than in the pilot symbols at low SNR.

Evaluation of Gaussian Signaling Capacity Lower Bound

Using absolutely optimal μ and γ at each SNR, the Gaussian signaling capacity lower bounds are plotted in Fig. 5.11 for PE and DE schemes along with perfect CSI Rayleigh capacity assuming. We assume that $\mathcal{M} = 20$ and $f_{\mathrm{D}} = 0.005$. The channel oversampling factor K is assumed to be 1 implying that the pilot symbols are inserted at the Nyquist rate. While different schemes behave almost identically at low SNR, it can be

[10]Though results are given for a particular $\mathcal{M}$ and f_{D}, the authors have verified that this is true in general.

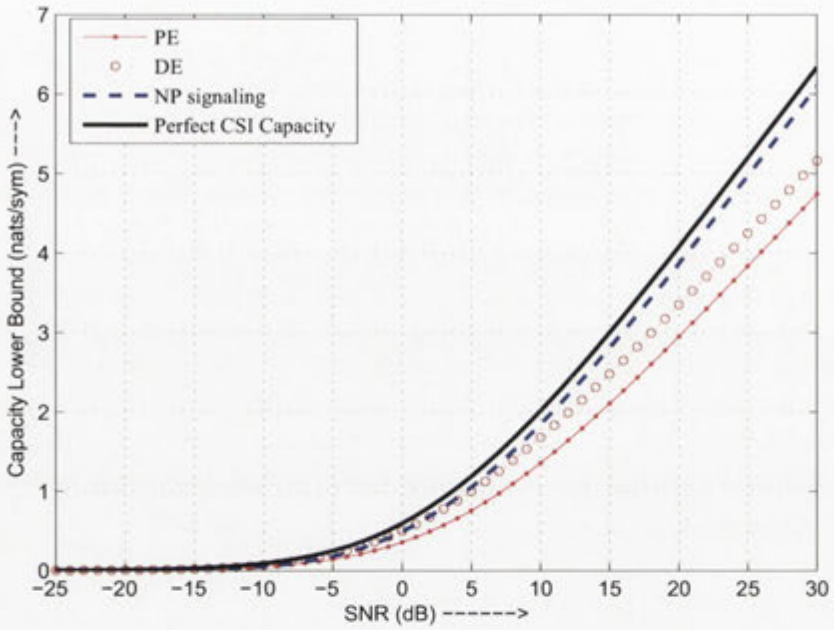

Figure 5.11: A comparison of Gaussian signaling capacity lower bound for the proposed schemes and NP scheme for $\mathcal{M} = 20$ and $f_{\mathrm{D}} = 0.005$. The perfect CSI capacity of Rayleigh fading channels is also shown as a benchmark.

observed that NP scheme performs better than the proposed schemes for moderate to high SNR. Moreover, the gap is widening with an increase in SNR. However, this behavior at moderate to high SNR is not true in general. Figures 5.12 and 5.13, where $C_{lb}^{\mathrm{DE}} - C_{lb}^{\mathrm{NP}}$ has been plotted respectively for different $\mathcal{M}$ and f_{D}, verify this assertion as we can see that the capacity lower bound with DE scheme can be higher than NP scheme at SNR as high as 25 dB. While the gains offered by peaky signaling may be insignificant at high SNR, the authors have verified that for very slow fading channels, it may always be advantageous to have some level of "peakiness" in the signaling for any operating SNR. This can be explained if we consider (5.36) for very slow fading scenario. When normalized fading rate is very low, corresponding minimum Nyquist rate is also very low and, equivalently, T_p is very large, *e.g.*, for $f_{\mathrm{D}} = 1 \times 10^{-7}$, Nyquist period, $T_N = T_p = 5 \times 10^6$. For such large T_p

$$\frac{T_p - \mathcal{M}}{T_p} \approx 1, \tag{5.54}$$

where the accuracy of the approximation would depend on $\mathcal{M}$. On the other side, the peakiness results in better MMSE estimates of channel gains by enhancing pilot SNR by factor $\mathcal{M}$ for uniform Doppler spectrum (Eq. (5.18)). Therefore, just using $\mathcal{M} = 2$ will double the pilot SNR which, in turn, would result in better ζ than NP scheme. This

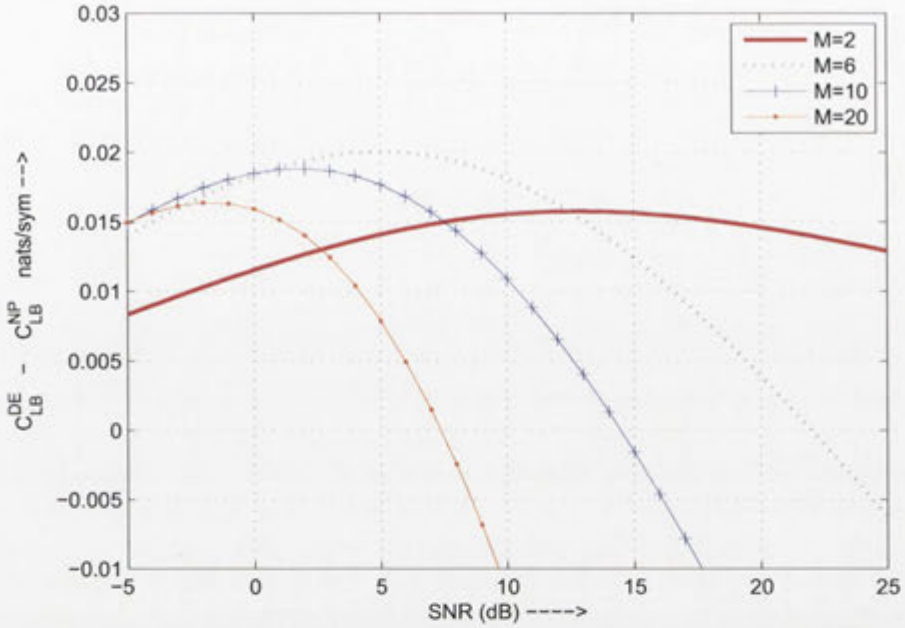

Figure 5.12: The plot of $C_{lb}^{\mathrm{DE}} - C_{lb}^{\mathrm{NP}}$ for different $\mathcal{M}$.

discussion implies that an overall "peakiness" gain is achievable even at high SNR $< \infty$.

In contrast to high SNR regime, the proposed scheme offers significant rate gain in the low SNR regime as shown in Fig. 5.14 for $f_{\mathrm{D}} = 0.01$ and $\mathcal{M} = \{6, \mathcal{M}_{\max}\}$. It can be observed that PE and DE schemes have *almost* identical lower bounds for SNR < 0 dB especially at low SNR and DE is better than NP scheme for all SNR < 0 dB when $\mathcal{M} = 6$ which is, however, not true when $\mathcal{M} = \mathcal{M}_{\max} = 48$. The increased peakiness has, on one hand, improved lower bound at low SNR and, on the other hand, has deteriorated performance of the proposed scheme as compared to NP scheme for moderately low operating SNR. Though not shown, the simulation results suggest that, for f_{D} approaching zero, the proposed scheme seems to achieve Rayleigh fading capacity in the limit of zero SNR. However, with that level of peakiness, the rates achievable with the non-peaky signaling can be significantly higher than the proposed scheme for SNR > 0. The validity of this argument can be observed in Fig. 5.14 where more peakiness resulted in the better performance of proposed scheme at lower SNR at the cost of deteriorated performance at SNR$\gtrsim -13$ dB. We argue that the proposed schemes achieve Rayleigh fading perfect CSI capacity when the peakiness tends to infinity which is possible only when f_{D} tends to zero.

We make use of the following result to examine the limiting behavior of C_{lb}^{x}

$$C_{\mathrm{Rayleigh}}(y) = \begin{cases} y, & y << 1; \\ \log(1+y) - \mathcal{Z}, & y >> 1 \end{cases} \tag{5.55}$$

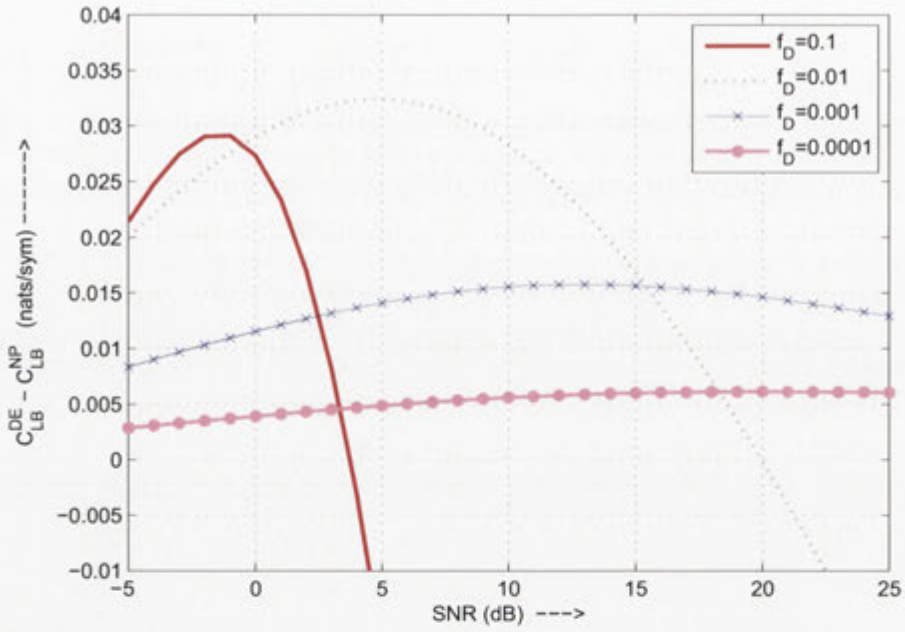

Figure 5.13: The plot of $C_{lb}^{\mathrm{DE}} - C_{lb}^{\mathrm{NP}}$ for different f_{D}

where $\mathcal{Z} \approx 0.577$ is the Eüler's constant.

For sufficiently low SNR, we have

$$\mu_{opt,L}^{\mathrm{PE}} \approx \frac{1}{2}\left(\frac{H}{G}\right), \tag{5.56}$$

$$\mu_{opt,L}^{\mathrm{DE}} \approx \frac{1}{2}\left(\frac{\mathcal{M}}{G}\right), \tag{5.57}$$

where $H = G - (\mathcal{M}-1)\gamma$. The corresponding optimal ζ^x are[11]

$$\zeta_{opt,L}^{\mathrm{PE}} \approx \frac{\mathcal{M}}{8f_{\mathrm{D}}\left(1 - \mathcal{M}2f_{\mathrm{D}}\right)}\rho\,, \tag{5.58}$$

$$= \zeta_{opt,L}^{\mathrm{DE}}. \tag{5.59}$$

Using (5.58) and (5.59) in (5.55), we get the following result

$$\lim_{\rho \to 0}\left(C_{lb}^{\mathrm{x}}/C_{lb}^{\mathrm{NP}}\right) \approx \mathcal{M},, \tag{5.60}$$

where C_{lb}^{NP} is the capacity lower bound for non-peaky signaling. Equation (5.60) implies that PE and DE schemes offer, to good approximation, identical gains in the low SNR regime as compared to non-peaky transmission scheme and, therefore, it does not really

[11]We additionally assume that $4(\mathcal{M}-1)f_{\mathrm{D}} \ll 1$ which, in fact, allows higher peakiness for low f_{D} and vice versa. This assumption also implies that $H \approx G$.

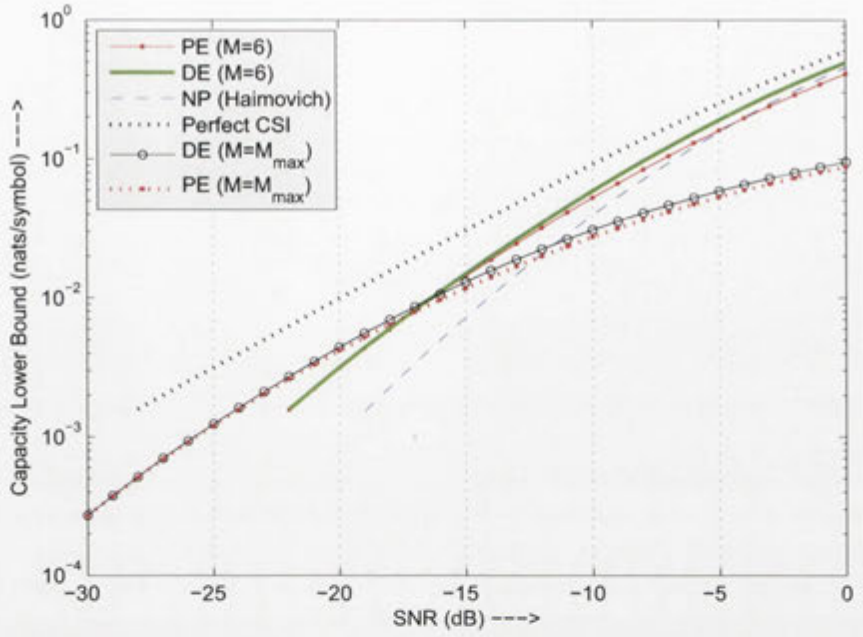

Figure 5.14: A comparison of Gaussian signaling capacity lower bounds at low SNR.

matter if the power savings are utilized to enhance the pilot symbol SNR or the data symbol SNR. Thus, in the low SNR regime, the proposed scheme offers $\mathcal{M}$ times the transmission rate achievable with the non-peaky Gaussian signaling of the same total available power. In order to emphasize rate gain in the low SNR regime offered by the proposed schemes over conventional non-peaky signaling scheme, we define the percentage rate gain, $\mathcal{R}_g$, as:

$$\begin{aligned}\mathcal{R}_g &= \lim_{\rho \to 0} \frac{C_{lb}^{\mathrm{x}} - C_{lb}^{\mathrm{NP}}}{C_L^{\mathrm{NP}}} \times 100, \\ &= 100(\mathcal{M} - 1),\end{aligned} \tag{5.61}$$

where we have made use of (5.60). Fig. 5.15 shows the result of a Monte Carlo simulation of $\mathcal{R}_g$ which, as we can see, exactly matches with the analytical result (Eq. (5.61)).

For sufficiently high SNR, the optimal μ for PE scheme is

$$\mu_{opt,H}^{\mathrm{PE}} = \lim_{\rho \to \infty} \mathcal{K}(\xi_{\mathrm{PE}}) \tag{5.62}$$

$$= \left(\frac{-\sqrt{G} R_{\mathrm{PE}} + \sqrt{R_{\mathrm{PE}}(G R_{\mathrm{PE}} + H Q_{\mathrm{PE}}) + (G - \mathcal{M}) Q_{\mathrm{PE}}^2}}{R_{\mathrm{PE}} \sqrt{G}} \right), \tag{5.63}$$

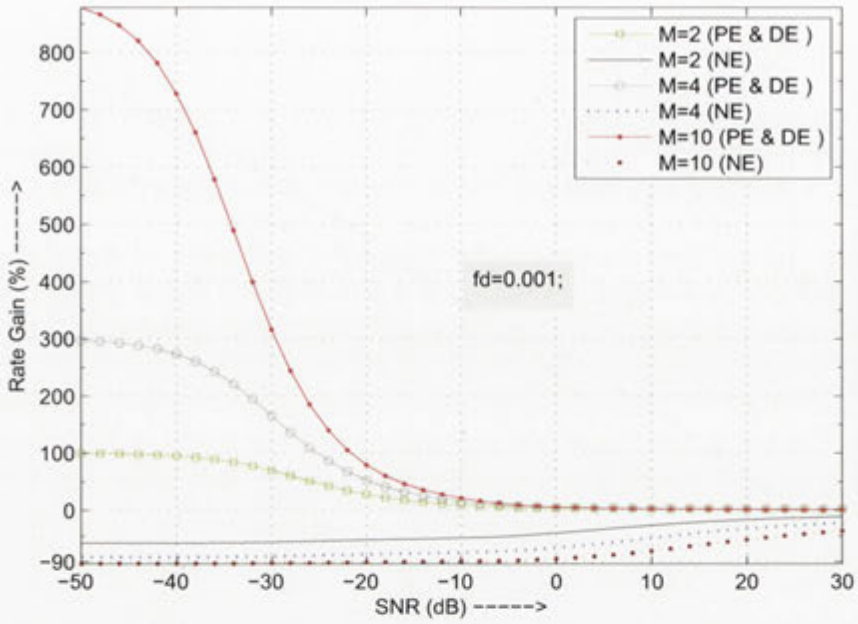

Figure 5.15: The impact of $\mathcal{M}$ and SNR on the percentage rate gain $\mathcal{R}_g$ for NE, PE and DE cases. Note that absolutely optimal γ and corresponding μ have been considered.

where we have defined

$$R_{\mathrm{PE}} = \mathcal{M}^2(1-\gamma) - Q_{\mathrm{PE}}$$

and for DE, the optimal μ in the high SNR regime is given as

$$\begin{aligned}\mu_{opt,H}^{\mathrm{DE}} &= \lim_{\rho\to\infty} \mathcal{K}(\xi_{\mathrm{DE}}),\\ &= \left(\frac{-\sqrt{G}2\mathcal{M}^2 f_{\mathrm{D}} + \sqrt{2\mathcal{M}^2 f_{\mathrm{D}}(2G\mathcal{M}^2 f_{\mathrm{D}} + \mathcal{M}Q_{\mathrm{DE}})}}{Q_{\mathrm{DE}}\sqrt{G}}\right).\end{aligned} \tag{5.64}$$

The corresponding values of ζ^x are

$$\zeta_{opt,H}^{\mathrm{PE}} = \frac{1}{\rho}\left(\frac{Y_{\mathrm{PE}}}{\left(\mu_{opt,H}^{\mathrm{PE}} Q_{\mathrm{PE}} + R_{\mathrm{PE}}\right)}\right)_{\gamma=M2f_{\mathrm{D}}}, \tag{5.65}$$

$$\zeta_{opt,H}^{\mathrm{DE}} = \frac{1}{\rho}\left(\frac{Y_{\mathrm{DE}}}{\left(\mu_{opt,H}^{\mathrm{DE}} Q_{\mathrm{DE}} + 2\mathcal{M}^2 f_{\mathrm{D}}\right)}\right), \tag{5.66}$$

so that we have the following result for Rayleigh capacity lower bounds in the high SNR regime (Eq. (5.55))

$$C_H^{\mathrm{x}} \approx (1 - 2\mathcal{M}f_{\mathrm{D}})\left(\log(1+\rho\,\zeta_{opt,H}^{x}) - \mathcal{Z}\right). \tag{5.67}$$

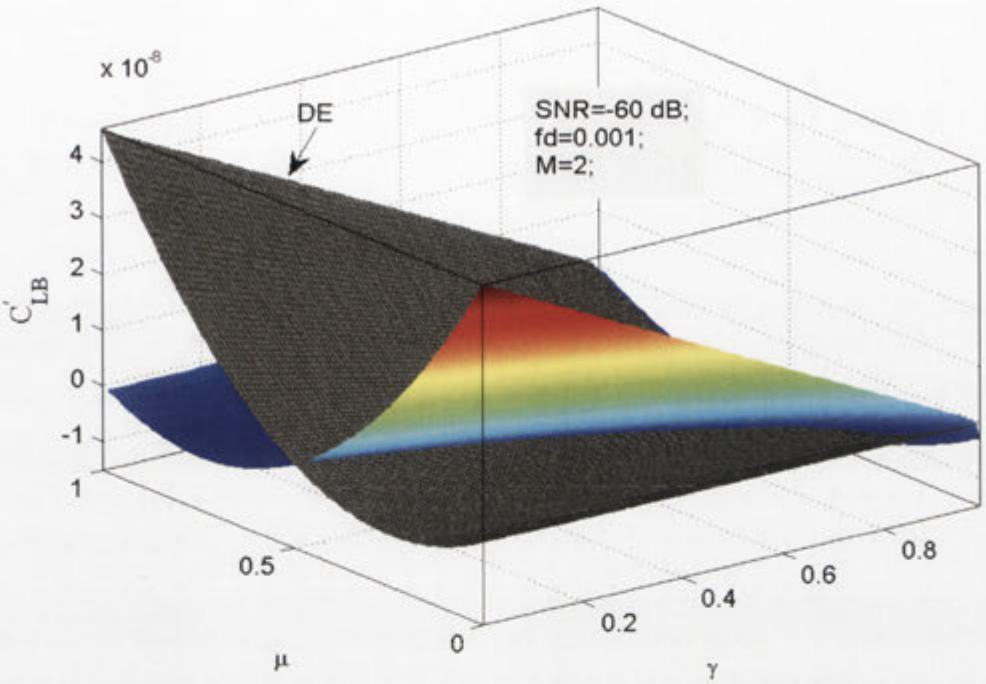

Figure 5.16: C'_{lb} for PE and DE cases. Observe that, in general, the optimal γ is a vector where each element corresponds to a particular μ.

5.5.2 Case 2: Optimal Pilot Insertion Frequency is Greater than Nyquist Rate

The optimality of a particular γ in the previous section allowed us to independently find optimal μ by maximizing the Rayleigh fading capacity lower bound. We, in this section, consider the possible scenario when the optimal pilot insertion frequency is not equal to the minimum Nyquist rate. In view of the complexity of the expressions involved when $(1-\gamma)(\ell_1 x + \ell_2 x) \not< 1$ in (5.39), arriving at a general analytical result regarding optimal resource allocation seems quite difficult. We therefore have to resort to numerical methods to find optimal γ and μ by investigating the behavior of C'^{x}_{lb} against γ and μ.

Fig. 5.16 shows the result of a simple Monte carlo simulation of (5.39) for PE and DE schemes. By looking at the figure, we can, at least, conclude that C'^{x}_{lb} is not, in general, nonpositive and, therefore, the optimal γ is not, in general, equal to the minimum possible as was the case in the previous subsection and [88].

It may be observed in Fig 5.16 that the optimal γ (the value of γ where the derivative of Rayleigh capacity lower bound is zero), in general, is a vector instead of being just a scalar as in [88, 137] and the previous section. Each element of the optimal γ vector cor-

responds to a particular optimal μ (Fig. 5.17), *i.e.*, there is a one-to-one correspondence between optimal γ and μ. We shall use bold symbols $\boldsymbol{\gamma}_{opt}$ and $\boldsymbol{\mu}_{opt}$ to indicate optimal γ and corresponding optimal μ vectors. We shall use γ_{opt} and μ_{opt} to respectively indicate a particular element of $\boldsymbol{\gamma}_{opt}$ and corresponding element of $\boldsymbol{\mu}_{opt}$. The one-to-one correspondence between $\boldsymbol{\gamma}$ and $\boldsymbol{\mu}$ implies that we can either fix some value of γ and then independently optimize μ as was the case in [88], or we can fix μ first and determine optimal γ. However, both the choices may be suboptimal. In order to determine *absolutely* optimal γ_{opt} and μ_{opt}, we have to jointly optimize μ and γ. The jointly optimized $(\gamma - \mu)_{opt}$ pair can be found by searching over $\{\boldsymbol{\gamma}, \boldsymbol{\mu}\}_{opt}$. The jointly optimized $(\gamma - \mu)$ pairs have been plotted in Fig. 5.17 whereas Fig. 5.18 shows the corresponding Rayleigh fading capacity lower bounds for PE, DE and NE cases. It can be observed that the support of the maximum of C_{lb}^{x} lies on the curved portion of $\{\boldsymbol{\gamma}, \boldsymbol{\mu}\}_{opt}$ in Fig. 5.17 an important implication of which is that the proposed transmission/channel estimation scheme offers a *trade-off* between the bandwidth and power resources to be allocated to the pilot symbols, *i.e.*, we can reduce γ at the cost of increased μ (and vice versa) without compromising optimal performance. This trade-off, however, is not possible in [88] and related work where there is a unique optimal γ and corresponding optimal μ for a fixed SNR and fading rate. This curved portion of $\{\boldsymbol{\gamma} - \boldsymbol{\mu}\}_{opt}$ plot can be termed as *trade-off curve*. Fig. 5.15 shows the comparison between the proposed peaky and non-peaky signaling schemes in terms of percentage rate gain, $\mathcal{R}_g$, offered by the proposed scheme with respect to non-peaky signaling.

When f_{D} and ρ are fixed, $\{\boldsymbol{\gamma}, \boldsymbol{\mu}\}_{opt}$ depends on $\mathcal{M}$. Fig 5.19 shows the impact of varying $\mathcal{M}$ on $\{\boldsymbol{\gamma}, \boldsymbol{\mu}\}_{opt}$ at very low SNR of -60 dB. Notice that with an increase in $\mathcal{M}$, the trade-off choice reduces. It may also be observed that PE and DE schemes are images of each other across the line of symmetry $\mu = 0.5$ at very low SNR (and, we argue, at sufficiently high SNR) as shown in Fig. 5.20 where this symmetry breaks with increasing SNR. We can also observe that the trade-off region decreases as we increase SNR for PE case. However, in case of DE, the trade-off curve first increases and then starts to decrease. When the SNR is sufficiently large, (though not shown) the trade-off regions for both schemes disappear and the $\gamma_{opt}^{\mathrm{x}} = 2\mathcal{M}f_{\mathrm{D}}$ which is the minimum required bandwidth (according to the Nyquist criterion) for the proposed scheme with $\mathcal{M} - 1$ zeros.

The normalized fading rate is an important design parameter. Fig. 5.21 depicts the behavior of percentage $\mathcal{R}_g$ as a function of f_{D} for different SNR based on Monte carlo simulations. We can observe that at very low SNR, the rate gain is independent of f_{D} which is a verification of the result obtained in (5.61). However, with an increase in SNR, the rate gain is reduced as compared to rate gain at very low SNR. Moreover,

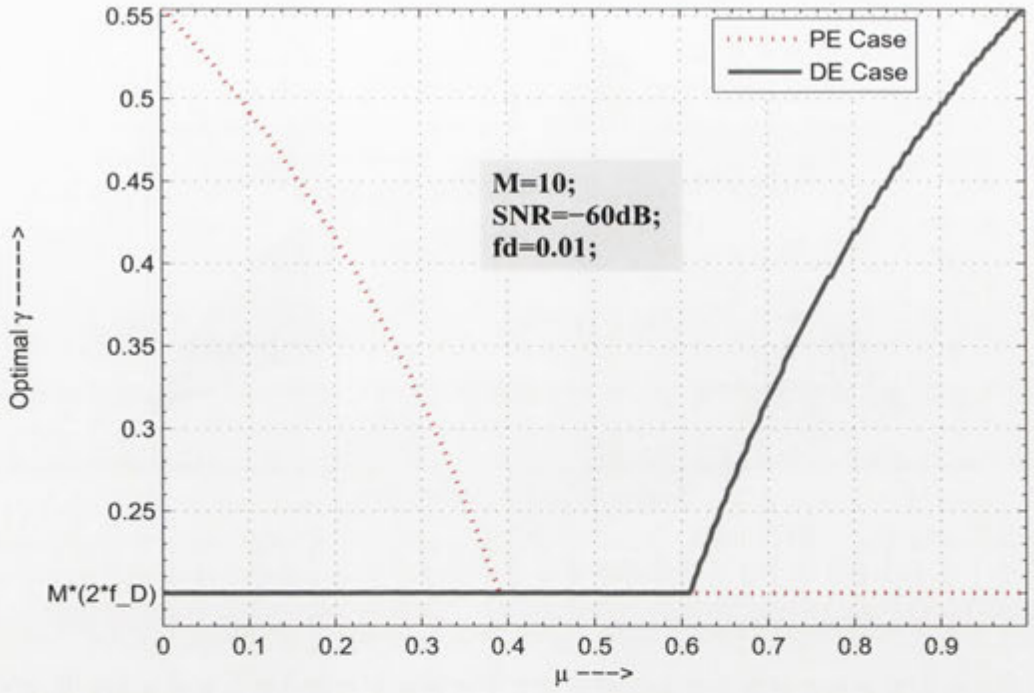

Figure 5.17: Optimal γ as a function of μ for PE and DE cases.

the rate gain is higher for low SNR and higher fading rates. However, this result is applicable only for $\mathcal{M} = 20$ which may not be optimum at low SNR. Fig. 5.22 shows the Monte Carlo simulation for the impact of f_{D} on optimal $\mathcal{M}$. Notice that the figure suggests large optimal $\mathcal{M}$ at low fading rate. The result of simulation for the impact of varying $\mathcal{M}$ on $\mathcal{R}_g$ for different SNR is shown in Fig. 5.23 where fading rate is fixed. The optimal $\mathcal{M}$ maximizing Rayleigh capacity lower bound is ≈ 110 when SNR is -15 dB. For $\rho > 0$ dB, the optimal $\mathcal{M}$ is ≈ 2 and increasing $\mathcal{M}$ beyond this value will be counterproductive resulting in lower achievable information rates than those achievable with non-peaky signaling.

5.6 Optimal Resource Allocation: Equal Pilot and Data symbol Power

In certain scenarios, a communication system may not have the option to allow different pilot and data symbol power. It is, therefore, of some interest to determine the optimal resource allocation between pilot and data symbols and corresponding Rayleigh capacity lower bound when there is the constraint that $\mathcal{E}_p^{\mathrm{x}} = \mathcal{E}_s$. In this section, we consider pilot and data enhancement (PDE) scheme for which it is easy to show that equal pilot and

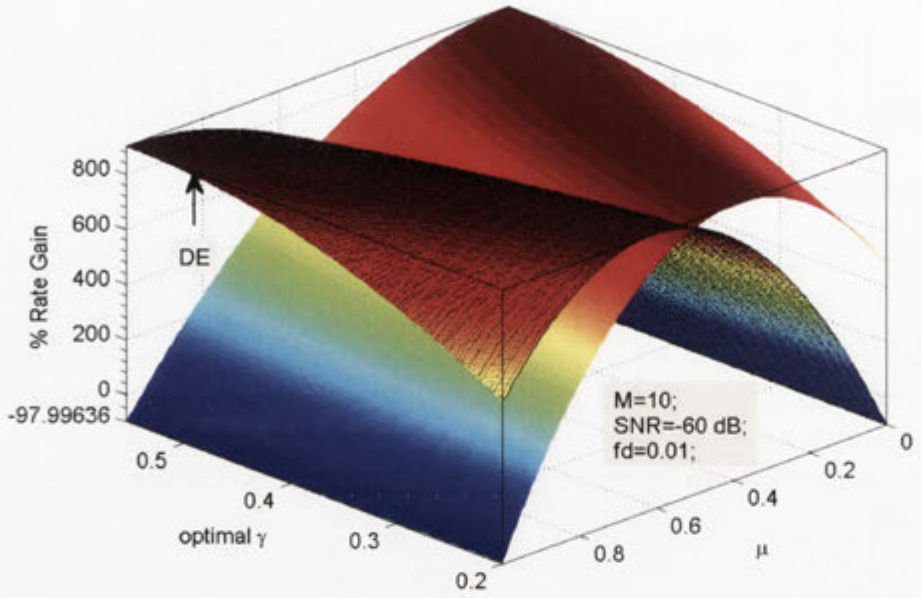

Figure 5.18: The percentage rate gain $\mathcal{R}_g$ as a function of optimal γ and μ for PE and DE schemes.

data symbol power requires

$$\mu = \frac{\gamma}{G}, \tag{5.68}$$

which collapses to $\mu = \gamma$ for non-peaky signaling. Using (5.68) and (5.35), we arrive at the following equation

$$\zeta^{\mathrm{PDE}} \approx 1 \frac{\mathcal{M}^2}{2f_{\mathrm{D}}(1/\gamma^\star)\left(G^\star\mathcal{M} + (G^{\star 2}/\rho)\right) + G^\star\mathcal{M}}, \tag{5.69}$$

where $G^\star = \mathcal{M} - (\mathcal{M}-1)\gamma^\star$. Notice a change in notation of γ which has been done simply to distinguish cases of equal and unequal pilot and data symbol power.

The optimal $\gamma^\star$ must maximize the following Rayleigh capacity lower bound

$$C^{\mathrm{PDE}} = (1-\gamma^\star)\, C_{\mathrm{Rayleigh}}(\zeta^{\mathrm{PDE}}\rho), \tag{5.70}$$

where the maximization has to be performed over $2\mathcal{M}f_{\mathrm{D}} < \gamma^\star < 1$. It does not seem possible to arrive at some simple analytical result for optimal $\gamma^\star$ due to the complexity of the expressions involved. We, therefore, have to resort to numerical means to determine optimal $\gamma^\star$ and the corresponding capacity lower bound as a function of ρ. Some simple and useful analytical results can be derived for high and low SNR as was done in the

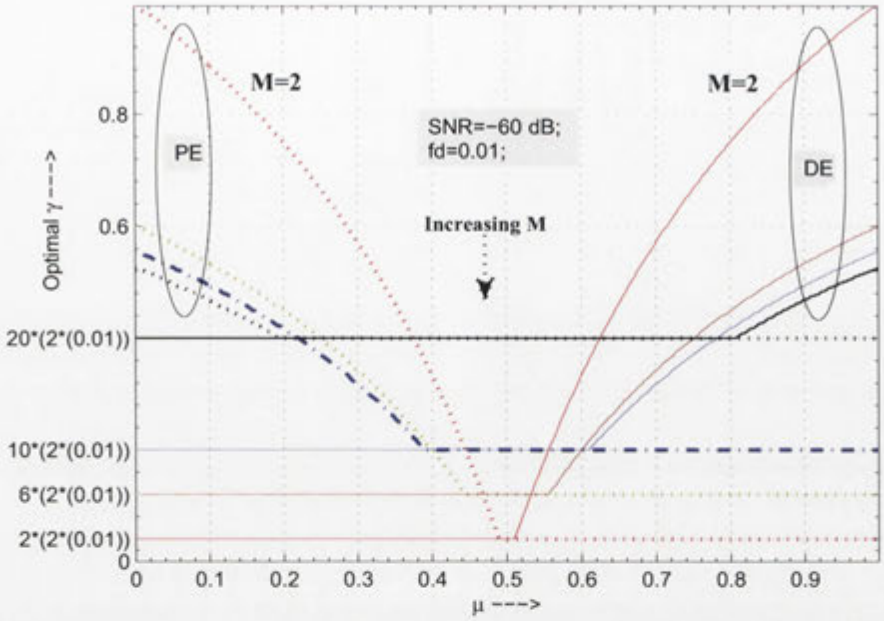

Figure 5.19: The impact of $\mathcal{M}$ on optimal γ and μ for PE and DE cases. The observed 'symmetry' across $\mu = 0.5$ is a result of very low SNR.

previous section for the case of unequal pilot/data symbol power.

Low SNR Regime

At sufficiently low SNR, ζ^{PDE} in (5.69) can be approximated as

$$\begin{aligned}\zeta_L^{\mathrm{PDE}} &= \frac{\mathcal{M}^2\rho}{2f_{\mathrm{D}}G^{\star 2}}, \\ &= \frac{\mathcal{M}^2\rho}{2f_{\mathrm{D}}\left[\mathcal{M}^2 - 2\mathcal{M}(\mathcal{M}-1)\gamma^\star + \{(\mathcal{M}-1)\gamma^\star\}\right]}.\end{aligned} \tag{5.71}$$

The $\gamma^\star$ that just maximizes ζ^{PDE} may not be optimal, *i.e.*, the same $\gamma^\star$ may not maximize the Gaussian signaling Rayleigh capacity lower bound, C^{PDE}. Therefore, in order to find out optimal γ that maximizes C^{PDE} in the low SNR regime, we make use of the approximation (5.55) and equate the first derivative of C^{PDE} with respect to $\gamma^\star$ to zero, *i.e.*,

$$\frac{\partial C^{\mathrm{PDE}}}{\partial \gamma^\star} = 0,$$

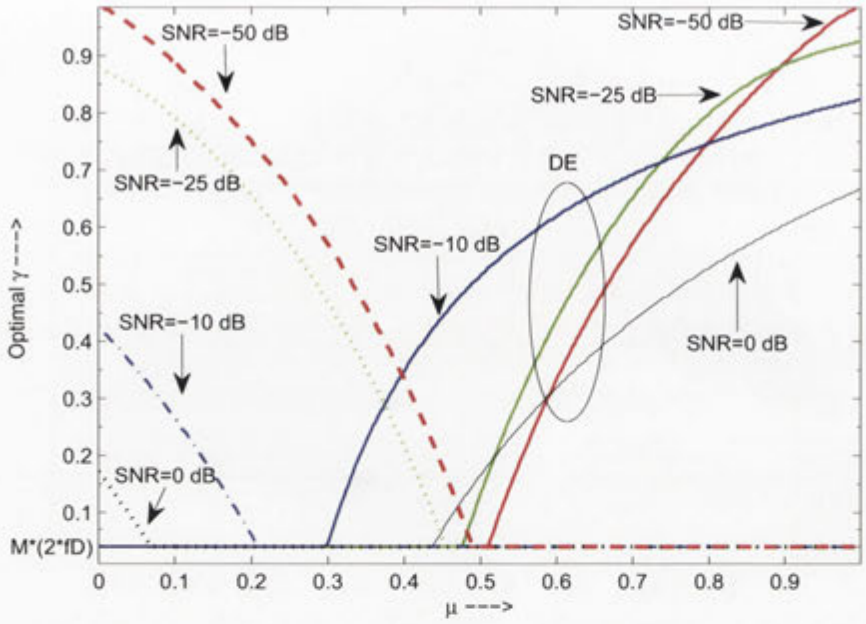

Figure 5.20: The impact of ρ on optimal γ and μ for PE and DE cases when $\mathcal{M} = 2$ and $f_{\mathrm{D}} = 0.01$. Observe that with an increase in ρ , the optimal γ for PE and DE tends to the minimum possible γ, *i.e.*, $2\mathcal{M}f_{\mathrm{D}}$ (for all μ) that satisfies the Nyquist criterion. The authors have verified that the value of ρ at which $\gamma_{opt} = 2\mathcal{M}f_{\mathrm{D}}$ is different for PE and DE cases, and is always greater for DE case.

which gives

$$\lim_{\rho \to 0} \gamma^{\star}_{opt,L} = \frac{\mathcal{M}}{\mathcal{M}+1}, \tag{5.72}$$

which equals $1/2$ for non-peaky signaling. Using (5.72), (5.71) and (5.55), we get

$$C_L^{\mathrm{PDE}} = \frac{\mathcal{M}}{8f_{\mathrm{D}}}\rho^2, \tag{5.73}$$

which is the same result as obtained for PE and DE cases in unequal pilot/data symbol power scenario and the non-peaky case [88]. We argue that PE and DE schemes would also have behaved identical to PDE in the low SNR regime for equal pilot/data symbol power. This implies that the choice of peaky or non-peaky signaling and constrained or unconstrained pilot/data symbol power does not really matter in the low SNR regime as far as quadratic dependence of the channel capacity on SNR is concerned. However, with peaky signaling combined with filtering as proposed in this chapter, the achievable rates are $\mathcal{M}$ times the rates achievable with non-peaky signaling in the low SNR regime.

High SNR Regime

At sufficiently high SNR, we can approximate ζ^{PDE} as

$$\zeta_H^{\mathrm{PDE}} = \frac{\mathcal{M}}{\mathcal{M}\{2f_{\mathrm{D}}(1/\gamma^\star)G^\star + G^\star\}}, \tag{5.74}$$

and the optimal $\gamma^\star$ in the high SNR regime can easily be determined by using ζ_H^{PDE} in the following ratio ($\mathcal{M}_{\min} 2f_{\mathrm{D}} < \gamma^\star < 1$)

$$\begin{aligned}
&\lim_{\rho\to\infty} \frac{C_H^{\mathrm{PDE}}}{(C_H^{\mathrm{PDE}})_{\mathcal{M}=\mathcal{M}_{\min}=2}} \\
&= \lim_{\rho\to\infty} \left[\frac{1-\gamma^\star}{1-2(2f_{\mathrm{D}})} \frac{\log\,\rho + \log\,\mathcal{M} - \log\,\{2f_{\mathrm{D}}(1/\gamma^\star)G^\star + G^\star\} - \mathcal{Z}}{\log\,\rho + \log\,2 - \log\,3(1-2f_{\mathrm{D}}) - \mathcal{Z}}\right], \\
&= \frac{1-\gamma^\star}{1-2(2f_{\mathrm{D}})},
\end{aligned} \tag{5.75}$$

where the first equality is based on (5.55). Notice that the last equality is decreasing in $\gamma^\star$ implying that, at high SNR, the optimal $\gamma^\star$ equals the minimum possible (which corresponds to $\mathcal{M} = 2$), *i.e.*,

$$\lim_{\rho\to\infty} \gamma_{opt}^\star = 2(2f_{\mathrm{D}}), \tag{5.76}$$

so that the optimal $\mathcal{M} = 2$ and the optimal ζ^{PDE} would be given as

$$\lim_{\rho\to\infty} \zeta_{opt,H}^{\mathrm{PDE}} = \frac{2}{3(1-2f_{\mathrm{D}})}, \tag{5.77}$$

$$> \frac{1}{2} \tag{5.78}$$

for $f_{\mathrm{D}} < 1/8$ which implies that the loss in effective SNR is *less* than 3-dB in the high SNR regime. Thus,

$$\zeta_{opt,H}^{\mathrm{PDE}} > \zeta_{opt,H}^{\mathrm{NP}}, \tag{5.79}$$

which is analytical verification of our discussion about DE in Section 5.5.1 regarding high SNR performance of the PE and DE schemes where we argued that no matter what the operating SNR is, some level of peakiness in the signaling may be desirable. Note that, even by definition, PDE is more similar to DE than to PE and, we argue, (5.79) might be true for DE but not for PE.

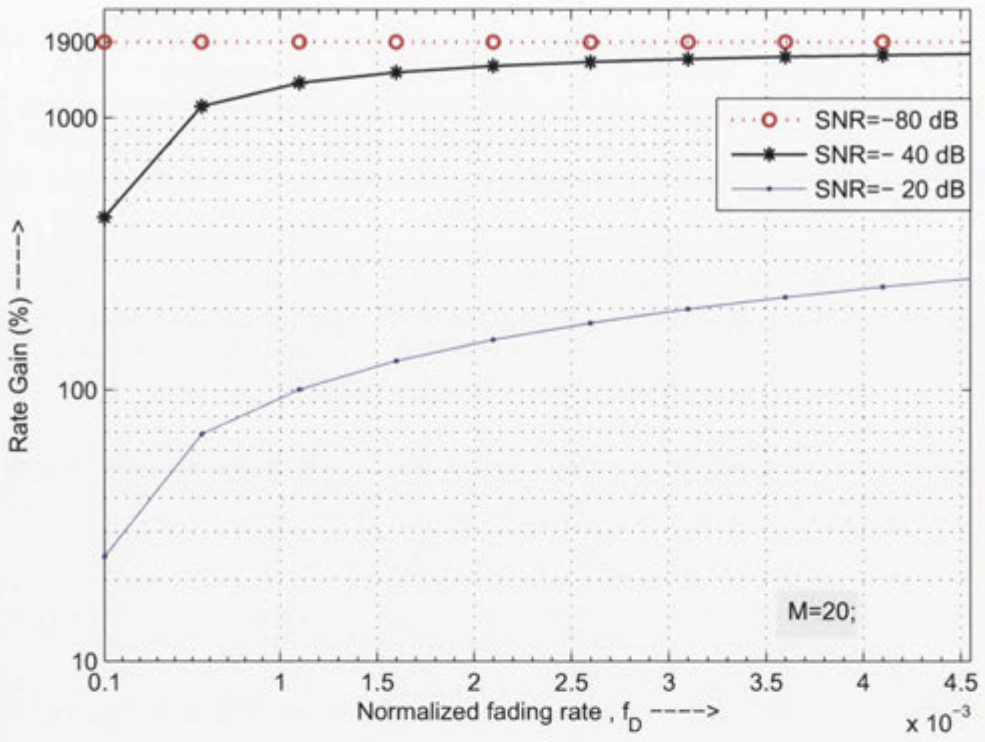

Figure 5.21: The Monte Carlo simulation of the impact of normalized fading rate on percentage rate gain $\mathcal{R}_g$ for different ρ when $\mathcal{M} = 20$ (PE case). Notice that the gain offered by the proposed scheme is independent of f_{D} at very low SNR which verifies the analytical result obtained in (5.61).

5.7 Summary and Contributions

For time-selective Rayleigh fading channels, a PACE scheme was proposed which makes use of the unused *dof* in a peaky signaling to improve the performance of channel estimation by introducing additional filtering followed by downsampling at the receiver. Assuming that the the output of the additional downsampler was input to the optimal Wiener filter, the proposed scheme resulted in $\mathcal{M}$ (the number of unused degrees of freedom plus one) times SNR enhancement of the pilot symbols that resulted in significant MMSE improvement over non-peaky signaling. The performance was enhanced even more when the power savings made possible due to unused degrees of freedom in the peaky signaling were also utilized to enhance pilot-data symbol power. The gains offered by the proposed scheme were non-trivially translated into gains of real-world parameters like bandwidth, power and achievable information rates. It turned out that in the limit of low SNR, peaky and non-peaky signaling schemes behave identically as far as quadratic behavior of channel capacity is concerned. However, the use of the proposed schemes in the low SNR regime resulted in $\mathcal{M}$ times information transmission

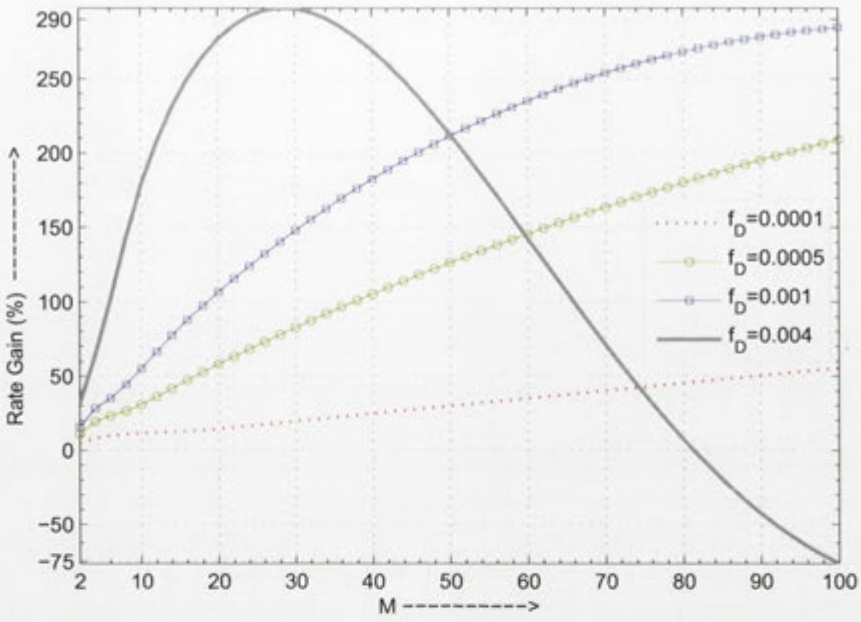

Figure 5.22: The impact of $\mathcal{M}$ on percentage rate gain $\mathcal{R}_g$ for different f_{D} when $\rho = -15$ dB. We can observe that the gains offered by the proposed scheme depend on $\mathcal{M}$ and are different for different fading rates.

rates achievable with the non-peaky scheme. In the high SNR regime, on the other hand, the use of peaky signaling with $\mathcal{M} > 2$ does not *always* warrant performance improvement as compared to the non-peaky signaling. The simulation results confirmed also by analytical results suggest that the proposed scheme with $\mathcal{M} = 2$ performs marginally better than non-peaky signaling implying that it is almost always feasible to have peaky signaling with some optimized peakiness, *i.e.*, $\mathcal{M}$.

Some specific contributions of this chapter are emphasized below:

1. A new PACE scheme is proposed which uses idle *dof* inherent in the use of the peaky signaling to significantly improve the performance, particularly, at low SNR. In fact, this scheme offers $\mathcal{M}$ times the achievable rates over Rayleigh fading channels in the low SNR regime as compared to non-peaky signaling.

2. The results suggest that the signal peakiness is always desirable from channel estimation point of view when the proposed PACE scheme is employed. However, better channel estimation may not translate into better overall performance of the communications systems.

3. The results of this chapter are, in fact, a generalization of the results previously reported in literature regarding non-peaky signaling [88]. In other words, the results

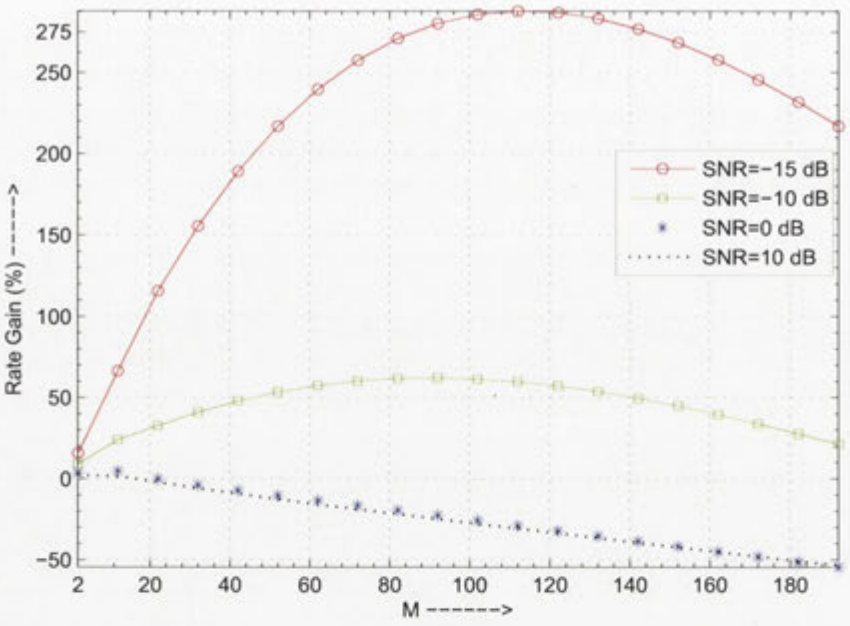

Figure 5.23: The impact of $\mathcal{M}$ on percentage rate gain $\mathcal{R}_g$ for different ρ when $f_{\mathrm{D}} = 0.001$.

of the non-peaky signaling based PACE scheme are a special case of the results of this chapter.

4. The proposed scheme offers a trade-off between bandwidth and power allocation to pilot symbols without disturbing its optimal performance. This is in contrast to non-peaky case where there is a unique allocation of resources to pilot symbols at a particular SNR and fading rate.

Chapter 6

A Framework to Calculate Space-Frequency Correlation in MultiCarrier Systems

6.1 Introduction

One of the most versatile ways to mitigate channel fading is through diversity which relies on redundancy in the communication system [223]. There are three fundamental types of diversity, *i.e.*, time, frequency and space, so that the channel fading can be mitigated by providing more than one independent copies of the transmitted signal to the intended receiver either in time and/or frequency and/or space. In this chapter, we consider a SIMO system with multicarrier modulation and derive a space-frequency cross correlation (SFCC) function which forms the basis for the analysis of interplay between space and frequency diversity. The results can be extended to MIMO system as discussed later. The multipath channel is assumed to be Rayleigh fading with time-invariant statistics characterized by a general joint angle-delay power distribution $\Psi(\widehat{\beta}, \tau)$ ($\widehat{\beta}$ is the AOA and τ denotes the delay spread) at the receiver. The motivation behind our work presented in this chapter is that the technical standards for most emerging wireless communications systems [33, 34, 224] specify the use of multiple antennas at the transmitter and the receiver utilizing multicarrier modulation to reduce intersymbol interference (ISI) resulting from very high data rate communications.

The MIMO digital communication that utilizes multiple antennas at the transmitter and receiver over a wireless link offers significant improvement in communications system performance without requiring extra spectrum or transmit power. It has emerged as one of the most significant technical breakthroughs in modern communications prompting progress in areas as diverse as information theory and coding, channel modeling,

signal processing, antenna design, cellular design and radar [225]. The future communications standards like, for example, mobileWiMax,WiBro (wireless broadband), Long-Term-Evolution (LTE) [33, 34, 224] and longer range extensions of WiMedia [45, 226] based on ultra wideband (UWB) technology which promise very high data rates are based on MIMO technology. The first generation WiBro is in fact mobile WiMax in SISO mode. The second generation WiBro is expected to be integrated with the MIMO technology [224].

The coherence bandwidth of a channel is a frequency domain description of the multipath channel and is inversely proportional the delay spread of the channel [227]. The coherence bandwidth usually ranges from several kHz to several MHz depending on the environment [228]. In the Chapters 2, 3 and 4, we assumed a narrowband (flat) fading channel which implies that the bandwidth of the transmitted signal must be less than the channel coherence bandwidth. Consequently, no channel equalizer at the receiver was required due to the absence of ISI. In emerging wireless communications systems where the data rate is above several MHz, the transmitted signal experiences frequency selective fading because of signal bandwidth exceeding channel coherence bandwidth necessitating the use of channel equalizers at the receiver to mitigate the effects of ISI which is in fact proportional to the data rate. A large number of taps in the equalizer may be required if good performance is desired in high data rate system thus adding to the complexity of the equalizer [229] proportional to the number of taps in the equalizer. Moreover, in high mobility environments it is difficult to maintain the accuracy of tap weights when the umber of taps is large. That is why most emerging technologies use multicarrier modulation in which a stream of data at higher rate is first subdivided into many substreams of lower data rate which are then transmitted over parallel subchannels where parallel subchannels are created using multiple carriers. The low data rate of individual substreams results in significantly reduced or eliminated ISI. If the carriers in the subchannels are orthogonal, the multicarrier modulation is called OFDM. Several state-of-the-art (cable and wireless) communications systems are OFDM based and it continues to be the modulation of choice for the future communication systems [230–233].

As mentioned above the use of MIMO technology promises many orders of magnitude performance enhancement for the communications system at no extra cost of spectrum and OFDM is a logical choice for very high data rate communications in view of its ability to eliminate ISI which limits the BER performance of the communications system and results in irreducible error floor. The technical standards for future communications systems like, for example, WiMax, WiBro, LTE and WiMedia promising very high data rates, therefore, specify MIMO-OFDM as the technology of choice. The analysis and design of MIMO-OFDM based systems require space-time cross correlation

among the underlying subchannels and SFCC among different subcarriers. The authors formulated a space-time cross correlation function between two omnidirectional antennas at the mobile receiver in a SIMO downlink channel with general scattering environment. The scattering was assumed to be rich enough to result in Rayleigh faded received signal envelope. This chapter is in fact concerned with the formulation of SFCC in a SIMO-OFDM system assuming that the underlying channel is time-invariant[1], *i.e.*, we seek to develop a function representing cross correlation between an OFDM subcarrier at one receive antenna and a subcarrier at the other receive antenna.

While space-time and SFCC actually reduce capacity of a MIMO-OFDM system as compared to uncorrelated MIMO with perfect CSI capacity, the correlations are all important when we do not have perfect CSI but do know the channel statistics[2]. Moreover, spatial and frequency correlations jointly offer a trade-off where spatial correlation (or, equivalently, spacing between antenna elements) and the frequency correlation can be sacrificed such that the received signal cross correlation remains fixed. The use of space diversity (or spatial correlation) to trade-off the requirement of spacing between two mobile-radio antennas was investigated in [234]. The effect of different parameters like the mean AOA, the beam width of the signal impinging on the antennae (angular spread), etc. on the cross-correlation between the signals received and the required spacing between the two antennas were first investigated in [235]. This work was generalized in [19] to wireless channels with delay spread, where the signals are received by two base-stations, separated in frequency as well as in space (space-frequency diversity). The space-frequency correlation model given in [19] assumes that APD at the receiver is uniform over a narrow range of angles. In addition, this model only considers very small angular spread values of the said APD to provide closed form expressions for space-frequency correlation. In [236], a closed-form expression for the space-frequency correlation is derived by taking in to account the power delay profile (or the angle-delay power distribution) of the channel and assuming the angular spread of the signals impinging on the antenna array is small and the antennas are placed in an uniform linear array. This model has been employed in [237] to investigate the impact of antenna spacing and propagation parameters on the performance of space-frequency coded broadband OFDM systems. Authors in [238] derived a space-frequency correlation model in 3D scattering environments which can be applied to multi-band OFDM in ultrawideband communication systems. This model however assumes that the antennas in each aperture are placed

[1]To be more precise, the assumption of time-invariance here implies that the channel is stationary, *i.e.*, it has time-invariant statistics. The channel itself can change over time. Under stationarity assumption, the SFCC is time-invariant and, therefore, the time parameter can be dropped.

[2]Recall that, throughout this thesis, our main assumption has been the absence of perfect CSI and knowledge of channel statistics at the mobile receiver.

in an uniform linear array and it also assumes that the angle of arrival, angle of departure and the delay of the multipath components are independent of each other.

We, here in this chapter, employ the modal analysis approach introduced in [36] to derive a space-frequency correlation model at the receiver side in closed form applicable in 2D and 3D scattering environments. In fact the derived model can be treated as a framework, which can be applied to calculate the space-frequency correlation in multicarrier communication systems in general multipath channel environments. The proposed framework is more general than previous frameworks [19, 234–236, 238] because

- it incorporates antenna locations instead of their spacing to capture the spatial information of the channel (*i.e.*, the model is not specific to any particular antenna configuration)
- it captures the frequency selectivity of the multipath channel for arbitrary joint angle-delay power distribution which could either be experimentally validated or could be any distribution that may be theoretically convenient
- it is applicable in general 2D and 3D scattering environments
- the angular spread in this model does not have to be either very small or very large to arrive at a closed form expression for SFCC function.

To demonstrate the strength of the proposed framework, we derive some special cases of the generalized space-time cross correlation function. Some detailed results are obtained for a receiver with two antennas symmetrically located across the origin. The scattering around the receiver is is not limited to uniform as in [19]. We also use the proposed framework for a SIMO-OFDM system to obtain the space-frequency correlation between two antenna elements at the receiver for two analytically derived joint angle-delay power distributions found in the literature. In addition we discuss the possible extensions and applications of the proposed model to investigate the impacts of antenna spacing, antenna configuration and channel parameters on the performance of multi-antenna multi-carrier communication systems.

The chapter is organized in the following manner: In Section 6.2, a discrete-time space-frequency selective channel model applicable to an OFDM system is described and a continuous-time generalization of that model is considered to facilitate the subsequent study. A general SFCC function is derived in Section 6.3 and is specialized to 2D and 3D scattering environments. Some special cases of the generalized model are derived in Section 6.4. The numerical evaluation of correlation for a particular multicarrier SIMO-OFDM system is discussed in Section 6.5. Another special case of the

generalized correlation function is obtained in Section 6.6 for a 2-Carrier SIMO system which, in fact, generalizes the previously reported results regarding SFCC [19]. Finally, the chapter summary and specific contributions are provided in Section 6.7.

6.2 Space-Frequency Selective Channel Model for MultiCarrier OFDM

We consider a stationary[3] frequency-selective wireless fading channel in which data is transmitted from a single transmit antenna to n_R receive antennas (*i.e.*, a SIMO system) (Fig. 6.1). The standard way is to model the fading channel as a tapped-delay-line [227, 229]. In this model, the complex channel impulse response between the transmit antenna and the pth receive antenna at time τ is written as

$$h_p(\tau) = \sum_{\ell=1}^{L} \alpha_p(\ell) \exp\left(-i2\pi f_c \tau_\ell\right) \delta(\tau - \tau_\ell), \tag{6.1}$$

where L is the number of non-zero taps (or the number of resolvable multipath components between the transmitter and the receiver), τ_ℓ is the delay of the ℓth multipath component with respect to LOS component (which does not actually exist in the channel under consideration but is taken as a reference as it corresponds to zero transmission delay), $\alpha_p(\ell)$ is the complex amplitude of the ℓth path between the transmit antenna and the pth receive antenna, f_c is the carrier frequency and $\delta(\cdot)$ is the Dirac delta function. We assume that the coefficients $\alpha_p(\ell)$ are zero-mean circularly symmetric complex Gaussian random variables with variances $\mathbb{E}\left\{|\alpha_p(\ell)|^2\right\} = \sigma_\ell^2$. Notice that the absence of $\ell = 0$ in (6.1) implies that there is no line-of-sight (LOS) component in the received signal and, therefore, the taps are Rayleigh distributed.

We assume that the SIMO communications system uses OFDM multicarrier modulation with N_s subcarriers. From (6.1), the frequency response at the nth subcarrier between the transmit antenna and the pth receive antenna is given by [239]

$$H_p(n) = \sum_{\ell=1}^{L} \alpha_p(\ell) \exp\left(-i2\pi(f_c - (n+0.5)\Delta f)\tau_\ell\right), \quad n = \frac{-N_s}{2}, \cdots, \frac{N_s}{2} - 1, \tag{6.2}$$

where $\Delta f = 1/T_s$ is the subcarrier separation in the frequency domain and T_s is the OFDM symbol duration. Note that in this model only a finite number of multipath

[3]The assumption of a stationary channel makes the frequency selectivity of the channel to be independent of time. We shall therefore freeze the time dimension throughout this chapter.

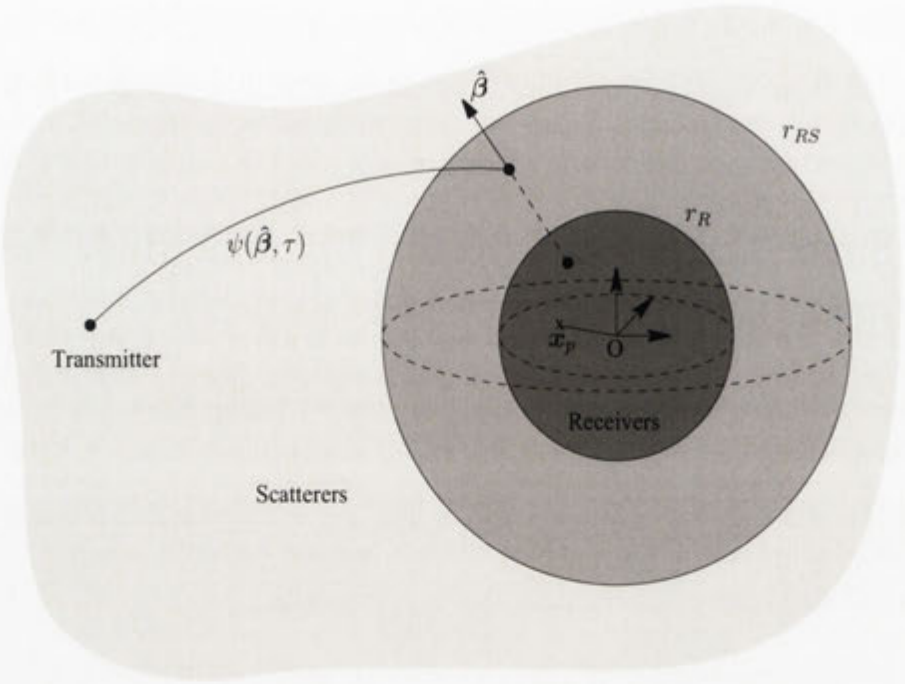

Figure 6.1: A general scattering model for the frequency-selective SIMO system. $\psi(\widehat{\boldsymbol{\beta}}, \tau)$ is the random complex scattering gain for the waves arriving in direction $\widehat{\boldsymbol{\beta}}$ with delay τ at the receiver aperture. $\boldsymbol{x}_p$ is the location of the pth receive antenna relative to the receiver origin 'O' and $p = 1, \cdots, n_R$ and . $r_R \geq \max ||\boldsymbol{x}_p||$ is the radius of the sphere which encloses the receiver antennas. Scatters are distributed outside of the sphere with radius $r_{RS} > r_R$ and assumed they are in the farfield from the receiver antennas.

components are considered with each path having a discrete delay. A generalization that subsumes (6.2) is

$$H_p(n) = \int_{\tau} \alpha_p(\tau) \exp(-i2\pi(f_c - (n + 0.5)\Delta f)\tau) d\tau, \tag{6.3}$$

where the fading coefficient $\alpha_p(\tau)$ is given by

$$\alpha_p(\tau) = \int_{\Omega_R} \psi(\widehat{\boldsymbol{\beta}}, \tau) \exp\left(-i\frac{2\pi}{c}(f_c - (n + 0.5)\Delta f)\boldsymbol{x}_p \cdot \widehat{\boldsymbol{\beta}}\right) d\widehat{\boldsymbol{\beta}}. \tag{6.4}$$

The derivation of (6.2) is given in Appendix E.1. Integration in (6.4) is over the unit sphere for a 3D scattering environment or the unit circle in the 2D case. Note that fading coefficient $\alpha_p(\tau)$ given in (6.4) captures the statistical properties of the frequency selective channel via the random complex scattering gain $\psi_p(\widehat{\boldsymbol{\beta}}, \tau)$ and physical configuration of the receiver antenna array, which is deterministic, via the location of the pth antenna $\boldsymbol{x}_p$. As a result, this framework can be applied to any receiver antenna configuration without constraining to a particular antenna configuration such as uniform linear array

or uniform circular array, etc.. In equation (6.4), $\psi(\widehat{\boldsymbol{\beta}}, \tau)$ is the zero-mean random complex scattering gain with respect to the array origin for the waves arriving in direction $\widehat{\boldsymbol{\beta}}$ with delay τ , $\boldsymbol{x}_p$ is the position of the pth receive antenna relative to the receiver origin 'O' as shown in Fig. 6.1. Notice that the factor $\exp\left(-i\frac{2\pi}{c}\left(f_c-(n+0.5)\Delta f\right)\boldsymbol{x}_p.\widehat{\boldsymbol{\beta}}\right)$ is a deterministic *angular-array constant* due to the displacement of antenna p from the origin.

6.3 Space-Frequency Cross Correlation for MultiCarrier OFDM

We use (6.2) and (6.3) in the Appendix E.2 to derive SFCC between the nth subcarrier on the pth receive antenna located at position $\boldsymbol{x}_p$ and the mth subcarrier on the qth receive antenna located at position $\boldsymbol{x}_q$ is

$$\begin{aligned}
&\Phi_{p,q}(n,m)\\
&\triangleq \mathbb{E}\left\{H_p(n)H_q^*(m)\right\}\\
&=\int_{\Omega_R}\int_{\tau}\Psi(\widehat{\boldsymbol{\beta}},\Delta f)\exp(-i2\pi(m-n)\Delta f\tau)\exp\left(-i\frac{1}{c}(\omega_n\boldsymbol{x}_p-\omega_m\boldsymbol{x}_q).\widehat{\boldsymbol{\beta}}\right)d\widehat{\boldsymbol{\beta}}d\tau,
\end{aligned} \tag{6.5}$$

where $\omega_k = 2\pi(f_c-(k+0.5)\Delta f)$ and

$$\Psi(\widehat{\boldsymbol{\beta}},\Delta f)=\Psi(\widehat{\boldsymbol{\beta}},n,m)\triangleq\int_{\tau}\Psi(\widehat{\boldsymbol{\beta}},\tau)\exp\left(i2\pi(m-1)\Delta f\,\tau\right)d\tau, \tag{6.6}$$

which represents *angular-delay power spectrum*. It may be mentioned here that the use of power spectra in channel modeling implicitly assume that the channel is WSS over basic space and frequency intervals of interest. The frequency interval of interest is the transmitted signal radio-frequency (RF) bandwidth and the spatial interval of interest is usually of the order of a wavelength called the local area [240]. The size of the local area is selected sufficiently small such that the channel parameters do not change due to large scale-fading (shadowing). If the power measurements are made by moving the receiver on the order of the wavelength, the obtained channel spectra are highly de-correlated resulting in improved average channel spectra over the local area [241].

As shown in Appendix E.2, the frequency cross correlation between the subcarriers of two antennas from a given direction is given by

$$\widetilde{\chi}(\widehat{\boldsymbol{\beta}},n,m)=\int_{\tau}\Psi(\widehat{\boldsymbol{\beta}},\tau)\exp\left(-i2\pi(m-n)\Delta f\tau\right)d\tau.$$

Therefore, $\Phi_{p,q}(n,m)$ in (6.5) can be rewritten as

$$\Phi_{p,q}(n,m) = \int_{\Omega_R} \widetilde{\chi}(\widehat{\boldsymbol{\beta}},n,m) \exp\left(-i\frac{1}{c}(\omega_n \boldsymbol{x}_p - \omega_m \boldsymbol{x}_q).\widehat{\boldsymbol{\beta}}\right) d\widehat{\boldsymbol{\beta}}. \tag{6.7}$$

Notice that we arrived at equation (6.7) assuming that the scattering is uncorrelated in the angle domain, *i.e.*, the scattering from one direction is uncorrelated with scattering from another direction (Eq. (E.9)) and that the channel process is uncorrelated in the delay domain [5, 242] (Eq. (E.12)), which in turn implies that the complex scattering channel gain is wide sense stationary in the frequency domain [55], *i.e.*,

$$\mathbb{E}\left\{a(\widehat{\boldsymbol{\beta}}_1,\tau_1)a^*(\widehat{\boldsymbol{\beta}}_2,\tau_2)\right\} = \begin{cases} 0, & \text{if } \tau_1 \neq \tau_2 \text{ and } \widehat{\boldsymbol{\beta}}_1 \neq \widehat{\boldsymbol{\beta}}_2; \\ \mathbb{E}\left\{|a(\widehat{\boldsymbol{\beta}}_1,\tau_1)|^2\right\}, & \text{otherwise.} \end{cases}$$

We have already discussed in Chapter 2 that the assumption of uncorrelated scattering (US) is widely used in channel modeling literature and is validated by practical measurements. One possible extension of the framework developed in this chapter is that takes into account the correlation among scatterers by following [113]. The second assumption that the channel process is uncorrelated in the delay domain is a standard assumption used in the channel modeling literature and verified through measurements [5, 59, 104, 110, 142].

Equation (6.7) gives the normalized cross covariance of the complex channel processes at the two antennas located at $\boldsymbol{x}_p$ and $\boldsymbol{x}_q$ with respect to the origin. We are often more interested in the cross correlation of the envelopes of the complex channel process at the two antennas in view of the fact that the envelope of the complex signal can be measured easily. The normalized cross covariance function (*i.e.*, the correlation coefficient) of the channel envelopes at the two antennas is, to a good approximation, equal to the squared magnitude of the normalized covariance function of the complex channels [19]. Therefore, the envelope cross correlation $\Phi_H^{p,q}(n,m)$ is given as follows

$$\Phi_H^{p,q}(n,m) = \left|\int_{\Omega_R} \widetilde{\chi}(\widehat{\boldsymbol{\beta}},n,m) \exp\left(-i\frac{1}{c}(\omega_n \boldsymbol{x}_p - \omega_m \boldsymbol{x}_q).\widehat{\boldsymbol{\beta}}\right)\right|^2. \tag{6.8}$$

6.3.1 2D Scattering Environment

When the multipath is restricted to the azimuth plane only (2D scattering environment), having no field components arriving at significant elevations, the term $\exp\left(-i(\omega_n \boldsymbol{x}_p - \omega_m \boldsymbol{x}_q).\widehat{\boldsymbol{\beta}}/c\right)$ in (6.7) can be expanded using 2D Jacobi-Anger expansion of the plane wave (Chapter

2) as follows

$$\exp\left(-i\frac{1}{c}(\omega_n \boldsymbol{x}_p - \omega_m \boldsymbol{x}_q).\widehat{\boldsymbol{\beta}}\right) = \sum_{v=-\infty}^{\infty} i^v J_v\left(\frac{1}{c}||\omega_n \boldsymbol{x}_p - \omega_m \boldsymbol{x}_q||\right) e^{iv(\beta_{p,q}-\beta)}, \quad (6.9)$$

where $J_v(\cdot)$ is the integer order v Bessel function, $\omega_n \boldsymbol{x}_p - \omega_m \boldsymbol{x}_q = \Delta_{n,m}^{p,q}, \beta_{p,q}$ where we have defined

$$\Delta_{n,m}^{p,q} \triangleq ||\omega_n \boldsymbol{x}_p - \omega_m \boldsymbol{x}_q||, \quad (6.10)$$

and $\widehat{\boldsymbol{\beta}} \triangleq 1, \beta$ in the polar coordinates system. Substitution of (6.9) in (6.7) yields

$$\Phi_{p,q}(n,m) = \sum_{\nu=-\infty}^{\infty} \gamma_\nu(n,m) i^\nu J_\nu\left(\frac{\Delta_{n,m}^{p,q}}{c}\right) \exp\left(i\nu\beta_{p,q}\right), \quad (6.11)$$

where

$$\begin{aligned}\gamma_\nu(n,m) &= \int_0^{2\pi} \widetilde{\chi}(\beta,n,m) \exp\left(-i\nu\beta\right) d\beta, \\ &= \oint \int_\tau \Psi(\beta,\tau) \exp\left(-i2\pi(m-n)\Delta f\tau\right) \exp\left(-i\nu\beta\right) d\tau d\beta, \end{aligned} \quad (6.12)$$

are the scattering environment coefficients which characterize the 2D scattering environment surrounding the receiver antenna array and $\Psi(\beta,\tau)$ is the joint azimuth angle-delay power distribution at the receiver aperture. Some examples for $\Psi(\beta,\tau)$ are: Elliptical and Circular scattering models in [5], Gaussian scatterer density model in [105] and inverted-parabolic spatial distribution model in [4].

6.3.2 3D Scattering Environment

We now generalize the space-frequency correlation function for a 3D scattering environment. The plane wave, $\exp\left(-i(\omega_n \boldsymbol{x}_p - \omega_m \boldsymbol{x}_q).\widehat{\boldsymbol{\beta}}/c\right)$ in (6.7) can be expanded using spherical harmonics as [89, page 32]

$$\exp\left(-i\frac{1}{c}(\omega_n \boldsymbol{x}_p - \omega_m \boldsymbol{x}_q).\widehat{\boldsymbol{\beta}}\right) = 4\pi \sum_{\vartheta=0}^{\infty} i^\vartheta j_\vartheta\left(\frac{\Delta_{n,m}^{p,q}}{c}\right) \sum_{\nu=-\vartheta}^{\vartheta} Y_{\vartheta,\nu}(\widehat{\boldsymbol{x}}_{p,q}) Y_{\vartheta,\nu}^*(\widehat{\boldsymbol{\beta}}), \quad (6.13)$$

where $j_\vartheta(r) \triangleq \sqrt{\pi/2r}J_{n+1/2}(r)$ are spherical Bessel functions, ϑ and ν are integers , $\widehat{\boldsymbol{x}}_{p,q} = (\omega_n \boldsymbol{x}_p - \omega_m \boldsymbol{x}_q)/\Delta_{n,m}^{p,q}$ and the spherical harmonics $Y_{\vartheta,\nu}$ are defined as

$$Y_{\vartheta,\nu}(\widehat{\boldsymbol{x}}) \equiv Y_{\vartheta,\nu}(\theta_{\boldsymbol{x}}, \varphi_{\boldsymbol{x}}) \triangleq \sqrt{\frac{2\vartheta+1}{4\pi}\frac{(\vartheta-|\nu|)!}{(\vartheta+|\nu|)!}} P_\vartheta^{|\nu|}(\cos\theta_{\boldsymbol{x}}) \exp(i\nu\varphi_{\boldsymbol{x}}),$$

where $\theta_{\boldsymbol{x}}$ and $\varphi_{\boldsymbol{x}}$ are respectively the elevation and azimuth of the unit vector $\boldsymbol{x}$ and $P_\vartheta^\nu(\cdot)$ are the associated Legendre functions of the first kind. Substitution of (6.13) in (6.7) gives

$$\Psi_{p,q}(n,m) = 4\pi \sum_{\vartheta=0}^{\infty} i^\nu j_\vartheta\left(\frac{\Delta_{n,m}^{p,q}}{c}\right) \sum_{\nu=-\vartheta}^{\vartheta} \gamma_{\vartheta,\nu}(n,m) Y_{\vartheta,\nu}\left(\frac{\omega_n \boldsymbol{x}_p - \omega_m \boldsymbol{x}_q}{\Delta_{n,m}^{p,q}}\right), \quad (6.14)$$

where

$$\gamma_{\vartheta,\nu}(n,m) = \int_{\Omega_R} \widetilde{\chi}(\beta,n,m) Y_{\vartheta,\nu}^*(\widehat{\boldsymbol{\beta}}) d\beta, \quad (6.15)$$

are the scattering environment coefficients which characterize the 3D scattering environment surrounding the receiver antenna array. Similar to the 2D case, the higher order spherical Bessel functions have small values for arguments near zero [243]. Therefore, only a few terms in the sum need to be evaluated in order to obtain a very good approximation for the space-frequency correlation of the channel.

6.3.3 Some Comments on Extension to MIMO-OFDM

It is important to mention here that the space-frequency correlation functions (equations (6.11) and (6.14)) can be extended from SIMO to MIMO following the approach introduced in [244] which would make it possible to eventually apply these correlation functions for the performance evaluation of emerging wireless communications systems based on MIMO-OFDM in non-coherent or partially coherent communication. For a MIMO system the statistical properties of the underlying channel are governed by a 3D angular power delay profile $\Psi(\widehat{\boldsymbol{\theta}}, \beta, \tau)$, where $\widehat{\boldsymbol{\theta}}$ is the angle-of-departure (AOD) at the transmitter aperture, β is AOA) at the receiver aperture and τ is the multipath delay. To the best knowledge of the authors, there does not exist a joint distribution to model the interdependency of the AOD, AOA and the multipath delay in the literature [245]. One possible option is to consider a Kronecker channel model and write the joint distribution $\Psi(\widehat{\boldsymbol{\theta}}, \beta, \tau) \triangleq \Psi'(\widehat{\boldsymbol{\theta}})\Psi'(\beta, \tau)$. However, as shown in [30], Kronecker type channel has certain limitations and therefore is not a general model to use when there are multiple

scattering clusters.

6.4 Special Cases of Space-Frequency Correlation for MultiCarrier OFDM

In order to demonstrate the generality of the SFCC $\Psi_{p,q}(n,m)$ given in (6.7), we specialize $\Psi_{p,q}(n,m)$ to the following different cases.

1. If we assume 2D scattering and $\Delta f = 0$, *i.e.*, $\omega_n = \omega_m = \omega_c$ (which corresponds to a frequency non-selective channel), the space-frequency correlation in (6.7) reduces to the following spatial correlation

$$\Psi_{p,q}(\boldsymbol{x}_q - \boldsymbol{x}_p) = \oint \Psi(\beta) \exp\left(-i\eta(\boldsymbol{x}_q - \boldsymbol{x}_p) \cdot \widehat{\boldsymbol{\beta}}\right) d\beta, \tag{6.16}$$

   where $\eta = 2\pi/\lambda_c$ and $\Psi(\beta)$ is the angular power distribution of the received signal. Equation (6.16) represents the spatial correlation between two antennas in a general scattering environment as derived in [36]. The array geometry is arbitrary due to the actual locations of the antennas involved. Similarly, we can show that the space-frequency correlation in 3D collapses to the corresponding spatial correlation function derived in [36].

2. Equations (6.5) and (6.7) consider that the angle-delay power distribution $\Psi(\beta,\tau)$ is a joint function of AOA and the multipath delay (or TOA). If the multipath delay is independent of the angle of arrival, which is the case considered in [238] for antennas placed in a uniform linear array, we can write $\Psi(\beta,\tau) = \Psi(\beta)\Psi(\tau)$ or in the frequency domain as $\widetilde{\chi}(\beta,n,m) = \Psi(\beta)\Phi_{\Delta f}(n,m)$ where the frequency cross correlation $\Phi_{\Delta f}(n,m)$ is given by

$$\Phi_{\Delta f}(n,m) = \int_t \Phi(\tau) \exp\left(-i2\pi(m-n)\Delta f\tau\right) d\tau, \tag{6.17}$$

   so that $\Phi_{p,q}(n,m)$ in (6.7), which is the SFCC in a SIMO-OFDM system in general rich scattering environment, simplifies to

$$\Phi_{p,q}(n,m) = \Phi_{\Delta f}(n,m) \int_{\Omega_R} \Psi(\beta) \exp\left(-i\frac{1}{c}(\omega_n \boldsymbol{x}_p - \omega_m \boldsymbol{x}_q).\widehat{\boldsymbol{\beta}}\right) d\beta. \tag{6.18}$$

3. Under the assumption of independent angle and time of arrival of waves in 2D scattering, the scattering coefficients of joint angle-delay power distribution $\gamma_\nu(n,m)$

in (6.12) become

$$\gamma_\nu(n,m) = \Phi_{\Delta f}(n,m)\gamma_\nu(\beta), \tag{6.19}$$

which implies that the scattering coefficients of joint angle-delay power distribution are simply the product of frequency cross correlation and the scattering coefficients of the angular distribution $\Psi(\beta)$ which are given as

$$\gamma_\nu(\beta) = \int_{\Omega_R} \Psi(\beta) Y^*_{\vartheta,\nu}(\widehat{\boldsymbol{\beta}}) d\beta. \tag{6.20}$$

In simple words, equation (6.19) suggests that νth scattering coefficient of the joint angle-delay power distribution equals the frequency cross correlation between subcarriers at the two antennas weighted by the νth scattering coefficient of the APD. Using (6.19), we can rewrite the space-frequency channel cross correlation in 2D scattering as (Eq. (6.14))

$$\Phi_{p,q}(n,m) = \overbrace{\Phi_{\Delta f}(n,m)}^{\text{Frequency Cross Correlation}} \overbrace{\sum_{\nu=-\infty}^{\infty} \gamma_\nu(\beta)(n,m) i^\nu J_\nu\left(\frac{\Delta^{p,q}_{n,m}}{c}\right) \exp\left(i\nu\beta_{p,q}\right)}^{\text{Spatial Cross Correlation}}. \tag{6.21}$$

In [36], closed-form expressions for $\gamma_\nu(\beta)$ are given for several well studied azimuth power distributions such as uniform limited, Gaussian, Laplacian, von-Mises, etc..

Similarly, when the scattering environment is 3D and the assumption of independence of AOA and TOA is maintained, the scattering coefficients $\gamma_{\vartheta,\nu}(\beta,n,m)$ (equation (6.15)) can be decomposed into space and frequency dependent parts as

$$\begin{aligned}\gamma_{\vartheta,\nu}(\beta,n,m) &= \Phi_{\Delta f}(n,m) \int_{Omega_R} \Psi(\beta) Y^*_{\vartheta,\nu}(\widehat{\boldsymbol{\beta}}) d\beta, \\ &= \Phi_{\Delta f}(n,m)\gamma_{\vartheta,\nu}(\beta).\end{aligned} \tag{6.22}$$

Using (6.3.2) and (6.22), SFCC $\Phi_{p,q}(n,m)$ in 3D becomes separable in frequency and spatial cross correlation functions as follows

$$\Phi_{p,q}(n,m) = \overbrace{\Phi_{\Delta f}(n,m)}^{\text{Frequency Cross Correlation}}$$

$$\overbrace{\times 4\pi \sum_{\vartheta=0}^{\infty} i^{\nu} j_{\vartheta}\left(\frac{\Delta_{n,m}^{p,q}}{c}\right) \sum_{\nu=-\vartheta}^{\vartheta} \gamma_{\vartheta,\nu}(n,m) Y_{\vartheta,\nu}\left(\frac{\omega_n \boldsymbol{x}_p - \omega_m \boldsymbol{x}_q}{\Delta_{n,m}^{p,q}}\right)}^{\text{3D Spatial Cross Correlation}}, \tag{6.23}$$

where

$$\gamma_{\vartheta,\nu}(\beta) = \int_{\Omega_R} \Psi(\beta) \exp\left(-i\nu\beta\right) d\beta. \tag{6.24}$$

4. For a SISO-OFDM system it is noted from (6.5) that the frequency correlation between subcarriers at the receiver from a particular angle is given by

$$\Phi(\beta, n, m) = \int_{\tau} \Psi(\beta, \tau) \exp\left(-i2\pi(m-n)\Delta f\, \tau\right) d\tau \tag{6.25}$$

and if we further assume that AOA and TOA of impingent waves are independent of each other, we get

$$\Phi(\beta, n, m) = \Psi(\beta)\Phi_{\Delta f}(n, m) \tag{6.26}$$

where $\Phi_{\Delta f}(n, m)$ is the Fourier transform of $\Psi(\tau)$ — the delay power spectrum or the power-delay profile. The normalized frequency correlation between mth and nth subcarriers is then obtained by integrating $\Phi(\beta, n, m)$ over the whole azimuth, *i.e.*,

$$\Phi(n, m) = \Phi_{\Delta f}(n, m). \tag{6.27}$$

As an example, when the angular power spectrum is uniform over azimuth and the multipath inter-arrival delay is exponentially distributed with delay spread Γ [19, 239], the correlation between subcarriers at the receiver is given by

$$\Phi(n, m) = \frac{1}{1 + i2\pi(m-n)\Delta f\, \tau} \tag{6.28}$$

5. From (6.5), frequency correlation between m'th and n'th sub-carriers on the pth receive antenna is given by

$$\Phi_{p,p}(n', m') = \int_{\Omega_R} \int_{\tau} \Psi(\beta, \tau) \exp\left(-i2\pi(m'-n')\Delta f \left[\tau + \frac{\boldsymbol{x}_p \cdot \widehat{\boldsymbol{\beta}}}{c}\right]\right) d\beta d\tau. \tag{6.29}$$

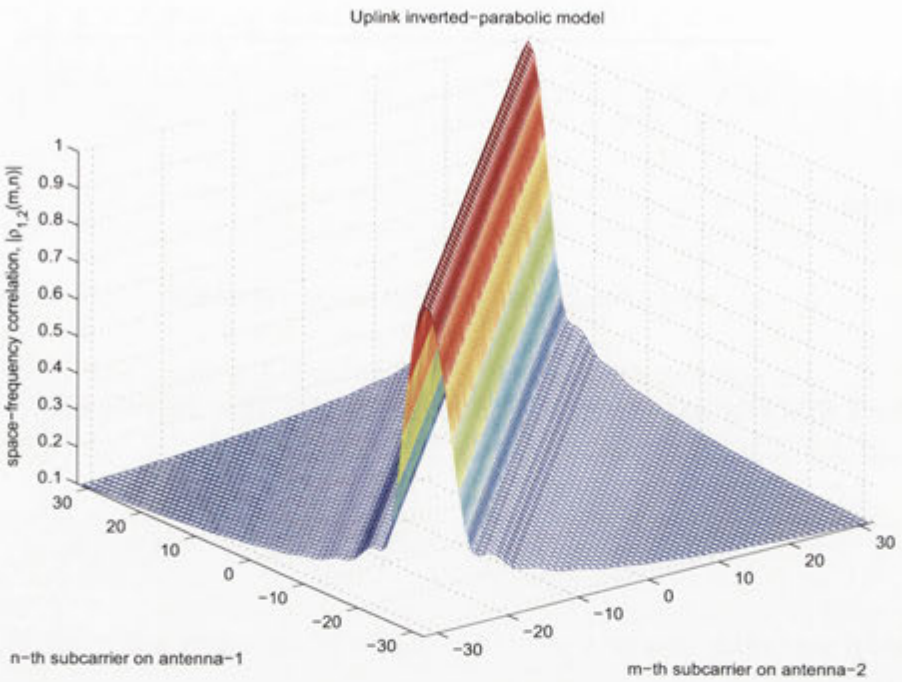

Figure 6.2: Absolute value of the space-frequency correlation function (6.11) across subcarriers on two receive antennas placed $d = 0.25\lambda$ apart for the IP uplink model (Fig. 3 in [4]).

6.5 Numerical Analysis of Space Frequency Correlation for MultiCarrier OFDM

We now demonstrate the strengths of the space-frequency correlation framework developed above by applying it on a SIMO-OFDM system with $f_c = 5.25$GHz, $N_s = 64$ sub-carriers and $\Delta f = 250$kHz. The joint angle-delay power distribution $\Psi(\beta, \tau)$ at the receiver aperture is modeled using two different distributions[4]: i) Elliptical scattering (ES) model derived in [5], ii) uplink and downlink inverted-parabolic (IP) spatial distribution models derived in [4]. Figures 6.2, 6.3 and 6.4 depict the absolute value of the space-frequency correlation function (6.11)[5] as a function of the subcarrier number for the IP uplink model (Fig. 3 in [4]), IP downlink model (Fig. 5 in [4]) and the ES model (Fig. 5 in [5]), respectively. We assume that two receive antennas are located on the x-axis symmetrically about the receiver origin and separated by a distance $d = 0.25\lambda$. It is observed that for all scattering distributions high space-frequency correlation is observed at adjacent subcarriers (see Fig. 6.5 for the contour plots of $|\Phi_{1,2}(n, m)|$ for the IP uplink model shown in Fig. 6.2.) and space-frequency correlation decreases as the frequency

[4]Readers are referred to [5] and [4] for details of these distributions. The space-frequency correlation plots given in this paper use the parameter values used in [5] and [4].

[5]Corresponding scattering environment coefficients $\gamma_\nu(n, m)$ are calculated numerically.

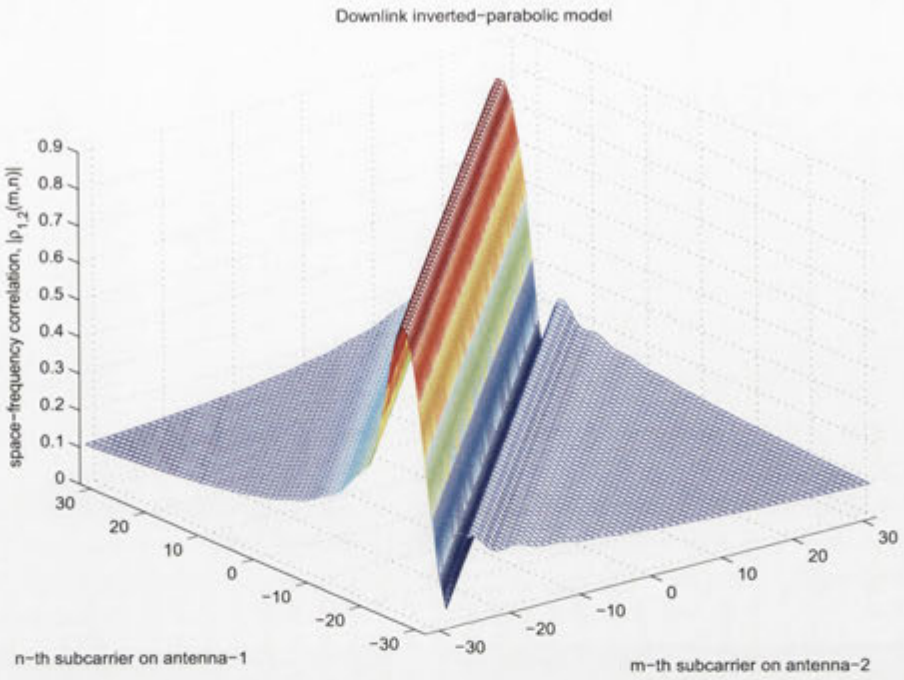

Figure 6.3: Absolute value of the space-frequency correlation function (6.11) across subcarriers on two receive antennas placed $d = 0.25\lambda$ apart for the IP downlink model (Fig. 5 in [4])

separation increases. With the IP uplink model, we observed higher space-frequency correlation compared to the other two models. This is due to the small angular spread at the receiver aperture for the IP uplink model. From all plots we observed that the absolute value of the space-frequency correlation is non-symmetric about the same subcarrier on both antennas (*i.e.*, $|\Phi_{1,2}(m,m)|$). However, when the multipath delay τ is independent of the angle of arrival $\widehat{\boldsymbol{\beta}}$, *i.e.*, $\Psi(\widehat{\boldsymbol{\beta}},\tau) = \Psi(\widehat{\boldsymbol{\beta}})\Psi(\tau)$, it can be shown using (6.11) and (6.19) that $|\Phi_{p,q}(n,m)| = |\Phi_{p,q}(m,n)|$, which implies that in this case the absolute value of the space-frequency correlation is symmetric about the same subcarrier on both antennas.

6.6 Generalization of Space-Frequency Cross Correlation for a 2-Carrier SIMO system

The space-frequency diversity trade-off in a SIMO uplink channel is explored in [19] assuming two signals at two different frequencies ω_1 and ω_2 transmitted by the mobile propagate by way of scattering and are received by a two-antenna base-station receiver where one antenna is tuned to receive the transmitted signal at ω_1 and the other at ω_2. The carrier frequency is assumed to be ω_c and ω_1 and ω_2 are separated by $\Delta\omega$ assuming

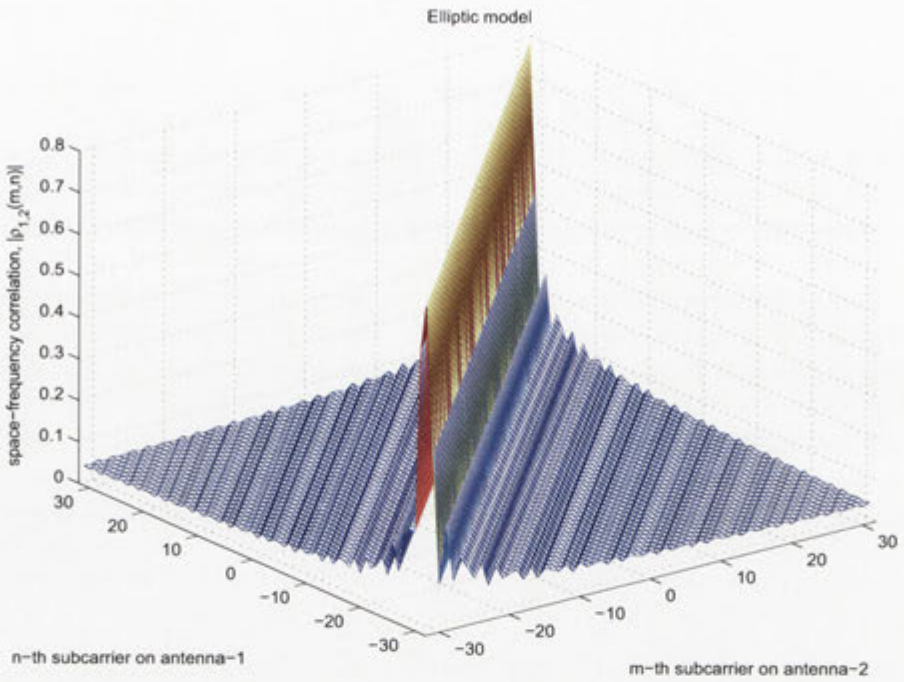

Figure 6.4: Absolute value of the space-frequency correlation function (6.11) across subcarriers on two receive antennas placed $d = 0.25\lambda$ apart for the elliptical scattering model (Fig. 5 in [5])

that the two frequencies are symmetrically located across ω_c, *i.e.*, $\omega_1 = \omega_c + \Delta\omega/2$ and $\omega_1 = \omega_c - \Delta\omega/2$. The two antennas are assumed to be vertical dipole so that electrical field (in the vertical direction) is proportional to the signal input to the antenna. The two antennas are located symmetrically across the origin on x-axis separated by a distance d. The scatterers are assumed to be in the far-field which implies that the AOA at two antennas are approximately the same due to wave propagation distance being much larger than d. The AOA and TOA of waves impingent on the two antennas are independent of each other. The distribution of AOA for all waves is identical and uniform over a very narrow range of angles which implies that scattered power is uniformly distributed in that short range of angles. The 2D scattering is assumed to be rich with the phases of the impingent waves uniformly distributed over $[-\pi, \pi]$ implying that the channel process is circularly symmetric complex Gaussian with independent imaginary and real parts of equal variance. Equivalently, the envelope of the received signal at each antenna is Rayleigh distributed.

In this section we seek to obtain a generalization of SFCC derived in [19] that assumed uniform APD over a limited azimuth around the base-station receiver to any scattering environment characterized by uniform or non-uniform AOA of waves. We do not employ the assumption of very small angular spread to arrive at closed form space-frequency correlation. An immediate implication of the generalization of space-

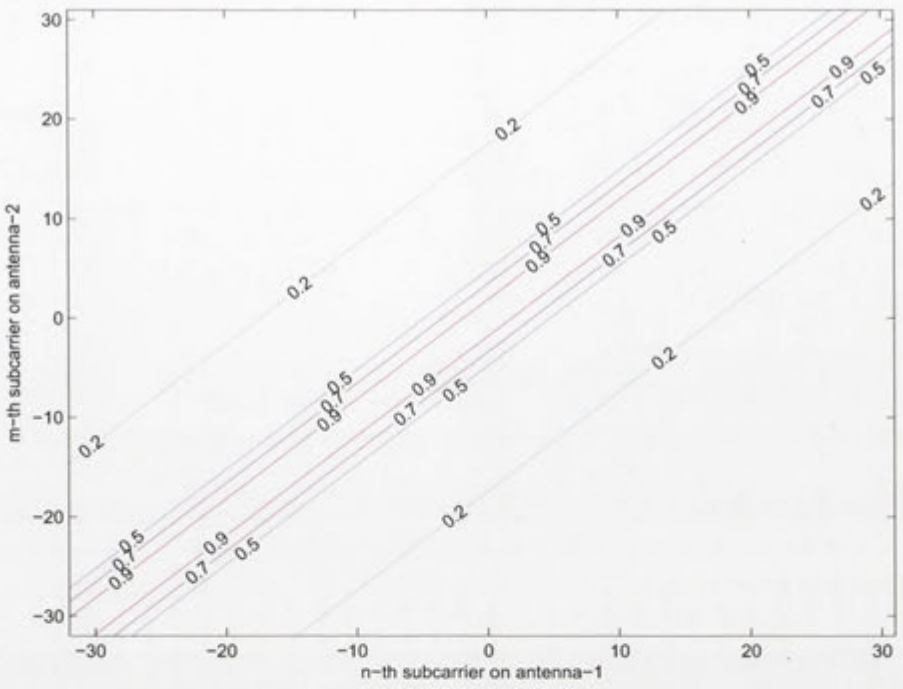

Figure 6.5: Contour plot of the space-frequency correlation function shown in Fig. 6.2 for the uplink inverted-parabolic model.

frequency correlation function is that it is applicable to base-station as well as mobile reception characterized respectively by small and small to large angular spreads. The relaxation of the assumption of uniform AOA makes it possible to explore the impact of different APD on the space-frequency trade-off.

In [19], the assumption of independence of AOA and TOA of waves resulted in the following SFCC between the channel processes at two antennas

$$\Phi_{1,2}(\Delta f, d) = \Phi_{1,2}(\Delta f)\Phi_{1,2}(d), \tag{6.30}$$

where $\Phi_{1,2}(\Delta f)$ is the frequency cross correlation obtained by assuming that the distribution of multipath delays with respect to propagation delay of the LOS component (T_{los}) is exponential with delay spread Γ and is given by

$$\Phi_{1,2}(\Delta f) = \exp\left(-i2\pi\Delta f T_{los}\right)\frac{1}{1+i2\pi\Delta f\Gamma}. \tag{6.31}$$

The spatial cross correlation correlation $\Phi_{1,2}(d)$ assuming equal probability of AOA of waves from a limited azimuth with mean AOA β_0 and deviation of Δ_r across β_0 was given as

$$\Phi_{1,2}(d) = \frac{1}{2\Delta_r}\int_{\beta_0-\Delta_r}^{\beta_0+\Delta_r}\exp\left(i\eta\cos\beta\right)d\beta. \tag{6.32}$$

Since the frequency and spatial selectivity of the channel are independent as a result of independence between AOA and TOA of waves, a change in scattering distribution around the receiver changes the spatial selectivity of the channel only. Therefore, the generalization of space-frequency correlation derived in [19] requires us to consider the spatial correlation function only. For that purpose we recall the technique developed in Section 2.2 of Chapter 2 and represent the channel gain at antenna-1 tuned to the frequency ω_1 at time t as follows

$$h_1(t) = \exp(-i\omega_1 t) \int_{\Omega_R} \Psi(\beta) \exp(-i\omega_1 \zeta_1), \tag{6.33}$$

where the scattering has been assumed to be 2D and

$$\zeta_1 = \frac{\boldsymbol{x}_1 \cdot \widehat{\boldsymbol{\beta}}}{c} \tag{6.34}$$

which takes into account the displacement of antenna-1 from the origin 'O'. Using (6.33) and the assumption of US in the angle domain, the normalized cross correlation at time t between two antennas is given by

$$\begin{aligned}
\Phi^{g}_{1,2} &= \mathbb{E}\{h_2(t) h_1^*(t)\}, \\
&= \int_{\Omega_R} \Psi(\beta) \exp(-i(\omega_2 \boldsymbol{x}_2 - \omega_1 \boldsymbol{x}_1))\, d\beta, \\
&= \int_{\Omega_R} \Psi(\beta) \exp\left(i \frac{2\pi}{\lambda_c} d\cos\beta\right) d\beta,
\end{aligned} \tag{6.35}$$

where we have arrived at the last equality using the geometry of the antenna array and the fact that $\omega_1 = \omega_c + \Delta\omega/2$ and $\omega_2 = \omega_c - \Delta\omega/2$. Equation (6.35) can be obtained from (6.21) by taking $\omega_n = \omega_1 = \omega_c + \Delta\omega/2$ and $\omega_m = \omega_2 = \omega_c - \Delta\omega/2$ which implies two subcarriers with frequencies symmetric about the carrier frequency. The superscript 'g' has been added to indicate that $\Phi^{g,Kal}_{1,2}(d)$ is applicable in general scattering environments whereas 'Kal' stands for Kalkan (the author of [19]). Compare the spatial correlation derived in [19] (equation (6.32)) and the generalized correlation in (6.35). Now $\Psi(\beta)$ and $\exp\left(i\frac{2\pi}{\lambda_c} d\cos\beta\right)$ are periodic functions of β. The Fourier series expansion of APD $\Psi(\beta)$ is defined as the follwoing pair of equations (equations (2.13a) and (2.13b))

$$\begin{aligned}
\gamma_\nu &= \oint \Psi(\beta) \exp(-i\nu\beta)\, d\beta, \\
\Psi(\beta) &= \frac{1}{2\pi} \sum_{m=-\infty}^{\infty} \gamma_\nu \exp(i\nu\beta),
\end{aligned} \tag{6.36}$$

where γ_ν are the scattering coefficients and $J_\nu(\cdot)$ is the Bessel function of integer order m. The plane wave $\exp\left(i\frac{2\pi}{\lambda_c}d\cos\beta\right)$ is expanded using Jacobi-Anger expansion as follows (equation (2.14))

$$\exp\left(i\frac{2\pi}{\lambda_c}d\cos\beta\right) = \sum_{\nu=-\infty}^{\infty} \underbrace{i^\nu J_\nu(2\pi K)}_{\xi'_\nu} exp\left(i\nu\beta\right), \tag{6.37}$$

where K is the antenna separation normalized by the carrier wavelength and ξ'_ν are the Fourier series coefficients of the Jacobi-Anger series expansion of the plane wave. As we discussed in Chapter 2, the multiplication of $\Psi(\beta)$ and $\exp\left(i\frac{2\pi}{\lambda_c}d\cos\beta\right)$ in (6.35) results in the convolution of their respective Fourier series coefficients (see footnote 5 Chapter 2) so that (6.35) can be written as (equation (2.15))

$$\begin{aligned}\Phi^g_{1,2}(K) &= \sum_{\nu=-\infty}^{\infty} \gamma_\nu \xi'_{-\nu}, \\ &= \sum_{\nu=-\infty}^{\infty} i^{-\nu}\gamma_\nu J_\nu(2\pi K),\end{aligned} \tag{6.38}$$

where we used the relation $J_{-\nu}() = (-1)^\nu J_\nu()$. The values of γ_ν have been tabulated in Table-2.1 for some common APDs. Using (6.38) and (6.31) in (6.30), the space-frequency correlation which is a generalization of [19] is given as

$$\Phi^g_{1,2}(\Delta f, K) = \exp\left(-i2\pi\Delta f T_{los}\right)\frac{2\pi}{1+i2\pi\Delta f\Gamma}\sum_{\nu=-\infty}^{\infty} i^{-\nu}\gamma_\nu J_\nu(2\pi K). \tag{6.39}$$

The generalized *envelope* cross correlation $\Phi^g_{1,2,|h|}(\Delta f, K)$ is then obtained by taking square of the absolute space-frequency correlation as follows

$$\begin{aligned}\Phi^g_{1,2,|h|}(\Delta f, K) &= \left|\frac{2\pi}{1+i2\pi\Delta f\Gamma}\right|^2 \left|\sum_{\nu=-\infty}^{\infty} i^{-\nu}\gamma_\nu J_\nu(2\pi K)\right|^2, \\ &= \frac{4\pi^2}{1+4\pi^2(\Delta f)^2\Gamma^2}\left|\sum_{\nu=-\infty}^{\infty} i^{-\nu}\gamma_\nu J_\nu(2\pi K)\right|^2.\end{aligned} \tag{6.40}$$

Given the envelope correlation, equation (6.40) suggests that a *trade-off* between frequency and spatial correlations exists which can be exploited to decrease the antenna spacing at the cost of increased frequency separation between the two antennas and vice versa.

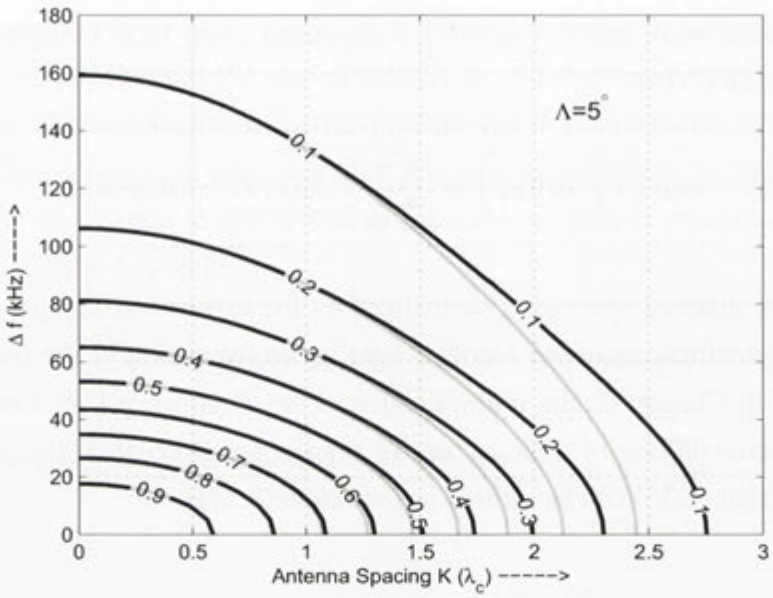

Figure 6.6: The contour plot of the space-frequency envelope correlations for truncated-uniform and von-Mises (black lines) azimuth power distributions for broadside antenna orientation. The angular spread is assumed to be 5°.

Numerical Evaluation of SFCC for 2-Carrier OFDM System

The coefficients γ_ν for the truncated-uniform (TU) and von-Mises (VM) power distribution given in Table-2.1 respectively are

$$\gamma_\nu^{TU} = \exp(-i\nu\beta_0)\,\mathrm{sinc}(\nu\Delta_r),$$
$$\gamma_\nu^{VM} = \exp(-i\nu\beta_0)\,\frac{I_{-\nu}(\kappa_r)}{I_0(\kappa_r)},$$

where $\mathrm{sinc}(\cdot)$ has been defined in (1.11) and $I_\nu(\cdot)$ is the modified Bessel function of the first kind and integer order ν, and κ_r is the non-isotropicity parameter [15].

The results of numerical evaluation of the SFCC (equation (6.40)) have been plotted in Figs. 6.6-6.10. The contour plot of SFCC in broadside antenna orientation for truncated-uniform and/or von-Mises scattering environments is depicted in Fig. 6.6. It can be observed that the two scattering environments are equivalent from the point of view SFCC between two antennas when the antenna spacing is small. At sufficiently large antenna spacing, however, the two scattering distributions have different trade-off characteristics. Observe that if the envelope correlation is 0.1 which is to be kept constant as we reduce the the antenna separation 2.38 to 1.5 wavelengths, the frequency separation has to be increased by 425% and 138% respectively for truncated-isotropic

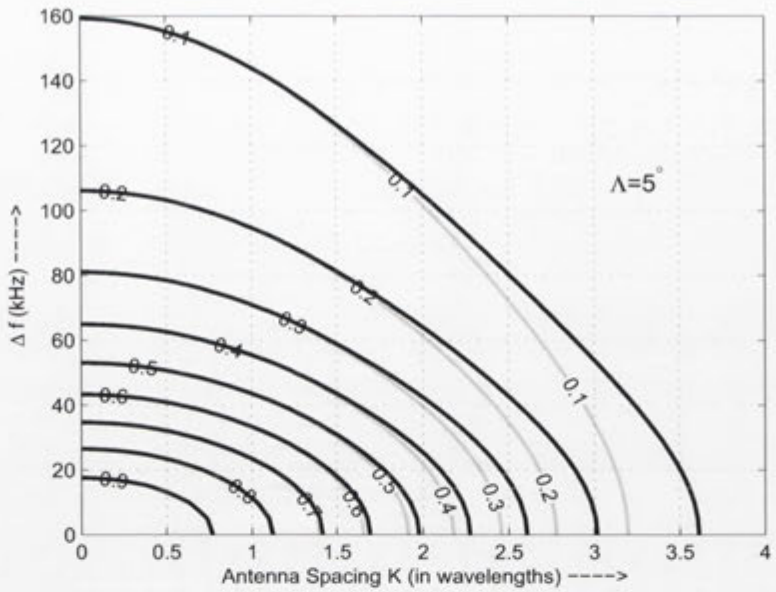

Figure 6.7: The contour plot of the space-frequency envelope correlations for truncated-uniform and von-Mises azimuth power distributions for $\beta_0 = 45°$ assuming angular spread as $5°$.

and von-Mises scattering power distributions. The figure suggests that the truncateduniform scattering results in noticeably faster (cross) decorrelation of the channels at the two antennas when the spacing between antennas is sufficiently large. An example of SFCC for a non-broadside antenna orientation is shown in Fig. 6.7 where the mean scattering angle is $50°$ The stretch of the correlation contours to the right on the antenna spacing axis for sufficiently small frequency separation suggests that the antenna spacing has to be larger than in broadside orientation to achieve the same level of decorrelation between the channels at the two antennas. In fact, a larger deviation from the broadside antenna orientation would result in worse antenna spacing requirement for achieving similar channel decorrelation for sufficiently large antenna separation.

A communications system may have to operate in different scattering environments where the angular spread varies over a range. One, therefore, might be interested in the impact on space-frequency trade-off characteristics of changing the angular spread of the scattering environment. Fig. 6.8 shows the behavior of a particular space-frequency correlation contour as a function of angular spread assuming $\beta_0 = 45°$. for von-Mises scattering environment. The almost flat contour corresponding to angular spread of $0.1°$ suggests that the cross correlation is only insignificantly affected by a change in antenna spacing (at least for the range of antenna spacing shown). In other words, a very large antenna separation results in only a very insignificant reduction in frequency separation

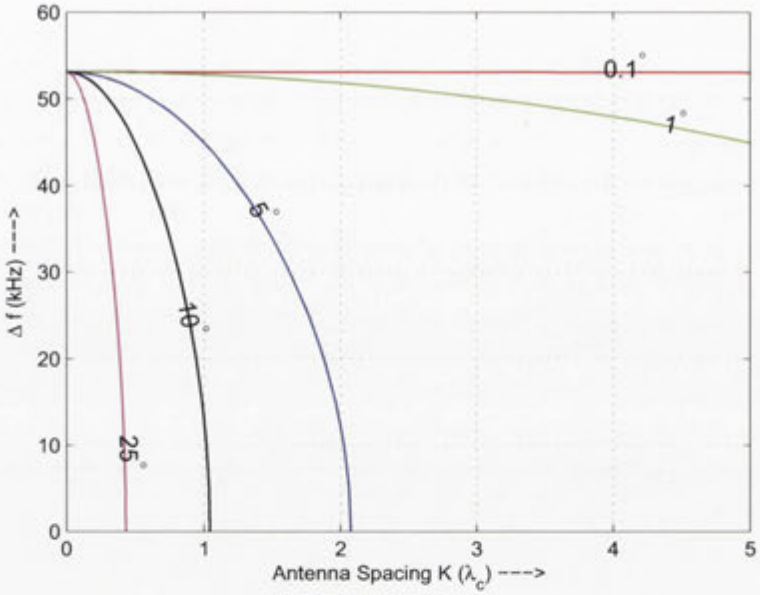

Figure 6.8: The impact of angular spread of the scattering on the space-frequency correlation function for truncated-uniform distribution. The correlation contour value is assumed to be fixed at 0.5 and the mean scattering angle is $45°$.

required to maintain the envelope cross correlation. When the angular spread increases to $1°$, the possibility of a viable space-frequency diversity trade-off is visible. Only a small change in required frequency separation is achieved by a large increase in the antenna separation. When the angular spread of the scattering is $5°$, a small change in antenna separation results in a large frequency separation requirement for maintaining a particular correlation value. Notice a significant change in space-frequency trade-off characteristics as the angular spread changes from $1°$ to $5°$. An angular spread of $25°$ allows a change in antenna separation only very slightly at the cost of a significant change in frequency separation. For example, the reduction of antenna separation by just $\lambda_c/3$ requires the frequency separation enhancement by $\approx 191\%$. It can be inferred from the figure that for larger angular spreads, an equivalent reduction in the amount of the antenna separation would require higher frequency separations. In Fig. 6.9, the space-frequency trade-off characteristics for von-Mises scattering have been plotted where the angular spread of the scattering environment is fixed at $5°$. but the location of scattering (β_0) changes with respect to the axis of the antenna array. The figure suggests a significant change in SFCC characteristics as the mean scattering angle changes from $5°$ to $20°$. For example, a reduction in antenna separation by $10\lambda_c$ would require frequency separation to be increased by $\approx$ 7kHz for $\beta_0 = 5°$. When $\beta_0 = 20°$, a reduction in separation of two antennas by just a λ_c requires frequency separation to be increased by

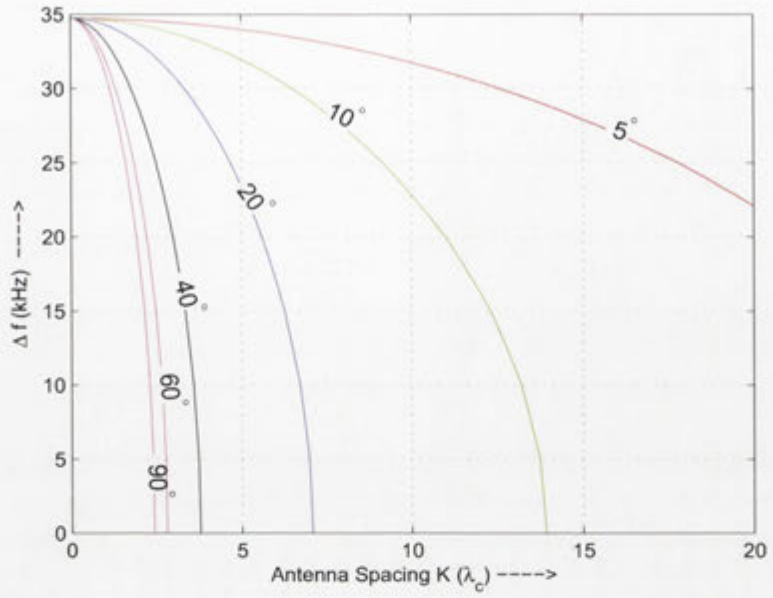

Figure 6.9: The effect of changing mean scattering angle on space-frequency envelope correlation of von-Mises distribution. The correlation contour value is assumed fixed at 0.7 and the angular spread is assumed to be 5° that corresponds to $\kappa_r = 130$ for von-Mises distribution.

$\approx$ 12kHz. It is also noted that the change of β_0 beyond 40° does not have significant impact on space-frequency trade-off characteristics.

Finally, a comparison of SFCC characteristics of truncated-uniform, Gaussian, Laplacian and von-Mises distributions is given for $\Lambda = \{2.25^\circ, 5^\circ, 45^\circ\}$ in Fig. 6.10. The mean scattering angle is assumed to be 20° and the correlation contour value is fixed at 0.2. Notice that, for sufficiently large antenna separation, the truncated-uniform and von-Mises distributions have almost identical space-frequency trade-off characteristics. The truncated-Gaussian distribution of scattered power around the receiver results in comparatively worse antenna spacing and antenna frequency separation requirements to maintain correlation value of 0.2. And the Laplacian distribution has worst spacefrequency trade-off characteristics. However, for sufficiently small antenna separations, SFCC characteristics for different scattering environments are almost identical. This implies that the more accurate evaluation of space-frequency diversity trade-off at a cellular base-station (where the antenna separation can be several wavelengths) requires more precise knowledge of the type of APD. And if one has to evaluate the spacefrequency diversity trade-off on the mobile receiver (where the antenna spacing has to be much smaller) and the angular spread is known, one can assume any of the scattering power distributions without significant errors in the design and analysis. The compari-

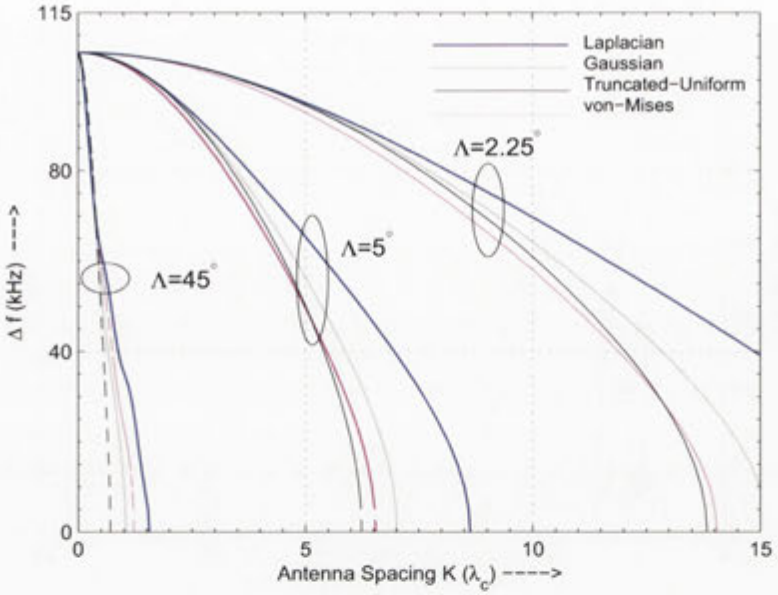

Figure 6.10: A comparison of space-frequency trade-off characteristics for truncated-uniform, Gaussian, Laplacian and von-Mises distributions for $\Lambda = \{2.25°, 5°, 45°\}$ assuming $\beta_0 = 20°$. The correlation contour value is assumed to be fixed at 0.2. Observe that von-Mises and truncated-uniform distributions have almost identical SFCC and Laplacian distribution requires more antenna separation for a given frequency separation (and vice versa) to maintain a given cross correlation.

son of the effect of different scattering environments on the autocorrelation of the time-selective channel fading process (Chapter 2, Section 2.2.3) and cross correlation in a space-frequency selective channel under consideration suggests that different scattering distributions do not have identical impact in both cases. Therefore, the results of comparison between different APDs derived in Chapter 2 for time-selective channel do not apply in the present space-frequency setting. For example, different scattering distributions in Chapter 2 resulted in almost identical autocorrelation of the channel fading process when the angular spread was very small. The impact of small angular spread on the cross correlation, however, depends on the antenna separation for a fixed β_0. If the antenna separation is sufficiently small, the choice of a particular APD does not really matter. But if the antenna separation is sufficiently large, different scattering distributions might result in significantly different space-frequency trade-off characteristics as suggested by Fig. 6.10.

6.7 Summary and Contributions

In this chapter, we proposed a framework which can be used to calculate the space-frequency correlation in multicarrier communication systems. The proposed framework incorporates: i) physical antenna positions relative to the receiver origin to capture the space dimensionality of the channel and ii) a general joint angle-delay power distribution $\Psi(\beta, \tau)$ to capture the random frequency-selective multipath field. We believe that this framework can be utilized to investigate the effects of antenna spacing, antenna configuration (*e.g.*, linear array, circular array, grid array, etc.), scattering environment parameters such as mean angle of arrival and angular spread at the receiver, and the delay spread of the channel on the design and the performance of multicarrier communication systems.

The framework proposed in this chapter can be extended to include the transmit aperture by following [244] and hence obtain a full frequency-selective MIMO model. In this model, the statistical properties of the underlying channel are governed by the joint angular power delay profile $\Psi(\widehat{\boldsymbol{\theta}}, \widehat{\boldsymbol{\beta}}, \tau)$ where $\widehat{\boldsymbol{\theta}}$ is the angle-of-departure at the transmitter aperture, $\widehat{\boldsymbol{\beta}}$ is the angle-of-arrival at the receiver aperture and τ is the multipath delay. Also, following [246], the proposed framework can be extended to time-selective fading channels. These possible extensions are a subject of future research.

The contributions of this chapter can be summarized as follows:

- A generalized SFCC model for a SIMO-OFDM system is derived which can be used with any joint angle-delay power distribution, arbitrary antenna geometry and angular spread, and can be extended to MIMO-OFDM system. Therefore, the performance of emerging high data rate wireless communications systems (mostly based on MIMO-OFDM) can be analyzed.

- The results in this contribution neither assume very small angular spread [19] which is typical for base-stations in cellular systems. The applicability of the generalized SFCC to arbitrary angular spread makes it possible to analyze downlink channels at the receiver side surrounded by scattering with moderate to high angular spread.

- A special case of the generalized space-frequency correlation model with some additional assumptions on the antenna geometry and the frequency separation between signals at two antennas is provided which happens to be a generalization of space-frequency correlation in [19] to general scattering environments. A brief comparison of different scattering APDs is also given with results not previously known.

Chapter 7

Conclusions and Future Research Directions

This chapter provides a summary of the research work presented in this thesis and highlights possible directions for future research. The contributions of each chapter have been described at the end of each chapter and are not repeated here.

7.1 Conclusions

The most of the work in this thesis has been based on the assumptions that channel state information (CSI) is unknown to the transmitter and the receiver but the channel statistics are perfectly known to the receiver only, and the channel is statistically homogeneous WSSUS . We proposed a generalization of Clarke's well known stationary Rayleigh fading channel model that assumes isotropic scattering environment to general scattering environments by assuming a perfect knowledge of the mobile dynamics. We showed through numerical evaluations that the perfect knowledge of the scattering and the mobile dynamics can lead to substantial improvement in the performance of the communications system. The truncated-uniform, truncated-Gaussian, truncated-Laplacian and von Mises distributions can be considered equivalent if the angular spread around the mobile receiver is either sufficiently small or large. Specifically, the truncated-Gaussian and von Mises distributions are almost identical for all angular spreads and mobile dynamics.

By relaxing the assumption of constant mobile velocity in the Clarke's model and allowing the mobile to have a constant acceleration, we developed a non-stationary Rayleigh fading model applicable in general scattering environments. The Wigner-Ville and instantaneous power spectra were derived for the non-stationary channel process. Specifically, the Wigner-Ville distribution was shown to be a natural generalization of

the Clarke's model from stationary to non-stationary scenario. We explored the impact of mobile acceleration on the performance of non-coherent systems in terms of frame overhead and payload as a function of initial mobile velocity and carrier frequency. The mobile acceleration seemed to have more impact if the initial mobile velocity or the carrier frequency is lower. The numerical results suggested that it is not feasible to use higher carrier frequencies for wireless communications if the mobile has constant acceleration.

We proposed a slight modification of the peaky signaling to significantly improve the the performance of pilot-aided channel estimation scheme (PACE) over Rayleigh fading channels. The modification of the peaky signaling in conjunction with some added signal processing at the receiver resulted in $\mathcal{M}$ times SNR enhancement at pilot symbol instants as compared to non-peaky signalling where $\mathcal{M}$ equals the number of unused degrees of freedom in the peaky signaling. Under the assumption of equal total power in both the peaky and non-peaky signaling, we analyzed the performance of the proposed PACE schemes against the non-peaky signaling. The results suggested significant gains in the overall performance of the communications system based on the proposed scheme particularly in the low SNR regime. In fact, the proposed schemes offered $\mathcal{M}$ times gain in overall performance in the limit of zero SNR.

Finally, a framework for the calculation of space-frequency cross correlation (SFCC) for OFDM-based SIMO system in general scattering environments was derived. The strength of the proposed framework was exhibited by calculating SFCC for elliptical and inverted-parabolic scattering models proposed in literature. It turned out that the inverted-parabolic scattering model is more 'optimistic' (*i.e.*, has higher correlation) as far as the cross correlation between OFDM subcarriers on two antenna in SIMO system is concerned. We also generalize the results available in literature regarding SFCC from truncated-uniform to general scattering environments. The results suggest that different non-isotropic scattering distributions are, to very good approximation, equivalent when the separation between the two antennas is sufficiently small. When the antenna separation is sufficiently large, different scattering environments exhibit unidentical space-frequency trade-off characteristics depending on the angular spread and mean scattering angle with respect to the antenna array orientation.

To sum up, this thesis has shown that with perfect knowledge of the scattering environment and mobile dynamics, we can significantly improve the overall performance of the communications systems in no-CSI circumstances. Equivalently, the perfect knowledge of the channel statistics can result in a significant performance enhancement of non-coherent (or partially coherent) communications systems (Chapter 3).

7.2 Future Research Directions

In this section we outline a number of future research directions to arise from the work presented in this thesis.

Space-time-frequency Model: In this thesis, we have studied time-selective SISO and space-frequency selective (OFDM-based) SIMO models under the assumptions of statistically homogeneous WSS uncorrelated scattering (WSSUS). Therefore, we plan to extend our work to space-time-frequency selective channels on the basis of relaxed assumptions, *e.g.*, we may allow correlated scattering which would imply non-WSSUS channels.

OFDM-based space-time-frequency selective MIMO Model: The specification of MIMO-OFDM as the technology of choice for most of the future wireless communications standards necessitates the development of an OFDM-based MIMO model that includes space-time-frequency selectivity. The extension of the work presented in this thesis regarding space-frequency selective SIMO system to space-time-frequency selective MIMO-OFDM systems based on *modal* approach seems to be of some interest. The relaxation of classical assumption of WSSUS would also make such model more practically relevant.

Achievable information rates over non-coherent MIMO-OFDM channels: In Chapter 3 we have explored achievable rates over SISO time-selective channels. It is of information theoretic interest to explore the achievable information rates for other communications systems (like MISO, SIMO and MIMO) and environments like space-frequency and space-time-frequency channels. The extension of the approach followed in Chapter 3 to such systems and environments would be very useful.

The degree of non-isotropicity and channel fading rate: In Chapters 2 and 3 we witnessed a 'slowing' down of the channel process in non-isotropic scattering environments suggesting that the degree of non-isotropicity and the channel time variation are related. While in this thesis we present this relationship in the form of numerical simulations, it may be useful to have some sort of analytical relationship between the degree of non-isotropicity and the effective channel fading rate.

Non-uniform pdf of mobile direction of travel: The simplistic assumption of i.i.d. uniform distribution of the mobile direction of travel over $[-\pi, \pi]$ in non-isotropic scattering scenarios results in *average* channel statistics identical to the isotropic scattering

environment. The relaxation of this assumption to incorporate non-uniform pdf of mobile direction of travel in non-isotropic scattering scenarios and evaluation of its impact on the average channel statistics is a possible direction for future research.

More practical pilot-aided channel estimation: The pilot-aided channel estimation based on peaky signaling proposed in Chapter 5 theoretically promises significant improvement in MMSE and, in turn, system performance. The main assumption has been the availability of infinite number of pilot symbols. Practically, only a finite number of pilot symbols can b made available to the receiver. The design and analysis of such channel estimation scheme when only a finite number of pilot symbols are available is needed to be done so as to make the channel estimation more practically relevant.

Pilot-aided channel estimation in MIMO systems: The pilot-aided channel estimation scheme based on peaky signaling proposed in Chapter 5 is related to SISO systems. The extension of the proposed scheme to MIMO systems is expected to offer offer significant advantage over existing non-peaky signaling based channel estimation schemes. This problem seems to be a possible direction of future research.

Velocity estimators and equalizers based on second order channel statistics: There are some results in literature related to mobile velocity estimation and channel equalization based on second order channel statistics. These results, however, are not applicable to general scattering environments. The problem of mobile velocity estimation and channel equalization in general scattering environments, in SISO and MIMO systems, seems to be a good problem for future research.

Appendix A

A.1 Proof of Equation (2.18)

The following identity exists for *continuous time Fourier transform* (CTFT) of the Bessel function of the first kind and integer order μ [28, 194]

$$\int_{-\infty}^{\infty} J_{\mu}(\omega_d \Delta t)\ \exp\left(-i\omega\Delta t\right) d\Delta t = \frac{F_{\mu}\left(\frac{\omega}{\omega_d}\right)}{i^{\mu}\omega_d}, \tag{A.1}$$

where

$$F_{\mu}(x) \triangleq 2\frac{\cos\left(\mu\cos^{-1}(x)\right)}{\sqrt{1-x^2}}. \tag{A.2}$$

We know from the basic Fourier theory that the DTFT of a sampled process is essentially a magnitude and frequency scaled version of CTFT of the continuous-time process with 2π periodicity [114]. Making use of (A.1) and (A.2), the DTFT of the sampled Bessel function of the first kind and integer order μ is given by

$$\begin{aligned}\sum_{p=-\infty}^{\infty} J_{\mu}(\omega_d p T_s)\ \exp\left(-i\omega p T_s\right) &= \frac{1}{T_s}\sum_{\ell=-\infty}^{\infty}\frac{F_{\mu}\left(\frac{1}{\omega_d T_s}(\omega-2\pi\ell)\right)}{i^{\mu}\omega_d},\\ &= \sum_{\ell=-\infty}^{\infty}\frac{F_{\mu}\left(\frac{1}{\omega_D}(\omega-2\pi\ell)\right)}{i^{\mu}\omega_D},\end{aligned} \tag{A.3}$$

where $\omega_D = \omega_d T_s$ is the Doppler spread normalized by the symbol rate.

Since we are working at the baseband level, only the low pass term ($\ell = 0$) in (A.3)

is of interest to us, *i.e.*,

$$\sum_{p=-\infty}^{\infty} J_\mu(\omega_d p T_s)\, \exp\left(-i\omega p T_s\right) = \frac{F_\mu\left(\frac{\omega}{\omega_D}\right)}{i^\mu \omega_D}. \tag{A.4}$$

Using (A.2) and (A.4), we can rewrite (2.17) to get the following desired expression for PSD

$$\Phi(\omega) = \frac{1}{\omega_D} \sum_{m=-\infty}^{\infty} \gamma_m\, \exp\left(im\phi_v\right)\, F_m\left(\frac{\omega}{\omega_D}\right). \tag{A.5}$$

Appendix B

B.1 Extrema of Information Rate Cost function

Equation (3.8b) is a function of the spectrum of the channel fading process through eigenvalues $\{\lambda_i\}$. Since the channel covariance matrix $\mathbf{C}$ has been assumed to be positive semidefinite, all eigenvalues are non-negative *i.e.*,

$$\lambda_i \geq 0, \qquad \text{for } i = 1, 2, 3 \cdots N. \tag{B.1}$$

Also we know from the elementary linear algebra [247] that the sum of eigenvalues of a matrix must be equal to its trace. Since $\mathbf{C}$ is a covariance matrix, trace of $N \times N$ matrix $\mathbf{C}$ is equal to N, *i.e.*,

$$\sum_{j=1}^{N} \lambda_j = N, \qquad \text{for } j = 1, 2, 3 \cdots N. \tag{B.2}$$

The maximum or minimum of no-CSI cost function P_δ^{norm} must obey constraints (B.1) and (B.2) to be a valid stationary point. We use N slack variables $s_i \in \mathbb{R}$ ($i = 1, 2, 3 \cdots N$) to convert inequality constraints $\lambda_i \geq 0$ to equality constraints so that we can use Lagrange multiplier technique to find stationary points of P_δ^{norm}. The Lagrangian, $\mathcal{L}(\cdot)$, and the constraint set are

$$\begin{aligned} \mathcal{L}(\boldsymbol{\lambda}, \mu, \boldsymbol{\vartheta}, \mathbf{s}) &= P_\delta^{norm} + \mu \left(\sum_{j=1}^{N} \lambda_j - N \right) + \sum_{r=1}^{N} \vartheta_r (\lambda_r + s_r^2), \\ \lambda_i - s_i^2 &= 0, \\ \sum_{j=1}^{N} \lambda_j &= N, \\ \vartheta_r &\geq 0, \end{aligned} \tag{B.3}$$

where μ and $\{\vartheta_r\}$ respectively are the Lagrange multipliers for equality constraint (equation (B.2)) and rth inequality constraint (equation (B.1)). Notice a negative sign in (B.3) which is due to '$\geq$' type inequality. This sign would be positive if we have '$\leq$' type inequality. If an inequality constraint is inactive at the optimum, its associated Lagrange multiplier is zero. Furthermore, if the constraint is active, the associated multiplier must be nonnegative [247].

The necessary conditions of the Lagrange Theorem give (with λ_i, μ, ϑ_i and s_i as unknowns) the following set of equations

$$\frac{\partial \mathcal{L}}{\partial \lambda_i} = \frac{1}{N} \sum_{i=1}^{N} \frac{\partial}{\partial \lambda_i} \log(1 + \rho\lambda_i) + \mu + \vartheta_i = 0, \tag{B.4}$$

$$\frac{\partial \mathcal{L}}{\partial \mu} = \sum_{i=1}^{N} \lambda_i - N = 0, \tag{B.5}$$

$$\frac{\partial \mathcal{L}}{\partial \vartheta_i} = \lambda_i + s_i^2 = 0, \tag{B.6}$$

$$\frac{\partial \mathcal{L}}{\partial s_i} = 2 s_i \vartheta_i = 0. \tag{B.7}$$

One solution can be obtained by setting $\{\vartheta_i\}$ to zero to satisfy (B.7) and solving (B.4), (B.5) and (B.6) simultaneously. The solution is

$$\lambda_1 = \lambda_2 \cdot \cdot = \lambda_N = 1, \tag{B.8}$$

which implies that $\mathbf{C} = \mathbf{I}$, *i.e.*, the channel fading process is uncorrelated. This solution is the stationary point of the objective function, P_δ^{norm}, and is candidate for being an extrema. It can be verified that this solution represents a maximum of P_δ^{norm} which is in fact a *global maximum* (with respect to the constraints) because in our case the objective function is a concave function and the set of linear equality and inequality constraints is a convex set [248].

As we have seen that no-CSI cost function is a maximum for an uncorrelated fading process, one can reasonably suspect a perfectly correlated process to define a minimum of P_δ^{norm}. If channel process is perfectly correlated, all entries of $\mathbf{C}$ are equal to 1 (for all N) and , therefore, rank($\mathbf{C}$)$\rightarrow$1 which implies that $\mathbf{C}$ has only one non-zero eigenvalue equal to its trace and all other eigenvalues equal to 0, *i.e.*,

$$\lambda_i = \begin{cases} N, & \text{if } i = j \text{ where } j = 1 \text{ or } 2 \cdots \text{or } N \\ 0, & \text{otherwise,} \end{cases} \tag{B.9}$$

which has N possibilities, each of which corresponds to a particular solution.

Notice that the solutions (B.9) do satisfy the set of constraints formulated above. Therefore, this solution is a valid stationary point of the objective function (no-CSI cost function). We can verify that these points correspond to *global minimum* because any move away from these points either violates the constraints or increases no-CSI cost function. Since our objective function is concave and the constraints define a convex region, any minimum has to be a global minimum. However, as we have observed, this global minimum occurs at more than one (in our case N) points [248]. Thus we have shown that the information rate cost function is maximum for an uncorrelated Rayleigh fading process and is minimum for a perfectly correlated process.

B.2 Information Rate Penalty for a Single Point Scatterer Case

If the angular spread of the scattering distribution approaches zero, *i.e.*, $\Lambda \rightarrow 0^\circ$, the scattering approaches a single point scatterer which scatters the electromagnetic wave equal in all directions. At any point on the trajectory of the mobile receiver, there is only one wave with no other interfering wave. Since there is no interference, there will be no fading. In other words, all entries of $\mathbf{C}$ would be equal to one implying a perfectly correlated process irrespective of the transmission block length N. In such scenario, the rank($\mathbf{C}$)$\rightarrow$1 which implies that $\mathbf{C}$ has only one non-zero eigenvalue equal to its trace with all other eigenvalues identically equal to zero. Applying these arguments to (3.8b), penalty in case of a single point scatterer, $P^{\mathrm{n}}_{\delta,0^\circ}$, for transmission block length N is given as

$$P^{norm}_{\delta,0^\circ} = \frac{1}{N}\log\left(1+\ \rho N\right). \tag{B.10}$$

Notice that $P^{norm}_{\delta,0^\circ}$ is nonzero for finite block length N despite the fact that the channel fading process is perfectly correlated. Also observe that unlike isotropic case [37], equation (B.10) no more represents a Toeplitz system and, therefore, Szegö's limit theorem can not be applied to evaluate penalty for $N \rightarrow \infty$. In fact, Szegö's limit theorem is not needed and asymptotic penalty as $N\rightarrow\infty$ is obtained using elementary calculus. Insertion of the limit $N\rightarrow\infty$ in (B.10) results in $\frac{\infty}{\infty}$ indeterminate form. We therefore apply L'Hospital rule to get

$$\begin{aligned}
\lim_{N\rightarrow\infty} P^{norm}_{\delta 0^\circ} &= \lim_{N\rightarrow\infty}\left(\frac{\rho}{\log\left(1+\ \rho N\right)}\right), \\
&= \frac{\rho}{\lim_{N\rightarrow\infty}\log\left(1+\ \rho N\right)}, \\
&= 0, \qquad\qquad \text{for } \rho<\infty.
\end{aligned} \tag{B.11}$$

Notice that the assumption of finite SNR is necessary as the limit does not exist otherwise.

Appendix C

C.1 Discrete-Time Fourier Transform of Bessel Function With Quadratic Argument

We first derive the Fourier transform of the Bessel function with quadratic argument and continuous lag τ, and then we shall obtain equivalent transform in discrete-time domain. We consider the following standard representation for the Bessel function of the first kind and integer order p [249]

$$J_p(x) = \frac{1}{2\pi} \int_{-\pi}^{\pi} \exp\left(n\phi - x\ \sin\phi\right)\ d\phi,$$

so that we have the following relationship for Bessel function with quadratic argument $J_p(a\,\tau^2)$ with $a > 0$ and continuous lag τ

$$J_p(a\,\tau^2) = \frac{1}{2\pi} \int_{-\pi}^{\pi} \exp\left(n\phi - a\,\tau^2\ \sin\phi\right)\ d\phi. \tag{C.1}$$

The Fourier transform of $J_p(a\,t^2)$ is given as

$$\mathcal{F}\left\{J_p(a\,\tau^2)\right\} = \int_{-\infty}^{\infty} \left(\frac{1}{2\pi} \int_{-\pi}^{\pi} \exp\left(i\left(n\phi - a\tau^2\ \sin\phi\right)\right)\ d\phi\right) \exp\left(-i\omega\tau\right)\ d\tau, \tag{C.2}$$

$$= \frac{1}{2\pi} \int_{-\pi}^{\pi} \exp\left(i\,n\phi\right) \left\{\int_{-\infty}^{\infty} \exp\left(i\,a\tau^2\ \sin\phi\right) \exp\left(-i\omega\tau\right)\ dt\right\} d\phi, \tag{C.3}$$

$$= \frac{1}{2\pi} \left(\int_{-\pi/2}^{\pi/2} \exp\left(i\,n\phi\right) \left\{\int_{-\infty}^{\infty} \exp\left(i\,a\tau^2\ \sin\phi\right) \exp\left(-i\omega\tau\right)\ d\tau\right\} d\phi \right.$$
$$\left. + \int_{\pi/2}^{3\pi/2} \exp\left(i\,n\phi\right) \left\{\int_{-\infty}^{\infty} \exp\left(i\,a\tau^2\ \sin\phi\right) \exp\left(-i\omega\tau\right)\ d\tau\right\} d\phi\right) \tag{C.4}$$

We make the following substitution

$$a \sin\phi = \mu \tag{C.5}$$

which implies that $-a \leq \mu \leq a$ and

$$\phi = \arcsin\left(\frac{\mu}{a}\right),$$

so that we get

$$d\phi = \frac{1}{\sqrt{a^2 - \mu^2}}\, d\mu. \tag{C.6}$$

For notational convenience, in the sequel we shall use the following Fourier transform of the linear Chirp signal (or the one-dimensional Fresnel Kernel[1] in optics) [251]

$$\begin{aligned}\mathcal{F}^{\xi}_{chirp}(\omega) &\triangleq \int_{-\infty}^{\infty} \overbrace{\exp\left(i\,\xi\tau^2\right)}^{\text{Linear Chirp Signal}} \exp\left(-i\omega\tau\right)\, d\tau, \\ &= \left(i\frac{\pi}{\xi}\right)^{1/2} \exp\left(-i\,\frac{\omega^2}{4\,\xi}\right),\end{aligned} \tag{C.7}$$

where $\xi > 0$ is some constant.

Using (C.5), (C.6) and (C.7), we can rewrite (C.4) as

$$\begin{aligned}\mathcal{F}\left\{J_p(a\,\tau^2)\right\} &= \frac{1}{2\pi}\left(\int_{-a}^{a} \frac{\exp\left(i\,p\,\arcsin\left(\mu/a\right)\right)}{\sqrt{a^2-\mu^2}}\, \mathcal{F}^{\mu}_{chirp}(\omega)\, d\mu \right. \\ &\qquad \left. - \int_{-a}^{a} \frac{\exp\left(i\,p\,\arcsin\left(\mu/a\right)\right)}{\sqrt{a^2-\mu^2}}\, \mathcal{F}^{\mu}_{chirp}(\omega)\, d\mu\right), \qquad \text{(C.8)} \\ &= \frac{1}{2\pi}\left(\int_{-a}^{a} \frac{\exp\left(i\,p\,\arcsin\left(\mu/a\right)\right)}{\sqrt{a^2-\mu^2}}\, \mathcal{F}^{\mu}_{chirp}(\omega)\, d\mu \right. \\ &\qquad \left. + \int_{-a}^{a} (-1)\frac{\exp\left(i\,p\,\arcsin\left(\mu/a\right)\right)}{\sqrt{a^2-\mu^2}}\, \mathcal{F}^{\mu}_{chirp}(\omega)\, d\mu\right), \qquad \text{(C.9)} \\ &= \frac{1}{2\pi}\left(\int_{-a}^{a} \frac{\exp\left(i\,p\,\arcsin\left(\mu/a\right)\right)}{\sqrt{a^2-\mu^2}}\, \mathcal{F}^{\mu}_{chirp}(\omega)\, d\mu \right. \\ &\qquad \left. + \int_{-a}^{a} \frac{\exp\left(i\,p\,(\pi - \arcsin\left(\mu/a\right))\right)}{\sqrt{a^2-\mu^2}}\, \mathcal{F}^{\mu}_{chirp}(\omega)\, d\mu\right), \qquad \text{(C.10)}\end{aligned}$$

[1] This kernel is essentially found in light diffraction related problems in optics. The fractional Fourier transform which is well-known to the signal processing community is another particular form of the Chirp transform [250].

Notice that the Fourier transform of $J_p(a\,t^2)$ is essentially the sum of two terms each involving the Chirp spectrum modulated by the Bessel function. Let us rewrite (C.10) as follows

$$\mathcal{F}\left\{J_p(a\,\tau^2)\right\} = (1+\exp(i\,p\,\pi)) \int_{-a}^{a} \frac{\exp(i\,p\,\arcsin(\mu/a))}{\sqrt{a^2-\mu^2}}\ \mathcal{F}^{\mu}_{chirp}(\omega)\,d\mu, \quad \text{(C.11)}$$

$$= (1+\exp(i\,p\,\pi))\ \text{BMFC}\,(\omega), \quad \text{(C.12)}$$

where we have defined Bessel-Modulated Fourier Chirp (BMFC) transform as follows

$$\text{BMFC}\,(\omega) \triangleq \frac{1}{2\pi} \int_{-a}^{a} \frac{\exp(i\,p\,\arcsin(\mu/a))}{\sqrt{a^2-\mu^2}}\ \mathcal{F}^{\mu}_{chirp}(\omega)\,d\mu. \quad \text{(C.13)}$$

Let us recall that the normalized acceleration α^N is given as (equation (4.79))

$$\alpha^N = \frac{\alpha}{|\boldsymbol{v}_0|\,(1/T_s)},$$

$$= \frac{\alpha}{|\boldsymbol{v}_0|} T_s, \quad \text{(C.14)}$$

and instantaneous normalized Doppler spread is given as (equation (4.78))

$$\omega_{D,0} = \frac{\omega_{d,0}}{1/T_s},$$

$$= \omega_{d,0} T_s,, \quad \text{(C.15)}$$

where we have just separated the normalization of acceleration and Doppler spread by the symbol rate. Let us define

$$\omega_{d,\alpha} = \frac{0.5\omega_{d,0}\alpha}{|\boldsymbol{v}_0|}, \quad \text{(C.16)}$$

which obviously is acceleration-dependent Doppler spread normalized by the initial speed. Equations (C.14), (C.15) and (C.16) are required to find the DTFT of the the sampled Bessel function $J_p(\omega_{d,\alpha}\,(kT_s)^2)$ given mathematically as

$$\mathcal{F}^{dmips}_{\alpha}(\omega) \triangleq \frac{1}{T_s} \sum_{k} J_p\left(\omega_{d,\alpha}\,(kT_s)^2\right)\,\exp\left(-i\omega k T_s\right), \quad \text{(C.17)}$$

which is an equivalent form of (4.117). When $J_p(\omega_{d,\alpha}\,(kT_s)^2)$ is identified with the continuous Bessel function given in (C.1), we have $a = \omega_{d,\alpha}$ and $\tau = kT_s$. Using this correspondence, we can use the same technique as employed in the Appendix A.1 to

arrive at the following DTFT from its continuous lag counterpart (equation (C.12))

$$\begin{aligned}&\mathrm{DTFT}\left\{J_p(\omega_{d,\alpha}\,(kT_s)^2)\right\}\\&\quad=(1+\exp(i\,p\,\pi))\;\mathrm{BMFC}_{dtft},\end{aligned}\tag{C.18}$$

where $|\omega|<\pi$ and BMFC_{dtft} is effectively a Bessel-Modulated discrete-time Fourier Chirp transform to be defined later. As a first step towards deriving DTFT for the sampled Bessel function with quadratic argument, let us first see what happens to the spectrum of the sampled chirp. We saw in the Appendix A.1 that DTFT is in fact a magnitude and frequency scaled version of the CTFT. Therefore, the discrete-time Fourier Chirp transform $(\mathrm{DTFT}^{\mu}_{chirp}(\omega))$ for $|\omega|<\pi$ is given as

$$\begin{aligned}\mathrm{DTFT}^{\mu}_{chirp}(\omega)&\triangleq\frac{1}{T_s}\sum_{k=-\infty}^{\infty}\exp\left(i\,\mu(kT_s)^2\right)\exp\left(-i\omega kT_s\right),\\&=\frac{1}{T_s}\mathcal{F}^{\mu}_{chirp}(\omega/T_s),\\&=\frac{1}{T_s}\left(i\frac{\pi}{\mu}\right)^{1/2}\exp\left(-i\,\frac{\omega^2}{4\,\mu T_s^2}\right),\\&=\left(i\frac{\pi}{\mu_N}\right)^{1/2}\exp\left(-i\,\frac{\omega^2}{4\,\mu_N}\right),\end{aligned}\tag{C.19}$$

where $\mu_N=\mu T_s^2$. We know that μ is related to $\omega_{d,\alpha}$ through the following relation (equation (C.5))

$$\begin{aligned}\mu&=\omega_{d,\alpha},\\\mu T_s^2&=T_s^2\omega_{d,\alpha},\\\mu_N&=\omega_{D,\alpha},\end{aligned}\tag{C.20}$$

where $\omega_{D,\alpha}$ (in radians) is acceleration-dependent normalized Doppler spread given in (4.115) that includes acceleration and initial Doppler spread. Notice that we had earlier deliberately removed the normalization by the symbol rate in order to match the conventional DTFT representation in (C.17). Finally, we are in a position to define BMFC_{dtft} as follows

$$\mathrm{BMFC}_{dtft}\triangleq\frac{1}{2\pi}\int_{-\omega_{D,\alpha}}^{\omega_{D,\alpha}}\frac{\exp\left(i\,p\,\arcsin\left(\mu_N/\omega_{D,\alpha}\right)\right)}{\sqrt{\omega_{D,\alpha}^2-\mu_N^2}}\;\mathrm{DTFT}^{\mu_N}_{chirp}(\omega)\,d\mu_N,$$

which is (4.120).

Appendix D

D.1 Optimal Wiener Filter and MMSE

The autocorrelation of the channel process is given as

$$\Phi_{c_k c_k}(s) = \mathbb{E}\left\{h_{c_k}(n+s)h^{\dagger}_{c_k}(n)\right\} = \Phi_h(sT_p), \tag{D.1}$$

so that the corresponding PSD will be

$$\mathcal{S}_{c_k c_k}(\omega) = \sum_{s=-\infty}^{\infty} \Phi_{c_k c_k}(s)\exp\left(-i\omega s\right) = \sum_{s=-\infty}^{\infty} \Phi_{c_k c_k}(sT_p)\exp\left(-i\omega s\right). \tag{D.2}$$

Notice that (D.1) and (D.2) do not depend on k implying that

$$\Phi_{c_k c_k}(s) = \Phi_{cc}(s),\ \ \mathcal{S}_{c_k c_k}(\omega) = \mathcal{S}_{cc}(\omega).$$

Similarly, the cross-correlation between channel gain at pilot symbol instant and channel gain at data symbol location shifted by k symbols from the preceding pilot symbol which is given as

$$\Phi_{c_k c}(s) = \mathbb{E}\left\{h_{c_k}(n+s)h^{\dagger}_{c}(n)\right\} = \Phi_{cc}(sT_p + k), \tag{D.3}$$

so that the corresponding cross spectral density is

$$\mathcal{S}_{c_k c}(\omega) = \sum_{s=-\infty}^{\infty} \Phi_{c_k c}(s)\exp\left(-i\omega s\right) = \sum_{s=-\infty}^{\infty} \Phi_{cc}(sT_p + k)\exp\left(-i\omega s\right). \tag{D.4}$$

Using (D.3), the autocorrelation and the PSD of the pilot observation process $\{x[n]\}$ would respectively be

$$\Phi_{xx}(s) = \mathbb{E}\left\{h_x(n+s)h^{\dagger}_{x}(n)\right\},$$

$$= \mathcal{E}_p \, \Phi_{cc}(s) + \frac{N_0}{\mathcal{M}} \left(f_{\mathrm{D}} T_p\right) \mathrm{sinc}\left(2\pi f_{\mathrm{D}} T_p s\right), \tag{D.5}$$

$$\begin{aligned} \mathcal{S}_{xx}(\omega) &= \sum_{s=-\infty}^{\infty} \Phi_{xx}(s) \exp\left(-i\omega s\right), \\ &= \mathcal{E}_p \, \mathcal{S}_{cc}(\omega) + \frac{N_0}{\mathcal{M}} \mathrm{rect}\left(\frac{\omega}{4\pi f_{\mathrm{D}} T_p}\right), \end{aligned} \tag{D.6}$$

where $\mathrm{sinc}(z) = \sin(z)/z$ and $\mathrm{rect}(u/W)$ is a rectangular function located symmetrically about $u = 0$ and width u. Notice that the noise is colored (or bandlimited white) unlike white noise assumed in previous work [88, 221]. The filtering of the stream of pilot-plus-unused symbols has two effects: Firstly, the out-of-band noise has been removed improving signal-to-noise ratio at pilot symbol instants. Secondly, filtering has changed white noise to colored noise. Since we have assumed perfect knowledge of the PSD (and autocorrelation) of the noise process, the knowledge of noise correlations can be exploited to improve the performance.

We would also require the following cross correlation

$$\begin{aligned} \Phi_{c_k x}(s) &= \mathbb{E}\left\{h_{c_k}(n+s) h_x^{\dagger}(n)\right\}, \\ &= \sqrt{\mathcal{E}_p} \, \Phi_{c_k c}(s), \end{aligned} \tag{D.7}$$

and the corresponding PSD

$$\mathcal{S}_{c_k x}(\omega) = \sum_{s=-\infty}^{\infty} \Phi_{c_k x}(s) \exp\left(-i\omega s\right) = \sqrt{\mathcal{E}_p} \, \mathcal{S}_{c_k c_0}(\omega). \tag{D.8}$$

We know from classical estimation theory [132] that MMSE and Linear MMSE are equivalent when the observation process and the channel process are jointly Gaussian [136] which is true in our case. In other words, MMSE estimate has the following form

$$\widetilde{c_k}(n) = \sum_{s=-\infty}^{\infty} w_{o,k}(s) \, x(s-n), \tag{D.9}$$

and the transfer function of the optimal Wiener smoother is given as (5.11). Using equations (D.1)-(D.8) and (5.11), we get the following

$$\begin{aligned} W_{o,k} &= \exp\left(i\omega k\right) \frac{\sqrt{\mathcal{E}_p} \, \mathcal{S}_{cc}(\omega)}{\left(\frac{N_0}{\mathcal{M}} \, \mathrm{rect}\left(\frac{\omega}{4\pi f_{\mathrm{D}} T_p}\right) + \mathcal{E}_p \, \mathcal{S}_{cc}(\omega)\right)}, \\ &= \exp\left(i\omega k\right) W_o(\omega) \end{aligned} \tag{D.10}$$

which implies that the optimal Wiener filter has the same frequency domain characteristics for any k except for a phase shift $\exp(i\omega k)$ that is linear in k. The corresponding MMSE is [252]

$$\begin{aligned}\sigma_{\epsilon d}^2 &= \frac{1}{2\pi}\int_{-\pi}^{\pi}\left(\mathcal{S}_{cc}(\omega) - \frac{|\mathcal{S}_{c_k x}(\omega)|^2}{\mathcal{S}_x(\omega)}\right)d\omega, \\ &= \frac{1}{2\pi}\int_{-\pi}^{\pi}\left(\mathcal{S}_{cc}(\omega) - \sqrt{\mathcal{E}_p}\,W_o(\omega)\right)d\omega, \end{aligned} \tag{D.11}$$

where (equation (D.10))

$$W_o(\omega) = \frac{\sqrt{\mathcal{E}_p}\,\mathcal{S}_{cc}(\omega)}{\left(\frac{N_0}{\mathcal{M}}\,\mathrm{rect}\left(\frac{\omega}{4\pi f_D T_p}\right) + \mathcal{E}_p\,\mathcal{S}_{cc}(\omega)\right)}$$

Equations (D.10) and (D.11) respectively give optimal Winer filter transfer function and the corresponding MMSE in terms of statistics of sampled channel process, $c_k[n]$. It is of interest to find optimal Wiener filter and MMSE in terms of the original channel process, *i.e.*, $h[m]$. Since $c_k[n]$ is a downsampled version of the original process $h[m]$, we have the following relationships[1] for $|\omega| \leq \pi$

$$\begin{aligned}\mathcal{S}_{cc}(\omega) &= \frac{1}{T_p}\mathcal{S}_h\left(\frac{\omega}{T_p}\right), \\ \mathcal{S}_{c_k c}(\omega) &= \exp(i\omega k)\,\frac{1}{T_p}\mathcal{S}_h\left(\frac{\omega}{T_p}\right), \end{aligned} \tag{D.12}$$

which give the following optimal wiener filter transfer function, $W_{o,k}(\omega)$, (equation (5.12))

$$\begin{aligned}W_{o,k}(\omega) &= \frac{1}{T_p}\exp(i\omega k)\,\frac{\sqrt{\mathcal{E}_p}\,\mathcal{S}_h\left(\frac{\omega}{T_p}\right)}{\left(\frac{N_0}{\mathcal{M}}\,\mathrm{rect}\left(\frac{\omega}{4\pi f_D T_p}\right) + \frac{\mathcal{E}_p}{T_p}\mathcal{S}_h\left(\frac{\omega}{T_p}\right)\right)}, \\ &= \exp(i\omega k)\,W_o\left(\frac{\omega}{T_p}\right), \end{aligned}$$

and the corresponding MMSE σ_ϵ^2, after a change of variable ($\frac{\omega'}{T_p} = \omega$) and manipulation,

[1] We firstly assume that the channel Doppler spectrum $\mathcal{S}_h(\omega)$ is a lowpass spectrum such that

$$\mathcal{S}_h(\omega) = 0 \quad \omega_N < |\omega| \leq \pi$$

and, secondly, there is no aliasing in the downsampled process $c_k[n]$ which requires that

$$\omega_N'' < \pi.$$

is given by (equation (5.13))

$$\sigma_\epsilon^2 = \frac{1}{2\pi}\int_{-2\pi f_{\mathrm{D}}}^{2\pi f_{\mathrm{D}}} \mathcal{S}_h(\omega)\left(1 - \frac{\mathcal{E}_p\,\mathcal{S}_h(\omega)}{T_p\left(\frac{N_0}{\mathcal{M}} + \frac{\mathcal{E}_p}{T_p}\mathcal{S}_h\left(\omega\right)\right)}\right) d\omega,$$

$$= \frac{1}{2\pi}\int_{-2\pi f_{\mathrm{D}}}^{2\pi f_{\mathrm{D}}} \mathcal{S}_h(\omega)\left(1 - \sqrt{\mathcal{E}_p}\,W_o(\omega)\right) d\omega.$$

D.2 MMSE for Uniform and Clarke's Doppler Spectra

The MMSE for a general bandlimited channel spectrum is given by (5.13). We first consider the uniform Doppler spectrum (equation (5.16)) for which MMSE can be written as (equation (5.13))

$$\sigma^2_{U,\epsilon} = \frac{1}{2\pi}\int_{-2\pi f_{\mathrm{D}}}^{2\pi f_{\mathrm{D}}} \frac{1}{2f_{\mathrm{D}}}\left(1 - \frac{\mathcal{E}_p\,/2f_{\mathrm{D}}}{\left(\frac{N_0}{\mathcal{M}}T_p + \frac{\mathcal{E}_p}{2f_{\mathrm{D}}}\right)}\right) d\omega, \tag{D.13}$$

which, after straightforward integration and simplification, gives (5.18). Notice the presence of factor $\mathcal{M}$ due to filtering and downsampling.

Using (5.13) and (5.17), MMSE for Clarke's U-shaped spectrum is given as

$$\sigma^2_{C,\epsilon} = \frac{1}{2\pi}\int_{-2\pi f_{\mathrm{D}}}^{2\pi f_{\mathrm{D}}} \frac{1}{\frac{1}{2}\sqrt{\omega_{\mathrm{D}}^2 - \omega^2} + \frac{\mathcal{M}\,\rho_p}{T_p}} d\omega. \tag{D.14}$$

If we make the change of variable such that $\omega = \omega_{\mathrm{D}}\sin(x)$, (D.14) can be written as

$$\sigma^2_{C,\epsilon} = \frac{1}{\pi}\int_{-\pi/2}^{\pi/2} \frac{1}{1 + \frac{\mathcal{M}\,\rho_p}{\pi f_{\mathrm{D}} T_p}\sec(x)} dx. \tag{D.15}$$

Observe the presence of $\sec(x)$ in the denominator instead of $\cos(x)$ as in [222]. Let $\chi = \frac{\mathcal{M}\,\rho_p}{\pi f_{\mathrm{D}} T_p}$. Using the following formula [116]

$$\int \frac{1}{1 + \chi\sec(x)} dx = x - \frac{2\chi\,\mathrm{arctanh}\left(\frac{1-\chi}{\sqrt{1-\chi^2}}\tan(\frac{x}{2})\right)}{\sqrt{1-\chi^2}},$$

equation (D.14) becomes

$$\sigma^2_{C,\epsilon} = 1 - \frac{4\chi\,\mathrm{arctanh}\left(\sqrt{\frac{1-\chi}{1+\chi}}\right)}{\sqrt{1-\chi^2}}. \tag{D.16}$$

Equation (D.16) gives the MMSE for the proposed scheme when channel doppler spectrum is characterized by U-shaped Clarke's spectrum. When $\mathcal{M} = 1$, (D.16) collapses to MMSE for NP schemes. Somewhat similar expression for MMSE has been derived for Clarke's spectrum in [222] for $\mathcal{M} = 1$. Observe that (D.16) is true for any χ.

D.3 Maximum of MMSE Gain Function

It is of some interest to determine at what SNR occurs the maximum of $\mathcal{G}$ function (equation (5.20)). For uniform Doppler spectrum, we have

$$\mathcal{G}^U = \frac{2f_{\mathrm{D}}T_p\rho_p\left(\mathcal{M}-1\right)}{\left(2f_{\mathrm{D}}T_p+\rho_p\right)\left(2f_{\mathrm{D}}T_p+\mathcal{M}\rho_p\right)}, \tag{D.17}$$

We take partial derivative of $\mathcal{G}^U$ with respect to ρ_p and set it equal to zero, *i.e.*,

$$\frac{\partial}{\partial\rho_p}\mathcal{G}^U = 0,$$

or

$$\begin{aligned} 0 \;=\; & \left(\left(2f_{\mathrm{D}}T_p+\rho_p\right)\left(2f_{\mathrm{D}}T_p+\mathcal{M}\,\rho_p\right)\right)2f_{\mathrm{D}}T_p(\mathcal{M}-1) \\ & -2f_{\mathrm{D}}T_p\rho_p\left(\mathcal{M}-1\right)\left(\left(2f_{\mathrm{D}}T_p+\rho_p\,\right)\mathcal{M}+\left(2f_{\mathrm{D}}T_p+\mathcal{M}\rho_p\right)\right) \end{aligned}$$

which, after some straightforward simplification, gives (5.22), *i.e.*,

$$\rho_p^{\mathrm{Umax}} = \frac{2f_{\mathrm{D}}T_p}{\sqrt{\mathcal{M}}}. \tag{D.18}$$

or we can write

$$\rho_p^{\mathrm{Umax}} \propto \frac{T_p}{\sqrt{\mathcal{M}}}.$$

Note that the equation (D.18) assumes that the power savings due to the transmission of zeros are not used for ρ_p enhancement so that this result is applicable for NE and DE cases. When the power savings are used to enhance pilot symbol power, we can proceed as above to determine optimal ρ_p.

Similarly, using (5.13), (5.17) and (D.16), we obtain the following expression for MMSE gain for Clarke's Doppler spectrum

$$\mathcal{G}^C = \frac{4\chi}{\pi\sqrt{1-\chi^2}}\mathrm{arctanh}\left(\sqrt{\frac{1-\chi}{1+\chi}}\right) - \frac{4\chi'}{\pi\sqrt{1-\chi'^2}}\mathrm{arctanh}\left(\sqrt{\frac{1-\chi'}{1+\chi'}}\right), \tag{D.19}$$

where $\chi = (\mathcal{M}\,\rho_p)/(\pi f_{\mathrm{D}}T_p)$ and $\chi' := \rho_p/(\pi f_{\mathrm{D}}T_p)$ respectively for the proposed and NP schemes. For notational simplicity, let $\varphi = \pi f_{\mathrm{D}}T_p$. Taking partial derivative of $\mathcal{G}^C$ with respect to ρ_p using the following identity [253]

$$\frac{d}{dx}\left(\mathrm{arctanh}(x)\right) = \frac{1}{1-x^2},$$

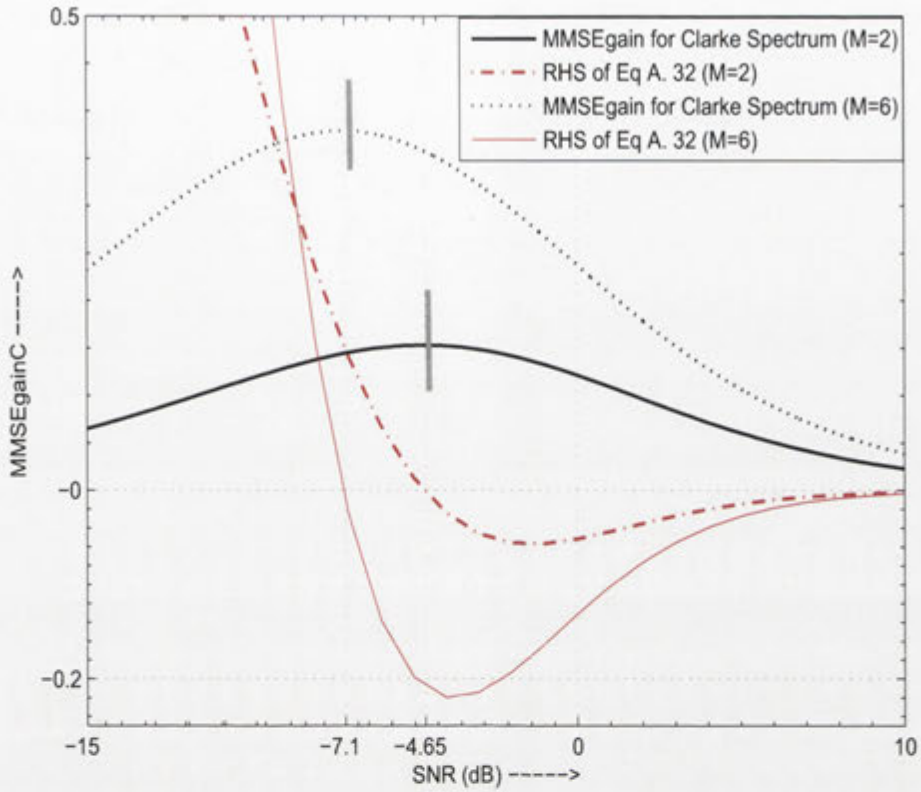

Figure D.1: RHS of Eq. (D.20) as a function of ρ_p highlighting maximum of $\mathcal{G}^C$ (MMSE gain with Clarke's isotropic scattering model). It may be observed that $\rho_p = -4.65$ dB and -7.1 dB result in maximum MMSE gains respectively for $\mathcal{M} = 2$ and 6.

and setting it equal to zero, we get

$$0 = -\frac{\mathcal{M}\varphi\left(\sqrt{\frac{\varphi-\mathcal{M}\rho_p}{\varphi+\mathcal{M}\rho_p}}\right)}{2(\varphi-\mathcal{M}\rho_p)\sqrt{\varphi^2-(\mathcal{M}\rho_p)^2}} + \frac{\operatorname{arctanh}\left(\sqrt{\frac{\varphi-\mathcal{M}\rho_p}{\varphi+\mathcal{M}\rho_p}}\right)\varphi^2 M}{(\varphi^2-(M\rho_p)^2)^{\frac{3}{2}}} + \frac{\varphi\left(\sqrt{\frac{\varphi-\rho_p}{\varphi+\rho_p}}\right)}{2(\varphi-\rho_p)\sqrt{\varphi^2-\rho_p^2}} - \frac{\operatorname{arctanh}\left(\sqrt{\frac{\varphi-\rho_p}{\varphi+\rho_p}}\right)\varphi^2}{(\varphi^2-\rho_p^2)^{\frac{3}{2}}}, \tag{D.20}$$

for which we have to resort to hit-and-trial method to obtain solution(s). First we can easily verify from (D.19) that two of the extrema lie at $\rho_p = 0, \infty$ which correspond to the minimum of $\mathcal{G}^C$ function. The right hand side (RHS) of (D.20) is plotted in Fig. D.1 as a function of ρ_p keeping T_p and f_D fixed for two different values of $\mathcal{M}$. We have also plotted $\mathcal{G}^C$ to verify that the zero(s) of the right hand side of (D.20) are valid extrema of $\mathcal{G}^C$ function.

Notice that one of the solutions (highlighted for each value of $\mathcal{M}$) actually corresponds to the maximum of $\mathcal{G}^C$ function. The solution obtained in (D.18) for uniform

spectrum is also highlighted with thick vertical line segments. It can be observed that, for the same parameters, the difference between maximum of MMSE gain function for Clarke's spectrum and that of uniform spectrum is not significant. Although there is some dependence of extremum on the value of $\mathcal{M}$ that can be observed in Fig. D.1, the following rule of thumb is more accurate for smaller values of $\mathcal{M}$

$$\rho_p^{\text{Cmax}} \approxeq \rho_p^{\text{Umax}}. \tag{D.21}$$

D.4 Some Auxiliary Constants Used in Chapter 5

$$
\begin{aligned}
A_{\mathrm{PE}} &= -G^2, \\
B_{\mathrm{PE}} &= -2G^2\xi_{\mathrm{PE}}, \\
C_{\mathrm{PE}} &= G(H\xi_{\mathrm{PE}} + G - \mathcal{M}), \\
\mathcal{Q}(\xi_{\mathrm{PE}}) &= -\frac{C_{\mathrm{PE}}}{A_{\mathrm{PE}}}, \\
A_{\mathrm{DE}} &= -G, \\
B_{\mathrm{DE}} &= -2G\xi_{\mathrm{DE}}, \\
C_{\mathrm{DE}} &= \mathcal{M}\xi_{\mathrm{DE}}, \\
\mathcal{Q}(\xi_{\mathrm{DE}}) &= -\frac{C_{\mathrm{DE}}}{A_{\mathrm{DE}}}, \\
Y_{\mathrm{NP}} &= (1-\mu^{\mathrm{NP}})\mu^{\mathrm{NP}}\rho\,, \\
X_{\mathrm{NP}} &= 2f_{\mathrm{D}}(1-\mu^{\mathrm{NP}})\rho \;+\; (1-\gamma^{\mathrm{NP}})(2f_{\mathrm{D}} + \mu^{\mathrm{NP}}\rho\,), \\
Q_{\mathrm{NP}} &= 1 - 4f_{\mathrm{D}}, \\
\xi_{\mathrm{NP}} &= \frac{2f_{\mathrm{D}}(1 - 2f_{\mathrm{D}} + \rho\,)}{\rho\, Q_{\mathrm{NP}}}, \\
\mathcal{Q}(\xi_{\mathrm{NP}}) &= \xi_{\mathrm{NP}}.
\end{aligned}
$$

D.5 Proof: Optimally $\mathcal{E}_p^{\mathrm{PE}} > \mathcal{E}_s$ (Unequal Pilot and Data Powers)

In order to prove that $\mathcal{E}_p^{\mathrm{PE}} > \mathcal{E}_s$, it suffices to show that (equation (5.26))

$$\frac{\mu_{o,e}^{\mathrm{PE}}}{2f_{\mathrm{D}}} > 1. \tag{D.22}$$

We assume $\gamma = \gamma_{opt} = 2Mf_{\mathrm{D}}$ in the following.

We consider the left-hand-side of (D.22) and proceed as follows.

$$\begin{aligned}
\frac{\mu_{oe}^{\mathrm{PE}}}{2f_{\mathrm{D}}} &= \frac{1}{2f_{\mathrm{D}}}\left(\mu_o^{\mathrm{PE}} + \frac{(\mathcal{M}-1)\gamma(1-\mu_o^{\mathrm{PE}})}{\mathcal{M}}\right), \\
&> \frac{\mu_o^{\mathrm{PE}}}{2f_{\mathrm{D}}}, \\
&= \frac{1}{2f_{\mathrm{D}}}\left(-\xi_{\mathrm{PE}} + \sqrt{\xi_{\mathrm{PE}}^2 + \mathcal{Q}(\xi_{\mathrm{PE}})}\right), \\
&= \frac{1}{2f_{\mathrm{D}}}\left(-\xi_{\mathrm{PE}} + \sqrt{\xi_{\mathrm{PE}}^2 + \frac{H\xi_{\mathrm{PE}} + G - \mathcal{M}}{G}}\right), \\
&= \frac{1}{2f_{\mathrm{D}}}\left(\frac{\xi_{\mathrm{PE}}}{\xi_{\mathrm{PE}} + \sqrt{\xi_{\mathrm{PE}}^2 + \frac{\xi_{\mathrm{PE}} - (\mathcal{M}-1)2f_{\mathrm{D}}(2\xi_{\mathrm{PE}}+1)}{G}}}\right), \\
&> \frac{1}{2f_{\mathrm{D}}}\left(\frac{\xi_{\mathrm{PE}}}{\xi_{\mathrm{PE}} + \sqrt{\xi_{\mathrm{PE}}^2 + \frac{\xi_{\mathrm{PE}}}{G}}}\right), \\
&> \frac{1}{2f_{\mathrm{D}}}\left(\frac{\xi_{\mathrm{PE}}}{\xi_{\mathrm{PE}} + \sqrt{\xi_{\mathrm{PE}}^2 + \xi_{\mathrm{PE}}}}\right), \\
&> \frac{1}{2f_{\mathrm{D}}}\left(\frac{\xi_{\mathrm{PE}}}{\xi_{\mathrm{PE}} + \sqrt{\xi_{\mathrm{PE}}(\xi_{\mathrm{PE}}+1)}}\right), \\
&= \frac{1}{2f_{\mathrm{D}}}\frac{1}{2}, \\
&> 1,
\end{aligned}$$

where the first inequality is the result of the facts that $0 < \mu^{\mathrm{PE}} \leq 1$, $\gamma_o > 0$ and $1 < \mathcal{M} < \mathcal{M}_{\max}$. The factor $\mathcal{Q}(\xi_{\mathrm{PE}})$, in second equality, is given in the Appendix D.4 and $H = G - (\mathcal{M}-1)\gamma$ in the third equality. The fact that $\xi_{\mathrm{PE}} > 0$ was utilized in arriving at the second inequality. The factor $G > 0$ by definition and is behind the third inequality. The fourth inequality came about by ignoring 1 in the denominator of the second factor of third inequality. The last inequality is true as long as $f_{\mathrm{D}} < 1/8$

which is what we have assumed throughout the chapter. Thus, optimally, the average pilot symbol power is *always* greater than the average symbol power if the pilot and data symbol powers are allowed to differ. We state without proof that the same is true for other peaky schemes discussed in this chapter.

Appendix E

E.1 Derivation of Frequency-Selective Channel Model

Consider a SIMO broadband transmission system consisting of n_R receive antennas located at positions $\boldsymbol{x}_p, p = 1, \cdots, n_R$, relative to the receiver array origin 'O' as shown in Fig. 6.1. $r_R \geq \max ||\boldsymbol{x}_p||$ denotes the radius that contains all the receive antennas. We assume that scatterers are distributed in the far-field from the receiver antennas. Consider the broadband transmission of a signal $s(t)$ through the general scattering environment shown in Fig. 6.1. Then the received signal at time t at the receiver origin 'O' from direction β is given by

$$y_0(t, \widehat{\boldsymbol{\beta}}) = \int_{\tau} \psi(\widehat{\boldsymbol{\beta}}, \tau) s(t - \tau) d\tau, \tag{E.1}$$

where $\psi(\widehat{\boldsymbol{\beta}}, \tau)$ is the random complex scattering gain for the waves arriving in direction β with delay τ. Using (E.1), the received signal at the pth receive antenna located at position $\boldsymbol{x}_p$, from direction β can be written as

$$y_p(t, \widehat{\boldsymbol{\beta}}, \boldsymbol{x}_p) = \int_{\tau} \psi(\widehat{\boldsymbol{\beta}}, \tau) s(t - t_p - \tau) d\tau, \tag{E.2}$$

where $t_p = \boldsymbol{x}_p \cdot \widehat{\boldsymbol{\beta}}/c$ is the factor that takes into account the position of p-th antenna with respect to the origin; c represents the speed of wave propagation. Therefore the received signal at the p-th receive antenna at time t is given by

$$y_p(t, \boldsymbol{x}_p) = \int_{\Omega_R} y_p(t, \widehat{\boldsymbol{\beta}}, \boldsymbol{x}_p) d\beta = \int_{\Omega_R} \int_{\tau} \psi(\widehat{\boldsymbol{\beta}}, \tau) s(t - t_p - \tau) d\tau d\beta. \tag{E.3}$$

Outer integration in (E.3) is over the unit sphere for a 3D scattering environment or the unit circle in the 2D scattering environment. We also assume that the angles of arrival at both receiving antennas are approximately the same since the propagation distance is large, compared to the antenna separation.

Taking the Fourier transform of (E.3) with respect to t yields

$$Y_p(\omega, \boldsymbol{x}_p) = \int_{\Omega_R} \int_{\tau} \psi(\widehat{\boldsymbol{\beta}}, \tau) S(\omega) \exp(-i(t_p + \tau)\,\omega) d\tau d\beta, \tag{E.4}$$

where $S(\omega) = \mathcal{F}\{s(t)\}$ is the Fourier transform of the transmitted signal $s(t)$. From (E.4), the channel frequency response[1] between the transmit antenna and the pth receive antenna can be obtained as

$$H_p(\omega) = \int_{\Omega_R} \int_{\tau} \psi(\widehat{\boldsymbol{\beta}}, \tau) \exp(-i\omega\tau) \exp\left(-i\omega \frac{\boldsymbol{x}_p \cdot \widehat{\boldsymbol{\beta}}}{c}\right) d\tau d\beta. \tag{E.5}$$

Now let f_c be the carrier frequency and suppose there are N_s subcarriers with spacing Δf. The channel frequency response at the nth subcarrier between the transmit antenna and the pth receive antenna located at $\boldsymbol{x}_p$ is then can be written as

$$\begin{aligned} H_p(n) = \int_{\Omega_R} \int_{\tau} & \psi(\widehat{\boldsymbol{\beta}}, \tau) \exp(-i2\pi(f_c - (n + 0.5)\Delta f)\tau) \\ & \times \exp\left(-i\frac{2\pi}{c}(f_c - (n + 0.5)\Delta f)\boldsymbol{x}_p \cdot \widehat{\boldsymbol{\beta}}\right) d\tau d\beta, \end{aligned} \tag{E.6}$$

which can be written as (6.3). Notice that, for notational simplicity, we have dropped ω in the notation for frequency response.

[1] by letting $s(t) = \delta(t)$

E.2 Derivation of the Space-Frequency Correlation Function

Let

$$A_p(\widehat{\boldsymbol{\beta}}, n) \triangleq \int_{\tau} \psi(\widehat{\boldsymbol{\beta}}, \tau) \exp\left(-i2\pi(f_c - (n+0.5)\Delta f)\tau\right) d\tau, \tag{E.7}$$

then, using (6.3) and (6.4), the space-frequency correlation between the nth subcarrier on the pth receive antenna located at position $\boldsymbol{x}_p$ and the mth subcarrier on the qth receive antenna located at position $\boldsymbol{x}_q$ can be written as

$$\begin{aligned}\Phi_{p,q}(n,m) = \int_{\Omega_R}\int_{\Omega_R} \mathbb{E}\left\{A_p(\widehat{\boldsymbol{\beta}}_1, n) A_q^*(\widehat{\boldsymbol{\beta}}_2, m)\right\} \exp\left(-i\frac{2\pi}{c}(f_c - (n+0.5)\Delta f)\boldsymbol{x}_p \cdot \widehat{\boldsymbol{\beta}}_1\right) \\ \times \exp\left(i\frac{2\pi}{c}(f_c - (m+0.5)\Delta f)\boldsymbol{x}_q \cdot \widehat{\boldsymbol{\beta}}_2\right) d\beta_1 d\beta_2.\end{aligned} \tag{E.8}$$

First we assume that complex scattering channel gain from different directions are independent of each other [36, 103], *i.e.*,

$$\mathbb{E}\left\{A_p(\beta_1, n) A_q^*(\beta_2, m)\right\} = \begin{cases} 0, & \text{if } \beta_1 \neq \beta_2; \\ \mathbb{E}\left\{A_p(\beta_1, n) A_q^*(\beta_2, m)\right\}, & \text{otherwise.} \end{cases} \tag{E.9}$$

This assumption yields

$$\begin{aligned}\Phi_{p,q}(n,m) = \int_{\Omega_R} \eta(\beta, n, m) \exp\left(-i\frac{2\pi}{c}(f_c - (n+0.5)\Delta f)\boldsymbol{x}_p \cdot \widehat{\boldsymbol{\beta}}\right) \\ \times \exp\left(i\frac{2\pi}{c}(f_c - (m+0.5)\Delta f)\boldsymbol{x}_q \cdot \widehat{\boldsymbol{\beta}}\right) d\beta,\end{aligned} \tag{E.10}$$

where we have defined

$$\begin{aligned}\widetilde{\chi}(\beta, n, m) &\triangleq \mathbb{E}\left\{A_p(\beta_1, n) A_q^*(\beta_2, m)\right\}, \\ &= \int_{\tau_1}\int_{\tau_2} \mathbb{E}\left\{\psi(\beta, \tau_1)\psi^*(\beta, \tau_2)\right\} \exp\left(-i\frac{2\pi}{c}(f_c - (n+0.5)\Delta f)\tau_1\right) \\ &\quad \times \exp\left(i\frac{2\pi}{c}(f_c - (m+0.5)\Delta f)\tau_2\right) d\tau_1 d\tau_2.\end{aligned} \tag{E.11}$$

is the frequency cross correlation between subcarriers at two antennas from a given direction β. We now assume that complex scattering channel gains for two different delays are uncorrelated, *i.e.*, the channel process is uncorrelated in the delay domain [5, 242]

implying

$$\mathbb{E}\left\{\psi(\beta,\tau_1)\psi^*(\beta,\tau_2)\right\} = \begin{cases} 0, & \text{if } \tau_1 \neq \tau_2; \\ \mathbb{E}\left\{|\psi(\beta,\tau_1)|^2\right\}, & \text{otherwise.} \end{cases} \tag{E.12}$$

Under this assumption, (E.11) simplifies to

$$\widetilde{\chi}(\beta,n,m) = \int_{\tau} \Psi(\beta,\tau)\exp\left(-i2\pi(m-n)\Delta f\tau\right)d\tau, \tag{E.13}$$

where $\Psi(\beta,\tau) \triangleq \mathbb{E}\left\{|\psi(\beta,\tau)|^2\right\}$ is the joint angular power-delay profile at the receiver aperture. Substitution of (E.13) in (E.8) gives $\Phi_{p,q}(n,m)$ defined in (6.5).

Bibliography

[1] J. T. Y. Ho, "Generalized doppler power spectrum for 3D non-isotropic scattering environments," in *IEEE Global Telecommunications Conference, GLOBECOM'05*, vol. 3, 2005, p. 13931396.

[2] R. H. Clarke, "A statistical theory of mobile-radio reception," *Bell Systems Technical Journal*, vol. 47, no. 6, pp. 957–1000, 1968.

[3] H. M. Jones, R. A. Kennedy, and T. D. Abhayapala, "On dimensionality of multipath fields: Spatial extent and richness," in *Proc. IEEE Int. Conf. Acoust., Speech, Signal Processing, ICASSP'02*, vol. 3, Orlando, Florida, May 2002, pp. 2837–2840.

[4] A. Y. Olenko, K. T. Wong, and M. Abdulla, "Analytically derived TOA-DOA distributions of uplink/downlink wireless-cellular multipaths arisen from scatterers with an inverted-parabolic spatial distribution arround the mobile," *IEEE Signal Processing Letters*, vol. 12, no. 7, pp. 516–519, Jul. 2005.

[5] R. B. Ertel and J. H. Reed, "Angle and time of arrival statistics for circular and elliptical scattering models," *IEEE journal on Selected Areas in Communications*, vol. 17, no. 11, pp. 1829–1840, Nov. 1999.

[6] M. Ibnkahla, Ed., *Signal Processing for Mobile Communications Handbook*. CRC Press, 2004.

[7] Y. Zhang and H.Chen, Eds., *Mobile WiMAX: toward broadband wireless metropolitan area networks*. CRC Press, 2007.

[8] D. S. Holder, Ed., *Electrical Impedance Tomography: Methods, History and Applications*. Bristol and Philadelphia: Institute of Physics, 2005.

[9] C.-C. Kuo, S.-H. Tsai, L. Tadjpour, and Y.-H. Chang, *Precoding Techniques for Digital Communication Systems*, 1st ed. Springer, 2008.

[10] S. Y. P. Ada, D. N. C. Tse, and R. W. Brodersen, "Impact of scattering on the capacity, diversity and propagation range of multiple antenna channels," *IEEE Transactions on Information Theory*, vol. 52, no. 3, pp. 1087–1100, 2006.

[11] A. Paulraj, R. Nabar, and D. Gore, *Introduction to Space-Time Wireless Communications*. Cambridge University Press, 2003.

[12] D. Gore, R. W. H. Jr., and A. Paulraj, "Transmit selection in spatial multiplexing," *IEEE Commun. Lett*, vol. 6, pp. 491–493, 2002.

[13] U. Madhow, *Fundamentals of Digital Communication*. Cambridge University Press, 2008.

[14] R. Kraemer and M. Katz, Eds., *Short-Range Wireless Communications: Emerging Technologies and Applications*.

[15] A. Abdi, J. A. Barger, and M. Kaveh, "A parametric model for the distribution of the angle of arrival and the associated correlation function and power spectrum at the mobile station," *IEEE Transactions on Vehicular Technology*, vol. 51, no. 3, pp. 425–434, May 2002.

[16] J. Dulmage and M. P. Fitz, "Non-isotropic fading channel model for the highway environment." in *IEEE Vehicular Tech. Conference (Fall)*, 2007, pp. 2144–2148.

[17] G. Acosta, M. A. Ingram, and K. Tokuda, "Measured joint doppler-delay power profiles for vehicle-to-vehicle communication at 2.4 GHz," *in Proc. IEEE GLOBECOM*, vol. 6, pp. 3813–3817, Dec. 2004.

[18] K. I. Pedersen, P. E. Mogensen, and B. H. Fleury, "Power azimuth spectrum in outdoor environment," *IEE Electronics Letters*, vol. 33, no. 18, pp. 1583–1584, Aug. 1997.

[19] M. Kalkan and R. Clarke, "Prediction of the space-frequency correlation function for base station diversity reception," *IEEE Transactions on Vehicular Technology*, vol. 46, no. 1, pp. 176–184, Feb 1997.

[20] L. Chan and S. Loyka, "Impact of multipath angular distribution on performance of MIMO systems," *Canadian Conference on Electrical and Computer Engineering*, CCECE, vol. 2, pp. 853–857, May 2004.

[21] G. Zhao and S. Loyka, "MIMO capacity of multipath-clustered channels using Fourier transform techniques," in *ICSP'04*, vol. 3, Aug-Sep 2004, pp. 1853–1856.

[22] K. Anim-Appiah, "Complex envelope correlations for non-isotropic scattering," *IEE Electronics Letters*, vol. 34, no. 9, pp. 1039–1052, Apr 1998.

[23] M. Pätzold and B. O. Hogstad, "A wideband MIMO channel model derived from the geometric elliptical scattering model," *Wirel. Commun. Mob. Comput.*, vol. 8, no. 5, pp. 597–605, 2008.

[24] H. S. Rad and S. Gazor, "A cross-correlation MIMO channel model for non-isotropic scattering environment and non-omnidirectional antennas," in *Candian Conference on Electrical and Computer Engineering, 2005.*, May 2005, pp. 25–28.

[25] P. Sharma, "Time-series model for wireless fading channels in isotropic and non-isotropic scattering environments," in *ISCC '04: Proceedings of the Ninth International Symposium on Computers and Communications 2004 Volume 2 (ISCC"04)*. Washington, DC, USA: IEEE Computer Society, 2004, pp. 633–638.

[26] H. S. Rad and S. Gazor, "The impact of non-isotropic scattering and directional antennas on MIMO multicarrier mobile communication channels," *IEEE transactions on wireless comm.*, vol. 56, no. 4, pp. 642–652, Apr. 2008.

[27] K. Mammasis, R. W. Stewart, E. Pfann, and G. Freeland, "Three-dimensional channel modelling using spherical statistics for multiple-input multiple-output systems," *IET Communications*, vol. 3, 2009.

[28] J. S. Sadowsky and V. Katedziski, "On the correlation and scattering functions of the WSSUS channel for mobile communications," *IEEE Transactions on Vehicular Technology*, vol. 47, no. 1, pp. 270–282, Feb. 1998.

[29] J. T. Y. Ho, "A novel 3D frequency-time-space non-isotropic scattering correlation model,," in *Second IASTED International Conference on Communication and Computer Networks,* ACTA Press, M. H. Hamza, Ed., Cambridge, MA, USA, vol. 1, Nov. 2004, pp. 155–160.

[30] T. A. Lamahewa, R. A. Kennedy, T. D. Abhayapala, and T. Betlehem, "MIMO channel correlation in general scattering environments," in *Proc. 7th Australian Communication Theory Workshop, AusCTW'06*, Perth, Western Australia, Feb. 2006, pp. 93–98.

[31] C. Tepedelenlioglu and G. Giannakis, "On velocity estimation and correlation properties of narrow-band communication channels," *IEEE Trans. Vehic. Technol.*, vol. 50, no. 4, pp. 1039–1052, July 2001.

[32] I. Akyildiz, J. Xie, and S. Mohanty, "A survey of mobility management in next-generation all-IP-based wireless systems," *IEEE Wireless Communications*, vol. 11, no. 4, pp. 16–28, Mar. 2004.

[33] S. Sesia, M. Baker, and I. Toufik, Eds., *LTE, The UMTS Long Term Evolution: From Theory to Practice*. John Wiley and Sons, 2009.

[34] M. Katz and F. Fitzek, Eds., *WiMAX Evolution: Emerging Technologies and Applications*. John Wiley and Sons, 2009.

[35] T. S. Pollock, T. D. Abhayapala, and R. A. Kennedy, "Introducing space into MIMO capacity calculations," *Journal on Telecommunications Systems, Kluwer Academic Publishers*, vol. 24, no. 2, pp. 415–436, 2003.

[36] P. D. Teal, T. D. Abhayapala, and R. A. Kennedy, "Spatial correlation for general distributions of scatterers," *IEEE Signal Processing Letters*, vol. 9, no. 10, pp. 305–308, Oct. 2002.

[37] X. Deng and A. M. Haimovich, "Information rates of time varying Rayleigh fading channels," in *Proc. IEEE International Conference on Communication , ICC'2004*, Paris, France, 2004.

[38] M. Jankiraman, *Space-time codes and MIMO systems*. Norwood, MA, USA: Artech House, Inc., 2004.

[39] W. C. Jakes, *Microwave Mobile Communications*. New York: John Wiley, 1974.

[40] G. L. Stüber, *Principles of Mobile Communication*, 2nd ed. Norwell, MA, USA: Kluwer Academic Publishers, 2001.

[41] J. Boccuzzi, *Signal Processing for Wireless Communications*. McGraw-Hill Professional, 2007.

[42] C. Charalambous and N. Menemenlis, "Stochastic models for long-term multipath fading channels and their statistical properties," in *Proc. of the 38th IEEE Conference on Decision and Control*, vol. 5, Dec. 1999, pp. 4947–4952.

[43] K. Rizk, J.-F. Wagen, and F. Gardiol, "Two-dimensional ray-tracing modeling for propagation prediction in microcellular environments," *IEEE Transactions on Vehicular Technology*, vol. 46, no. 2, pp. 508–518, May 1997.

[44] G. E. Athanasiadou, A. R. Nix, and J. P. McGeehan, "A microcellular ray-tracing propagation model and evaluation of its narrow-band and wide-band predictions," *IEEE Journal on Selected Areas in Communications*, vol. 18, no. 3, pp. 322–335, Mar. 2000.

[45] H. Arslan, Z. N. Chen, and M. D. Benedetto, *Ultra wideband wireless communication*. John Wiley & Sons, Inc., 2005.

[46] Z. Blazevic, I. Zanchi, and I. Marinovic, "Deterministic wideband modeling of satellite propagation channel with buildings blockage," *IEEE Transactions on Vehicular Technology*, 2005.

[47] M. Rahnema, *UMTS Network Planning, Optimization, and Inter-Operation with GSM*. Wiley-IEEE Press, 2008.

[48] M. K. Simon and M. S. Alouini, *Digital Communications over Fading Channels*, 2nd ed. Hoboken, New Jersey, USA: John Wiley & Sons, Nov. 2004.

[49] P. Beckman, *Probability in Communications Engineering*. New York, USA: Harcourt Brace & World, 1967.

[50] J. J. Ossana, "A model for mobile radio fading due to building reflection: Theoretical and experimental fading waveform power spectra," *Bell Systems Technical Journal*, vol. 43, no. 6, pp. 2935–2971, Nov. 1964.

[51] D. C. Champeney, *A Handbook of Fourier Transforms*. U.K.: Cambridge University Press, 1987.

[52] R. H. Clarke and W. L. Khoo, "3d mobile radio channel statistics," in *IEEE Transactions on vehicular technology*, vol. 46, no. 3, 1997, pp. 798–799.

[53] J. Salz and J. H. Winters, "Effect of fading correlation on adaptive arrays in digital mobile radio," *IEEE Trans. Vehic. Technol.*, vol. 42, no. 4, pp. 1049–1057, Nov. 1994.

[54] B. H. F. K. I. Pedersen, P. E. Mogensen, "A stochastic model of the temporal and azimuthal dispersion seen at the base station in outdoor environments," *IEEE Trans. on Vehicular Technology*, vol. 49, no. 2, pp. 437–447, May 2000.

[55] R. Vaughan and J. B. Anderson, *Channels, Propagation and Anetennas for Mobile communications*. UK: The IEE, 2003.

[56] W. R. Braun and D. Dersch, "A physical mobile radio channel model," *IEEE Trans. Vehic. Technol.*, vol. 40, pp. 472–472, May 1991.

[57] M. Patzold, L. Yingchun, and F. Laue, "A study of a land mobile sattelite channel model with asymmetrical doppler power spectrum and lognormally distributed line-of-sight component," *IEEE Trans. Vehic. Technol.*, vol. 47, no. 1, pp. 297–310, May 1998.

[58] J. Fuhl, J. P. Rossi, and E. Bonek, "High resolution 3-D direction-of-arrival determination for urban mobile radio," *IEEE Transactions on Antennas and Propagation*, vol. 45, no. 4, pp. 672–682, Apr. 1997.

[59] Q. Spencer, M. Rice, B. Jeffs, and S. H. Jensen, "A statistical model for angle of arrival in indoor multipath propagation," in *Proc. IEEE Vehicular Technology Conference, VTC'97*, vol. 3, Phoenix, AZ, May 1997, pp. 1415–1419.

[60] J. Wang, A. Mohan, and T. Aubrey, "Angles-of-arrival of multipath signals in indoor environments," in *Proc. IEEE Vehicular Technology Conference, VTC'01-Fall*, Atlanta, GA, USA, 1996, pp. 155–159.

[61] T. Lo and J. Litva, "Angles of arrival of indoor multipath," *Electronics Letters*, vol. 28, pp. 1687–1689, 1992.

[62] J. K. Cavers, *Mobile Channel Characteristics.* Norwell, MA, USA: Kluwer Academic Publishers, 2000.

[63] W. C. Y. Lee, "Finding the aproximate angular probability density function of wave arrival by using a directional antenna," in *IEEE transactions on Antennas and Propagation*, vol. AP-21, 1973, pp. 328–334.

[64] A. Kuchar, M. Tangemann, and E. Bonek, "A real-time DOA-based smart antenna processor," *IEEE Trans. on Vehicular Technology*, vol. 51, no. 6, pp. 1279–1293, Nov. 2002.

[65] P. C. F. Eggers, "Angular dispersive mobile radio environments sensed by highly directive base station antennas," in *Proc. IEEE Symp. on Personal, Indoor and Mobile Radio Comm.*, Toronto, Canada, Sep. 1995, pp. 522–526.

[66] T. C. Jeff, J. Boleng, and V. Davies, "A survey of mobility models for ad hoc network research," *Wireless Communications & Mobile Computing (*WCMC*): Special issue on Mobile Ad Hoc Networking: Research, Trends and Applications*, vol. 2, pp. 483–502, 2002.

[67] J. G. Markoulidakis, G. L. Lyberopoulos, D. F. Tsirkas, and E. D. Sykas, "Mobility modeling in third-generation mobile telecommunications systems," *IEEE Personal Commun.*, vol. 4, no. 4, pp. 41–56, Aug. 1997.

[68] G. Matz and F. Hlawatsch, "Wigner distributions (nearly) everywhere: time-frequency analysis of signals, systems, random processes, signal spaces, and frames," *Signal Process.*, vol. 83, no. 7, pp. 1355–1378, 2003.

[69] C. H. Page, "Instantaneous power spectra," *Journal of Appl. Phy.*, vol. 23, no. 1, pp. 103–106, Jan. 1952.

[70] M. J. Levin, "Instantaneous spectra and ambiguity functions," *Journal of Appl. Phy.*, pp. 95–97, 1964.

[71] J. S. Seybold, *Introduction to RF Propagation*. Wiley-Interscience, 2005.

[72] I. C. Abou-Faycal, M. D. Trot, and S. Shamai, "The capacity of discrete-time memoryless Rayleigh fading channels," *IEEE Transactions on Information Theory*, vol. 47, no. 4, pp. 1290–1301, May 2001.

[73] G. Taricco and M. Elia, "Capcity of fading channels with no side information," vol. 33, no. 16, pp. 1368–1370, July 1997.

[74] L. Zheng and D. N. C. Tse, "Communication on grassmann manifold: A geometric approach to the noncoherent multiple-antenna channel," in *IEEE Transactions on Information Theory*, vol. 48, no. 2, Feb. 2002, pp. 359–383.

[75] T. L. Marzetta and B. M. Hochwald, "Capacity of a mobile multiple-antenna communication link in Rayleigh flat fading," *IEEE Transactions on Information Theory*, vol. 45, no. 1, pp. 139–157, Jan. 1999.

[76] M. Peleg and S. Shamai, "On the capacity of blockwise incoherent MPSK channel," in *IEEE Transactions on Communications*, vol. 46, no. 5, May 1998, pp. 603–609.

[77] A. J. Goldsmith and P. P. Varaiya, "Capacity, mutual information and coding for finite-state Markov channels," *IEEE Trans. on Information Theory*, vol. 42, no. 3, pp. 868–886, May 1996.

[78] L. Zheng, M. Médard, D. Tse, and C. Luo, "Channel coherence in the low SNR regime," in *IEEE International Symposium on Information Theory (ISIT)*, 2004, pp. 976–997.

[79] Y. Liang and V. V. Veeravalli, "Capacity of non-coherent time-selective Rayleigh-fading channels," in *IEEE Transactions on Information Theory*, vol. 50, no. 12, Dec. 2004, pp. 1290–1301.

[80] W. C. Y. Lee, "Estimate of channel capacity in Rayleigh fading environment," in *IEEE transactions on Vehicular Technology*, vol. 39, no. 3, May 1990, pp. 187–189.

[81] K. A. Baddour and N. C. Beaulieu, "Improved pilot symbol aided estimation of Rayleigh fading channels with unknown autocorrelation statistics," *Proceedings of IEEE Vehicular Technology Conference (VTC-Fall 2004), Los Angeles, CA*, vol. 3, pp. 2101–2107, Sep. 2004.

[82] S. H. Chang and H. J. Lee, "Low-biased Doppler frequency estimation scheme employing variable prefilter and sampling rate," in *The 57th IEEE Semiannual Vehicular Technology Conference, VTC 2003-Spring*, vol. 3, 2003, pp. 2095–2100.

[83] R. D. Gitlin and S. B. Weinstein, "Fractionally-spaced equalization: An improved digital transversal equalizer," *Bell Systems Technical Journal*, vol. 60, pp. 275–296, 1981.

[84] C. B. Papadias and D. T. M. Slock, "Fractionally spaced equalization of linear polyphase channels and related blind techniques based on multichannel linear prediction," *IEEE Transactions on Signal Processing*, vol. 47, no. 3, pp. 641–654, Mar. 1999.

[85] D. K. Borah, R. A. Kennedy, Z. Ding, and I. Fijalkow, "Sampling and prefiltering effects on blind equalizer design," *IEEE Transactions on Signal Processing*, vol. 49, no. 1, pp. 209–218, Jan. 2001.

[86] I. E. Telatar and D. N. C. Tse, "Capacity and mutual information of wideband multipath fading channels," *IEEE Transactions on Information Theory*, vol. 46, pp. 1384–1400, 2000.

[87] S. Verdu, "Spectral efficiency in the wideband regime," *IEEE Transactions on Information Theory*, vol. 48, no. 6, pp. 1319–1343, Jun. 2002.

[88] X. Deng and A. M. Haimovich, "On pilot symbol aided channel estimation for time varying Rayleigh fading channels," *Proceedings of Conference on Information Sciences and Systems (*CISS*04)*, pp. 78–82, March 2004.

[89] D. Colton and R. Kress, *Inverse Acoustic and Electromagnetic Scattering Theory*, 2nd ed. New York: Springer, 1998, vol. 93.

[90] D. Schafhuber, "Wireless OFDM systems: Channel prediction and system capacity," Ph.D. dissertation, Vienna Univ. of Technology, Austria, March 2004.

[91] D. Schafhuber, H. Bolsckei, and G. Matz, "System capacity of wideband OFDM communications over fading channels without channel knowledge," in *Proceedings International Symposium on Information Theory,* ISIT., 27 June- 2 July 2004, p. 389.

[92] T. Aulin, "A modified model for the fading signal at a mobile radio channel," *IEEE Trans. on Vehicular Technology*, vol. VT-28, no. 3, pp. 182–203, 1979.

[93] J. D. Parsons, *The mobile radio propagation channel.* London, UK: Pentech Press, 1992.

[94] J. D. Parsons and A. M. D. Turkmani, "Characterisation of mobile radio signals: model description," in *IEE Proceedings-I*, vol. 138, no. 6, 1991, pp. 549–556.

[95] S. Thoen, L. V. der Perre, and M. Engels, "Modeling the channel time-variance for fixed wireless communications," *Electronics Letters*, vol. 6, no. 8, pp. 331–333, Aug. 2002.

[96] A. Abdi and M. Kaveh, "Envelope PDF in multipath fading channels with random number of paths and nonuniform phase distributions," pp. 275–282, 1999.

[97] F. D. Neeser and J. L. Massey, "Proper complex random processes with applications to information theory," *IEEE Trans. Info. Theory*, vol. 39, pp. 1293–1302, Jul. 1993.

[98] T. A. Lamahewa, T. D. Abhayapala, R. A. Kennedy, and J. T. Y. Ho, "Space-time cross correlation and space-frequency cross spectrum in non-isotropic scattering environment," *International Conference on Acoustics, Speech, and Signal Processing*, vol. 4, May 2006.

[99] D. Torrieri, *Principles of Spread-Spectrum Communication Systems.* Springer, 2005.

[100] D. Tse and P. Viswanath, *Fundamentals of wireless communication.* New York, NY, USA: Cambridge University Press, 2005.

[101] J. R. Barry, D. G. Messerschmitt, and E. A. Lee, *Digital Communication: Third Edition.* Norwell, MA, USA: Kluwer Academic Publishers, 2003.

[102] C. Xiao, J. Wu, S. Leong, Y. R. Zheng, and K. Letaief, "A discrete-time model for triply selective MIMO Rayleigh fading channels," *IEEE Trans. on Wireless Comm.*, vol. 3, no. 5, pp. 1678–1688, Sep. 2004.

[103] P. A. Bello, "Characterization of randomly time-variant linear channels," *IEEE transactions on communications*, vol. 11, pp. 360–393, 1963.

[104] P. Petrus, J. H. Reed, and T. S. Rappaport, "Geometrically based statistical channel model for macrocellular mobile environments," in *Proc. GLOBECOM 96*, vol. 4, 1996, p. 11971201.

[105] R. Janaswamy, "Angle and time of arrival statistics for the Gaussian scatter density model," *IEEE Transactions on Wireless Communications*, vol. 1, no. 3, pp. 488–497, Jul. 2002.

[106] A. Abdi and M. Kaveh, "A versatile spatio-temporal correlation function for mobile fading channels with nonisotropic scattering," in *Proc. Tenth IEEE Workshop on Statistical Signal and Array Processing*, Pocono Manor, PA, 2000, pp. 58–62.

[107] ——, "A space-time correlation model for multielement antenna systems in mobile fading channels," *IEEE journal on Selected Areas in Communications*, vol. 20, pp. 550–560, May 2002.

[108] R. B. Ertel and H. Reed, "Angle and time of arrival statistics for circular and elliptical scattering models," *IEEE journal on Selected Areas in Communications*, vol. 17, pp. 1829–1840, Nov. 1999.

[109] J. W. Wallace and M. A. Jensen, "Statistical characteristics of measured MIMO wireless channel data and comparison to conventional models," in *Proc. IEEE Vehicular Technol. Conf., VTC'01*, vol. 2, 2001, pp. 1078–1082.

[110] Q. H. Spencer, B. D. Jeffs, M. A. Jensen, and A. L. Swindlehurst, "Modeling the statistical time and angle of arrival characteristics of an indoor multipath channel," *IEEE journal on Selected Areas in Communications*, vol. 18, pp. 347–360, Mar. 2000.

[111] V. U. Reddy, A. Paulraj, and T. Kailath, "Performance analysis of the optimum beamformer in the presence of correlated sources and its behaviour under spatial smoothing," *IEEE Transactions on Acoustics, Speech and Signal Processing*, vol. 35, no. 7, pp. 927–937, 1987.

[112] T. J. Shan and T. Kailath, "Adaptive beamforming for coherent signals and interference," *IEEE Transactions on Acoustics, Speech and Signal Processing*, vol. 33, no. 3, pp. 527–536, 1985.

[113] T. Betlehem and T. D. Abhayapala, "Spatial correlation for correlated scatterers," in *Proc. IEEE International Conf. on Acoustics, Speech, and Signal Processing (ICASSP)*, vol. 4, Toulouse, France, May 2006, pp. 5–8.

[114] A. V. Oppenheim and R. Shafer, Eds., *Discrete-Time Signal Processing*, 2nd ed. New Jersey: Prentice Hall, 1989.

[115] M. Kalkan and R. H. Clarke, "Prediction of the space frequency correlation function for base station diversity reception," *IEEE Trans. Vehic. Technol.*, vol. VT-46, no. 1, pp. 176–184, Feb. 1997.

[116] M. Abramowitz and I. A. Stegun, *Handbook of Mathematical Functions*. New York: Dover Publications, Inc., 1972.

[117] G. B. Folland, *Real Analysis*, 2nd ed. New York: Wiley-Interscience, 1972.

[118] F. Comte, Y. Rozenholc, and M. L. Taupin, "Penalized contrast estimator for density deconvolution," in *The Candian Journal of Statistics*, vol. 34, no. 3, 2006.

[119] O. Darvishi, B. Abolhassani, and H. S. Rad, "A correlation approach to time fequency representations," in *IEEE Sarnoff Symposium, 2009*, Apr. 2009, pp. 1–5.

[120] D. Chizhik, "Slowing the time-fluctuating MIMO channel by beam forming," *IEEE transactions on wireless comm.*, vol. 3, no. 5, pp. 1554–1565, Sep. 2004.

[121] M. de Smith, M. F. Goodchild, and P. A. Longley, *Geospatial Analysis: A Comprehensive Guide to Principles, Techniques and Software Tools*. Troubador Publishing, 2007.

[122] K. Mardia, *Statistics of directional data*. New York: Academic Press, 1972.

[123] N. Zink and X. Yin, "Estimation of cluster angular spread in MIMO indoor environments," in *Proc. 3rd Workshop on Signal Processing for Wireless Communication*, UK, 2005.

[124] M. Evans, N. Hastings, and B. Peacock, Eds., *Statistical distributions*. New York: Wiley, 2000, vol. 3.

[125] T. M. Cover and J. A. Thomas, *Elements of Information Theory*. New York: Wiley Interscience, 1991.

[126] A. A. Farid, Z. Q. Luo, and Z. Ding, "Blind channel equalization based on second order statistics," *International Conference on Acoustics, Speech, and Signal Processing*, vol. 3, pp. 557–560, 2005.

[127] L. Tong, G. Xu, B. Hassibi, and T. Kailath, "Blind channel identification based on second-order statistics: A frequency-domain approach," *IEEE Trans. on Inform. Theory*, pp. 329–334, 1995.

[128] C. E. Shannon, "A mathematical theory of communication," *Bell Systems Technical Journal*, vol. 27, pp. 379–423, Jul and Oct 1948.

[129] E. Biglieri, J. G. Proakis, and S. Shamai, "Fading channels: Information-theoretic and communication aspects," in *IEEE Transactions on Information Theory*, vol. 44, no. 6, Oct 1998, pp. 2619–2692.

[130] L. Tong, B. M. Sadler, and M. Dong, "Pilot-assisted wireless transmissions," *IEEE Signal Processing Mag*, vol. 21, pp. 12–25, 2004.

[131] J. Baltersee, G. Fock, and H. Meyr, "Achievable rate of MIMO channels with data-aided channel estimation and perfect interleaving," *IEEE Journal on Selected Areas of Communications*, vol. 19, December 2001.

[132] S. M. Kay, *Fundamentals of statistical signal processing: estimation theory*. Upper Saddle River, NJ, USA: Prentice-Hall, Inc., 1993.

[133] H. H. Zeng and L. Tong, "Blind channel estimation using the secondorder statistics: algorithms," *IEEE Trans. Signal Processing*, vol. 45, pp. 1919–1930, 1997.

[134] A. Lapidoth and S. Shamai, "Fading channels: How perfect need "Perfect side information" be?" *IEEE Transactions on Information Theory*, vol. 48, no. 5, pp. 1118–1134, 2002.

[135] M. Médard, "The effect upon channel capacity in wireless communications of perfect and imperfect knowledge of the channel," *IEEE Trans. Info. Theory*, vol. 46, no. 3, pp. 933–946, May 2000.

[136] J. Baltersee, G. Fock, and H. Meyr, "An information thoeretic foundation of synchronized detection," *IEEE Transactions on communication*, vol. 49, no. 12, pp. 2115–2123, Dec. 2001.

[137] B. Hassibi and B. M. Hochwald, "How much training is needed in multiple-antenna wireless links?" *IEEE Transactions on Information Theory*, vol. 49, no. 4, pp. 951–963, April 2003.

[138] O. Al-Askary and S. Slimane, "Effect of error in channel state information on the channel capacity with QAM signalling and the design of robust signal constellations," *IET Communications*, pp. 1118–1125, Dec. 2007.

[139] P. Sadeghi, Y. Liu, R. A. Kennedy, and P. B. Rapajic, "Pilot symbol transmission for time-varying fading channels: An information-theoretic optimization," in *Proc. Int. Conf. on Signal Processing and Commun. Syst. (ICSPCS)*, Goldcoast, Australia, Dec. 2007.

[140] J. K. Cavers, "An analysis of pilot symbol assisted modulation for Rayleigh fading channels," *IEEE Trans. Vehic. Technol.*, vol. 40, no. 4, pp. 686–693, Nov. 1991.

[141] D. Samardzija and N. Mandayam, "Pilot assisted estimation of MIMO fading channel response and achievable data rates," *IEEE Transactions on Signal Processing, Special Issue on* MIMO, vol. 51, pp. 2882–2890, Nov. 2003.

[142] T. L. Marzetta, "BLAST training: Estimating channel characteristics for high-capacity space-time wireless," in *Proc. 37th Annual Allerton Conference on Communications, Control, and Computing*, 1999, pp. 22–24.

[143] D. Katselis, E. Kofidis, and S. Theodoridis, "Training-based estimation of correlated MIMO fading channels in the presence of colored interference," *Signal Process.*, vol. 87, no. 9, pp. 2177–2187, 2007.

[144] C. Fragouli, N. Al-Dhahir, and W. Turin, "Training-Based Channel Estimation for Multiple Antenna Broadband Transmissions," *IEEE Transactions on Wireless Communications*, vol. 2, no. 2, pp. 384–391, 2003.

[145] M. Kiessling, J. Spiedel, and Y. Chen, "MIMO channel estimation in correlated fading environments," in *Proc. of IEEE Vehicular Technology Conference,* VTC, Oct. 2003.

[146] J. G. Proakis, *Digital Communications*, 4th ed. New York: McGraw-Hill, 2000.

[147] T. S. Rappaport, *Wireless Communications: Principles and Practice*. New Jersey: Prentice Hall, 1996.

[148] U. Grenander and G. Szegö, Eds., *Toeplitz Forms and Their Applications*. New York: McGraw-Hill, 1954.

[149] R. Iqbal and T. D. Abhayapala, "On statistics of the mobile Rayleigh fading channel in non-isotropic scattering environments," in *Proc. IEEE 7th Interna-*

tional Symposium on Communications and Information Technologies, Sydney, Oct 2007, pp. 814–818.

[150] A. Papoulis, *Probability, Random Variables, and Stochastic Processes*. McGraw Hill, 1984.

[151] F. J. Scire, "A probability density function thoerem for the modulo y values of the sum of two statistically independent processes," in *Proceedings of the IEEE*, vol. 56, no. 2, Feb. 1968, pp. 204–205.

[152] J. P. Romano and A. F. Siegel, *Counterexamples in Probability and Statistics*. CRC Press, 1986.

[153] L. Tong, B. M. Sadler, and M. Dong, "Pilot assisted wireless transmission: General model, design criteria, and signal processing," *IEEE Signal Processing Magazine*, vol. 21, no. 6, pp. 12–25, Nov. 2004.

[154] K. E. Baddour and N. C. Beaulieu, "Autoregressive models for fading channel simulation," in *Proc. IEEE Global Commun. Conf. (GLOBECOM)*, San Antonio, TX, Nov. 2001, pp. 1187–1192.

[155] K. S. Miller, "Complex Gaussian processes," SIAM R*eview*, vol. 11, no. 4, pp. 544–547, Oct 1969.

[156] R. Bellman, *Introduction to matrix analysis (2nd ed.)*. Philadelphia, PA, USA: Society for Industrial and Applied Mathematics, 1997.

[157] S. Qian and D. Chen, "joint time-frequency analysis," *IEEE Sig. Proc. Mag.*, pp. 53–67, Mar. 1999.

[158] W. Martin and P. Flandrin, "Wigner-Ville spectral analysis of nonstationary processes," *Proc. IEEE Int. Conf. Acoust., Speech Signal Processing*, vol. ASSP-33, pp. 1461–1470, Dec. 1985.

[159] F. Hlawatsch and W. Kozek, "Second-order time-frequency synthesis of nonstationary random processes," *IEEE Trans. Info. Theory*, vol. 41, no. 1, pp. 1461–1470, Jan. 1995.

[160] E. M. Gibson, *The Mobile Communications Handbook*, J. D. Gibson, Ed. Boca Raton, FL, USA: CRC Press, Inc., 1998.

[161] E. Lutz, D. Cygan, M. Dippold, F. Dolainsky, and W. Papke, "The land mobile satellite communication channel — recording, statistics, and channel model,"

IEEE Transactions on Vehicular Technology, vol. VT-40, no. 2, pp. 375–386, May 1991.

[162] M. S. Karaliopoulos and F. N. Pavlidou, "Modelling the land mobile satellite channel: a review," *Electronics & Communication Engineering Journal*, vol. 11, no. 5, pp. 235–248, Oct. 1999.

[163] O. Florens, D. Roviras, N. Thomas, and J. Lanciaux, "Effect of non-stationarity on radio-mobile channel capacity," in *Proceedings 2004 International Information and Communication Technologies: From Theory to Applications, 2004*, Apr. 2004, pp. 253–254.

[164] T. M. Duman and A. Ghrayeb, Eds., *Coding for MIMO Communication Systems*. John Wiley and Sons, 2007.

[165] M. Afgani, S. Sinanović, K. Kashaba, and H. Haas, "Radio frequency signature correlation based speed estimation for indoor positioning," *Journal of Communications*, vol. 4, no. 2, pp. 96–107, Mar. 2009.

[166] P. Roy and A. A. Beex, "Flat fading channel envelope prediction and equalization," in *Proc. Thirty-Fifth IEEE Asilomar Conference on Signals, Systems and Computers*, vol. 2, Pacific Grove, CA, USA, 2001, pp. 1116–1120.

[167] J. Wheat, R. Hiser, J. Tucker, A. Neely, and A. McCullough, *Designing a wireless network*. USA: Syngress Publishing, 2001.

[168] R. Steele, "Toward a high-capacity digital cellular mobile radio system," *Proc. Inst. Elect. Eng*, vol. 132, pt. F, pp. 405–415, Aug. 1985.

[169] A. M. Hammoudeh, M. G. Sánchez, and E. Grindrod, "Experimental analysis of propagation at 62 GHz in suburban mobile radio microcells," *IEEE Trans. Vehic. Technol.*, vol. 48, no. 2, pp. 576–588, Mar. 1999.

[170] M. E. Ware and C. L. Brewer, Eds., *Handbook for teaching statistics and research methods*, 2nd ed. Lawrence Erlbaum Associates, 1998.

[171] G. Matz, "On non-WSSUS wireless fading channels," *IEEE Transactions on Wireless Communications*, vol. 4, no. 5, pp. 2465–2478, 2005.

[172] E. B. Corrochano, *Handbook of Geometric Computing: Applications in Pattern Recognition, Computer Vision, Neural computing, and Robotics*. Secaucus, NJ, USA: Springer-Verlag New York, Inc., 2005.

[173] D. Gabor, "theory of communication," *Journal of the Institution of Electrical Engineers (IEE)*, vol. 93, pp. 429–457, Nov. 1946.

[174] A. Prochazka, N. G. Kingsbury, P. J. W. Payner, and J. Uhlir, *Signal Analysis and Prediction*. Birkhäuser, 1998.

[175] P. M. Oiviera and V. Barroso, "Uncertainty in the time-frequency plane," in *Proc. of the Tenth IEEE Workshop on Statistical Signal and Array Processing*, 2000, pp. 607–611.

[176] L. Cohen, "Time frequency distributions- a review," *Proceedings of IEEE*, vol. 77, no. 7, pp. 941–981, 1989.

[177] M. Perry, "A correlation approach to time fequency representations," in *Proceedings of the IEEE-SP International Symposium on Time-Frequency and Time-Scale Analysis*, Oct. 1992, pp. 249–252.

[178] E. P. Wigner, "On the quantum correction for thermodynamic equilibrium," *Physical Review*, vol. 40, p. 749, Mar. 1932.

[179] J. Ville, "theorie et applications de la notion de signal analytique," *C & T*, vol. 2-A, no. 1, 1948.

[180] A. P. Suppappola, Ed., *Applications in time-frequency signal processing*. CRC Press, 2002.

[181] L. M. Khadra, "The smoothed pseudo-Wigner distribution in speech processing," *International Journal of Electronics*, vol. 65, no. 4, pp. 743–755, 1988.

[182] T. A. C. M. Claasen and W. F. G. Mecklenbräuker, "The Wigner distribution-a tool for time-frequency signal analysis, part i. continuous-time signals," *Philips J. Res.*, vol. 35, pp. 217–250, 1980.

[183] A. M. Sayeed and D. L. Jones, "Optimal kernels for nonstationary spectral estimation," *IEEE Trans. on Signal Processing*, vol. 43, no. 2, pp. 478–491, Feb. 1995.

[184] A. W. Rihaczek, "Signal energy distribution in time and frequency," *IEEE Trans. Info. Theory*, vol. IT-14, no. 3, pp. 369–374, May 1968.

[185] S. Aviyente and W. S. Evans, "Phase synchrony measures for the study of functional brain networks," in *Forty-Fifth Annual Allerton Conference Allerton House, UIUC, Illinois, USA*, Sep. 2007, pp. 1268–1275.

[186] B. P. Lathi, *Modern Digital and Analog Communication Systems*, 3rd ed. Oxford University Press, 1998.

[187] R. D. hippenstiel and P. M. Oliviera, "Instantaneous power spectrum," in *Twenty-Second Asilomar Conference on Signals, Systems and Computers*, 1988, pp. 214–218.

[188] T. A. C. M. Claasen and W. F. G. Mecklenbräuker, "The Wigner distribution-a tool for time-frequency signal analysis, part i. continuous-time signals," *Proc. IEEE Int. Conf. Acoust., Speech Signal Processing*, vol. ASSP-31, no. 5, pp. 1067–1072, Oct. 1983.

[189] S. S. Abeysekera, "computation of Wigner-Ville distribution for complex data," *IEEE Elect. Lett.*, vol. 26, no. 16, pp. 1315–1317, Aug. 1990.

[190] T. A. C. M. Claasen and W. F. G. Mecklenbräuker, "The Wigner distribution-a tool for time-frequency signal analysis, part i. continuous-time signals," *Philips J. Res.*, vol. 35, no. 4/5, pp. 276–300, 1980.

[191] D. S. K. Chan, "A non-aliased discrete time Wigner distribution for time-frequency signal analysis," in *Proc. IEEE Int. Conf. Acoust., Speech Signal Processing*, Paris, France, 1982, pp. 1333–1336.

[192] I. S. Gradshteyn and I. M. Ryzhik, Eds., *Tables of Integral, Series and Products*, New York, 2000, vol. VI.

[193] Y. T. Takizawa, K. Oda, and A. Fukasawa, "instantaneous spectral estimation of nonstationary signals," in *Proc. IEEE Int. Conf. Acoust., Speech Signal Processing*, Paris, France, 1982, pp. 329–332.

[194] A. Y. Rom, "Ground state of a spinless charged particle in a periodic magnetic field," *Physical Review B*, vol. 55, no. 17, pp. 11 025–11 028, May 1997.

[195] R. Iqbal, T. Abhayapala, and T. Lamahewa, "Generalized Clarke model for mobile radio reception," *IET Communications*, vol. 3, no. 4, pp. 644–654.

[196] L. Deng and D. O'Shaughnessy, *Speech processing: a dynamic and optimization-oriented approach*. CRC Press, 2003.

[197] P. W. Atkins, *Galileo's finger: the ten great ideas of science*. Oxford University Press, 2003.

[198] P. S. Naidu, *Modern Digital Signal Processing: An Introduction*. Alpha Science, 2003.

[199] H. Meyr, M. Moeneclaey, and S. Fechtel, *Digital Communication Receivers: Synchronization, Channel Estimation, and Signal Processing*. New York, NY, USA: John Wiley & Sons, Inc., 1997.

[200] J. Baltersee, G. Fock, and H. Meyr, "An information theoretic foundation of synchronized detection," vol. 49, no. 12, pp. 2115–2123, Dec. 2001.

[201] F. J. Harris, "On the use of windows for harmonic analysis with the discrete Fourier transform," *Proc. IEEE*, vol. 66, pp. 51–83, Jan. 1978.

[202] S. V. Narasimhan and S. Pavanalatha, "Estimation of evolutionary spectrum based on short time Fourier transform and modified group delay," *Signal Processing*, vol. 84, no. 11, pp. 2139–2152, 2004.

[203] G. Zelniker and F. J. Taylor, *Advanced Digital Signal Processing: Theory and Applications*. New York, NY, USA: Marcel Dekker, Inc., 1993.

[204] M. Jaskula, "New windows family based on modified Legendre polynomials," in *Proceedings of the 19th IEEE Instrumentation and Measurement Technology Conference, 2002. IMTC/2002*, vol. 1, 2002, pp. 553–556.

[205] G. Casinovi, "Windowing techniques in frequency-domain simulation," in *Proceedings of the 2002 IEEE International Workshop on Behavioral Modeling and Simulation, Santa Rosa, CA*, Oct. 2002, pp. 54–60.

[206] M. Abramowitz and I. Stegun, *Handbook of Mathematical Functions with Formulas, Graphs, and Mathematical Tables*, 9th ed. New York: Dover, 1964.

[207] S. F. Su, *The* UMTS *air-interface in* RF *engineering: design and operation of* UMTS *networks*. McGraw-Hill Professional, 2007.

[208] J. Dixon and C. Wijting, "Considerations in the choice of suitable spectrum for mobile communications," Wireless World Research Forum, Nov. 2008, http://www.wireless-world-research.org/fileadmin/sites/default/files/publications/Outlook/Outlook2.pdf.

[209] S. Verdu, "Fading channels in the power-limited regime," in *IEEE Information Theory Workshop.*, 2001, pp. 99–100.

[210] B. Hassibi and B. M. Hochwald, "How much training is needed in multiple-antenna wireless links?" *IEEE Trans. Info. Theory*, vol. 49, no. 4, pp. 951–963, Apr. 2003.

[211] J. J. van de Beek, O. Edfors, M. Sandell, S. K. Wilson, and P. O. Börjesson, "On channel estimation in OFDM systems," in *Proc. of the IEEE Vehicular Technology Conference, VTC 95*, 1995, pp. 815–819.

[212] L. Huang, C. K. Ho, and F. M. J. Willems, "Pilot-aided angle-domain channel estimation techniques for MIMO-OFDM systems," *IEEE Trans. Vehic. Technol.*, vol. 57, no. 2, pp. 906–920, Mar. 2008.

[213] Y. Li, L. J. Cimini, and N. R. Sollenberger, "Robust channel estimation for OFDM systems with rapid dispersive fading channels," *IEEE Trans. Commun.*, vol. 46, no. 7, pp. 902–915, Jul. 1998.

[214] O. Edfors, M. Sandell, J. J. van de Beek, S. K. Wilson, and P. O. Börjesson, "OFDM channel estimation by singular value decomposition," *IEEE Trans. Commun*, vol. 46, pp. 931–939, 1996.

[215] V. Subramanian and V. G. Subramanian, "Broadband fading channels: Signal burstiness and capacity," *IEEE Transactions on Information Theory*, vol. 48, pp. 809–827, 1999.

[216] M. Mèdard and R. G. Gallager, "Bandwidth scaling for fading multipath channels," *IEEE Trans. Info. Theory*, vol. 48, pp. 840–852, Apr. 2002.

[217] D. S. Lun, M. Mèdard, and I. C. Abou-faycal, "On the performance of peaky capacity-achieving signaling on multipath fading channels," *IEEE Trans. Commun*, vol. 52, pp. 931–938, 2003.

[218] S. Akin and M. C. Gursoy, "Achievable rates and training optimization for fading relay channels with memory," *in 42nd Annual Conference on Information Sciences and Systems (CISS)*, pp. 185–190, Mar. 2008.

[219] S. Weiβ, A. Stenger, R. Rabenstein, and R. W. Stewart, "Lower error bound for oversampled subband adaptive filters," *Electronics Letters*, vol. 34, no. 16, pp. 1555–1557, Aug. 1988.

[220] T. Kailath, A. Sayed, and B. Hassibi, *Linear Estimation*. Prentice-Hall, 2000.

[221] K. Yu, J. Evans, and I. Collings, "Performance Analysis of Pilot Symbol Aided QAM for Rayleigh Fading Channels," in *IEEE International Conference on Communications*, vol. 3, 2002, pp. 1731–1735.

[222] X. Cai and G. B. Giannakis, "Adaptive PSAM accounting for channel estimation and prediction errors," *IEEE transactions on communications*, vol. 4, no. 1, pp. 246–256, Jan 2005.

[223] R. K. Morrow, *Bluetooth operation and use*. McGraw-Hill Professional, 2002.

[224] J. Zhang, J. W. Mark, and X. Shen, "An adaptive resource reservation strategy for handoff in wireless CDMA cellular networks," in *Canadian Journal of IEEE*, vol. 29, no. 1, Jan-Apr. 2004, pp. 77–83.

[225] D. Gesbert, M. Shafi, D. S. Shiu, P. Smith, and A. Naguib, "From theory to practice: An overview of MIMO space-time coded wireless systems," *IEEE Journal on Selected Areas in Communications, Special Issue on MIMO Systems*, vol. 21, no. 3, pp. 281–302, Apr. 2003.

[226] B. Bing, *Emerging Technologies in Wireless LANs: Theory, Design, and Deployment*. Cambridge University Press, 2007.

[227] J. G. Proakis, *Digital Communications*. New York: McGraw-Hill, 1995.

[228] K. K. Parhi and T. Nishitani, Eds., *Digital signal processing for multimedia systems*. CRC Press, 1999.

[229] A. Goldsmith, *Wireless Communications*. New York: Cambridge Unniversity Press, 2005.

[230] J. Armstrong, *OFDM: Principles and Applications of Orthogonal Frequency Division Multiplexing*. John Wiley & Sons, Limited, 2007.

[231] H. Schulze and C. Luders, *Theory and Application of OFDM and CDMA: Wideband Wireless Communication*. John Wiley & Sons Inc, 2005.

[232] W. Webb, *Wireless Communications: The Future*. John Wiley & Sons Inc, 2007.

[233] F. Xiong, *Digital Modulation Techniques (Artech House Telecommunications Library)*, 2nd ed. Artech House, 2006.

[234] W. C. Y. Lee, "Antenna spacing requirements for a mobile radio base-station diversity," *Bell Systems Technical Journal*, vol. 50, pp. 1859–1876, July-Aug 1971.

[235] ——, "Effects on correlation between two mobile radio base-station antennas," *IEEE Transactions on communications*, vol. COM-21, pp. 1214–1224, Nov 1973.

[236] D. Asztély, "On antenna arrays in mobile communication systems: Fast fading and GSM base station receiver algorithms," Royal Inst. of Technology, Stockholm, Sweden, Tech. Rep. IR-S3-SB-9611, Mar. 1996.

[237] H. Bölcskei and A. J. Paulraj, "Space-frequency coded broadband OFDM systems," in *Wireless Comm. Networking Conf. (WCNC)*, vol. 1, Chicago, IL, Sep. 2000, pp. 1–6.

[238] S. K. Yong, C. C. Chong, A. Pandharipande, and S. S. Lee, "Space-frequency correlation model for multi antenna, multi-band OFDM in UWB communication systems," in *Intelligent Vehicles Symposium*, Jun. 2005, pp. 520–524.

[239] R. Nee and R. Prasad, *OFDM for Wireless Multimedia Communications*. Norwell, MA: Artech House, 2000.

[240] G. Durgin, *Space-time wireless channels*. Upper Saddle River, NJ, USA: Prentice Hall Press, 2002.

[241] K. Witrisal, K. Yong-Ho, and R. Prasad, "A new method to measure parameters of frequency-selective radio channels using power measurements," *IEEE Transactions on Communications*, vol. 49, no. 10, pp. 1788–1800, Oct. 2001.

[242] A. Saleh and R. Valenzuela, "A statistical model for indoor multipath propagation," *IEEE journal on Selected Areas in Communications*, vol. 5, no. 2, pp. 128–137, 1987.

[243] T. D. Abhayapala, T. S. Pollock, and R. A. Kennedy, "Characterization of 3D spatial wireless channels," in *Proc. IEEE Vehicular Technology Conference, VTC'03-Fall*, vol. 1, Orlando, Florida, USA, Oct. 2003, pp. 123–127.

[244] ——, "Spatial decomposition of MIMO wireless channels," in *Proc. 7th International Symposium on Signal Processing and its Applications*, vol. 1, Paris, France, Jul. 2003, pp. 309–312.

[245] G. Fochsini and S. Verdù, Eds., *Multiantenna channels: capacity coding and signal processing: DIMACS Workshop Signal Processing for Wireless Transmission, October 7-9, 2002, DIMACS Center*. AMS bookstore, 2003.

[246] T. A. Lamahewa, T. D. Abhayapala, R. A. Kennedy, and J. T. Y. Ho, "Space-time cross correlation and space-frequency cross spectrum in non-isotropic scattering environments," in *Proc. IEEE Int. Conf. Acoust., Speech Signal Processing*, vol. IV, Toulouse, France, May 2006, pp. 609–612.

[247] D. Poole, *Linear Algebra: A Modern Introduction (with CD-ROM)*. Brooks Cole, Jan 2005.

[248] C. ReVelle, A. E. McGarity, and editors, *Design and Operation of Civil and Environmental Engineering Systems*. New York: Wiley Interscience, 1997.

[249] G. N. Watson, Ed., *A Treatise on the Theory of Bessel Functions*, 2nd ed. Cambridge Mathematical Library, 1995.

[250] D. H. Bailey and P. N. Swarztrauber, "The Fractional fourier transform and applications," *SIAM review*, vol. 33, no. 3, pp. 389–404, Sep. 1991.

[251] L. Onural, "Some mathematical properties of the uniformly sampled quadratic phase function and associated issues in digital Fresnel diffraction simulations," *Optical Engineering*, vol. 43, no. 11, pp. 2557–2563, Nov. 2004.

[252] Z. Chen, S. Haykin, J. J. Eggermont, and S. Becker, Eds., *Correlative Learning: A Basis for Brain and Adaptive Systems*. Wiley-Interscience, Nov. 2007.

[253] B. C. Reed, *Quantum Mechanics*. Massachusetts: Jones & Bartlett Publishers, 2007.